...dedicated to my parents

in love and gratitude

Erfolg erfordert oft eine Kombination vieler Faktoren: harte Arbeit, Intelligenz, Kreativität, Organisationstalent - und auch Glück.

Wolfgang Ketterle, Nobelpreisträger Physik 2001

Strukturelle und elektrochemische Charakterisierung rußgeträgerter Pt-Ru und Pt-Ru-W Katalysatoren für die Anwendung in Membran-Brennstoffzellen

Dem Fachbereich Material- und Geowissenschaften
der Technischen Universität Darmstadt
zur
Erlangung des akademischen Grades eines
Doktor-Ingenieurs
genehmigte Dissertation

vorgelegt von
Dipl.-Ing. Christina Roth
aus Jugenheim

Referent:	Prof. Dr.-Ing. H. Fueß
Korreferenten:	Prof. Dr. C. Lamy
	Prof. Dr. E. Exner
Tag der Einreichung:	16.04.2002
Tag der mündlichen Prüfung:	13.06.2002

Darmstadt 2002

D 17

Diese Arbeit wurde in der Zeit von Oktober 1998 bis Januar 2002 am Institut für Materialwissenschaft der Technischen Universität Darmstadt unter der Leitung von Herrn Prof. Dr.-Ing. H. Fueß durchgeführt.

Zusammenfassung

Aufgrund der stetig anwachsenden Umweltbelastung, u.a. durch Industrie- und Autoabgase, ist die Nachfrage nach alternativen schadstoffarmen Energiewandlern mit hohem Wirkungsgrad sprunghaft angestiegen. In diesem Zusammenhang zählt besonders die Brennstoffzellentechnik mit diversen Anwendungen sowohl im stationären, aber vor allem auch im mobilen Bereich zu den Schlüsseltechnologien des 21. Jahrhunderts. So können Niedertemperatur-Brennstoffzellen (PEM-BZ) schon in naher Zukunft eine ernstzunehmende Konkurrenz für den konventionellen Ottomotor werden, ihn vielleicht sogar komplett ablösen. Dazu muß allerdings zuerst deren Preis weiter gesenkt werden, was u.a. durch die Verwendung von billigeren und zur bereits vorhandenen Infrastruktur kompatiblen Brennstoffen, wie z.B. Methanol, erreicht werden soll.

Die Verstromung von Methanol kann entweder direkt in der sogenannten DMFC erfolgen, oder über eine vorgeschaltete Methanolreformierungsstufe an Bord des Fahrzeugs (IMFC). Nachteilig sind hierbei jedoch einschneidende Leistungseinbußen bei der Zellperformance durch bei der direkten Methanolumsetzung entstehendes bzw. im Reformat enthaltenes Kohlenmonoxid, das die aktiven Katalysatorzentren vergiftet. Bei typischen Brennstoffzellen-Temperaturen um 80 °C kann das Katalysatorgift nur oxidativ durch auf Nachbarplätzen adsorbierte Sauerstoffspezies entfernt werden. Solche werden jedoch an reinen Platinelektroden erst bei Potentialen oberhalb 700 mV gegen die reversible Wasserstoffelektrode bereitgestellt (Wasseraktivierung). Aus diesem Grund konzentriert sich die Brennstoffzellen-Forschung gegenwärtig auf die Entwicklung binärer und ternärer Katalysatorsysteme, welche die Wasseraktivierung schon bei niedrigeren Potentialen ermöglichen und somit die anodische Überspannung reduzieren bzw. letztlich die Zelleistung steigern. Bereits kommerziell eingesetzt wird ein rußgeträgerter Pt-Ru (1:1)-Katalysator, der bislang die besten Ergebnisse im Reformatbetrieb gezeigt hat. Allerdings sind erst kürzlich zahlreiche Veröffentlichungen zu weiteren binären und ternären Systemen erschienen, und die Suche nach besser geeigneten und kostengünstigeren Alternativen geht ungebrochen weiter.

Der Schwerpunkt der vorgelegten Arbeit liegt auf der kombinierten strukturellen und elektrochemischen Charakterisierung ausgewählter binärer und ternärer Anodenkatalysatoren mit der Zielsetzung, zu einem besseren Verständnis der Korrelation zwischen der Katalysatorstruktur und der resultierenden elektrokatalytischen Aktivität zu gelangen.

Dazu wurden verschiedene rußgeträgerte binäre und ternäre Katalysatorsysteme nach unterschiedlichen Synthesemethoden hergestellt, deren Struktur mit diversen Bulk- und Oberflächenmethoden ermittelt und die resultierende elektrokatalytische Aktivität bestimmt. Binäre Pt-Ru (1:1) Systeme wurden einerseits in wäßriger Phase unter Verwendung zweier unterschiedlicher Reduktionsmittel, andererseits nach der *Bönnemann* Kolloidmethode präpariert, wohingegen ternäre Pt-Ru-W-Katalysatoren verschiedener Stöchiometrie ausschließlich über Kolloidbildung synthetisiert wurden. Die Auswahl der unterschiedlichen Synthesevorschriften erfolgte gemäß den Angaben der entsprechenden Autoren, daß Reduktion in wäßriger Phase zu separat vorliegenden Pt- und Ru-Nanoteilchen führt, während mit der *Bönnemann*-Methode eine Legierung erzielt werden sollte. Das Gelingen der Synthese und die korrekte Stöchiometrie der synthetisierten Systeme wurde mit Röntgenfluoreszenzanalyse (RFA) überprüft. Informationen zur Dispersion der katalytisch aktiven Partikel auf dem Träger und zum Vorliegen kristalliner Phasen wurden dagegen mit Röntgenbeugung (XRD) und Transmissions-elektronenmikroskopie (TEM) erhalten. Aufgrund ihrer besonderen Bedeutung für die elektrokatalytische

Aktivität wurden die Partikelgröße und die Partikelgrößenverteilung sowohl mit XRD nach der Scherrer-Gleichung als auch mit dem Transmissionselektronenmikroskop bestimmt. Zusätzlich konnte im TEM mittels einer nano-EDX Vorrichtung die Zusammensetzung einzelner Teilchen untersucht werden, wobei allerdings eine gewisse Mindestgröße der Partikel Voraussetzung ist. Als ergänzende Charakterisierungsmethoden wurden noch Röntgenphotoelektronenspektroskopie (XPS) und Röntgenabsorptionsspektroskopie (XAS) gewählt, mit deren Hilfe auch amorphe Phasen und röntgenamorphe, sehr kleine Nanoteilchen erfaßt werden können. Vor den elektrochemischen Messungen wurden alle synthetisierten Katalysatorsysteme mit sämtlichen oben aufgeführten Methoden charakterisiert.

Zur Messung der elektrokatalytischen Aktivität der einzelnen Katalysatoren wurden zwei verschiedene Techniken verwendet, und zwar zyklische Voltametrie (CV) bzw. zyklische Voltametrie in Kombination mit Infrarotspektroskopie (CV/FTIRS) und realitätsnahe Brennstoffzellen-Tests in Einzelzellen. Die CV und CV/FTIRS-Untersuchungen wurden mit konventioneller Drei-Elektroden-Anordnung unter Verwendung verschiedener Vorschubgeschwindigkeiten und entweder in Methanol oder im CO-stripping Modus durchgeführt. Dazu wurde das geträgerte Katalysatorpulver mit einer entsprechenden Menge Nafion®-Ionomer zu einer dickflüssigen Tinte verarbeitet und auf eine Glaskohlenstoff-Scheibe aufgebracht. Für die spektroelektrochemischen Messungen (CV/FTIRS) kamen zwei verschiedene Meßmodi zur Anwendung, von denen der eine besser zur Detektion von adsorbierten Spezies geeignet ist und der andere zur Untersuchung von Spezies in Lösung. Aus der potentialabhängigen CO-Adsorption bzw. Oxidation können dann Rückschlüsse auf unterschiedliche Reaktionsmechanismen und die unterschiedliche Aktivität der verschieden hergestellten Systeme gezogen werden. Zur Durchführung von Einzelzellmessungen wurden Elektrode-Membran-Elektrode-Einheiten hergestellt und mit Rasterelektronenmikroskopie (SEM), Atomabsorptionsspektroskopie (AAS) und BET-Analyse hinsichtlich ihrer tatsächlichen Edelmetallbeladung und ihrer Porosität charakterisiert. Reale Brennstoffzellen-Versuche wurden mit Wasserstoff, H_2/CO-Gasmischungen (75 ppm CO/H_2, 150 ppm CO/H_2) oder einer gasförmigen wäßrigen 1M-Methanollösung durchgeführt.

Da ein Ziel der vorgelegten Arbeit darin bestand, das Verhalten der Katalysatoren in der Brennstoffzelle unter realen Betriebsbedingungen zu verfolgen, wurde eine neuartige in-situ Zelle für Brennstoffzellen-Messungen am Strahlplatz X1 am Hamburger Synchrotronlabor konstruiert. Obwohl bereits einige in-situ XAS-Studien in konventionellen elektrochemischen Zellen veröffentlicht wurden, sind die im Rahmen dieser Dissertation gezeigten Röntgenabsorptionsmessungen während des Betriebs einer realen Brennstoffzelle mit Wasserstoff bzw. Methanol die ersten ihrer Art.

Im Anschluß an die erfolgten Brennstoffzellen-Tests wurden die Katalysatorpulver nach einer durchschnittlichen Laufzeit von 10 Tagen nochmals mit XRD und TEM untersucht, um strukturelle Änderungen, wie z.B. Partikelwachstum oder Oxidbildung, aufzudecken.

Verglichen mit dem kommerziell erhältlichen Pt-Ru Standardkatalysator von E-TEK zeigt das selbsthergestellte ternäre Pt-Ru-W System im Brennstoffzellen-Betrieb geringfügig höhere Leistung, wobei die erzielte Leistungssteigerung von der Stöchiometrie abhängt. Die strukturelle Charakterisierung ergab, daß Wolfram ausschließlich in Form von röntgenamorphem WO_3 vorliegt, während Platin und Ruthenium metallisch auftreten und zumindest teilweise legiert sind. TEM-Aufnahmen zeigen kristalline Partikel mit einer durchschnittlichen Größe von 2 nm, welche homogen über den Rußträger verteilt sind. Für die verschieden synthetisierten Pt-Ru Katalysatoren wurden in Abhängigkeit von der Synthesevorschrift unterschiedliche mittlere Partikelgrößen und Verteilungen erhalten. Dabei wiesen die

in wäßriger Phase präparierten Systeme größere Partikel und eine inhomogenere Verteilung der Kristallite auf dem Träger auf. Von größerer Bedeutung ist jedoch der Legierungsgrad: Platin und Ruthenium sind im kommerziell erhältlichen und im nach der *Bönnemann* Kolloidmethode hergestellten Katalysator zumindest in teilweise legierter Form vorhanden. Dagegen liegen in den aus wäßriger Phase synthetisierten Pt-Ru Systemen Platin und Ruthenium als separate Phasen vor.

Aufgrund widersprüchlicher Ansichten, ob eine Legierungsbildung im System Pt-Ru eine notwendige Voraussetzung für eine ausreichende elektrokatalytische Aktivität ist oder nicht, wurde in der vorgelegten Arbeit auch der Extremfall eines nicht-legierten Systems betrachtet, indem zusätzlich zu den Katalysatoren mit separat vorliegenden Pt- und Ru-Phasen auch einfache Gemenge rußgeträgerter Pt-Katalysatoren und Ru-Katalysatoren untersucht wurden. Dabei wurde eine überraschend hohe Aktivität für niedrige Methanol- und CO-Konzentrationen im Anodenbrennstoff gefunden, die neue Perspektiven für die Katalysatorentwicklung eröffnen könnten. Da diese Ergebnisse in starkem Gegensatz zur bisher vorherrschenden Meinung stehen, wird die Problematik in den Kapiteln 4 und 7 aufgegriffen, kommentiert und mit Blick auf die erhaltenen Resultate interpretiert.

Structural and electrochemical characterization of carbon-supported Pt-Ru and Pt-Ru-W catalysts for PEM fuel cell applications

Christina Roth
Institute for Materials Science
Darmstadt University of Technology

Summary

Due to growing environmental problems, largely caused by industrial and automotive exhausts, the fuel cell technology experienced increasing attention during the last two decades. Nearly emission-free and highly-efficient, both high and low temperature fuel cells present an attractive alternative for stationary and particularly mobile applications in industry and in the automotive sector. In this context, the polymer electrolyte fuel cell (PEMFC) using pure hydrogen as anode feed seems particularly well-suited for automotive applications. However, the indirect methanol fuel cell (IMFC) and the direct methanol fuel cell (DMFC) represent more cost-efficient alternatives, that are better-adapted to the existing infrastructure.

In IMFC and DMFC technology, pure hydrogen is replaced either by CO-containing reformate produced via on-board methanol reforming (IMFC) or by methanol (DMFC). In contrast to the oxidation of pure hydrogen, the oxidation of CO-containing reformate or methanol presents a severe problem for the Pt catalyst. CO impurities still present in the anode feed gas or autocatalytically-formed by methanol dehydrogenation are strongly adsorbed at the catalyst surface, thereby blocking the electrocatalytic active Pt sites. At fuel cell relevant-temperatures of about 80 °C, active platinum sites can only be freed from adsorbed CO by oxidative removal via oxygen-containing species nearby (water activation). However, pronounced water activation, providing these species near the blocked Pt atoms, takes place at bulk Pt electrodes not below 700 mV vs RHE. For this reason, binary and ternary catalyst formulations were developed, which facilitate the formation of surface oxides at lower potentials. Thereby, the anodic overpotential is reduced, and increased power densities of the fuel cell can be achieved. At the moment, a carbon-supported Pt-Ru (1:1) system is supposed to be the most active catalyst for PEMFC applications using reformate gas. Nevertheless, numerous investigations on other binary and ternary systems have been published recently, and the search for improved catalyst formulations is still going on.

The work presented puts its emphasis on the combined structural and electrocatalytical characterization of selected binary and ternary anode catalyst systems, aiming at a more detailed understanding of the apparent correlation between the nanomorphology of the catalysts and their electrocatalytic activity.

In this context, different binary and ternary carbon-supported catalysts for application in DMFC and IMFC anodes were synthesized by different preparation methods. Binary Pt-Ru (1:1) systems, synthesized via two preparation routes in aqueous phase or via the *Bönnemann* colloid method, and ternary carbon-supported Pt-Ru-W of varying tungsten stoichiometry were the subjects chosen for investigation. The synthesis routes employed were selected, based on the information that reduction in aqueous phase should result in separate platinum and ruthenium phases, whereas the *Bönnemann* synthesis should lead to a Pt-Ru alloy system. The respective catalysts were characterized by a number of different bulk and surface techniques before, during and after operation to get detailed information on the specific structural features induced by the different synthesis routes. X-ray fluorescence analysis (XFA) was applied to verify the correct stoichiometry of the synthesized catalyst systems. Data on the nanocrystallite dispersion on the support and on the crystalline phases were obtained by X-ray diffraction (XRD) and transmission electron microscopy (TEM). As the average size and the size distribution of the catalytic active nanoparticles are important parameters for the resulting electrocatalytic activity, they were measured by both, XRD using the *Scherrer* equation and TEM. A nano-EDX device, attached to the transmission electron microscope, was used to investigate the stoichiometry of individual particles. In addition to the XRD measurements, X-ray photoelectron spectroscopy (XPS) and X-ray absorption

spectroscopy (XAS) were applied, as very small nanocrystallites and amorphous phases can not be detected by X-ray diffraction. Prior to the electrochemical testing, data were collected by the above-mentioned techniques for all catalysts.

The electrocatalytic activity of the binary and ternary catalyst systems was determined by cyclic voltammetry (CV), cyclic voltammetry in combination with infrared reflectance investigations (CV/FTIRS), and in fuel cell tests in single cell arrangements. CV and CV/FTIRS measurements were conducted on catalyst deposits in a three-electrode electrochemical cell, using different sweep rates and either methanol or CO-stripping. The "quasi in-situ" FTIRS studies were performed in two different modes, each offering specific features in monitoring preferentially either adsorbed species or species in solution. Data obtained on potential-dependent CO adsorption and oxidation were correlated with the catalysts different performances. For the single cell measurements, membrane electrode assemblies (MEA) were prepared and characterized by scanning electron microscopy (SEM), atomic absorption spectroscopy (AAS), and BET analyses. Their electrocatalytic performance was tested in pure hydrogen, H_2/CO mixtures (75 or 150 ppm CO), and methanol operation.

Since monitoring the catalysts behaviour during operation was one aim of this work, a new in-situ fuel cell was constructed. This allows to pursue possible changes of the catalyst structure, induced by the specific fuel cell conditions during operation, by in-situ XAS at the Pt L_3 edge. Although several in-situ studies in three-electrode electrochemical cells have already been reported, the in-situ XAS investigations in single cell arrangements under hydrogen or methanol operation, presented in this work, were the first of their kind.

After the electrochemical testing in single cell arrangements, TEM and XRD measurements were applied to establish changes in the catalysts structure, e.g. particle growth and differences in the dispersion on the support before and after operation.

Depending on their stoichiometry, the ternary Pt-Ru-W systems showed good electrocatalytic performances compared to the standard Pt-Ru catalyst purchased by E-TEK inc. According to the combined structural characterization, the ternary catalysts consisted of at least partially-alloyed Pt-Ru and a not well-defined, amorphous WO_3 phase. Crystalline nanoparticles with an average particle size of approximately 2 nm were found homogeneously dispersed on the carbon support. In the binary Pt-Ru system, different syntheses led to apparent differences in particle size and particle distribution. Catalysts achieved by preparation from an aqueous phase showed increased particle sizes and particle agglomeration as compared to the commercially-available E-TEK catalyst. However, the most striking difference between the differently-synthesized systems was, that the catalysts synthesized in aqueous phase consisted of mainly separate Pt and Ru phases (in crystallographic terms), whereas the E-TEK and the *Bönnemann* catalysts seemed to be at least partially-alloyed.

Due to contradictory opinions on the question, if alloy formation is a prerequisite for enhanced electrocatalytic activity or not, this work compares (partially-) alloyed Pt-Ru catalysts with catalysts consisting of partly separate Pt and Ru phases, and finally plain catalyst mixtures as the extremest case of non-alloy systems. Investigations on their electrocatalytic activities regarding low methanol and CO concentrations show surprisingly good results for the separate Pt and Ru phases and the plain mixtures, hence offering new perspectives in catalyst development. As these findings seem to be in strong contrast to the commonly accepted ideas, the intention of chapters 4 and 7 is to comment on as well as try to interprete the experimental results.

1 Introduction

One of the main issues in fuel cell research is the development of new and the improvement of already-existing catalyst systems, that exhibit less CO-sensitivity, when applied in an indirect or direct methanol fuel cell. For this reason, numerous investigations deal with the synthesis and characterization of new Pt-based catalyst formulations. But while rotating disc experiments, CO-stripping voltammetry, differential electrochemical mass spectrometry and single cell measurements belong to the well-known routine techniques in electrocatalyst research, comparatively few spectroscopic and diffraction studies were reported. However, the emphasis in fuel cell research will probably shift, since recently obtained results on the effects of different syntheses and degradation in real cell operation and by air-bleed techniques attract increasing attention. As structural parameters, e.g. the particle size, the particle size distribution and the oxide content, strongly influence the electrocatalytic activity, it seems to be about time to adopt new strategies in fuel cell research.

In our view, in this respect mainly two publications marked the beginning of a new era in fuel cell research at the end of the 1990s: Arico et al. [1] and Rolinson and coworkers [2]. In both studies, the structure of commercially-available carbon-supported Pt-Ru catalysts purchased from E-TEK inc. was investigated by spectroscopic and diffraction techniques. As a main result, both groups concluded that X-ray diffraction measurements have to be complemented by other techniques to obtain a more precise idea of the catalysts real structure. In the opinion of Rolinson et al., not only the crystalline parts of the catalyst material, but also amorphous oxide species, particularly hydrous ruthenium oxide, seem to be decisive for the electrocatalytic performance. For this reason, both groups applied complementary techniques like X-ray photoelectron spectroscopy and X-ray absorption spectroscopy for a more detailed structural characterization, since these methods are particularly well-adapted for the characterization of amorphous phases and X-ray amorphous nanoparticles. Due to their results obtained by the combination of spectroscopic, microscopic and diffraction analyses, these two teams were the first who doubted a total alloy formation in the respective binary Pt-Ru system, as it has been reported so far by numerous other authors [3, 4].

In this background, the intention of the work presented is to contribute to the questions raised above on alloy formation and its necessity for exceptional electrocatalytic performance. The combination of not only structural but also electrochemical characterization is aiming at a more precise understanding of the apparent correlation between the nanomorphology of the catalysts and their electrocatalytic activity. The obtained results give evidence, that systematic investigation of the synergetic effects observed and combined structural and electrochemical characterization in fact present a convincing approach in catalyst development. Thus, the work presented is a contribution to close the gap between numerous findings in model systems and so far comparatively little studies of real-life catalysts by characterization of the respective real catalyst systems *before*, *during* and *after* operation in a real fuel cell.

Essay: Alloy formation essential for the electrocatalytic performance?

During the course of the work presented, it became more and more evident that alloy formation in the fuel cell catalyst systems plays an important role for their electrocatalytic activity - but not in the sense, everyone had expected.

In the very beginning of systematic structural research, there was no doubt about a binary Pt-Ru alloy system showing the highest activities [3, 4]. However, as catalyst characterization by a combination of several bulk and surface techniques was carried out, the results obtained indicated at least an incomplete alloy formation [1] and a surprisingly high content of (hydrous) ruthenium oxide [2]. Hence, the question, if alloy formation is a prerequisite for superior electrocatalytic performance or not, had been vividly discussed in the fuel cell community.

In this respect, first important results were obtained by systematic investigations of Ru-modified single crystal electrodes [5, 6]. Fundamental differences were found for those Ru-decorated model systems compared to conventionally applied Pt-Ru alloys. For instance, Friedrich et al. [5] studied CO adsorption and oxidation at a Pt(111)/Ru electrode by infrared spectroscopy. In contrast to Pt-Ru alloys, an additional CO vibrational band - CO/Ru - has been observed, that does not appear for the alloy surfaces. The observation of two separate vibrational bands for CO bonded to Pt and to Ru indicates the presence of relatively large areas that exhibit the specific properties of the respective pure elements. STM images gave evidence of monoatomic ruthenium islands approximately 3 nm in diameter. Hence, the Ru-decorated Pt(111) electrode can be considered as an oriented Pt substrate with ruthenium "nano-electrodes" deposited on it. Surprisingly enough and despite the spatially separated Pt and Ru areas, these Ru-modified electrodes showed a clear promoter effect for CO electrooxidation. Due to an interpretation within the framework of the bifunctional mechanism, CO oxidation at the Ru sites is expected at lower potentials, thereby making water activation at the freed ruthenium sites possible. The remaining mechanistic steps will proceed similarly to the bifunctional mechanism proposed by Watanabe and coworkers [7]. As only a single oxidation process has been observed for the Pt(111)/Ru electrode, despite the presence of two different adsorption sites, surface diffusion of Pt/CO to adjacent ruthenium sites has been proposed. Therefore, Friedrich et al. postulated active Pt sites in close proximity to the ruthenium islands and a high mobility of the CO/Pt adsorbate layer.

A rather different approach has been presented by Davies and coworkers [6], who characterized Ru-modified Pt(111) electrodes by LEED, LEIS and XPS, and probed the resulting electrocatalytic activity in voltammetric measurements. They found that the CO electrooxidation at Pt(111)/Ru in H_2SO_4 electrolyte is characterized by two oxidation peaks in the stripping voltammogram, both at an overpotential significantly lower than that obtained at pure platinum. This is in strong contrast to the findings of Friedrich et al. [5], who observed merely one oxidation process and therefore proposed a high mobility of the CO/Pt adsorbate layer. Davies et al. [6], however, interpreted the two oxidation peaks in terms of two different oxidation zones: zone I is the result of a fast *Langmuir-Hinshelwood* oxidation kinetics associated with platinum sites neighboring the ruthenium cluster, whereas the remaining sites, which lie at least one Pt atom away from the Ru sites, belong to zone II. In the presence of the sulfate anions (from the electrolyte), the mobility of CO from zone II to unoccupied zone I sites is supposed to be relatively low. Therefore, the authors suggested that the slower oxidation kinetics represented by the second peak might be attributed to the rate of spill-over and diffusion of oxygen-containing species, formed via water activation at Ru sites. However, a final conclusion on either CO or OH diffusion as the rate-limiting step in the CO oxidation reaction has not been drawn yet.

A big step towards the development of real fuel cell systems has been reported by Waszczuk et al. [8], decorating platinum nanoparticles instead of model Pt single crystal surfaces with ruthenium. It could be evidenced by CV and potentiostatic measurements that the activity of Ru-modified nanoparticles for methanol electrooxidation surpasses that of a commercial catalyst approximately by a factor of two.

However, the reported activity is referenced to the current density per real Pt surface area, and not to the mass of platinum used. The oxidation mechanism was assumed to proceed like that described by Watanabe et al. [7], in which the decorated Pt nanoparticles were assumed to act similarly to a Ru-decorated smooth Pt surface. In agreement with Friedrich and coworkers [5], Waszczuk et al. [8] proposed CO transfer from methanol decomposition at Pt sites to Ru islands via surface diffusion. The enhanced activity of the Ru-modified nanoparticles might be accounted for by the increased number of Ru edge atoms, that proved to be more active for water activation than the Pt/Ru pair sites in the alloy.
Similar observations have been presented by Long et al. [9], who found orders of magnitude less activity in methanol oxidation for a Pt-Ru alloy than for a mixed-phase electrocatalyst containing Pt metal and hydrous ruthenium oxides. Hydrous ruthenium is a mixed proton and electron conductor and innately expresses Ru-OH speciation [2]. These properties are of key importance in the mechanism of methanol oxidation, in particular, Ru-OH is a critical component of the bifunctional mechanism, since it is the oxygen-transfer species, which oxidatively dissociates CO fragments from the Pt surface. Due to this mechanism, the structure of a custom-designed catalyst must maximize the contact area between metallic Pt and the RuO_xH_y phase in order to maintain high activity for methanol oxidation [9].
Despite the variety of different interpretations, there is one fact that all the studies cited above have in common: a clear promoter effect can be seen for Ru-decorated surfaces without any alloy formation. Hence, the presence of a bimetallic Pt-Ru alloy seems to be not the essential criterion for a high electrocatalytic activity. Moreover, an enhanced performance of the separate Pt and Ru systems might be achieved, if the contact area between the two phases can be optimized by systematic variation of the synthesis. In this respect, the balance between OH- and CO-determined surface sites and the distance between them seems to be the limiting factor of activity. Thus, the presence of hydrous Ru oxide plays a crucial role mainly at the beginning of the oxidation reaction at low potentials, as the oxygen-containing species are already inherently present and do not have to be formed via water activation at Ru sites.

2 Basic concepts

2.1 Fuel cell technology

More than 150 years ago, in 1839, the Welsh lawyer Sir William Grove invented the first fuel cell. Inspired by the fact that sending an electric current through water splits the water into its components, Grove attempted to reverse the reaction by combining hydrogen and oxygen to produce water and electricity. The fuel cell technology got its start, when Grove immersed two platinum strips, surrounded by closed tubes containing hydrogen and oxygen, into dilute sulfuric acid (fig. 2.1). Already in 1842, Sir Grove presented his invention in all details, but it was not until 1889 that the name “fuel cell” was first – and incidentally - coined by William White Jacques.

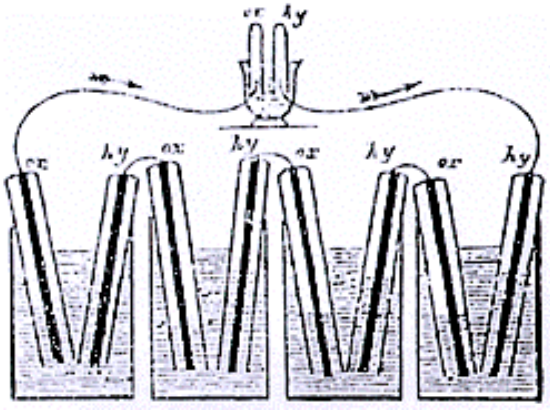

Fig 2.1 Sir William Grove and his new invention: Pt strips, surrounded by closed tubes containing hydrogen and oxygen, were immersed into an acidic electrolyte (*Philos. Mag.*, *Ser. 3*, **1839**, 14, 127)

From this point on, the fuel cell might well have developed rapidly, had it not been for mainly two important occurrences at the same time: (i) the invention of the internal combustion engine and (ii) the discovery of petroleum. In contrast to the technologically advanced fuel cell concept, internal combustion engines were to a greater extent adapted to the existing level of understanding at that time. Hence, this new idea was quite rapidly adopted by most people with automotive interests. With the option of petroleum as fuel, and an internal combustion engine as power supply, almost all other forms of creating energy were suspended for the time being.

Thus, it took more than a hundred years, until in the 1960s a new government agency in the US was about to undertake the first step in maturing fuel cell technology. The National Aeronautics and Space Administration (NASA) was looking for a source of electricity for the first prolonged manned flight into space (Apollo and Gemini project). Batteries were ruled out due to the size, weight and toxicity necessary to support a mission of eight days in space. Also photovoltaics were not practical at that time because of the size and weight of the solar panels needed. In consequence, the long forgotten fuel cell became the technological solution to NASA's dilemma of how to provide power for extended missions in space.

Moreover, as the spacecraft was already carrying liquid hydrogen and oxygen, the earlier problems of cost and fuel supplies became irrelevant. An additional benefit of fuel cells over other technologies was that the astronauts could consume the pure water produced by the H_2/O_2 fuel cell.
Since their adoption by the space program, fuel cell technology has achieved widespread recognition by industry and government as a clean energy source for the future. Thus, the demand for highly-efficient, low to zero emission processes turning fossile and renewable combustibles into fast-available energy increased constantly during the last two decades, due to growing environmental problems caused among others by air pollutants. In this respect, fuel cells present an attractive alternative for both stationary as well as mobile applications in industry and in the transportation sector.

Fuel cells: Definition and concept

The fuel cell concept is quite similar to the working principle of a battery; both consist of an anode and a cathode electronically separated by the electrolyte. In the anodic compartment of the fuel cell (or battery) an oxidation reaction takes place, while the electrons produced are used for the reduction process taking place at the cathode. Spatially separating both processes - oxidation at the anode and reduction at the cathode - ions can still diffuse through the electrolyte, whereas the electrons have to make their way via the external wire thereby closing the electric circuit. In dependence of the ions produced at the anode, an appropriate electrolyte has to be chosen in order to allow adequate ion diffusion. A marked difference between fuel cells and batteries is the continuous fuel supply in the fuel cell, while batteries have to be recharged after consumption of their reaction depots. The reaction process in a low-temperature polymer-electrolyte membrane fuel cell (PEMFC) using pure hydrogen as anode feed gas is shown in fig. 2.2.
As long as pure hydrogen and oxygen are supplied, the only reaction product is pure water (equations 2.1-2.3). Hence, no harmful air pollutants are present in the exhaust gas, and the whole reaction is a convincing example for a true zero emission process.

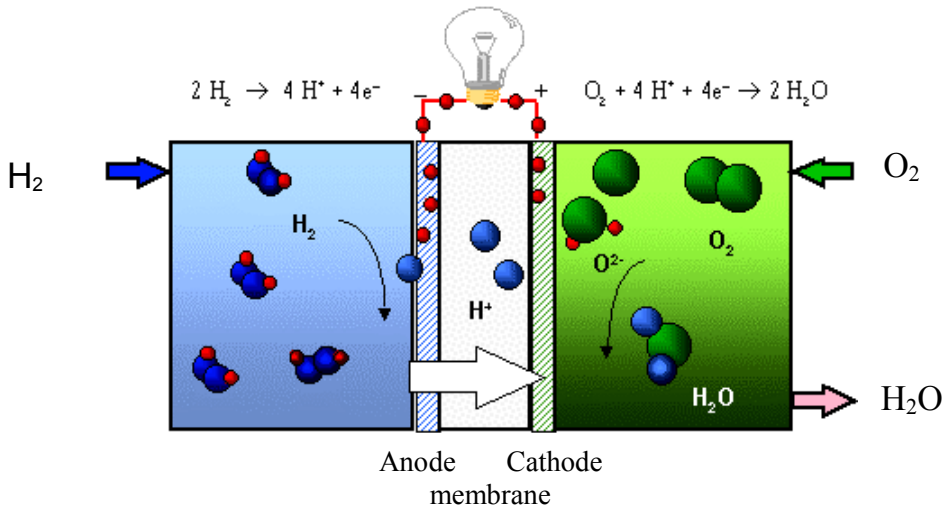

Fig. 2.2 Electrode reactions in a PEM fuel cell using pure hydrogen

Anode reaction: $H_2 \rightarrow 2H^+ + 2e^-$ [2.1]

Cathode reaction: $1/2\ O_2 + 2H^+ + 2e^- \rightarrow H_2O$ [2.2]

Total process: $H_2 + 1/2\ O_2 \rightarrow H_2O$ [2.3]

Fuel cells: Efficiency compared with Carnot-process

Besides their pollution-free operation, fuel cells offer still another advantage compared with conventional combustion engines working on the basis of the well-known *Carnot*-process: a higher efficiency.
The theoretical efficiency $\eta_{th,\ electro}$ of an electrochemical process is defined as the ratio of the *Gibbs* free energy ΔG_R and the reaction enthalpy ΔH_R.

Theoretical efficiency of a fuel cell: $\eta_{th,electro} = \Delta G_R / \Delta H_R$ [2.4]

For combustion engines the theoretical efficiency $\eta_{th,Carnot}$ is determined by their upper (T_u) and lower (T_l) working temperature in the *Carnot*-process.

Theoretical efficiency of a combustion engine: $\eta_{th,Carnot} = 1 - T_l / T_u$ [2.5]

In fig. 2.3, a comparison of the temperature-dependent efficiencies of a hydrogen-fed fuel cell and a *Carnot*-process at T_l = 300 K is shown. Since the electrochemical efficiency increases with decreasing temperature, while the *Carnot* efficiency is simultaneously decreasing, fuel cells seem to be mainly attractive for low temperature applications.

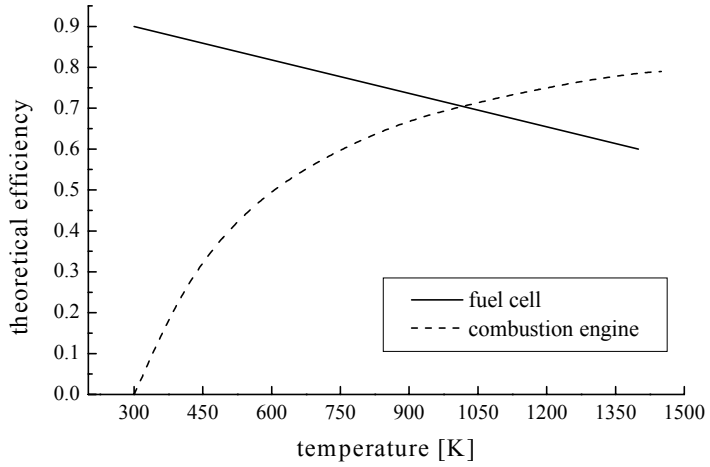

Fig. 2.3 The *T*-dependent efficiencies of a H_2-fed fuel cell and a *Carnot*-process, T_l = 300 K

Fuel cells: Types and applications

Mainly five different types of fuel cell systems are known, covering a working temperature range from 60 °C up to 1000 °C. A summary of these, their working temperatures, electrode reactions and electrolytes can be found in table 2.1. The alkaline fuel cell (AFC), the polymer-electrolyte fuel cell (PEMFC) and the phosphoric acid fuel cell (PAFC) are generally summarized as low-temperature fuel cells. The molten carbonate fuel cell (MCFC) and the solid oxide fuel cell (SOFC) belong to the group of high-temperature fuel cells working at temperatures above 700 °C.

Table 2.1 Overview of different low and high temperature fuel cell systems

Type	Working temperature [°C]	Electrolyte	Electrode reactions
AFC	80-90	Caustic potash lye	$H_2 + 2\mathbf{OH}^- \rightarrow 2H_2O + 2e^-$ $½\ O_2 + H_2O + 2e^- \rightarrow 2\mathbf{OH}^-$
PEMFC	80-90	Polymer membrane	$H_2 \rightarrow 2\mathbf{H}^+ + 2e^-$ $½\ O_2 + 2\mathbf{H}^+ + 2e^- \rightarrow H_2O$
PAFC	200	Phosphoric acid	$H_2 \rightarrow 2\mathbf{H}^+ + 2e^-$ $½\ O_2 + 2\mathbf{H}^+ + 2e^- \rightarrow H_2O$
MCFC	650	Li, K carbonate	$H_2 + \mathbf{CO_3}^{2-} \rightarrow H_2O + CO_2 + 2e^-$ $CO + \mathbf{CO_3}^{2-} \rightarrow 2CO_2 + 2e^-$ $½\ O_2 + CO_2 + 2e^- \rightarrow \mathbf{CO_3}^{2-}$
SOFC	850-1000	Zirconia	$H_2 + \mathbf{O}^{2-} \rightarrow H_2O + 2e^-$ $CO + \mathbf{O}^{2-} \rightarrow CO_2 + 2e^-$ $CH_4 + 4\mathbf{O}^{2-} \rightarrow 2H_2O + CO_2 + 8e^-$ $½\ O_2 + 2e^- \rightarrow \mathbf{O}^{2-}$

Because of their working temperatures, high temperature fuel cells are particularly well-suited for stationary applications, whereas alkaline fuel cells and polymer-electrolyte fuel cells show properties attractive for the use in mobile devices, like cars and mobile phones. From the beginning of the 1960s the AFC was chosen to serve as energy generator and for water production in space shuttles (Gemini and Apollo mission). However, for commercial use the AFC is out of question today, as its successful operation requires pure - and therefore expensive - feed gases. Since the early 1990s, the automotive industry put much effort in developing zero emission, fuel cell-driven vehicles, and the PEMFC concept

proved to be the most suitable technology for these mobile applications. Due to its advantages and its suitability, it was adopted to replace or at least compete with the internal combustion motor conventionally used in automobiles.

Polymer-electrolyte membrane fuel cells

The PEMFC consists of a layered, sandwich-like structure of anode, electrolyte and cathode, a unit usually denoted as membrane electrode assembly (MEA). The main characteristic of this kind of fuel cell is its electrolyte: a special proton-conducting polymer membrane. Such a proton exchange membrane applied in a PEM fuel cell should mainly provide high thermal and mechanical stability, good proton exchange activity and low electronic resistance. Up to now, a perfluorinated polysulfonic acid polymer (Nafion©, DuPont) meets the requirements in fuel cell operation best.

As electrodes either carbon-supported, highly-dispersed platinum nanoparticles or platinum black were used, which serve as electrocatalysts for both the oxidation and the reduction reaction. In the case of carbon-supported catalysts, an ink of the catalyst powders, water and Nafion© ionomer is fixed to the membrane by a spraying or hotpressing technique to form a porous electrode. The resulting pore structure is very important to facilitate the transport of the combustibles and reaction products through the MEA as well as to extend the three-phase boundary, at which the reaction takes place (fig. 2.4).

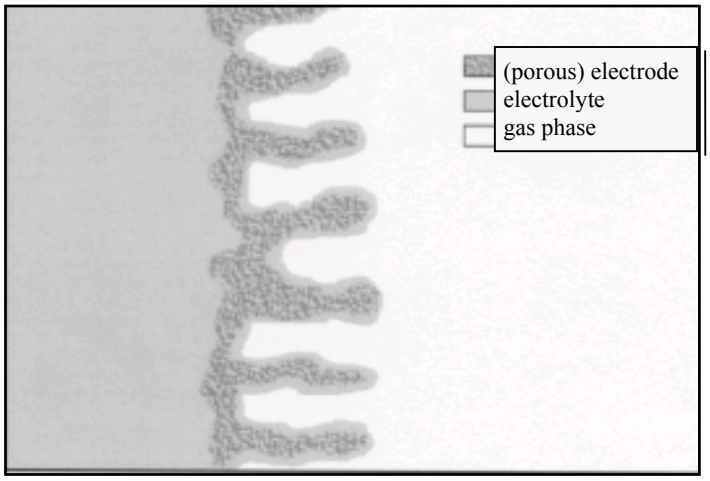

Fig. 2.4 Three-phase boundary in a porous fuel cell electrode

As a single MEA has a comparatively little power output - depending on the current flow, cell voltages of approximately 0.7 V can be supplied - a certain quantity of membrane electrode assemblies is connected to form a so-called stack.

A schematic drawing of part of a PEM fuel cell stack is shown in fig. 2.5. Bipolar plates with integrated gas flow fields guarantee a homogeneous distribution of the feed gases, a gastight separation of anodic and cathodic cell compartments and the electronic connection between the single MEAs. Two endplates per stack serve as current collectors.

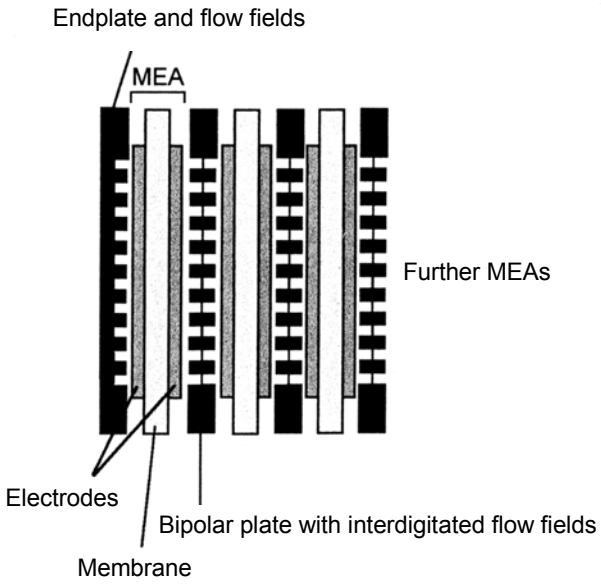

Fig. 2.5 Schematic drawing of a PEM fuel cell stack

PEMFC, IMFC and DMFC

Three types of polymer-electrolyte membrane fuel cells can be distinguished, due to the different combustibles used in operation: 1) the PEMFC using either pure hydrogen or reformate as anode feed gas, 2) the IMFC (indirect methanol fuel cell) equipped with a reformer unit for on-board reformation of methanol and 3) the DMFC (direct methanol fuel cell) operated with liquid or gaseous methanol.
The application of pure hydrogen in the PEM fuel cell is limited by mainly two factors: its high cost and its low energy density of only 0.4 kWh/kg compared to 9.5 kWh/kg for gasoline used in an *Otto* motor [10]. Liquid hydrogen yields higher energy densities (up to 4.8 kWh/kg), but causes higher costs due to the energy consumption by its liquefaction and the evaporation loss of about 1 percent per day. Besides, a suitable infrastructure for the distribution of liquid hydrogen is missing. For these reasons, the use of methanol in PEM fuel cells is highly-favored by the German automotive industry. In contrast to hydrogen, the energy density of methanol is comparable to that of diesel fuel (approx. 7 kWh/kg) and, as it is liquid under standard conditions, it can be distributed via the already-existing infrastructure. Although methanol is produced at large-scale by the BASF-process today, a replacement of this process by a more ecologically beneficial method seems feasible, as methanol can also be obtained via gasification of biomass [11]. Another advantage is the easy biodegradation of methanol compared with conventional fuels.

Reforming of methanol to a hydrogen-containing reformate gas is a quite simple process:

Cracking: $CH_3OH \rightarrow CO + 2H_2$ [2.6]

Conversion: $CO + H_2O \leftrightarrow CO_2 + H_2$ [2.7]

Total process: $CH_3OH + H_2O \rightarrow CO_2 + 3H_2$ [2.8]

In the indirect methanol fuel cell (IMFC), methanol reforming is done on-board by a reforming unit attached to the fuel cell. On-board reforming does not display a huge technical problem, but the high weight, the energy consumption and the additional costs of such a reformer device are very disadvantageous for its commercial application. By methanol reforming a CO-containing gas is produced, that can not be fed directly into the fuel cell, as CO is strongly poisoning the catalytic active Pt sites. Hence, the CO content of the reformate gas is reduced to approximately 0.5% by a shift reaction and then further decreased to less than 100 ppm by preferential oxidation of the CO impurities (PROX reaction).

Reducing the CO content of the reformate in the IMFC:

Shift reaction: $H_2O + CO \leftrightarrow CO_2 + H_2$ [2.9]

PROX reaction: $CO + ½\ O_2 \rightarrow CO_2$ [2.10]

Despite its costly technology, the IMFC has been tested successfully by various automobile manufacturers, among others by *DaimlerChrysler* (Necar 3), yielding efficiencies of 36% [12] compared to 21% in a conventional *Otto* motor [13].
The DMFC (direct methanol fuel cell) presents an attractive alternative to the IMFC, since no reformer device is needed, as the methanol is directly fed into the fuel cell.

Anodic oxidation of aqueous methanol solution in the DMFC:

Anodic oxidation reaction: $CH_3OH + H_2O \rightarrow CO_2 + 6H^+ + 6e^-$ [2.11]

However, the reduction of cost and weight due to the simplified technical system are paid by much lower current densities. The best anode catalysts applied up to now catalyze the anodic methanol oxidation with comparatively high overvoltages at the low working temperatures of PEM fuel cells. Therefore, current research concentrates on the development of new and the improvement of existing catalyst systems as well as on temperature-stable membranes. In case, the DMFC operation temperatures can be increased to 120 °C and above, the direct methanol fuel cell might be a promising concept for automotive applications

that could easily compete with the IMFC. In this context, approaches replacing methanol by ethanol [14], propanol [15], formic acid [16] and formaldehyde [17] and others should be mentioned.
From a technical point of view, fuel cell systems are quite sufficiently sophisticated in these days. But as long as their costs can not be reduced (table 2.2), they will not have any chance in competing with the *Otto* motor on the free market.

Table 2.2 Summary of the costs of different components in the PEMFC in 1998 [18]

Component / Materials	**Weight** [kg/kW]	**Cost** [$/kW]
Membrane	0.025	120
Electrode	0.082	31.16
Catalysts	0.016	243.2
Bipolar plates	3.3	825
End plates	0.12	0.24
Overall cost	3.543	1219.6

Nevertheless, one has to take into account the potential cost-reduction in PEM fuel cell manufacturing by large-scale production. Particularly, an expected price-reduction of the bipolar plates, the membrane and the electrodes should help to reduce today's prices to a minimum.

2.2 The fuel cell reactions

Replacing expensive pure hydrogen by either methanol (DMFC) or CO-containing reformate (IMFC) causes serious losses in the performance, primarily due to the poisoning of the catalytic active Pt sites.
However, in the case of the DMFC, not only the autocatalytic poisoning of the Pt sites by intermediate CO represents a problem. Also the further decrease of the power output due to methanol, passing the membrane (*methanol cross-over*) and causing a reduced cathode potential by a mixed potential formation, is a severe drawback.
Thus, an additional challenge in DMFC technology is the reduction of the methanol cross-over. Possible technical solutions aim at a) the modification of the polymer electrolyte by either sputtered Pd thin film coatings or inorganic fillers, e.g. layered phosphates or ZrO_2 and b) improving the catalysts selectivity for the oxygen reduction reaction.

Different strategies were adopted to solve the CO poisoning in IMFC and the CO poisoning and methanol cross-over in DMFC technology, covering both the membrane electrolyte as well as the anode and cathode catalysts (fig. 2.6).

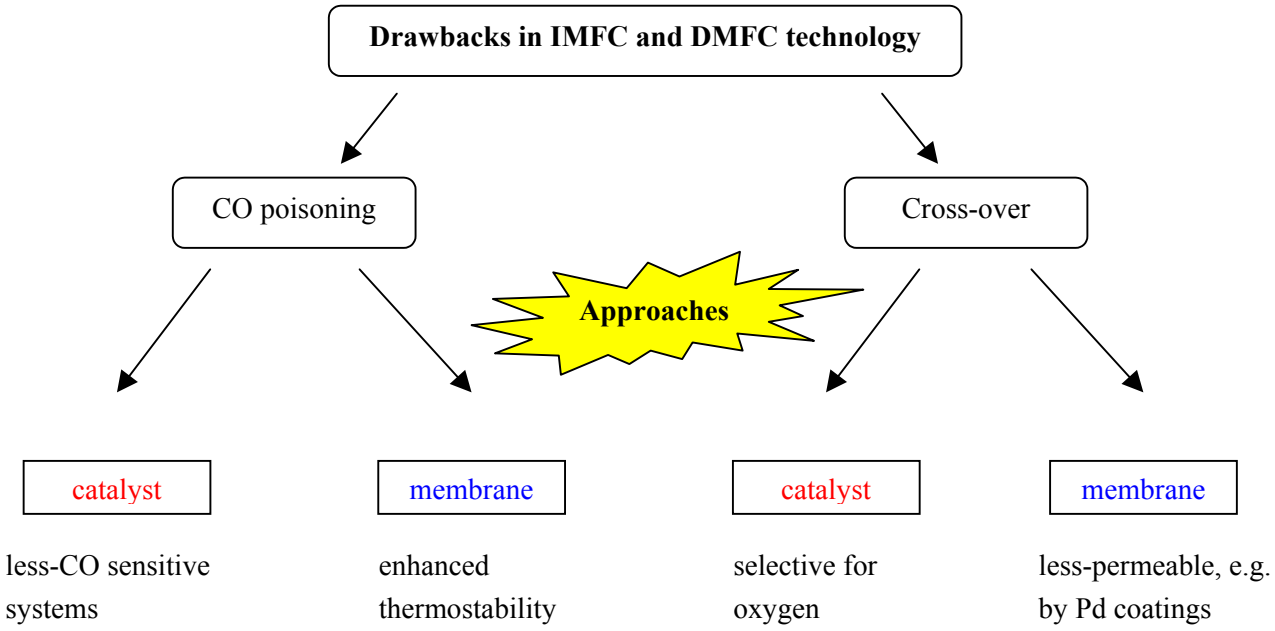

Fig. 2.6 Drawbacks in DMFC technology and their (possible) solutions

Approaches concerning the CO poisoning concentrate on a) the development of less CO-sensitive catalyst formulations and b) the preparation of membranes thermostable to temperatures above 120 °C.
By application of such thermostable electrolytes increased working temperatures can be realized and problems of CO poisoning might be overcome due to thermal activation of the anode reaction. However, up to now commercially-available membrane electrolytes are limited to operation temperatures far below the required ones. This is not only due to their reduced mechanical stability at elevated temperatures, but also to their proton conductivity that can be maintained only by a well-defined water content (degree of swelling). In this respect, the substitution of water as proton solvent by polymer-bound imidazoles [19] and the reduction of water and methanol uptake by the development of new, grafted polymers, e.g. modified, non-fluorinated polyetherketones [20], yield among other approaches promising results. However, these new polymer electrolytes are still not fit to replace the commercial Nafion©, as the reduced swelling is linked to a decreased proton conductivity and an increased brittleness.

Regarding the catalyst, less CO-sensitive binary catalyst systems are already in commercial use. At the moment, a carbon-supported Pt-Ru (1:1) alloy system is supposed to be the most active catalyst for PEMFC applications using reformate gas. In this respect, especially alloy formation is believed to play a major role for the electrocatalytic activity in these systems.
However, in fuel cell-relevant literature the term “alloy” is not well-defined and often used contradictory. Throughout this work, the following definition is applied, according to Bargel et al. [21]: An *alloy* is a material, that is obtained by the ‘willful’ addition of one or more element(s) (B) to another element

(matrix metal A), in order to modify specific properties of the latter. However, not only the properties, but also the structure of the matrix metal A can be changed significantly in dependence of the added element(s). Thus, different crystal types can be achieved, like (i) solid solutions, (ii) intermediate compounds and (iii) eutectic mixtures. In the case of binary Pt-Ru catalysts, as they are used in fuel cell applications, only the first crystal type - the solid solution - is of importance. For binary systems, it is defined as follows:

(i) Solid solution

Two different types of solid solutions can be distinguished: a) substitutional and b) interstitial compounds. In substitutional compounds, atoms of the matrix metal A are replaced by atoms of the added element B, whereas in interstitial compounds atoms of the added element B occupy tetrahedral and octahedral sites. In the case of the binary Pt-Ru system, platinum atoms (A) in the fcc lattice of the Pt matrix metal are replaced by ruthenium atoms (B) up to a concentration of approx. 60 at.% Ru (see phase diagram, fig. 4.1).

In general, since no directed attractive or repulsive forces act upon the different atoms, the atoms of the added element should form a stochastic distribution within the host lattice. However, if attractive forces between A and B atoms are stronger than those between equal atoms (A-A, B-B), a so-called superlattice is created. For the formation of such a characteristic long-range order specific conditions are required, e.g. specific concentration of B in A, low temperatures and prolonged cooling time, and thus a superlattice is not expected for fuel cell-relevant Pt-Ru systems.

A totally stochastic distribution of B in A is likewise unlikely, due to pronounced lattice distortions in the matrix metal, which are mainly caused by differences in the atomic radii. In consequence, atoms of the added element B occupy less often neighboring sites, and a so-called short-range order is formed. In the extremest case, this will lead to the formation of single-phase zones by segregation.

In Pt-Ru nanoparticulate systems, as they are described in this work, the term '*alloy*' corresponds to a substitutional solid solution of ruthenium in a Pt fcc matrix. In this context, an almost stochastic distribution is named '*well-mixed*' or '*homogeneous*', whereas the opposite is termed '*inhomogeneous*', according to the formation of some kind of short-range order. The presence of single-phase ruthenium and single-phase platinum zones in the catalyst is described either as '*segregation*' (zones occur within a single particle) or as '*separate phases*' (pure platinum particles as well as pure ruthenium particles are present). In addition, '*partially-alloyed*' is used, when part of the ruthenium is present in zerovalent state in a Pt-Ru alloy, whereas the remainder forms the respective ruthenium oxide.

However, one should keep in mind that not only the alloy formation, as discussed in detail above, but also the presence of oxide and amorphous phases and their effect on the electrocatalytic activity have to be considered in order to obtain a reliable and less CO-sensitive catalyst. Although up to now, binary Pt-Ru systems represent the most prominent catalysts for the electrooxidation of CO-containing hydrogen, numerous investigations on other binary and ternary systems, as for example Pt-W [22], Pt-Sn [23] and Pt-Mo [24], have been published recently. And the search for improved catalyst formulations is still going on.

2.2.1 Cathodic oxygen reduction reaction (ORR)

The cathodic oxygen reduction at a Pt catalyst in acidic media can proceed via two different reaction pathways: 1) direct reduction to water by a four-electron process (equation 2.12) [25] or 2) intermediate hydrogen peroxide formation followed by its immediate reduction or disproportionation to oxygen and water (equations 2.13-2.15). The equilibrium electrode potentials are given versus the reversible hydrogen electrode (vs RHE).

Direct reduction to H_2O: $O_2 + 4H^+ + 4e^- \rightarrow 2H_2O$ $E_0 = 1.229$ V vs RHE [2.12]

Reduction to H_2O_2: $O_2 + 2H^+ + 2e^- \rightarrow H_2O_2$ $E_0 = 0.682$ V vs RHE [2.13]
Reduction of H_2O_2: $H_2O_2 + 2H^+ + 2e^- \rightarrow 2H_2O$ $E_0 = 1.776$ V vs RHE [2.14]
Disproportionation: $2\ H_2O_2 \rightarrow 2H_2O + O_2$ [2.15]

At potentials above 0.3 V vs NHE at Pt in acidic electrolytes, the four-electron process (2.12) dominates by far, whereas the reduction to hydrogen peroxide can be neglected, as could be shown by rotating disc investigations [26]. Potentials higher than 0.7 V vs NHE cause at least at bulk Pt the electrochemical formation of surface oxides (equation 2.16) that are inactive for the oxygen reduction reaction [26, 27, 28].

Surface oxide formation at bulk Pt: $Pt + H_2O \rightarrow Pt\text{-}OH + H^+ + e^-$ [2.16]

With increasing potential, the amount of surface oxides increases, thereby reducing the number of metallic Pt sites available for the ORR. By this, the electrocatalytic activity of the Pt catalyst decreases, until the complete surface is covered by oxide species and therefore inactive for the ORR. This actually happens at a cathode potential of approximately 1000 mV vs RHE. Hence, for the application of platinum as catalyst for the ORR in an acidic electrolyte, an overvoltage of at least -200 mV to -300 mV is required in any case.

Studies of other systems for the ORR

At the moment, only platinum is known to show long-term stability and considerably high activity at potentials between 800 and 1300 mV vs RHE in acidic conditions and under oxygen atmosphere. Application of transition metals, like V, Cr, Fe and Co [29], has not led to encouraging results, as the pure metals are not corrosion-resistant in PEMFC conditions. Attempts in developing binary Pt-X alloys (X = transition metal), e.g. Pt-Fe, Pt-Ni and Pt-Cr, did not prove successful, as these materials suffer from oxide formation at comparatively low potentials and show only marginally-enhanced activities for the ORR. With respect to the methanol cross-over in direct methanol fuel cells, carbon-supported macrocyclic transition metal complexes were tested for their suitability, as they are inactive for methanol oxidation and comparatively cheap [30, 31, 32]. However, no complex material has been found, offering the necessary long-term stability, since the operation conditions cause an oxidative decomposition of the complex, leading to a pronounced decrease in its electrocatalytic activity [33]. Although special temperature treatments and partial pyrolysis are known to improve the activity and stability of the

complexes, the achieved results are still far away from the benchmarks of a commercial pure Pt cathode catalyst. Nevertheless, electron spin resonance (ESR), Mössbauer- and Fourier transform infrared (FTIR) measurements were applied to yield detailed information on the catalysts structure, as the underlying mechanisms for the activity enhancement by those temperature treatments are still unclear [30]. Dhar et al. [34] assume the stabilization of the complex cycle by some kind of compound formation between the carbon support and the reactive parts of the complex molecule, while van Baar and coworkers [35] were able to show that in the case of Ir tetraphenyl porphine metallic particles were formed only to a minor extent at temperatures below 700 °C. Van Veen et al. [33], however, found by their measurements isolated metal ions linked to the graphite surface by the thermally-modified ligands. Due to the contradictory statements on both the activity and stability of the transition element macrocycles in PEMFC conditions as well as regarding the underlying catalytic mechanisms, further investigations in this field are necessary.

2.2.2 Anodic hydrogen oxidation reaction (HOR)

As is well-known, the standard equilibrium electrode potential of the anodic hydrogen oxidation is defined as 0 V vs RHE, and the electrode potential series is based on this value. The anodic hydrogen oxidation reaction at a Pt electrode starts with the transport of molecular hydrogen to the electrode surface and its molecular adsorption, followed by the breaking of the H-H bond. The next reaction steps - ionization and hydration - can proceed via two different mechanisms: 1) the *Tafel-Volmer* mechanism and 2) the *Heyrovski-Volmer* mechanism.

<u>*Tafel-Volmer* mechanism:</u>

Tafel reaction: $H_{2,\,ads} \rightarrow 2H_{ads}$ [2.17]

Volmer reaction: $H_{ads} + H_2O \rightarrow H_3O^+ + e^-$ [2.18]

<u>*Heyrovski-Volmer* mechanism:</u>

Heyrovski reaction: $H_{2,\,ads} + H_2O \rightarrow H_3O^+ + H_{ads} + e^-$ [2.19]

Volmer reaction: $H_{ads} + H_2O \rightarrow H_3O^+ + e^-$ [2.20]

The dominance of either the *Tafel-Volmer* or the *Heyrovski-Volmer* mechanism is due to the hydrogen adsorption enthalpy of the respective metal. As the main part of the energy necessary for the dissociative H-H bond breaking is provided by the adsorption enthalpy of atomic hydrogen, the *Tafel* reaction proceeds the faster the higher the respective adsorption energy. On the other hand, high adsorption enthalpies slow down the *Volmer* reaction. Hence, a maximum exchange current density is obtained for intermediate adsorption enthalpies, as can be seen from the *Volcano* curve (fig. 2.7) [36].

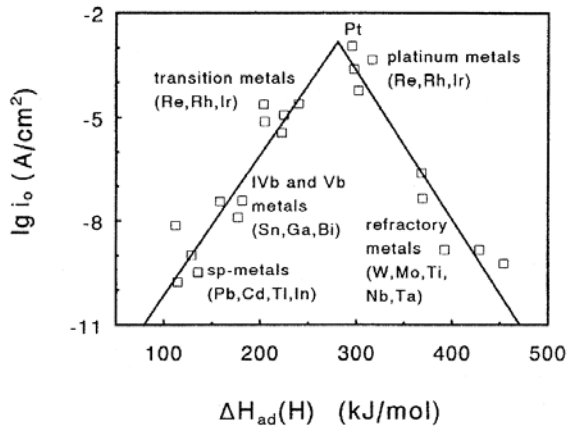

Fig. 2.7 *Volcano* curve: hydrogen exchange density i_0 vs adsorption enthalpy ΔH_{ad} for different metals

Due to its favorable hydrogen adsorption enthalpy, platinum is the anode catalyst of choice for the H_2-PEM fuel cell. Its exchange current density amounts to $7.9 \cdot 10^{-4}$ Acm^{-2} at standard conditions [37] compared to just $0.5 \cdot 10^{-6}$ Acm^{-2} for the oxygen reduction at the cathode side, which means that the oxidation proceeds without any remarkable reaction inhibition.

Oxidation of CO-containing hydrogen or reformate

In contrast to the oxidation of pure hydrogen, the oxidation of CO-containing reformate, as produced by on-board reforming of methanol (and other fuels) in the IMFC, presents a severe problem for the Pt catalyst. CO impurities still present in the anode feed gas in concentrations between 10 and 1000 ppm, depending on the feed pretreatment, are strongly adsorbed at the catalyst surface, thereby blocking the catalytic active Pt sites. For example, a concentration of only 10 ppm CO in the feed leads to nearly complete catalyst coverage by adsorbed CO at temperatures up to 100 °C [38].
The Pt-CO bond is formed according to

$$y\ Pt + CO \rightarrow Pt_y\text{-}CO \qquad \text{with } y = 1 \text{ or } 2 \qquad [2.21],$$

while y varies with the kind of CO bond. CO can be adsorbed on Pt in a linear- or bridge-bonded form, blocking either one or two platinum atoms per CO molecule, respectively. Transitions from the linear- to the bridge-bonded state are possible [38], whereas the ratio between the two forms is determined by the CO coverage (Θ_{CO}) of the surface. For CO coverages smaller than 23 % only bridge-bonded CO is found, whereas CO coverages above 90 % result in exclusively linear-bonded CO. Due to the very slow desorption of CO at fuel cell-relevant temperatures [39], catalytic active Pt sites can only be freed of adsorbed CO via oxidative removal. Hence, an oxygen-containing species near the blocked Pt atoms is

required. This has to be formed by dissociative water adsorption, due to the absence of molecular oxygen in the electrolyte. The respective process is usually denoted as water activation and corresponds to the anodic oxidation of platinum surface atoms.

Dissociative water adsorption: $Pt + H_2O \rightarrow Pt\text{-}OH + H^+ + e^-$ [2.22]

Oxidative removal of adsorbed CO: $Pt\text{-}OH + Pt_y\text{-}CO \rightarrow y+1\ Pt + CO_2 + H^+ + e^-$ [2.23]

According to equation 2.23, weakly-adsorbed CO_2 is released, leaving behind free Pt sites, which are active for the hydrogen oxidation once more.
As the water activation on platinum surfaces does not take place to a sufficient degree at potentials lower than 700 mV vs RHE (T < 100 °C), the anode potential required for CO_{ads} oxidation at a bulk Pt electrode has to be above this value. Replacement of the Pt bulk electrode by highly-dispersed platinum nanoparticles lowers the required potential to some extent, as the formation of Pt-OH species proceeds at more negative potentials. However, the performance and efficiency of the whole cell is considerably reduced by the high anodic overvoltage necessary for the formation of oxygen-containing species needed to oxidize CO_{ads}. This means a severe drawback for the application of pure Pt in a PEM fuel cell working on reformate.

Technological approaches

Two different strategies have been adopted to solve the problem of high anodic overvoltages.

(i) The first is the development of binary (up to multinary) catalyst systems, in which the second (third, fourth,...) metal enhances the electrocatalytic activity for the electrooxidation of CO-containing hydrogen by some kind of synergetic mechanism. Hence, among others, one essential feature of the added element represents its capacity to provide oxygen-containing species under fuel cell-relevant conditions. These species might be produced by water activation at potentials lower than on pure Pt (see chapter 3.2.1, bifunctional mechanism) or by weakening of the Pt-CO bond.
For instance, in binary Pt-Ru alloys, oxygen-containing species are provided at ruthenium sites at significantly lower potentials, and transferred to neighboring Pt atoms to oxidize the adsorbed CO. For Pt-Sn catalysts, a similar mechanism is proposed to account for the higher electrocatalytic activities achieved for the electrooxidation of CO-containing hydrogen. The only difference is that, in contrast to ruthenium, Sn works only as oxygen supply, since the HOR does not take place at Sn atoms.
A completely different mechanism, however, is made responsible for the increase of activity in Pt-W systems, in which the non-noble tungsten is primarily present in oxidized form. It is supposed that at the tungsten oxide phase not only adsorbed CO is more easily oxidized than at pure Pt, but also adsorbed hydrogen. These hydrogen species are transferred to the WO_3 by a so-called spill-over process. In addition, significant water activation is postulated at rather low potentials at tungsten oxide species.

(ii) The second approach is the addition of small amounts of oxygen to the anode gas in order to form oxygen adsorbates on the catalyst surface. This method is known as "air-bleed" and is already

successfully applied in industrial prototypes [40]. It decreases the CO poisoning to a remarkable extent, but leads also to a loss in fuel and to an undesirable increase of the cell temperature, as a minor share of the hydrogen is oxidized in a heterogeneous catalytic reaction. In how far the application of the air-bleed technique effects the degradation of the catalysts, has not been investigated yet, but surely has to be taken into account for possible long-term applications.

2.2.3 Anodic methanol oxidation reaction (MOR)

In contrast to the anodic hydrogen oxidation reaction, the anodic methanol oxidation is a very complex, six-electron process that is not yet completely understood.

Anodic methanol oxidation: $CH_3OH + H_2O \rightarrow CO_2 + 6H^+ + 6e^-$ [2.24]

However, an understanding of this mechanism is of considerable interest for the optimization of the direct methanol fuel cell. Hence, numerous studies deal with the elucidation of the oxidation mechanism, suggesting different intermediate dehydrogenation steps [e.g. 41, 42, 43].
In 1967, Bagotzky and coworkers proposed a widely-accepted mechanism for the anodic methanol oxidation at a Pt bulk electrode [44]. According to their work, the reaction starts with the adsorption of methanol, followed by its successive dehydrogenation, both summarized as "dissociative methanol adsorption". Subsequently, the adsorbed hydrogen atoms formed during dissociative methanol adsorption were electrochemically oxidized.

Dissociative methanol adsorption:

$CH_3OH + Pt \rightarrow Pt\text{-}CH_2OH + H_{ads}$ [2.25]

$Pt\text{-}CH_2OH + Pt \rightarrow Pt_2\text{-}CHOH + H_{ads}$ [2.26]

$Pt_2\text{-}CHOH + Pt \rightarrow Pt_3\text{-}COH + H_{ads}$ [2.27]

$Pt_3\text{-}COH \rightarrow Pt_y\text{-}CO + 3\text{-}y\ Pt$ y = 1 or 2 [2.28]

Electrochemical oxidation: $H_{ads} \rightarrow H^+ + e^-$ [2.29]

The number y takes into account the two different CO bonding states (either linear-(1) or bridge-bonded(2)).

Thermodynamically a value of 0.016 V vs RHE is calculated for the methanol oxidation reaction in equilibrium, in contrast to the actually observed potentials of about 500 mV vs RHE in acid medium on a Pt electrocatalyst. The resulting overpotential of about 450 mV vs RHE is due to the oxidation of CO_{ads} to weakly-bonded CO_2, which is the rate-determining step of the overall reaction, as evidenced by H(ydrogen)/D(euterium) measurements by Jusys and Behm [45]. Similar to the process, already explained for CO-containing reformate as fuel cell feed, the autocatalytically formed CO has to be removed from active Pt sites by oxidative removal (see equations 2.22 and 2.23). As pointed out before, the addition of other (transition) metals presents one possibility to lower the anodic overpotential by providing oxygen-containing species at more negative potentials than on pure platinum.

Besides the apparent similarities between the CO poisoning by CO impurities in the feed gas and CO produced via catalytic methanol dehydrogenation, marked differences in the adsorption characteristics and therefore in the poisoning mechanism were obtained. Due to geometric considerations and calculations by Gasteiger et al. [46], only three neighbored Pt atoms in the so-called C_{3v}-symmetry provide an electrocatalytic active site enabling methanol dehydrogenation. Either one or two of these Pt atoms are freed during the reaction, depending on the bonding state of the CO species (linear- or bridge-bonded). For a potential of 500 mV vs RHE, Gasteiger and coworkers determined a number of approximately 0.5 CO atoms per Pt atom, according to a bridge-bonded state, whereas for the CO-containing anode feed values of 0.85-0.9 CO per Pt atom (linear bonding) were reached [46]. These results point out different CO adsorption mechanisms, depending on the specific adsorption conditions, e.g. whether CO is produced as the result of methanol dehydrogenation or carried as trace impurity in the anode feed. According to the above-mentioned findings, multinary catalyst compositions behave differently in the IMFC and the DMFC reaction, respectively. Therefore, a binary catalyst that proved to be highly active in the IMFC anode, does not necessarily present an attractive solution for the anodic methanol oxidation [47].

Although a reasonable methanol oxidation mechanism has already been suggested in the 1960s, with the recently increasing interest in DMFC technology, numerous groups started to enroll their research activities in this field anew. In this context, newly-developed, highly-sophisticated techniques, as for example differential electrochemical mass spectrometry (DEMS) and Fourier transform infrared reflection absorption spectroscopy (FT-IRAS), came into operation and shed new light on the possible real mechanism. In principle, a combination of cyclic voltammetry and IR spectroscopy can achieve a direct identification of adsorbed species formed during the electrooxidation of methanol [48]. By this means, only linear- and bridge-bonded CO were detected in earlier studies. However, more recent investigations by Lamy et al. [41] and other groups, using special IR techniques, reported the detection of HCHO and HCOOH as well. DEMS studies performed by the Baltruschat group [42] and by Behm and coworkers [45] gave also strong evidence of formaldehyde and formic acid formation depending on the applied potentials. Based on their results, they proposed a parallel path mechanism via both, the oxidation of adsorbed CO and the oxidation of other dissolved intermediates. In agreement with their findings, a dual-path mechanism was also assumed by Wieckowski et al. [49] who modelled the process of methanol oxidation using a three-term rate equation.

2.3 Electrochemical techniques

In the following, a brief overview of the electrochemical techniques applied in the present work will be given. As the emphasis of this work lies upon the structural characterization of the catalysts, only the theory of those electrochemical and fundamental aspects, that are important for the understanding of the results, will be highlighted. In chapter 2.3.1, basic electrochemical definitions will be introduced, followed by a detailed introduction to cyclic voltammetry and spectroelectrochemical measurements in chapters 2.3.2 and 2.3.3.

2.3.1 Electrode kinetics

According to Vetter et al. [50], important tasks of the electrochemical kinetics are the determination of electrode reaction rates and the elucidation of coupled electrode processes. In this context, the dependence of the current density on several parameters, e.g. the electrode potential and the ion concentration in solution, plays a crucial role. Prior to a basic introduction to electrode kinetics, useful concepts and terms of equilibrium electrochemistry will be defined. For further information and details see textbooks of electrochemistry [e.g. 51, 52].

Equilibrium (zero-current) conditions

The discharge of a galvanic cell corresponds to a chemical process that can be divided into two spatially-separated electrode reactions. These can be combined to form an electronically-neutral overall cell reaction (see exemplary equations (2.1-2.3) for the PEMFC). In case, one formula unit of reactants is transformed into the respective products in the galvanic cell, an amount of electrical work $nF\Delta V$ will be performed in the external electrical circuit, connecting the electrodes. The maximum electrical work that can be obtained for a specific reaction corresponds to the equilibrium - zero-current - cell voltage E_0, also termed the electro-motive force (EMF).

Maximum electrical work and zero-current cell voltage: $W_{el,max} = nF \cdot \Delta V = nF \cdot E_0$ [2.30]

with F = Faraday constant,
n = number of exchanged electrons
ΔV = potential difference between the electrodes

It can be achieved only, if the reaction proceeds essentially infinitely slow (zero-current conditions).
The electro-motive force at standard conditions, assuming ideal properties of participating ions (activities are unity) and partial pressures of the reactants equal to the standard pressure p^0, is termed standard EMF E^0. In principle, its calculation is possible, using the *Gibbs* free energy ΔG_r for the overall cell reaction.

Standard electro-motive force (EMF): $E^0 = -\Delta G_r / nF$ [2.31]

In table 2.3, respective data for the PEMFC and DMFC reactions are summarized.

Table 2.3 Thermodynamic data for hydrogen and methanol oxidation [53, 51]

Reaction	**ΔH^0_r [kJ/mol]**	**ΔG^0_r [kJ/mol]**	**$\Delta G^0_r/\Delta H^0_r$**	**E^0 [RT, V]**	**n**
Hydrogen	-285.9	-237.5	83 %	1.23	2
Methanol	-726	-707.9	97 %	1.22	6

In addition, the concentration and partial pressure dependencies of the EMF are given by the general *Nernst* equation [2.33].

Nernst equation:

$$E_o = E^0 + \frac{RT\,ln\prod_i a_i^{n_i}}{nF} \qquad [2.32]$$

Cell voltage and electrode reactions during current flow

The previous part has focussed on the situation of electrochemical equilibrium at zero-current conditions. In the following part, however, the electrode reactions during current flow will be considered in some detail.

Figure 2.8 shows an electrochemical cell with the corresponding simple equivalent circuit during passage of an electric current. The electrolyte resistance, R_e, is independent of the current magnitude or direction, whereas the electrode resistances, R_I and R_{II}, are non-ohmic resistances. The equilibrium electro-motive force of the cell is the difference of the two electrode potentials without current flow, E_r, the so-called rest potentials (see also fig. 2.9).

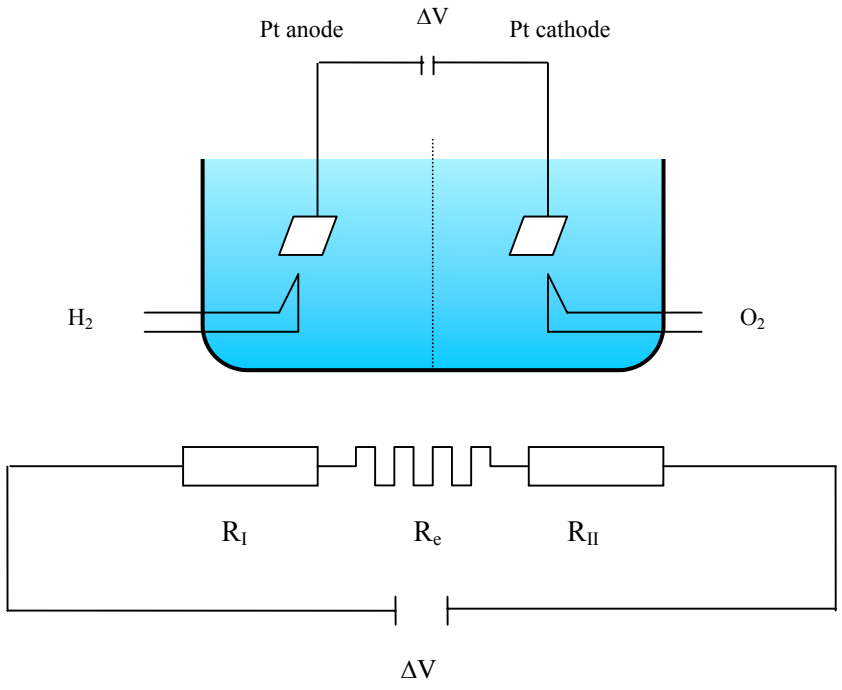

Fig. 2.8 Electrochemical cell and its simple equivalent circuit

Allowing for the flow of electrical current through the cell, the overall cell voltage will change characteristically, due to both, the ohmic potential drop across the electrolyte and the respective current-voltage behavior of each electrode (equation 2.33). The magnitude of the deviation of the single electrode potential from the equilibrium value E_r at either the anode or the cathode side is termed the overpotential η.

Overall cell voltage E: $E = E_0 - (\eta_A - \eta_C) - IR$ [2.33]

with I = current
R = resistance
η_A, η_C = anodic/ cathodic overpotentials

A schematic representation of equation 2.33 is given in fig. 2.9: the variation of the overall cell voltage E versus current i (a) and the anodic and cathodic overpotentials η (b). For simplification, the curves are represented in linear approximation.

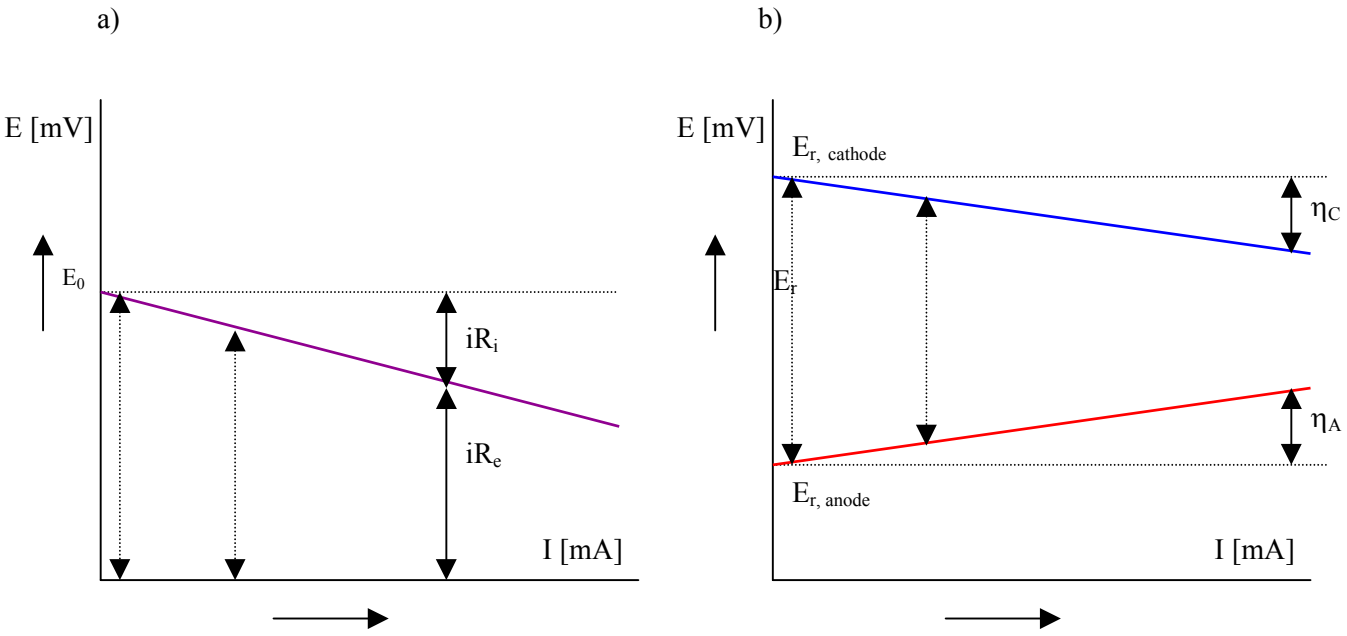

Fig. 2.9 Cell voltage vs current in a galvanic cell (curves in linear approximation)

The potential of a current-carrying electrode (the *working electrode*) can not be defined with respect to the other current-carrying electrode in the cell (the *counter electrode*). Therefore, a third electrode has to be introduced into the electrochemical cell as a *reference electrode*, that enables the determination of the overpotential at the working electrode only. Obviously, in order to avoid any overpotential contribution from the reference electrode, a high impedance voltmeter is applied to hinder significant currents between the reference and the working electrode. This so-called three-electrode arrangement (fig. 2.10) is essential for all measurements of electrode characteristics, as long as the contributions from the solution resistance and the counter electrode are not negligible. Additionally, in order to reduce the electrolyte resistance, in most cases a salt bridge with a *Haber-Luggin* capillary tip, ending directly in front of the working electrode, is used.

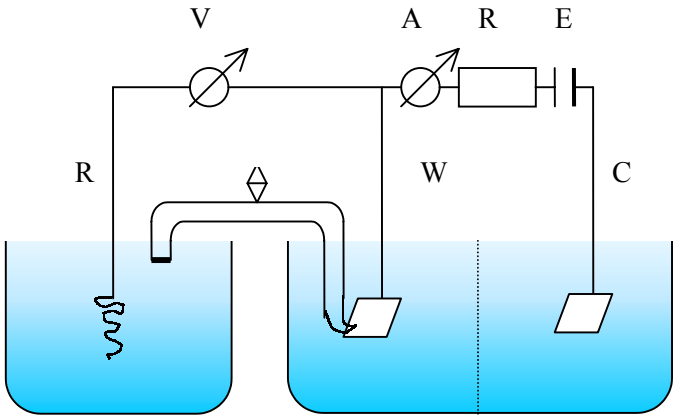

Fig. 2.10 Conventional three-electrode arrangement

The variation of current with potential, measured in a three-electrode arrangement as described above, is termed the current-potential characteristics of a single electrode.

Similar to reaction kinetics, in electrode kinetics the overall reaction rate is determined by the slowest intermediate step. And exactly this step determines both, the magnitude and the kind of the observed electrode overpotential. At least three different kinds of reaction inhibition can be distinguished: 1) charge transfer overpotential, 2) mass transport overpotential and 3) reaction overpotential.
The *charge transfer rate* at a given potential has been found to depend on the nature of the species, participating in the reaction, and the properties of the electrolyte and the electrode itself. At higher current densities, the charge transfer rate is usually no longer limiting, but mass transport processes become rate-determining. Limitations arise from either the slow transport of reactants to or products away from the electrode surface (*mass transport overpotential*) or the inability of coupled chemical reactions to keep pace with the charge transfer step (*reaction overpotential*).
In the following passage, the different kinds of overpotentials and the resulting mathematical concepts will be discussed in some detail.

Charge transfer overpotential

A charge transfer overpotential η_t will be observed, if the passage of the charge-carriers through the electrode/electrolyte phase boundary is the rate-determining step of the overall reaction [54]. In this case, the rate of the transfer reaction depends on the potential difference across the electrolytic double-layer.
For the general process

$$Ox + e^- \leftrightarrow Red$$

at equilibrium, the cathodic and anodic processes must take place at the same rate. Generally, these rates are not zero, and the equilibrium is a dynamic one.

Summation of both component current densities, i_a and i_c, results in the total current density i.

Total current density: $$i = i_a + i_c \quad [2.34]$$

With increasing electrode potential, the anodic component current density i_a increases, whereas $|i_c|$ decreases, and vice versa for a decreasing electrode potential. At the rest potential E_r, the total current density is zero, i.e. the anodic and cathodic currents are equal:

Total current density without current flow: $$i_0 = i_a = |i_c| \quad [2.35]$$

i_0 is termed exchange current density. It is a multiplicative factor, affecting both branches of the curve equally, and a measure of the charge transfer rate at equilibrium. Its value clearly depends on the concentration of the species, participating in the electrochemical reaction, and the free energy of activation at the rest potential. Its magnitude is a central quantity in electrochemistry, and in particular, it is the value of i_0, that is increased, when the electrochemical reaction is catalyzed.

In fuel cell research, the exchange current density is used as a measure for the electrocatalytic activity of the electrode material. For that reason, some data for fuel cell-relevant reactions will be given in this context. Under standard conditions, the exchange current density for the HOR at a platinum electrode is comparably high and amounts to $i_0 = 7.9 \cdot 10^{-4}$ A/cm² [37]. In contrast, the current exchange densities for the ORR ($5 \cdot 10^{-7}$ A/cm² [51]) and MOR ($5 \cdot 10^{-8}$ A/cm² [55]) at Pt indicate severe reaction inhibitions. In these cases, high overpotentials have to be accepted, in order to achieve current densities of technical relevance.

The variation of the total current density i with the charge transfer overpotential η_t is given by the *Butler-Volmer* equation (comprehensive treatment of one-electron and multielectron charge transfer in [54]).

Butler-Volmer equation: $$i = i_a + i_c = i_0 \left\{ exp\left(\frac{\alpha_a F}{RT} \eta_t \right) - exp\left(-\frac{\alpha_c F}{RT} \eta_t \right) \right\} \quad [2.36]$$

with $\alpha_{a,c}$ = anodic / cathodic charge transfer coefficient
For one-electron charge-transfer reactions, α equals the so-called symmetry factor β.

Equation (2.36) shows, that the partial current densities will increase or decrease exponentially with overpotential, the steepness of the rise or fall depending on the symmetry factor β (α in the special case of a one-electron charge transfer). For $\beta_a = \beta_c = 0.5$, the anodic and cathodic branches of the total current will be symmetric, but for β_a near unity, the anodic branch would rise more steeply than the cathodic branch, as shown in fig. 2.11 (dashed), whereas for β_a near zero, the inverse is found (dotted line). Experimentally, values close to 0.5 are found for β_a and β_c. As a rule, at potentials close to the equilibrium potential, where reversibility prevails, the sum of α_a and α_c has to equal the stoichiometric number of electrons ν_e of the potential-determining electrode reaction. Therefore, only for simple one-electron charge transfer reactions the sum of α_a and α_c is unity. For high anodic and cathodic

overpotentials, however, the respective reactions may proceed according to very different mechanisms, resulting in different i_0 values for the forward and backward reaction.

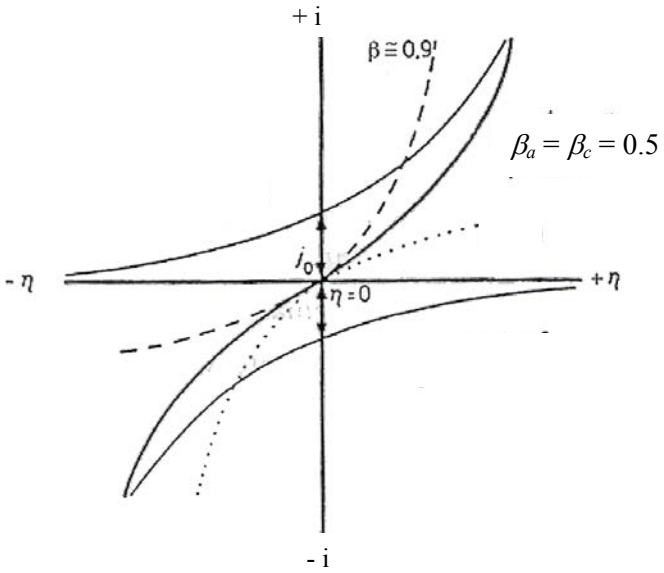

Fig. 2.11 Graphical representation of the *Butler-Volmer* equation

The Tafel plot

For high anodic or cathodic overpotentials ($|\eta| >> RT/F$), the current density of the reverse reaction can be neglected. Thus, in a good approximation, equations (2.37) and (2.38) are obtained.

High anodic overpotentials: $$i = i_0 \cdot exp\left(\frac{\beta_a F}{RT}\eta_{a,t}\right) \qquad [2.37]$$

High cathodic overpotentials: $$i = -i_0 \cdot exp\left(-\frac{\beta_c F}{RT}\eta_{c,t}\right) \qquad [2.38]$$

Taking the natural logarithms results in the so-called *Tafel* equations, that can be schematically written down as:

Tafel equation: $$\eta_t = A + B \cdot \ln|i| \qquad [2.39]$$

If the charge transfer overpotential η_t is plotted against the natural logarithm of the current density ln i, for high overvoltages linear slopes are found (*Tafel* slopes). A graphical representation of the *Tafel*

equation for $\beta_a = \beta_c = 0.5$, with the normal logarithmic instead of the natural logarithmic current is given in fig. 2.12.

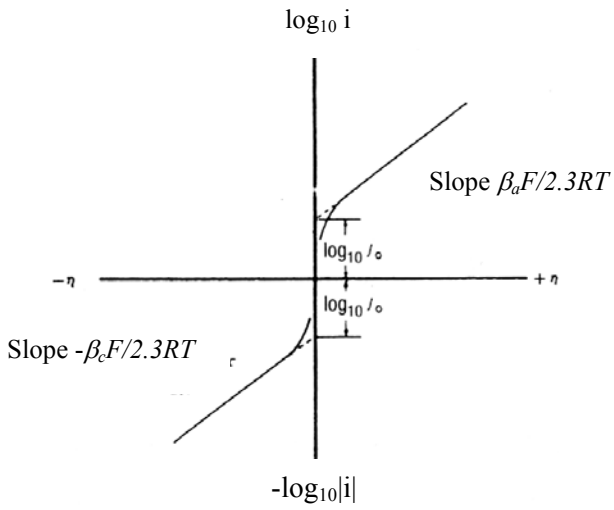

Fig. 2.12 *Tafel* plot for $\beta_a = \beta_c = 0.5$, normal logarithmic current

Both values, the exchange current density i_0 and the symmetry parameter β, can be obtained directly from the intercept with the potential axis and the slope of the *Tafel* plot, respectively. For $0 < \alpha < 1$, the presence of linear slopes serves as criterion for a mainly charge transfer-controlled overall electrode reaction.

Transport processes and concentration overpotential

Save at very low current densities, the transport of reactants to or products from the electrode surface will not be sufficiently rapid to maintain the same concentration of species at the electrode surface as in the bulk solution. Thus, if transport processes are slow compared to the other reaction steps, the surface concentration c_s will be different from the bulk concentration c_0 ($c_s < c_0$ or $c_s > c_0$). This in turn leads to the necessity of increasing the potential in order to maintain the desired current density, and this increased potential is termed the *concentration overpotential*.

The total overpotential can be written, according to equation (2.40).

Total overpotential: $\eta_{tot} = \eta_t + \eta_c$ [2.40],

where η_t refers to the charge transfer overpotential, discussed above, and η_c to the concentration overpotential.

Several possible transport processes contribute to the observed concentration overpotential, that have to be considered separately. In general, the total flux density J_i of species i is expressed by the *Nernst-Planck* equation, that is composed of three terms: 1) diffusion, 2) migration and 3) convection.

With respect to the situation in a real fuel cell, material transport by migration and convection can be neglected. Hence, only the diffusion overpotential is discussed here in some detail.

Diffusion overpotential

As an example of a process, in which diffusion is the rate-determining step, the cathodic deposition of a metal from an unstirred solution with excess supporting electrolyte will be considered.
In zero-current conditions, the concentration has a constant value of c_0 (bulk concentration) all over the electrochemical cell, as is shown in fig. 2.13. With current flow, the surface concentration at the electrode decreases to the value c_s.
The magnitude of δ_N, the so-called *Nernst* diffusion layer thickness, is time-dependent, increasing with the total charge passed, until an approximately constant value is reached because of the always present natural convection. Values of δ_N are usually in the range of 10^{-4} cm.

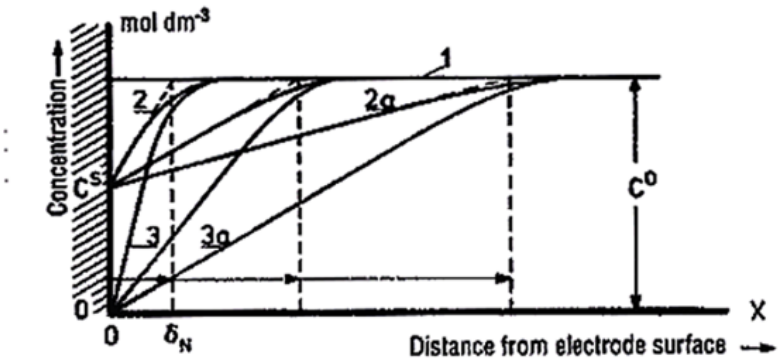

Fig. 2.13 Non-steady concentration profiles near the electrode after various times *t* (see text):
1 at zero current, $t = 0$
2 various times after initiation of a current
3 various times after initiation of the limiting current

If a sufficiently high overpotential is chosen, the current density is usually no longer determined by charge transfer but entirely by the diffusion rate. Applying *Fick*'s first law in unidimensional form, leads to equation (2.41): the flux density J_i corresponds to the current density for charged species i_i.

Fick's first law:

$$nFJ_i = i_i = -n_i F D_i \left(\frac{\delta c_i}{\delta x} \right) \qquad [2.41]$$

Hence, at the electrode surface (x = 0) with $c_s \rightarrow 0$, the limiting current density for diffusion can be calculated, according to:

Limiting current density: $$i_d = nFD\left(\frac{\delta c}{\delta x}\right)_{x=0} = nFD \cdot \frac{c_0}{\delta_N} \quad [2.42]$$

The corresponding overpotential region is termed the limiting current region. The relationship between overpotential and current density, assuming a fast charge transfer step, is given in the following equation (2.43).

Diffusion overpotential: $$\eta_d = \frac{RT}{nF} \cdot ln\left(1 - \frac{i}{i_d}\right) \quad [2.43]$$

Current-time behavior (E = const., c_s = const.)

Considering diffusion at a planar electrode of infinite size, the current-time behavior at constant potential and constant surface concentration can be derived, using *Fick*'s second law in its one-dimensional form.

Fick's second law: $$\frac{\delta c(x,t)}{\delta t} = D \cdot \frac{\delta^2 c(x,t)}{\delta x^2} \quad [2.44],$$

where, as before, x is the distance from the electrode surface.

Assuming the following boundary conditions,

$c(x, t = 0) = c_0$
$c(x = 0, t) = c_s$
$c(x = \infty, t) = c_0$,

the respective solution of *Fick*'s second law is given as:

$$c(x,t) = (c_0 - c_s) \cdot erf\left(\frac{x}{\sqrt{4Dt}}\right) + c_s \quad [2.45]$$

If this solution is put into *Fick*'s law and differentiated for x = 0 at the electrode surface, the *Cottrell* equation results.

Cottrell equation: $$j = \frac{nFD}{\sqrt{\pi Dt}} \cdot (c_0 - c_s) \quad [2.46]$$

In case, diffusion is the rate-determining step, it follows from equation (2.46), that a plot of i vs $1/\sqrt{t}$ will be linear. At high potentials, where $c_s \rightarrow 0$ is valid, the diffusion coefficient D can be calculated from the slope of this line.

2.3.2 Cyclic voltammetry (CV)

In principle, all electrochemical techniques aim at the investigation of electrode processes to achieve a more detailed understanding of the reaction rate, the reaction mechanism, possible reaction intermediates and adsorption processes. The variety of existing methods can be roughly divided into three strategies: 1) stationary techniques, 2) quasistationary methods and 3) instationary measuring procedures.
As part of this work, cyclic voltammetry was applied to study the electrocatalytic activity of the catalysts in question. The main advantage of this technique is, that a rough idea of the specific features of an electrochemical system can be obtained in very short time, in contrast to several other, more time-consuming procedures. It is particularly suited to detect typical surface reactions and the formation of oxide layers on noble metal catalysts as well as the electrochemical conversion of adsorbates. Cyclic voltammetry belongs to the quasistationary measuring techniques and will be treated in some detail in this passage.
With the abrupt change of one of the electrode parameters, e.g. current, potential or concentration, a predefined system will need a distinct time to react to the new situation and to gain its new stationary state. Hence, the slower the parameter change takes place, the more one will expect stationary conditions. Exemplary, quasistationary conditions will be anticipated, if a moderate potential course, linear or sinusoidal in time, is imposed on the electrode. However, as these methods might work with rapid potential changes as well, they are characterized as transient methods at present.
In cyclic voltammetry, a potential is forced upon the working electrode, that changes triangular with time, and the resulting current response is recorded (fig. 2.14).

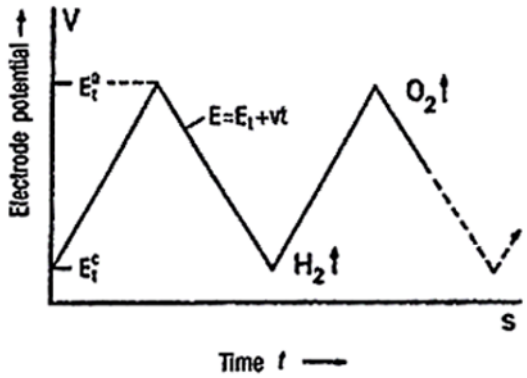

Fig. 2.14 Potential vs time course in CV

The negative and positive turn-round potentials are usually chosen with respect to the potentials of hydrogen and oxygen evolution at the respective working electrode. A potential range between these two electrode processes offers the advantage of inherent electrode cleaning by oxidative or reductive removal of adsorbed species that may hinder desired electrode processes by blocking active surface sites.

As cyclic voltammetry reacts very sensitive to even little perturbations in the electrochemical environment, reproducible CV results can only be obtained in a three-electrode cell. Additionally, a

couple of parameters affect the reproducibility of the cyclic voltammograms, like the purity of the electrolyte, the specific features of the (metal) electrode and electrode pretreatment steps.

The characteristic features of the cyclic voltammogram obtained, depend - among others - on the sweep rate $v = dE/dt$. Peaks in the voltammograms, corresponding to maxima and minima in the current response, indicate the progress of specific reactions. However, the number, precise potential and height of these peaks are strongly-influenced by the respective system characteristics.

Voltammograms in supporting electrolyte only

In fig. 2.15, a base voltammogram of a bulk platinum electrode in aqueous solution is shown. If there are no species in the aqueous solution, which are redox-active in the potential region between the turn-round potentials, the observed current-potential behavior will correspond to the formation and dissolution of chemisorbed hydride and oxide layers on the electrode surface.

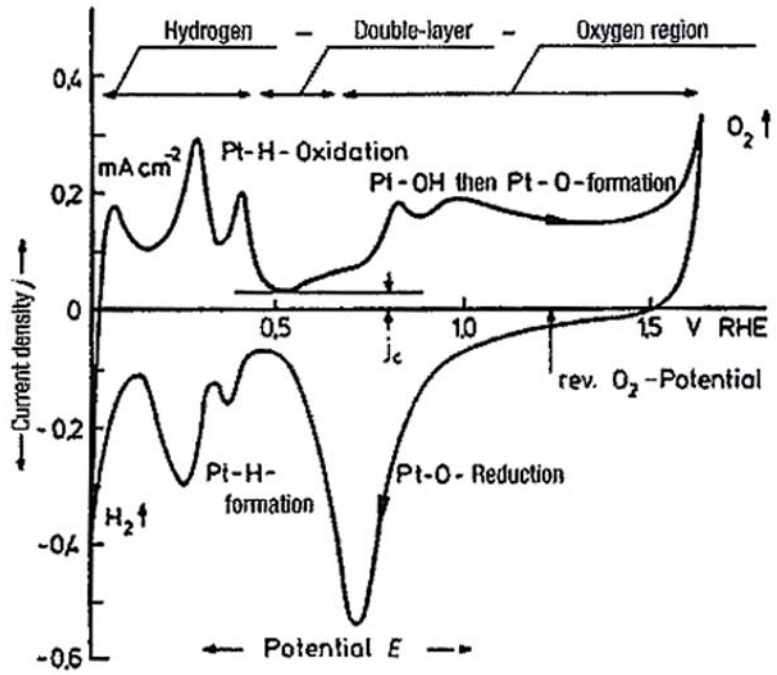

Fig. 2.15 Base voltammogram of a bulk Pt electrode in 1 N KOH, sweep rate 100 mV/s

In the following, the respective electrode processes causing the specific shape of the voltammogram will be described in detail.
For the discussion, all potentials will be given versus the reversible hydrogen electrode (RHE, $Pt/H_2/H_{aq}^+$, a_{H^+} variable, E_R = -0.059 pH). Starting in positive direction (forward sweep), between 450 and 550 mV vs

RHE only minor currents were recorded that are needed for the charging of the electrolytic double layer (for basic concepts see [51, 52]). At approximately 550 mV vs RHE, the formation of an oxygen adsorption layer begins.

$$Pt + OH^- \rightarrow Pt\text{-}OH + e^- \qquad [2.47]$$

At more positive potentials of about 800 mV vs RHE, another oxygen adsorbate species is formed (equation 2.48), until at ca. 1600 mV vs RHE oxygen evolution sets in.

$$2Pt\text{-}OH \rightarrow Pt\text{-}O + H_2O + Pt \qquad [2.48]$$

In negative direction (reverse scan), the oxygen adsorbate layers were reduced with an overpotential of several 100 mV first, followed by a comparatively small double layer region at around 500 mV. Adsorption of hydrogen starts at approximately 350 mV vs RHE.

$$Pt + H_2O + e^- \rightarrow Pt\text{-}H + OH^- \qquad [2.49]$$

Reaching the hydrogen potential, hydrogen evolution occurs, indicated by a strong increase in the cathodic current. As the sweep direction is reversed again, molecular as well as adsorbed hydrogen is oxidized with increasing potential.
The cyclic voltammogram explained above was measured at a polycrystalline electrode. In contrast to this, cyclic voltammograms at single-crystals show a strong sensitivity to the Miller indices of the face exposed [56] (fig. 2.16). This is often assigned to energetically different surface sites by many authors [57, 58]. However, these two interpretations can easily be linked together.

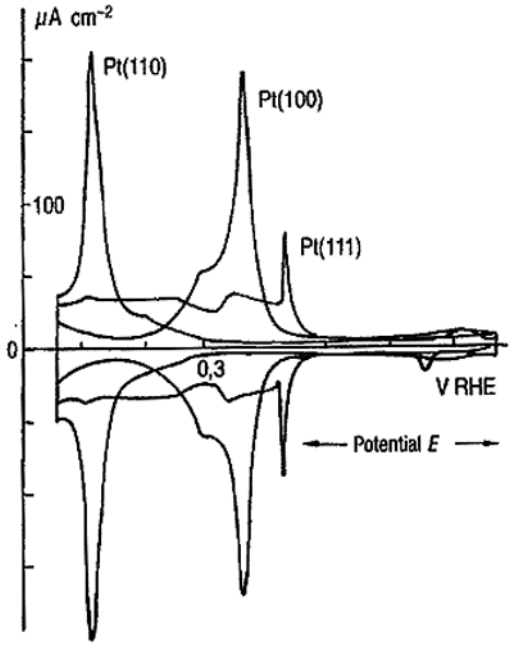

Fig. 2.16 Base voltammograms of different Pt single crystal surfaces in 0.5 M H_2SO_4 [56]

The integral amount of charge Q_B required for the electrochemical formation and destruction of the respective adsorption layers can be evaluated by current integration. By this method the real surface area of rough electrodes as well as the coverage θ with adsorbed species can be determined. For example, taking into account the number of lattice atoms per cm² of the respective metal, the integration of the hydrogen peaks results in a coverage of approximately $\theta = 1$. The value of the differential adsorption layer capacity and hence the shape of the base voltammogram is only slightly affected by the electrolyte, but depends characteristically on the electrode material. Many substances can adsorb onto a platinum electrode and inhibit the hydrogen electrode reactions. Evidence for this effect is the decrease in accumulated charge in the adsorbed hydrogen region of the *E*/*i*-curve, when such substances (carbon monoxide and many organic compounds) are added to the system. Also, the formation of an adsorbed oxygen (or oxide) layer on platinum inhibits many oxidation processes (e.g. the oxidation of hydrogen and of a number of organic substances).

Electrochemical active substances in the electrolyte

Due to the addition of electrochemical active substances to the electrolyte, the adsorption layer currents are superimposed by the current-voltage characteristics of the respective electrode reaction. If the considered electrode processes become more complex, voltammograms with e.g. more than one current maximum are obtained (fig. 2.17). This is particularly due to the addition of soluble organic substances.

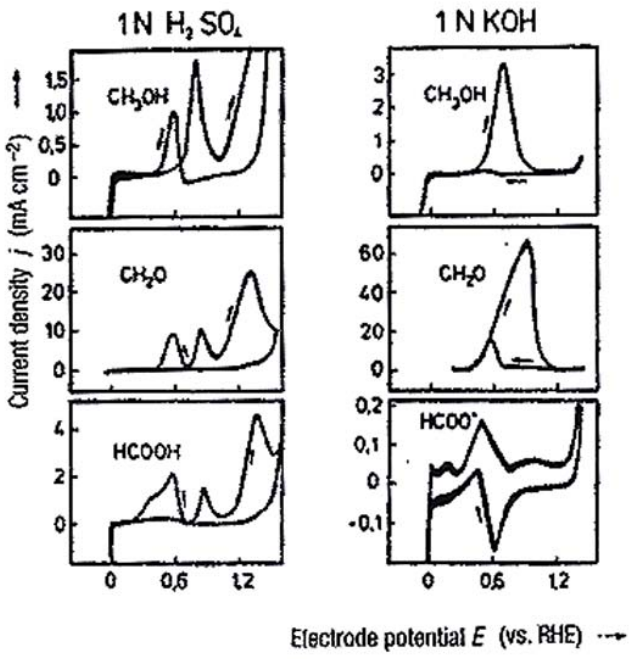

Fig. 2.17 Cyclic voltammograms adding soluble organic substances to the electrolyte

With regard to fuel cell research, it should be emphasized, that cyclic voltammetry offers the possibility of immediately gaining qualitative evidence on the electrocatalytic activity of the electrode materials in

question. The obtained results can be used to draw conclusions on oxygen reduction, hydrogen oxidation and the oxidation of solved organic substances (e.g. methanol) in real fuel cells.
Usually, the shape of the voltammogram and the position of the current maxima are not accessible by calculation. However, in some simple cases, the potential, at which a peak maximum occurs, may be calculated. Simple means in this context an electrode reaction only determined by diffusion of the reaction partners to the electrode surface and their passage/cross-over. Precise calculations are even possible in the case of preliminary and following chemical equilibria. But in contrast to the above-mentioned examples, adsorption processes and electrode coverages in real systems make correct calculations nearly impossible.

In the following, the processes leading to a peak in the voltammogram will be discussed in detail. A redox reaction at an inert, smooth bulk electrode (diffusion limited to the x direction) will be considered, assuming exclusively soluble species. Only the first cycle will be taken into consideration.
Starting the sweep at a potential clearly more negative than the equilibrium potential E_0, only minor non-faradaic currents occur. With increasing potential, nearby E_0 the oxidation of the soluble electrochemical active species sets in and causes an increase in the recorded current. If the potential is still increased, the surface concentration of the reduced species decreases and enhanced diffusion to the electrode appears. The measured current runs through a maximum at potentials slightly more positive than E_0, until it decreases again due to the depletion in reduced species at the electrode.
Completing the sweep in reverse direction, a high concentration of oxidized species is found nearby the electrode surface, as their diffusion from the electrode surface into the solution takes place quite slowly. As the potential approaches E_0 once more, the oxidized species will be reduced at the electrode again. The observed current minimum resembles the maximum in the forward sweep due to the analoga in their origin. However, the observed decrease of the peak current with increasing or decreasing potential might be initiated by several other factors as well, like an inhibiting adsorption of reactants or reaction products or passivation processes at a corroding electrode. As the absolute peak potentials, the potential difference between oxidation and reduction peak and the peak height are dependent on the sweep rate, it is in principle possible to draw conclusions on the present reaction mechanism. Based on calculations for different boundary conditions, criteria have been developed that depend on the ratio of the peak currents and the peak potentials at varying sweep rates and that give indications of the respective mechanism. In the case of more complex systems, an additional chemical analysis of the reaction products might be helpful.

2.3.3 Spectroelectrochemistry

From a general point of view, all spectroscopic methods use the interaction of electromagnetic radiation with matter and analyze the specific response of the system in question. The obtained information ranges from concentrations and layer thicknesses to crystallographic and chemical data, depending on the wavelengths applied.
In this context, the simultaneous application of spectroscopic and electrochemical techniques is described as spectroelectrochemistry and defined as spectroscopy at the electrode/electrolyte interface. However, comparison of the data obtained by spectroelectrochemical methods with tabulated values might result in

definite wavelength shifts, because of the interaction of radiation with adsorbates and the influence of the electrode potential.

In table 2.4, an overview of information that can be obtained by the different spectroelectrochemical methods is given.

Table 2.4 Potential applications of spectroelectrochemical techniques

Applied method	**Information**	
Specular Reflectance Spectroscopy, Ellipsometry	Optical	Optical constants of metals, Film growth on electrode surfaces
LEED	Structural	2-dimensional surface structure, Orientation of adsorbates
Raman, FTIRS, XPS, AES	Chemical	Fingerprint identification, Coordination of ligands

In principle, a spectroelectrochemical approach seems to be predestined for in-situ applications, as the progress of certain reactions can be pursued by the occurence of educts, products and reaction intermediates at the electrochemical interface. A conventional in-situ spectroelectrochemical setup using electromagnetic radiation $h\nu$ is shown in fig. 2.18. Electromagnetic radiation is preferred to elementary particles as probe molecules, as it is better adapted to the conditions at the phase boundary.

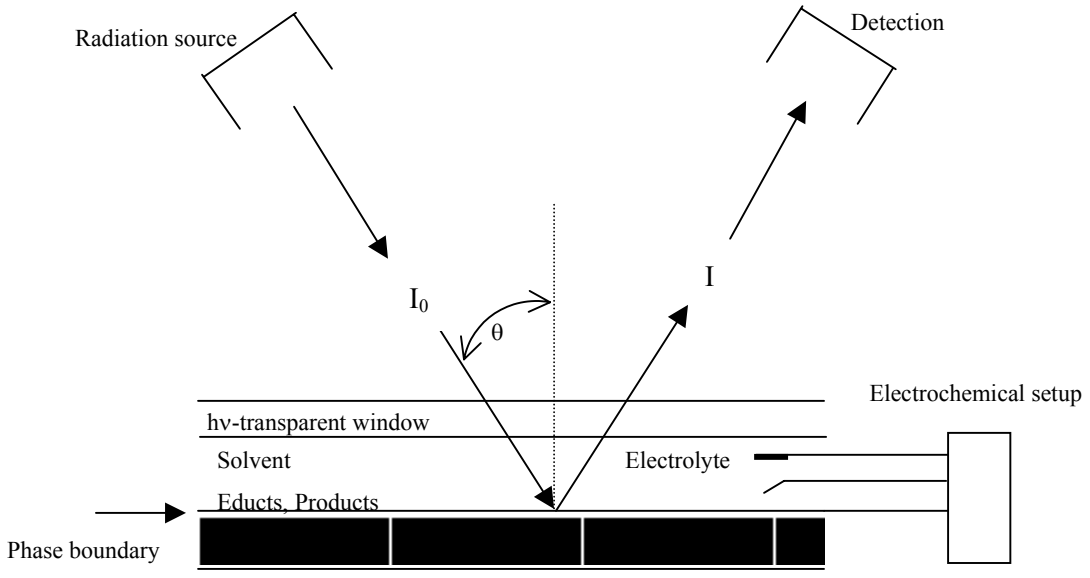

Fig. 2.18 Schematic drawing of an in-situ spectroelectrochemical setup

More than 30 different techniques are mentioned in the current literature [59], the applied frequencies range from microwaves to synchrotron radiation. A list of the most prominent methods using different parts of the wavelength continuum can be found in table 2.5.

Table 2.5 In-situ techniques in spectroelectrochemistry

Method	Abbreviation	Wavelength	Information
Electron spin resonance spectroscopy	ECESR	Microwaves	Structure of radicals
Fourier transform infrared spectroscopy	FTIRS	Infrared	Vibrational spectroscopy (permanent dipole)
	SPAIRS		Chemical nature of adsorbates
	SNIFTIRS		Molecules in solution
Surface-enhanced Raman spectroscopy	SRS	VIS to IR	Vibrational spectroscopy (no dipole needed)
Ellipsometry		Polarized VIS-light	Thickness of adsorption layers
Extended X-ray absorption spectroscopy	EXAFS	Synchrotron radiation	Metallic adsorbates, upd-layers

Due to only minor quantities of absorber atoms / molecules in the analyzed volume, the signal intensities obtained are usually very weak. Hence, high apparative sensitivity and resolution and as little disturbing factors as possible play a decisive role for a successful measurement. However, a kinetic mechanism should not be proposed, until the results have been checked and verified by another spectroelectrochemical technique. Hence, serious studies take into account a combination of two or more spectroelectrochemical methods, as not every method is sensitive to all species at the phase boundary and in the vicinity of the electrode.

Optical vibrational spectroscopies are most suitable to investigate and characterize in-situ electrode/electrolyte interfaces. They serve to elucidate the interfacial structure and composition, the type of adsorbates and intermediates, their bonding sites and orientation to the surface, to name just a few applications. Essentially three classes of optical vibrational spectroscopy exist: 1) Raman spectroscopy, 2) Infrared spectroscopy and 3) Sum Frequency Generation (SFG). Though particularly the latter technique offers an enormous potential, up to now only infrared spectroscopy in combination with electrochemical

methods (e.g. CV/FTIRS) has found wide-spread applications in various fields, and of course in fuel cell research as well.
As part of this work, in-situ infrared techniques were applied in order to obtain more detailed information on the electrocatalytic activity of the fuel cell catalysts (these are marked in the above table). Therefore, the following text will concentrate on special CV/FTIRS techniques, namely SPAIRS and SNIFTIRS.

In-situ infrared spectroelectrochemistry

Vibrational modes in real molecules are described by the anharmonic oscillator model. As it is sufficiently precise for the following explications, the simplified harmonic oscillator model will be used here.
According to the classical electromagnetic theory, a system emits electromagnetic radiation by periodical changes of its dipole moment. The frequency of the emitted radiation and the frequency of the dipole vibration are alike. With respect to IR spectroscopy, the absorption of electromagnetic radiation by a molecule can be seen as the reverse process. This implies a permanent dipole moment in the molecule. The most prominent IR-active molecules are CO, NH_3 and NO, while among others HSO_4^-, SO_4^{2-}, ClO_4^- and CN^- belong to the IR-active ions.
A frequently used spectroelectrochemical cell type is shown in fig. 2.19. Due to the strong absorbance of water and other solvents in the infrared region and in order to minimize the attenuation of the reflected IR radiation, the experiments have to be performed in a thin layer configuration with the electrolyte layer having a thickness of less than 10^{-3} cm. Unfortunately, the thinner the electrolyte layer, the more faradaic electrochemical processes as well as adsorption and desorption of molecules and ions are inhibited, if the solution concentration of the respective species is too small.

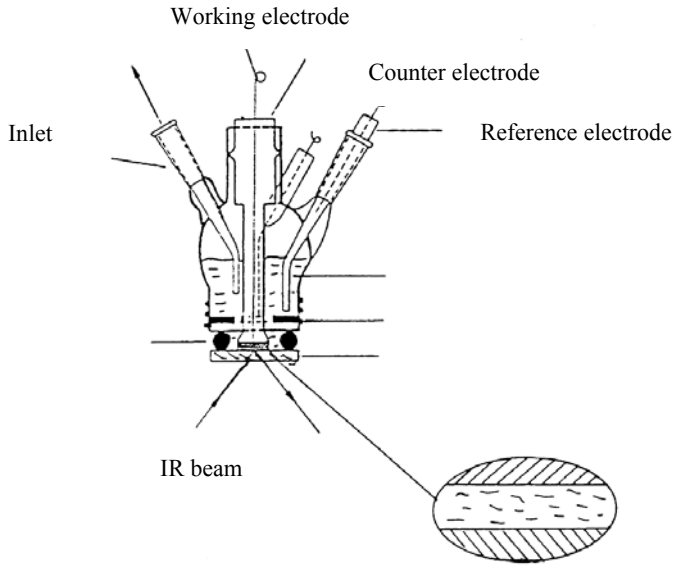

Fig. 2.19 Spectroelectrochemical thin layer cell

Fourier transform infrared spectroscopy (FTIRS)

In essence, the main advantages of the FTIR technique are its inherently high sensitivity and the rapid spectral collection times. The routine use of FTIR spectrometers has meant that in-situ spectroscopic studies requiring high sensitivity, e.g. investigation of adsorbed species, were no longer limited to fast, reversible electrochemical systems. Thus, the collection of spectra during a slow voltammetric sweep, during a series of potential steps or as a function of time after a single potential step has been made feasible by the Fourier transform technique [60].
The heart of an FTIR spectrometer is the *Michelson* interferometer (fig. 2.20) that makes measurements with polychromatic light and without monochromator in the beam path possible [61]. Due to this technique, no more than 1 s acquisition time per full spectrum is needed.

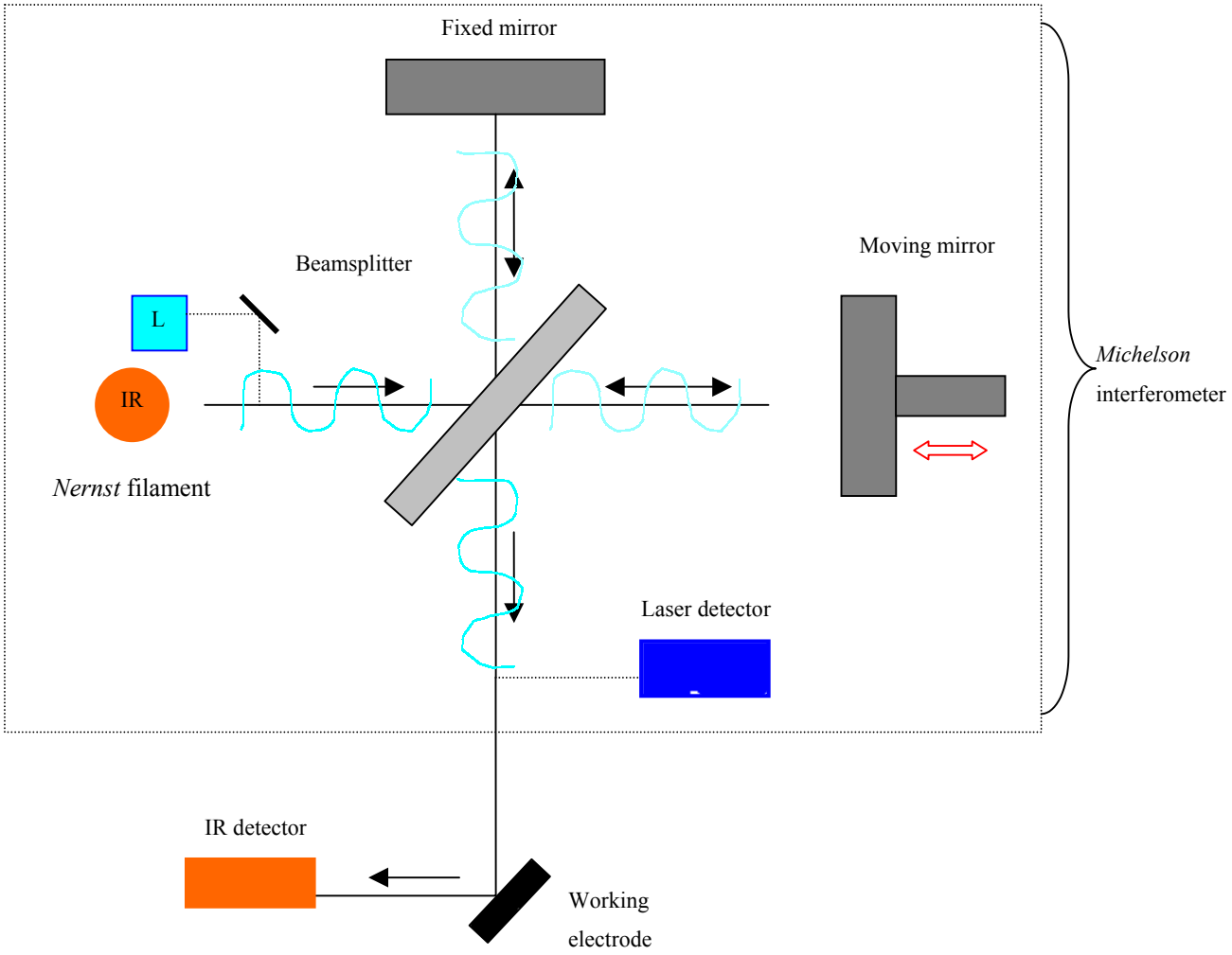

Fig. 2.20 *Michelson* interferometer

In principle, the IR beam is emitted by a *Nernst* filament, and hits a beamsplitter. The beamsplitter allows 50 % of the radiation to pass to a moving mirror, whereas the rest is transmitted to a fixed mirror. On reflection, these two rays recombine and interfere at the beamsplitter, before reaching the IR detector via the IR-transparent window and the reflective working electrode of the spectroelectrochemical cell. The

system also includes a reference laser, which follows the same path through the interferometer and which is then intercepted and directed at the laser detector. Monochromatic light, such as the laser beam, passing through the interferometer gives rise to a sinusoidal signal at the detector, due to constructive and destructive interference (fig. 2.21 a). By counting the maxima in the separately monitored laser signal, the position of the moving mirror at any time (retardation) is accurately-determined. A plot of intensity vs retardation is termed an "interferogram". Due to the velocity of the mirror movement, the interferogram is time-dependent, and the mirror movement can be converted into wavenumbers by Fourier transformation. Applying this mathematical procedure, all the individual cosine waves contributing to the interferogram may be deconvoluted and a plot of intensity I vs wavelength λ, or more usually frequency ν, is obtained. The resolution (line width) of the spectrometer is determined by the maximum possible mirror movement x_{max} giving infinitely sharp peaks for $x_{max} = \infty$. In order to eliminate the spectrometer characteristics, the difference of the sample and the reference spectrum is used to obtain the absorption spectrum of the sample in transmission.
In fig. 2.21 b, the case of two different wavelengths entering the interferometer is considered. The respective interferogram and the corresponding FT absorption spectrum is shown on the right hand side. Fig. 2.21 c displays a schematic of a conventional FTIRS experiment and the obtained results.

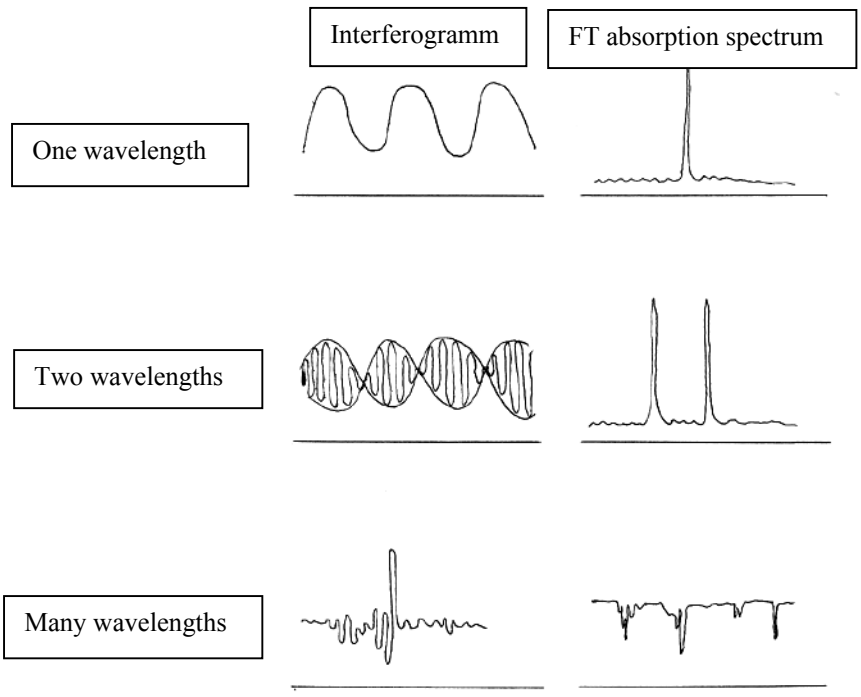

Fig. 2.21 Different interferograms converted to absorption spectra by Fourier transformation

However, the main challenge in all infrared reflectance techniques is how to achieve a sufficient signal enhancement in order to extract the much weaker signals of adsorbed species. Therefore, data processing plays an important role to sort out the information, which corresponds to surface species, from the bulk contributions and to improve the weak signal-to-noise ratio inherent to this type of experiment.

As part of this work, two special FTIR reflectance techniques were applied to gain some insight into the adsorption, desorption and reaction of CO species at the catalyst surface in dependence on the potential: SPAIRS (single potential altered infrared reflectance spectroscopy) and SNIFTIRS (subtractively normalized interfacial Fourier transform infrared reflectance spectroscopy).

SPAIRS and SNIFTIRS are based essentially on the same concept, that is to record difference FTIR spectra at different potentials. Both techniques allow qualitative and quantitative analysis not only of reaction products in the electrolyte but also of species adsorbed on the surface. By computing normalized difference spectra, one obtains data almost free of bulk contributions. Only adsorbed or desorbed species remain present in the differential spectra, usually seen as negative and positive going spectral bands, respectively. However, SPAIRS is more convenient for the detection of species in solution, whereas SNIFTIRS is better adapted to the detection of adsorbed species.

In SPAIRS, also denoted as "real-time FTIRS", reflectivities are recorded each 50 mV during a slow voltammetric scan. The spectra obtained result from the addition of several interferograms. As the spectral acquisition times are reduced compared with conventional IR techniques, it is possible to follow for example slow adsorption processes at the electrode surface. In contrast, in SNIFTIRS no voltammogram is recorded, but the electrode potential is switched between two distinct values $E1$ and $E2$. Reflectivities are obtained at these two electrode potentials, added 50 times at each potential, and finally normalized as $(R_{E2}-R_{E1})/R_{E1}$.

For more details regarding these specific techniques and their application, see [62, 63, 64, 65].

3 Survey of recent literature

As fuel cell research is a field of growing interest, an enormous number of research papers on various aspects is published each year, ranging from technological developments, like airbleed [66] and light-weight bipolar plates [67], to detailed mechanistic studies of methanol oxidation on single-crystal electrodes [52]. For this reason, only selected studies, that are of particular interest for the work presented, will be quoted and discussed in the following section.

3.1 Structural characterization in fuel cell research

Due to the structure-sensitivity of many electrocatalytic reactions, structural characterization plays an important role in fuel cell research [68]. In this context, three different approaches have to be distinguished: 1) the structural characterization of the whole electrode structure (the MEA in fuel cell technology), 2) the structural characterization of the catalyst and 3) the identification and characterization of the reaction products and intermediates. In general, structural investigations concentrate mainly on 2) and 3), whereas only a few studies on MEA characterization by scanning electron microscopy and porosimetry have been reported.

The catalyst structure is usually determined before and hardly ever after operation in the fuel cell by spectroscopic, microscopic or diffraction methods or a combination of them. In-situ measurements are generally conducted in conventional three-electrode cells in aqueous electrolytes, whereas in-situ monitoring of structural changes during operation in a real fuel cell has not been reported so far.

In contrast to the structural characterization of the catalyst, the identification and characterization of reaction products and intermediates is exclusively possible in an electrochemical environment. For this reason, so-called *quasi* in-situ techniques were applied, that make process studies at the electrode/electrolyte interface possible. In the context of fuel cell research, *quasi* refers to the fact that the measurements are conducted in a conventional electrochemical cell, not in a fuel cell under real operating conditions. Frequently, the real catalysts are replaced by model (single crystal) systems in order to achieve a deeper insight into mechanistic details that are often not accessible using supported nanosystems, due to insufficient signal-to-noise ratio and poor reproducibility.

3.1.1 Frequently-used methods: XRD, XPS, TEM

Both, supported catalyst systems as well as bulk electrodes are frequently characterized by X-ray diffraction (XRD), X-ray photoelectron spectroscopy (XPS) and transmission electron microscopy (TEM). The applied methods can be divided into spectroscopic, microscopic or diffraction methods, and further subdivided into surface and bulk techniques, according to the penetration depth of the incoming and the origin of the detected signal. However, the characterization of nanoparticles makes extremely high demands on the instrumental resolution of the applied characterization methods.

X-ray diffraction

X-ray diffraction appears to be an important tool for the characterization of bulk electrodes, as it can be applied to determine present phases as well as alloy formation in multinary compositions. For example, Gasteiger et al. [46] investigated the correlation of the lattice parameter with the alloy composition in the binary Pt-Ru system, and found a linear dependence, according to *Vegard*'s law. Thus, prior to the electrochemical testing, the phases in the bulk electrode were identified and the obtained electrocatalytic activities could be related to the apparent electrode composition. As an example for multinary catalyst compositions, the work of Gurau and coworkers [69] should be considered. Binary, ternary and quaternary platinum alloy catalyst formulations were synthesized as bulk and unsupported high surface area catalysts, and their structural and electrochemical properties have been investigated. X-ray diffraction proved to be very effective in the investigation of the bulk electrodes, whereas the interpretation of the X-ray patterns of nanosystems in the as-synthesized state is rather difficult. As prepared, the pattern of a Pt-Ru-Os-Ir sample shows only one nanocrystalline Pt fcc phase. However, after heat-treatment under nitrogen at 500 °C an either poorly-ordered or nanocrystalline hcp phase, most likely Ru, appears as a minor component. Regarding the appearance of this second phase, two different explanations have been discussed: either the as-synthesized catalyst contains a single nanocrystalline phase, which disproportionates T-dependent into a Pt-rich fcc and a Ru-rich hcp phase, or the Ru-rich phase is initially present in amorphous form (zerovalent state or hydrous oxide) and crystallizes during heat treatment. In this case, it is evident, that X-ray diffraction alone is not sufficient to determine the structure of the quaternary catalyst system properly, as amorphous phases and coherently-scattering areas below a certain size do not contribute to the X-ray pattern.

Characteristic features of nanosystems in XRD

In X-ray patterns, the width of the specific reflections depends among other factors on the size of the coherently scattering regions. Hence, this relation is often used for the evaluation of particle sizes, whereas it should be emphasized that only crystalline areas are taken into account. Average particle sizes can be calculated, using the *Scherrer* equation (see chapter 4, equation [4.1]), while particle size distributions might be derived by the *Warren-Averbach* method [70, 71].
The *Scherrer* equation is known to be one of the integral breadth methods, relating the average particle size to the peak width. Different crystallite shapes are taken into account by a shape parameter, the so-called *Scherrer* constant K, that is generally close to unity. However, it is a major drawback of this method, that strain effects are not considered in the mathematical treatment. Hence, the *Williamson-Hall plot* has been developed, in which the peak width is related to both, particle size and strain broadening [72].
Compared to the integral breadth methods for particle size determination, the *Warren-Averbach method* provides a real improvement, as the entire peak profile is described by a Fourier series, allowing for a complete correction of instrumental broadening and the effects of strain. The cosine Fourier coefficients, which describe the symmetric broadening, are then used for further analysis, e.g. to derive a crystallite size distribution. Provided that systematic errors arising from background determination, truncation and sampling effects have been considered, the Fourier approach of *Warren-Averbach* is a powerful tool in

studying the microstructure of highly-symmetric materials, and it has been widely used for this purpose. However, in its original form, the method is usually applied only to a few reflections, whereas it should lead to more proper results, when the complete powder pattern is used in microstructural analysis. Thus, large systematic errors could be reduced, even for moderate overlap of the tails of line profiles. Hence, in recent literature, new methods have been developed to obtain a more accurate analysis of diffraction profiles [73, 74]. Two different procedures for the determination of crystallite size distributions in the presence of strain were presented. The first method applies the three apparent size parameters obtained from the full width half maximum (FWHM), the integral breadths and the first few Fourier coefficients of the diffraction curves using modified *Williamson-Hall* and *Warren-Averbach* procedures. The measured size parameters are matched to the calculated values from the theoretical size profile by a least-squares fit. In the second method, the Fourier transforms of the experimentally determined peak profiles are fitted by the Fourier coefficients of *ab initio* physical functions of the size and strain profiles. In this case, the only fitting parameters are the median and the variance of the size distribution function, the density and arrangement of dislocations, and one or two parameters corresponding to the dislocation contrast factors. In general, a powder pattern can be simulated for a given distribution of sizes, if it is assumed that on average the crystals have a regular and uniform shape. This can be compared with experimental data leading to refined parameters, which define the distribution. Unlike 'traditional' methods of line-profile analysis, this entirely physical approach can be applied to powder patterns with severe overlap of reflections. Verification of the mathematical treatment is usually done by comparing the calculated size distribution with TEM results.

Debye function analysis (DFA) presents another approach to determine the size distribution and structure of small clusters by simulation calculations [75, 76, 77]. In contrast to the wide-spread analysis of only parts of the X-ray pattern, for instance the Fourier line profile analysis or the integral intensities of single *Bragg* peaks (see above), the DFA provides detailed structural information in a range of dispersion (approx. > 40 %), which is usually not accessible by the methods discussed before. The DFA method is based on the *Debye* functions of a sequence of model clusters with increasing size, which are added for comparison with the experimental intensity. A set of free parameters is used for the number fractions of the individual clusters, using the *Debye-Waller* factor, the average spacing within the individual clusters and a constant, which corrects for errors in the background subtraction. In principle, the measured diffraction curves are fitted by a set of *Debye* functions with the 'magic' numbers N = 13, 55, 147, ... for cuboctahedra and icosahedra; N = 54, 181 for decahedra and N = 13, 57, 154 for hexagonal close-packed clusters [78]. Evaluation of the full pattern results in a histogram plotting the mass fraction of specific structural units present within the sample against their average size. Vogel et al. [79] reported the structural characterization of surfactant-stabilized Pt-Ru catalysts and silica-supported Pt-Ru colloids in the as-synthesized state and after several heat treatments under various atmospheres. Numerical simulation using *Debye* functions yields information on both, the intrinsic structure of the colloids including the average lattice constant and the size distribution of the assembly of coherently scattering particles within the sample. However, it has to be mentioned, that the use of a discrete set of model clusters does not imply their real existence, as a quasi-continuous distribution would fit equally well. In the binary Pt-Ru system, simple model calculations have been carried out to investigate the effect of lattice site occupancy on the diffraction pattern. As expected, only minor changes in the scattered intensity occur for a) an ideal (stochastic) alloy, b) a Pt core with Ru shell or c) a Ru core with Pt shell, whereas distinct deviations from the known bulk bimetallic lattice constants should appear. In the case of

as-prepared Pt-Ru colloids, fluctuations in composition are intrinsically large, owing to their low nuclearity, and the fitting procedure did not yield completely satisfying results [79]. However, for the silica-supported Pt-Ru colloids in the as-synthesized state and after several heat treatments under different atmospheres interesting data were achieved. In brief, while the reduced catalyst shows an average size of 1.8 nm, a bulk Pt:Ru (1:1) lattice parameter and fcc structure, samples heat-treated in H_2 and in CO-, O_2- and CO-atmosphere again display a twinned fcc structure with average particle sizes of about 4 nm [79].
According to Garnier [80], a quick clue to the real structure of a carbon-supported Pt-Ru catalyst sample, gives the intensity ratio of the Pt(111) and Pt(200) reflection. Thus, a slightly-increased ratio $intensity_{Pt(111)}$: $intensity_{Pt(200)}$ can be interpreted as a first indication of the presence of very small individual Ru nanoparticles (< 1.5 nm) within carbon-supported Pt-Ru catalysts.

X-ray photoelectron spectroscopy

As diffraction techniques are only applicable to crystalline materials and as particles smaller than a certain value (d ≤ 2nm) appear to be X-ray amorphous, XPS measurements are a common supplement in the characterization of (supported) catalysts. But also in the characterization of bulk electrodes, X-ray photoelectron spectroscopy is a quite popular method in order to investigate the electrode surface, primarily in terms of oxidation processes and surface enrichment in a specific alloy component.
For example, Gasteiger et al. [81] carried out XPS measurements in combination with low energy ion scattering spectroscopy (LEIS) to study the surface enrichment in platinum of annealed Pt-Ru bulk alloys. The obtained results were contrasted with the segregation observed for bimetallic supported clusters of Pt and Ru [82]. As evident from the data presented, annealing at 800 °C produces a strong platinum surface enrichment that follows a smooth decay from the outermost layer to the bulk and does not exhibit any oscillatory behavior. This is in good agreement with calculations, applying ideal solution thermodynamics with the surface free energies and molar areas as input parameters.
From a similar point of view, Wieckowski and coworkers [83] investigated Pt-Ru, Pt-Os and Pt-Ru-Os bulk electrodes to learn more about the metals oxidation states and the surface composition of the alloys. The recorded spectra confirm that the Pt component is metallic at fuel cell-relevant potentials, whereas the second (third) metal appears in a partially oxidized state even at very low potentials, suggesting that the alloying elements act as oxygen transfer agents in a bifunctional mechanism. Additionally, no significant surface segregation has been found in the respective alloy systems.
A quite different interpretation of obtained XPS information has been given by Watanabe et al. [84]. In order to achieve a deeper insight into mechanistic details, a series of different binary Pt alloy electrocatalysts with non-noble metals of various compositions were investigated by XPS and cyclic voltammetry. Regardless of the composition, Pt-Fe, Pt-Ni, Pt-Co and Pt-Mo alloys have been found to exhibit excellent CO tolerance, comparable to that of Pt-Ru catalyst systems. At these CO-tolerant electrodes, the equilibrium coverage of CO was suppressed to values less than approximately $\theta = 0.6$. Based on the obtained XPS results, Watanabe and coworkers proposed a Pt skin effect with an electronic surface structure different from that of pure platinum, weakening the CO bond strength and thereby improving rapid CO oxidation and 'depoisoning' of the surface. A weakening of bond strength between the Pt skin layer and CO was also indicated by in-situ FTIRS, suggesting that the H_2 oxidation sites were not blocked by CO due to its enhanced mobility.

XPS measurements in combination with current-potential curves on a series of binary carbon-supported nanosystems were reported in an early publication of Hamnett and Kennedy [85]. In accordance with studies published on bulk systems [83], the main emphasis of their work was put on the elucidation of the predominant mechanism, by which the second (third) element improves the CO sensitivity of the resulting catalyst system. However, no clear statement could be made regarding mechanistic details in nanoparticle catalysts.

Characteristic features of nanosystems in XPS

In the characterization of nanosystems, e.g. carbon-supported Pd-Pt catalysts [86], at least two characteristic effects are of importance: a) a binding energy shift in dependence of the particle size and b) the assumption of XPS being a bulk method for sufficiently small particles. For example, measurements at Pt clusters by Kao et al. [87] showed a 0.3 eV increase of the Pt *4f* binding energy (BE) compared to Pt bulk systems. A continuous increase of the Pt *4f* binding energy with decreasing cluster size was also observed by Eberhardt et al. [88]. In their experiments, monodispersed Pt clusters consisting of 1-6 atoms were deposited onto a smooth substrate, the respective BEs ranging from 73.2 eV to 72.4 eV. For each particle diameter, the number of atoms per cluster can be calculated, applying a simple model with cubic closest packed structure of spherical atoms in spherical nanoparticles. Typical values are given by Franke [89] and are summarized in table 3.1. For particle sizes below 2.6 nm, at least half of the atoms in the cluster belong to the surface. Hence, the surface-sensitive X-ray photoelectron spectroscopy, usually probing the first few Å of the samples surface, becomes a bulk method for small particles.

Table 3.1 Variation of the binding energy and the number of surface atoms with particle size [89]

Particle size [nm]	**Pt *4f*7/2 [eV]**	**Number of surface atoms**
3.9	71.1	37 %
2.6	71.1	51 %
1.5	71.2	75 %
1.2	71.4	85 %

Transmission electron microscopy at nanosystems

In general, microscopy as an exclusive method does not play an important role in the structural characterization of fuel cell catalysts. Thus, microscopic investigations are rather combined with other spectroscopic and diffraction techniques to obtain a comprehensive idea of the catalysts real structure. However, in the case of whole membrane electrode assemblies, TEM and SEM are suitable methods to determine the electrode's morphology, the ionomer distribution, and the catalyst utilization [90].
A very detailed study of carbon-supported nanoparticles by TEM and XRD is reported by Radmilovic et al. [91]. The focus of their work was put on the characterization of a commercially-available carbon-

supported Pt-Ru (1:1) catalyst in terms of both, particle size and completeness of alloy formation. As already discussed in detail for XRD and XPS investigations (see above), the nanosize of these particles presents challenges to their microstructural characterization. In the authors' opinion, many of these challenges can be addressed by transmission electron microscopy. Especially the lattice structure can be studied by high resolution electron microscopy, including the presence of defects as dislocations, twins, etc. High resolution TEM (HRTEM) presents an interesting tool in catalyst characterization, as it can be used to determine the geometric shape of faceting planes, the presence of surface steps, the surface roughness, as well as size and distribution of nanoparticles. For the commercial catalyst investigated, a uniform distribution of spherical particles with an approximate size of 2 nm was found. However, according to Radmilovic and coworkers, apparent rounding of particles might be caused by two different effects: a) due to the inclination of the particles from the low index zone axis, faceted corners appear to be slightly curved; b) even when particles are aligned along a low index zone axis, they can appear to be spherical because of interference from the carbon support and confusing contrast that obscures sharp edges and corners [91]. The latter effect can be avoided by analyzing particles close to the edge of the carbon grains. Detailed analyses of crystallites on or close to the edges of the carbon substrate show faceting on (111) and (200) planes, characteristic of fcc cuboctahedral nanocrystals. In this respect, the Fourier filtering technique is a helpful tool in removing the contribution from incoherent scattering of electrons from the amorphous carbon, so that particles within the support can be imaged as well. Lattice spacings within the nanoparticles were determined, using the copper grid (TEM sample holder) as an internal calibration. However, the lattice constant measurement from interplanar spacings does not have sufficient accuracy to determine compositional variations between particles in the Pt-Ru system, since ±1 % covers the whole range of lattice parameters between pure Pt and a 1:1 Pt-Ru alloy.

As already indicated in the previous paragraph, the characterization of supported nanoparticles by transmission electron microscopy presents extreme challenges to the instrument and the operator. In particular, the measurement of lattice spacings is erroneous, as the lattice parameter observed depends on the particle size. Goyhenex and Henry [92] investigated this dependence by in-situ surface electron energy-loss fine-structure spectroscopy (SEELFS) and ex-situ transmission electron microscopy at supported Pd clusters. In this case, an expansion of the palladium lattice, increasing with decreasing cluster size has been observed. However, for almost all other metals a lattice contraction with decreasing particle size is reported (e.g. for platinum, see [93]). This is due to the *Laplace* law, expecting a contraction of the clusters proportional to their surface tension. Typical values of distortion range between 2 and 6 % for particles with an average size of 2-3 nm, which means that the above-mentioned 1 % change in lattice spacing due to compositional differences [91] is negligible and would not be detected. Hence, for small particle sizes the determination of particle compositions using lattice spacings from TEM images is not feasible.

A likewise interesting approach has been reported by Narui et al. [94], applying transmission electron microscopy as in-situ method. This was made possible by using a special specimen chamber. In their work, in-situ measurements were carried out at elevated temperatures to monitor the particle growth and sinter behavior of alumina-supported Pt-PdO catalysts. Temperature-dependent TEM studies might also be a promising approach in the investigation of fuel cell catalysts.

3.1.2 Combination of methods

Despite promising results, the characterization of carbon-supported fuel cell catalysts by a combination of several bulk and surface methods is comparatively scarce so far, whereas combining electrochemical testing with structural characterization, in special cases referred to as spectroelectrochemistry (see chapter 2.33), presents a widely-accepted approach. In the following part, merely a small choice of research work on binary Pt-Ru and ternary Pt-Ru-X catalysts will be quoted.

Schmidt et al. [95] presented a combined XPS, atomic force microscopy (AFM), HRTEM and rotating disc electrode (RDE) study on Pt-Ru alloy colloids, synthesized according to the *Bönnemann* method. In this context, HRTEM and AFM investigations were carried out to quantify the effect of temperature-induced sintering, as the colloidal particles have to be heat-treated in various atmospheres to remove the surfactant shell. For the TEM and AFM measurements, the conventional carbon black was replaced by a glassy-carbon model substrate to simplify the evaluation. Spherically shaped particles with a mean diameter of 1.7 ± 0.5 nm and an almost 1:1 overall stoichiometry were found prior to reactive annealing. After the two step heat-treatment in oxygen and hydrogen atmosphere, respectively, only slight sintering could be seen and an average particle size of 2.2 nm was determined. X-ray photoelectron measurements were performed to monitor the removal of the surfactant shell. After annealing in oxygen, complete removal of the surfactant shell could be confirmed, while the treatment in hydrogen was applied to reduce previously oxidized ruthenium to its metallic state. Finally, the electrocatalytic activity of the carefully characterized Pt-Ru catalyst was tested in rotating disc experiments.

Combined characterization of metallic platinum-ruthenium electrodeposits supported on a gold substrate by X-ray diffraction, Auger electron spectroscopy (AES) and XPS measurements was reported by Cattaneo and coworkers [96]. In the X-ray patterns of the model catalysts, only a single fcc phase could be seen, which was assigned to a platinum-ruthenium alloy, as no indication of additional reflections of hexagonal ruthenium was found. Evaluation of the alloy composition was done according to *Vegard*'s law. Due to the XPS measurements, both, platinum and ruthenium were primarily present in the zerovalent state in good agreement with the XRD and AES investigations.

Results on ternary Pt-Ru-MeO_x (Me = W, Mo, V) catalysts, synthesized by a slightly modified *Adams* method, were presented by Lasch et al. [97]. The catalyst systems were characterized by X-ray diffraction, X-ray photoelectron spectroscopy, energy-dispersive X-ray analysis (EDX), and the Brunauer-Emmett-Teller sorption method (BET), and their electrocatalytic activity was checked by both, cyclic voltammetry and stationary current-voltage measurements. Quantitative EDX and XPS analyses showed that the bulk and surface composition of the materials were almost identical, taking into account errors resulting from the surface roughness of the samples. Both, platinum as well as ruthenium were present in zerovalent state and as an oxidized species in the catalyst. By X-ray diffraction no evidence for transition metal oxides was found, probably due to their presence in an amorphous form. In essence, Lasch and coworkers interpreted the structural information obtained by assuming the coexistence of Pt-Ru alloy particles next to Pt-Ru oxides and amorphous transition metal oxides. These results seem to be in quite good agreement with our work in the ternary Pt-Ru-W system [98].

While the combination of X-ray diffraction and X-ray photoelectron spectroscopy with an electrochemical testing method presents an almost standardized approach, Hagans and coworkers [99] applied a rather unusual combination of methods, that proved to be quite effective. In their investigations, XPS, thermogravimetric (TGA) and differential thermal analysis (DTA) as well as X-ray absorption near

edge structure (XANES) measurements were combined in order to determine the chemical state of ruthenium in Pt-Ru direct methanol fuel cell anode catalysts. Different, commercially-available supported and unsupported Pt-Ru catalysts purchased either from E-TEK or from Johnson Matthey were checked and compared with respect to their oxygen content and the amount of ruthenium oxide species present. In contrast to the predominant opinion, Hagans et al. proposed that hydrous ruthenium oxide plays the major role in fuel cell electrocatalysis and not the bifunctional mechanism in a Pt-Ru alloy system, as assumed by most other researchers. Data obtained by a combination of the above mentioned methods provided strong evidence for the presence of ruthenium oxides and hydrous ruthenium oxide species, thereby backing their theory.
In summary, almost identical results on Pt-Ru fuel cell anode catalysts were obtained in the different studies, no matter which specific methods were combined. However, the data interpretation differed a lot, as the information provided is not sufficient to draw a clear and unquestionable conclusion. Hence, a lot of additional efforts in this specific field of interest seem necessary to gain a detailed and conclusive impression of the catalysts real structure.

3.1.3 More special methods

Apart from XRD, XPS and TEM, more special methods applied for the investigation of supported nanosystems are X-ray absorption spectroscopy (XAS) and Fourier transform infrared spectroscopy (FTIRS), but also metal-nuclear magnetic resonance spectroscopy (NMR), scanning tunneling microscopy (STM), electrochemical impedance measurements (EIS), small angle X-ray scattering (SAXS), Mössbauer spectroscopy and temperature programmed reaction (TPR). Each of these methods offers characteristic features for the characterization of fuel cell catalysts regarding either the catalyst structure or the electrocatalytic mechanism or both. However, most of them are not very popular, as they are not easy accessible or require a costly instrumental setup.
Impedance studies, for example, are carried out on a complete membrane-electrode assembly and provide data on its mass-transport properties and the reaction mechanism for methanol electrooxidation [100, 101]. The deactivation mechanism by carbon monoxide poisoning was investigated using electrochemical impedance spectroscopy by Schiller et al. [102]. They found an increasing pseudo-inductive behavior, which can be explained by a surface relaxation process, according to the competitive oxidation of hydrogen and carbon monoxide at the anode. A problem of the impedance spectroscopy is still the very complex fitting of the spectra by insufficient models.
As could be shown by Hamnett and coworkers [103], Mössbauer studies at a carbon-supported Pt-Ru fuel cell catalyst are in principle possible and can be used to determine the oxidation state of the ruthenium. An in-situ Mössbauer investigation of an operating fuel cell has also been reported [104]. However, information on the oxidation states of metals present in the catalyst could be achieved more easily and less costly by XPS.
To yield a deeper insight into mainly mechanistic aspects of the fuel cell reactions, temperature programmed desorption (TPD) and reaction measurements were performed [105, 106]. Although these techniques belong to the well-known routine tools in heterogeneous catalysis, they are only rarely applied in fuel cell research. Bergeld et al. [106] investigated the CO oxidation at a Pt(111) model system and its promotion by coadsorbed water. According to the authors, who considered possible mechanisms for the

promotion of CO_2 formation by H_2O, a reaction route via intermediate OH (from the water) is an obvious candidate. However, it should be taken into account, that TPR and TPD techniques obtain mechanistic data via gas phase reactions, but that the mechanisms are not necessarily transferable to an electrochemical environment.

Quasi in-situ SAXS measurements during cyclic voltammetry in an electrochemical flow cell were reported by Haubold et al. [107]. A special technique, anomalous scattering in contrast variation, allowed to separate the scattering contributions from the catalyst particles and the pores in the porous carbon support. Fitting of the obtained curve resulted in a bimodal size distribution for the platinum particles, with 88 % of the particles less than 1 nm in size and 12 % of 6 nm average size. Scattering curves were also measured at 250 mV vs Ag/AgCl in the reduced state and at 1100 mV in the oxidized state during a potential sweep. The matched size distributions gave mean radii of 0.9 nm for the reduced and 1.1 nm for the oxidized particles, with the apparent increase in size attributed to the formation of a platinum oxide. However, it is obvious that there exist less expensive alternatives to determine the particle size distribution within a catalyst.

Starting with the invention of scanning tunneling microscopy (STM), a variety of scanning probe microscopies (SPM) with different detection probes have been developed, providing the opportunity to sense for example attractive and repulsive interactions, magnetic, electrostatic and frictional forces with a high spatial resolution and in three dimensions [108]. Consequently, these techniques were soon utilized to study the properties of catalytic active metal clusters on smooth substrates in terms of cluster size and shape, distribution, local electronic structure and support-metal interactions. One example for the use of STM in fuel cell research is the work of Crown and Wieckowski [109], monitoring the different behavior of ruthenium and osmium deposited onto Pt single crystal substrates. Homogeneous deposition of ruthenium at low-index Pt(*hkl*) surfaces was observed, whereas osmium showed preferential deposition at surface defect sites and step edges. Nevertheless, STM and related techniques require extremely smooth surfaces as particle support and are therefore limited to model systems.

In 1989, solid state NMR spectroscopic investigations have been carried out for the first time at fuel cell related electrocatalytic systems in an electrochemical environment [110], followed by a number of publications, mainly by Wieckowski and coworkers, on characteristic features of platinum fuel cell catalysts [111, 112, 113, 114]. By ^{195}Pt NMR measurements, performed in combination with cyclic voltammetry, a particle size increase from 2 to 9 nm due to sintering effects during repetitive scans was observed [111]. More detailed studies of metal-ligand interactions, e.g. CO adsorption on a carbon-supported platinum electrocatalyst, were reported in [112, 113]. According to these studies, NMR investigations provide useful correlations between electronic properties and more conventional chemical descriptors, such as ligand electronegativity, that will be helpful in understanding the electronic structure of metal-adsorbate interfaces. In this context, a rather sophisticated approach is the correlation of solid state ^{13}C NMR results [114] with SNIFTIRS measurements on a supported platinum catalyst, that has been presented by Rice et al. [115, see also below].

Fourier transform infrared spectroscopy

As already explained in chapter 2.3.3, infrared spectroscopy belongs to the spectroelectrochemical in-situ techniques at the electrode/electrolyte interface and presents an important tool in monitoring the

characteristic, potential-dependent features of small molecules adsorbed at the catalyst surface. In fuel cell research, CV/FTIRS and related methods are generally termed *quasi in-situ* due to the fact, that they are not conducted in a real operating fuel cell. In the following paragraph, a short overview of selected, fuel cell-relevant FTIRS literature will be given. The main emphasis of these studies is put on mechanistic aspects of CO or methanol electrooxidation at either model (single crystal) electrodes or supported nanosystems.

In this field of interest, an early work was reported by Kunimatsu et al. [116] on the mechanism of CO electrooxidation at a polycrystalline platinum disc electrode. According to the results obtained, two CO oxidation mechanisms could be distinguished in dependence of the adsorption potential, namely an island and a random oxidation mechanism. Consequently, the history of the bulk electrode concerning initial adsorption potential and electrode pretreatment plays an important role in detailed CO adsorption and oxidation studies.

From a more kinetic point of view, Petukhov and coworkers [117] investigated the CO surface diffusion at a Pt(111) single crystal electrode, both theoretically and experimentally by recording and modelling the CO oxidation current during a potential step (transient method). Comparing the experimental and theoretical results, it had been found that the reaction kinetics were significantly affected by the diffusion of the small CO molecule. In their simulation, three different diffusion cases were distinguished, using the CO hopping rate k_d and the true reaction rate k_0 as parameters to model the position of the CO oxidation maximum and its width.

The dependence of CO adsorption and oxidation on the substrate composition was investigated by Ianniello and coworkers [118] at several polycrystalline Pt-Ru alloy electrodes. Only linear-bonded CO could be detected within the resolution limits and no frequency shift was observed due to different alloy compositions. However, significant peak broadening of the CO stretch band for the alloy systems indicates an increased inhomogeneity of the surface leading to a larger spread in vibration frequencies. Virtually the same has been found by Zheng et al. [119] for nanometer scale thin film Pt-Ru alloy electrodes, showing an increase in the FWHM of the CO stretching frequency with increasing ruthenium content.

Investigations of the promoting effect of ruthenium and tin additions in methanol electrooxidation were reported by Morimoto et al. [120]. While on pure platinum linear-bonded CO_{ad} formation is clearly indicated by the peaks around 2070 cm^{-1}, the peaks for the Pt-Ru and Pt-Sn surfaces were not as well distinguished. Hence, it was suggested, that the CO_{ad} coverage on the alloy systems is much lower than on pure platinum. In agreement with the cyclic voltammetry results, carbon dioxide, which is the final product of methanol oxidation, is detected at 400 mV vs RHE for Pt and Pt-Ru. On Pt-Sn, CO_2 already emerges at 340 mV vs RHE, indicating the promoter effect of tin for methanol oxidation at lower potentials. However, the electrocatalytic activity of platinum-tin alloys for CO and methanol electrooxidation is controversially discussed in literature.

Characteristic features of nanosystems in FTIRS

The investigation of supported nanoparticles instead of model surfaces is quite a challenge for both the instrument and the operator, as only poor signal-to-noise ratios are obtained. Hence, most studies have

been carried out at model systems due to their easier preparation and measurement, although important information on particle size effects and catalyst-support interactions will be lost.
In general, the particle size influences three parameters in the infrared spectra significantly: 1) the CO stretching frequency, 2) the *Stark* tuning rate and 3) the CO surface coverage. Superposition of these effects leads to the higher electrocatalytic activity observed for the nanoparticles compared to bulk metals.
In the following two publications, which are quoted here, a detailed analysis of particle size effects in infrared spectroscopy has been performed for fuel cell-relevant catalyst systems. The first in-situ FTIRS study of the electrochemical methanol oxidation at small platinum particles has been published by Christensen and coworkers [121], showing significant differences between the mechanism at bulk and at particle electrodes. Thus, methanol chemisorption at small Pt particles takes already place at 50 mV vs RHE compared with 150 mV at a platinum bulk electrode. The other notable difference between bulk and nanosystems was the frequency shift of the CO absorption band to lower frequencies with increasing potential in nanoparticle systems. In contrast, the corresponding shift for bulk metal platinum was to higher frequencies due to a combination of *Stark* tuning and a coverage dependent shift. The *Stark* shift itself was reported to be about 30 $cm^{-1}V^{-1}$ for linear-bonded CO on macroscopic platinum. As the *Stark* tuning effect also appeared on Pt nanoparticles, the coverage dependence had to be of a much more complex nature in macro-systems to account for the reversed shift to lower frequencies. According to the results obtained, Christensen et al. proposed the migration of linear-bonded CO from terraces to edge or kink sites. Additionally, a much more pronounced appearance of multibonded CO has been observed on the nanoparticles, probably due to an easy conveyance mechanism between single- and triple-bonded CO, which might be a consequence of the migration suggested above.
With respect to CO electrooxidation, Rice and coworkers [115] presented an in-situ infrared study of CO adsorbed on carbon-supported platinum nanoparticles, which they correlated with earlier ^{13}C NMR results (see above). It has been found by SNIFTIRS measurements, that the infrared stretching frequency and the *Stark* tuning rate showed a strong dependence on the platinum particle size. The infrared stretching frequency increased with increasing particle size, while the *Stark* tuning rate was found to decrease. The increase in the IR stretching frequency at a constant electrode potential with increasing particle size could arise from a change in CO coverage, a change in coordination number or changes in Pt-CO bond strength. Its correlation with the information, obtained by solid state NMR, indicated that the particle size-dependent variations in stretching frequency and *Stark* tuning rate are due to strong interactions between platinum nanoparticles and the conductive carbon support. As other parameters, influencing the stretching frequency, like different CO coverages and dominant crystal planes, could be ruled out, an electronic mechanism seems to be the most plausible reason for the observed effect. With respect to current fuel cell research, the obtained results might be summarized in terms of the higher the metal-support interaction, the easier the CO bond can be weakened at lower potentials, thus facilitating CO oxidation.

X-ray absorption spectroscopy at nanosystems

In the following paragraph, it has been assumed, that the reader is familiar with basic XAS concepts. For a more detailed treatment of x-ray absorption spectroscopy, see textbooks of spectroscopy [61].

In general, the X-ray absorption spectrum of a sample can be divided into two regions: the near edge region (X-ray absorption near edge structure, XANES, 0-50 eV above the absorption edge) and the oscillatory part of the spectrum (extended X-ray absorption fine structure, EXAFS, > 50 eV above the absorption edge). Due to its specific features, in fuel cell-relevant literature primarily EXAFS measurements were reported, extracting structural information from a fuel cell catalyst by analysis of the oscillatory part of its X-ray absorption spectrum. With respect to the structural characterization of nanoparticles, EXAFS presents the advantage that the chemical environment of an element can be determined in terms of number and type of neighbors, interatomic distances and structural disorder [122], independently of its crystallinity. By XANES measurements information on oxidation states, valence band vacancies and adsorption geometries of molecules at the surface can be obtained. However, as the evaluation of the spectra is quite complex, due to multiple scattering processes, EXAFS analysis is generally preferred. As X-ray absorption measurements can be carried out under any kind of atmosphere, the EXAFS technique proves to be uniquely suitable for in-situ studies in applied catalysis. In the following passage, a small choice of recent publications in ex-situ X-ray absorption analysis of fuel cell catalysts will be quoted. The corresponding in-situ XAS investigations will be cited in chapter 3.1.4.

Structural characterization of two different carbon-supported Pt-Ru catalysts, a commercial one and an in-house synthesized sample, by ex-situ EXAFS measurements has been reported by Lin et al. [123]. Fuel cell tests of the respective catalyst systems, using 250 ppm CO in the hydrogen anode feed, showed different electrocatalytic activities in operation. Hence, EXAFS investigation was applied to account for the differences observed in performance. Analysis of the absorption spectra resulted in different degrees of Pt-Ru alloying: the data of the in-house synthesized sample indicated the formation of Pt-Ru bonds, whereas no significant Pt-Ru contributions were observed for the commercial catalyst. Thus, the authors concluded, that the catalyst synthesized in-house was at least partially alloyed, while the commercial catalyst system seemed to contain mixed phases of Pt and RuO_x.

Several binary Pt-X (X = Ru, Fe, Co, Ni, Cu) electrocatalysts for methanol electrooxidation were investigated by Hormes and coworkers [124]. Prior to the X-ray absorption measurements, the electrocatalytic activity of the respective catalysts was determined by cyclic voltammetry, using different methanol concentrations. As the Pt-Ru catalyst exhibited a quite poor performance for the electrooxidation of methanol, accurate determination of its morphology seems necessary to reveal structural features, that might be responsible for its poor electrocatalytic activity. XANES measurements indicate a decrease in *d* band vacancies, while a Pt-core/Ru-shell structure is proposed, according to the EXAFS results. The differences obtained for the electronic and geometric structure of the in-house synthesized Pt-Ru catalyst compared to the conventionally used commercial catalyst were held responsible for its comparatively poor performance in methanol electrooxidation.

A detailed treatment of particle size effects in XAS can be found in Frenkel et al. [125]. According to them, mainly three different effects are known: the particle size effect on 1) the electronic structure, 2) the lattice parameter and 3) the phase dynamics. While it is obvious that the cluster properties become increasingly bulk-like as the cluster size increases, additionally specific structural effects can arise, determined by size-sensitive perturbations of the electronic structure or the nature and range of the interatomic interactions. Size-sensitive changes in the electronic structure become visible in a shift of the absorption edge and a modified white-line intensity. The shift of the absorption edge is similar to the one observed in X-ray photoelectron spectroscopy (see above). Contraction and expansion of the lattice parameter in very small metal clusters have already been discussed in the context of transmission electron

microscopy (chapter 3.1.1), and can be seen in the EXAFS data as well by a corresponding reduction / dilatation in the average nearest neighbor interatomic distances. By direct calculation of the nearest neighbor interatomic distances along with their static and dynamic disorder, a size-dependent static disorder in the atomic positions has been found that increases markedly with decreasing particle size. In the authors' opinion [125], the most plausible explanation for this behavior is a cluster surface relaxation, probably driven by the substantial surface tension. In response to this compressive tension, the atomic positions of the surface atoms should shift away from ideal fcc sites and towards the cluster's core.
Exemplary for fuel cell-relevant studies of particle size effects in several binary anode and cathode catalyst formulations, the work of Mukerjee et al. [126] and Min and coworkers [127] will be cited here. In [126], Mukerjee et al. present their findings, how the particle size affects the electrocatalytic activity of a pure platinum electrocatalyst in methanol electrooxidation. In their opinion, an increase of the Pt L_3 white line intensity indicates the adsorption of OH species at higher potentials, whereas the broadening of the white line at 0 V vs RHE is related to adsorbed hydrogen. It has been shown that the *d* band vacancy decreases with increasing particle size, indicating that the electronic effects due to adsorption of H and OH are larger for smaller particles. Thus, with decreasing particle size the adsorption strength of H, OH and CO is increased, resulting in reduced methanol oxidation activities for particles below a certain size. Cycling the potential between 0 V and 0.5 V vs RHE, induced morphological changes in the platinum clusters, which are reflected in an increase of the coordination number *N* in the EXAFS data. Due to the stronger H adsorption on small particles, reconstruction and morphological changes get more pronounced with decreasing particle size.
With respect to the oxygen reduction reaction (ORR) at the fuel cell cathode, Min and coworkers [127] investigated particle size and alloying effects in Pt-based Pt-Co, Pt-Ni and Pt-Cr catalysts. As the structure-sensitivity of those catalysts for oxygen reduction seems associated with the adsorption strength of oxygen intermediates on the Pt surface atoms, particle size and alloy formation play a decisive role for the catalyst activity. By evaluation of the XANES region of the spectra, a decrease of the *d* band vacancy with increasing particle size has been found, in agreement with Mukerjee et al. [126]. Referring to the ORR, this result suggests a lowered adsorption strength of adsorbed oxygen species, thus facilitating the reaction at larger particles.

3.1.4 In-situ XAS investigations

In principle, there exists a multitude of methods, that can be applied for in-situ investigations. Main prerequisites for a characterization technique to become an in-situ method are that it might be carried out under any kind of atmosphere and that the time scale of the measurements is faster than the studied effects. In fuel cell-relevant literature, in-situ XRD, Mössbauer, EIS, Raman, and XAS measurements have been reported. Nevertheless, in-situ XAS proved to be the most appropriate technique for this purpose, as might be seen from the comparatively large number of in-situ XAS studies, that have been published during the last decade [128, 129]. Due to its relevance in fuel cell research, this chapter focusses exclusively on in-situ XAS investigation.
However, the term in-situ investigation is not very well-defined and comprises at least two different approaches: gas treatment measurements under various atmospheres and at different temperatures and investigations in an electrochemical environment, e.g. a standard three-electrode cell. In the following

paragraph, it should be stressed by a small choice of selected in-situ XAS investigations, that a variety of problems in fuel cell research can be addressed by this specific technique. Thus, not only structural changes of the catalysts under different atmospheres and at various temperatures can be monitored, but also the effect of different electrochemical potentials and the impact of H, OH and CO adsorption on the catalyst structure.

As an example of gas treatment measurements, Nashner and coworkers [130] applied X-ray absorption spectroscopy to characterize carbon-supported Pt-Ru nanoparticles synthesized from the molecular cluster precursor $PtRu_5C(CO)_{16}$. On the basis of ex-situ EXAFS measurements in combination with transmission electron microscopy a detailed structural model of the nanoparticles has been deduced, and its results have been compared with in-situ data under hydrogen and oxygen atmosphere. Under H_2 atmosphere, Pt shows a pronounced preference for segregation to the particle surfaces, as indicated by a stronger weighting of the homometallic coordination in the EXAFS data. After chemisorption of oxygen at room temperature, a significant reduction in the amplitude observed for the first-shell metal-metal bonding and the formation of metal-oxygen bonds has been found. Additionally, changes in the calculated coordination numbers have been obtained, the origin of these still being unclear. Supplementary investigations at various temperatures [131] show that the nanoparticles are initially present in a highly disordered structure, in which platinum is found preferentially at the core of the condensing particle. Only after further temperature treatment, the nanoparticles adopt the inverted structure described above.

In order to account for support effects, Hills et al. [132] applied either carbon black, fullerene soot or desulfurized carbon black as particle support. In principle, the EXAFS data recorded under hydrogen and oxygen atmosphere indicated, that the nanoparticles behaved similarly to those data reported previously [130], independently of the support material. The influence of the different carbon supports can only be seen by the presence or absence of Ru-C interactions. In the case of the fullerene soot, catalyst-support interaction suggests the formation of a Ru carbide phase at the nanoparticle/support boundary.

A combination of both, in-situ gas treatment measurements and in-situ investigation in an electrochemical environment, has been carried out by Lampitt et al. [133] to study the structure of carbon-supported platinum electrocatalysts for methanol oxidation. EXAFS data obtained at the Pt L_3-edge indicate that preparation of the catalyst by oxidation of $Na_6Pt(SO_3)_4$ forms highly-dispersed PtO_x species. After reduction by either hydrogen in the gas treatment cell or potentiostatically in the electrochemical cell, small platinum particles are formed, as can be seen from the presence of Pt neighbors in the first coordination shell. Carbon neighbors from the support are also evident in the first coordination shell at 2.6 Å and 3.6 Å, respectively.

However, much more often than gas treatment measurements at various temperatures and under various atmospheres, in-situ investigations in an electrochemical environment will be found in literature. In early studies, Mc Breen and coworkers [134] investigated changes in the structure of Pt-Ru electrocatalysts in dependence of the applied potential in an electrochemical in-situ cell, using 1 M $HClO_4$ as supporting electrolyte. Spectra of the Pt L_3-edge confirmed the formation of a Pt-Ru alloy, with ruthenium increasing the Pt *d* band vacancies and decreasing the Pt-Pt bond distances. Data obtained from the Ru *K*-edge were less conclusive because of a large excess of unalloyed ruthenium in the catalyst. XANES results at various potentials suggested that alloying with ruthenium affects and most likely reduces the adsorption of hydrogen on platinum. An indication of hydrous ruthenium oxide formation and a relaxation of the Pt-Ru bonding is found by evaluation of the EXAFS oscillations. In essence, the results obtained point out

that the bifunctional mechanism needs to be modified to take into account the effect of the increase in Pt *d* band vacancies on the adsorption of H and CO residues.

Hydrogen electrocatalysis at carbon-supported platinum alloyed with several first row transition metals (Cr, Mn, Fe, Co, Ni) has also been reported by Mukerjee et al. [135]. Compared with a pure platinum catalyst, ex-situ investigations of the alloy systems showed changes in the *d* band vacancies and a pronounced lattice contraction. Repeated cycling between the double layer region (approx. 0.5 V vs RHE) and 0 V vs RHE caused significant changes in the XAS spectra of the pure platinum catalyst, whereas none was observed for the alloys. Thus, XANES data of a platinum catalyst indicated the generation of empty electronic states in the vicinity of the Fermi level, due to the adsorption of hydrogen. Additionally, an increase in the coordination number of the first Pt-Pt shell has been determined by EXAFS measurements. This is in close agreement with the gas treatment measurements of Nashner et al. [130] under hydrogen and oxygen atmosphere, respectively, in which changes in the coordination numbers have also been observed. However, the reason for this is not yet completely understood, although either particle growth or ordering processes have been proposed. Alloying of the platinum with first row transition metals is found to suppress both the electronic and structural effects at 0 V.

XANES studies of the CO electrooxidation have also been published [136]. Spectra obtained at the same electrochemical potential under either inert gas or carbon monoxide show significant differences in shape, due to a change in the ruthenium oxidation state. A much lower state of oxidation was found in the presence of adsorbed CO than in an inert gas atmosphere. However, in CO variations in the electrode potential do not change the XANES data significantly, whereas potential variations under inert gas atmosphere cause severe changes in the shape of the spectra, which can be assigned to differences in the electronic and geometrical environment of the Ru atoms. Obviously, the oxidation of ruthenium with increasing electrochemical potential is hindered by adsorbed CO molecules.

More recently, Maniguet and coworkers [137] demonstrated the applicability of in-situ EXAFS in probing adsorbate structures. In their work, the potential dependence of the extended X-ray absorption fine structure obtained at the Pt L_3-edge for a carbon-supported platinum electrocatalyst exposed to CO is presented. The data have been analyzed using the difference file method to separate the dominant contributions of the Pt neighbors from that of the adsorbed species. By detailed examination of the remaining non-Pt neighbors the presence of adsorbed CO with a Pt-C distance of 1.85 Å at potentials less than 0.5 V vs RHE is clearly evidenced. Increasing the potential above 0.5 V resulted first in the removal of the adsorbed CO and at more positive potentials in the formation of an oxide layer, indicated by the presence of a Pt-O coordination shell at 2.00 Å. However, contributions from the C neighbors of the carbon support prevent the determination of the effect of the applied potential on the CO bond length and independent discrimination between the various possible adsorption sites, e.g. linear- or bridge-bonded.

Finally, O'Grady et al. [138] compared ex-situ XANES data of two different Pt-Ru catalyst systems with either the respective in-situ spectra at a potential of 0.1 V vs $Pd/H_2/H^+$ or after operation in a real fuel cell using methanol. In the ex-situ investigations, the as-prepared catalysts were found to be predominantly in the form of Pt oxides and Ru oxides. However, either placed in an electrochemical cell and held in the potential region, where methanol oxidation occurs, or after DMFC operation, XANES data indicated that the metal oxides were reduced to the metallic form. According to these results, the authors postulated that conclusions about the electrocatalytic activity of Pt/Ru materials for methanol oxidation drawn from the characterization of as-prepared samples have comparatively little relevance.

Atomic X-ray absorption spectroscopy

A relatively new development is the atomic X-ray absorption spectroscopy (AXAFS), which takes also into account the specific long-range oscillatory behavior revealed as a well-resolved peak in the low *R* region of the Fourier transform. This underlying structure in the XAS spectrum has already been observed by Holland et al. [139] in 1978, and was explained by photoelectrons scattered off from electrons of the original absorber atom, instead of electrons of neighboring atoms as in EXAFS. Although this physical interpretation has been given, AXAFS is still controversial, as the observed structures in the background have also been attributed to multi-electron excitations. However, since the first publications of Ramaker et al. [140] and Rehr and coworkers [141], atomic X-ray absorption fine structure studies became more and more popular.
Atomic X-ray absorption spectroscopy has been applied to spherical platinum metal clusters, where the AXAFS intensity of the central atom turned out to be much larger than that of the surface atoms [140]. However, the average AXAFS intensity per Pt atom is found to depend not significantly on the cluster size. On the other hand, a variation of the metal cluster support considerably changes the intensity as well as the imaginary part of the atomic X-ray absorption fine structure. Hence, this method can be a very effective probe for the effects of interactions between the metal and the support in supported noble-metal catalysts, like those applied in fuel cells.
Recently, the first in-situ AXAFS study has been presented by O'Grady and coworkers [142], showing systematic electrochemical and chemical effects on the AXAFS structure in dependence of the applied potential. Changes of the atomic X-ray absorption fine structure as a result of platinum alloyed with ruthenium have also been shown. In another study, O'Grady et al. [143] applied the AXAFS technique to examine an electrode/electrolyte interface, where systematic changes in the magnitude of the atomic X-ray absorption fine structure have been observed for the in-situ charging of a Pt/C electrode in 0.1 M $HClO_4$. Data for the carbon-supported platinum electrode at three different potentials do not show a significant change in the peak positions, indicating a constant atomic radius with no change in the immediate chemical environment. However, the magnitude of the peaks show a strong and systematic increase, as the electrode potential is increased. According to the authors, the effects on the AXAFS spectra with charging arise from a 'chemical' or charging shift, which alters the cross-section for AXAFS scattering. These results hold out the possibility of providing spectroscopic information on the surface charge of electrocatalytic systems under reaction conditions, that is not accessible in-situ by other spectroscopic techniques.
At present, the development of a specially designed fuel cell suitable to conduct catalyst characterization during real fuel cell operation is in the focus of many research activities [144, 145]. However, up to now only a few attempts of in-situ characterization in real fuel cells, e.g. by Mössbauer spectroscopy, have been presented and, up to our knowledge, not any in-situ XAS investigations in fuel cell operation have been reported so far.

3.2 Model system studies

As already mentioned before, real electrocatalysts were frequently replaced by model systems in order to get a more detailed understanding of electrocatalytic mechanisms. In principle, model systems offer the

advantage that many parameters are either preset or can be defined more precisely than in real catalysts, thus allowing for the selective variation of a specific parameter. Besides, better signal-to-noise ratios were usually obtained on smooth electrode surfaces, e.g. in FTIR spectroscopy [68]. However, information on parameters that are only affected by real system characteristics, like catalyst-support interactions and particle size, will be lost.
A number of different model systems is known in literature, ranging from bulk alloy electrodes [46] to decorated single crystals [146]. Due to their characteristic properties, results of bulk alloy electrodes are very close to reality, whereas single crystal studies are preferred for the investigation of mechanistic details. In the next paragraph, examples for model studies will be quoted with respect to the bifunctional mechanism and the CO bond weakening in Pt-Ru systems (3.2.1), followed by an overview on recent investigations of the methanol oxidation reaction (3.2.2).

3.2.1 **Oxidation of H_2/CO mixtures:** Bifunctional mechanism

The oxidation of pure hydrogen, CO and simulated reformate (H_2/CO mixtures) at Pt-Ru alloy surfaces will be discussed in dependence of temperature and CO concentration. In previous studies, as early as 1975, ruthenium has been found to enhance the CO tolerance of platinum under fuel cell-relevant conditions. In this context, two theories regarding the underlying mechanism are currently discussed in fuel cell research: 1) the bifunctional mechanism and 2) CO bond weakening or the so-called ligand effect. The bifunctional mechanism has been proposed by Watanabe and coworkers [7] and is based on the assumption that ruthenium acts as oxygen transfer agent. As water activation at Ru sites already starts at very low potentials compared to platinum, oxygen-containing species adsorbed on the ruthenium surfaces may serve to oxidize adsorbed CO and to thereby free the poisoned platinum sites at potentials below 600 mV vs RHE. On the other hand, it has been shown in several studies that ruthenium alters the inherent electronic structure of platinum [147, 27]. Due to this effect, the bond strength of CO adsorbed at catalytic active platinum sites is reduced by a certain amount and CO can be more easily oxidized at lower potentials. In this context, interesting results were obtained by electrochemical and spectroelectrochemical techniques, like cyclic voltammetry (CV), rotating disc electrode (RDE) studies, CV/FTIRS and differential electrochemical mass spectrometry (DEMS).
The electrooxidation of carbon monoxide on Pt-Ru alloy electrodes was last studied in the late 1960s in the context of the electrooxidation of hydrogen derived from steam-reformed hydrocarbons. However, reports on the optimum Ru composition differed widely, clearly requiring further investigation on more carefully characterized alloy surfaces. With increasing interest in fuel cell technology, these efforts experienced their revival in the early 1990s. In 1994, Gasteiger et al. [148] reported an investigation of the CO electrooxidation on well-characterized Pt-Ru alloys at room temperature. The precise surface composition of the alloy surfaces prepared in UHV was obtained by low-energy ion scattering measurements (LEIS), while the electrocatalytic activity of the respective electrode was measured by CO-stripping and by potentiostatic oxidation of adsorbed CO. Determination of the CO electrooxidation rate on these well-characterized Pt-Ru alloy electrodes as a function of the Ru surface composition served as a test case for the previously proposed bifunctional character. Comparison of a pure Ru with a bulk platinum electrode showed a significantly lowered potential for the onset of CO oxidation that is explained by the adsorption of oxygen-containing species on Ru surfaces at very low potentials. The

intrinsic reaction rate constant for the reaction of surface-bound species of CO and oxygen, however, seems to be lower on ruthenium as indicated by the greater width of the CO-stripping peak. For sputter-cleaned Pt-Ru alloy electrodes, even minor ruthenium additions (approx. 7 at.%) lowered the onset potential for CO electrooxidation compared with that for pure platinum. Increasing the surface concentration of ruthenium further improves their electrocatalytic activity, with the 46 at.% Ru alloy exhibiting the best performance in CO oxidation. Furthermore, the optimum alloy electrode displayed strikingly synergistic properties which could not be rationalized by a mere linear superposition of the pure metal properties. In contrast to the results in sputter-cleaned systems, annealed alloy electrodes with comparable Ru surface compositions do not show significant synergistic effects, but merely a linear superposition of the features of the pure elements. In the authors' opinion, this is due to the thermodynamic preference for cluster formation on annealed surfaces, which would essentially create Ru "nano-electrodes" embedded in a Pt bulk.

Detailed studies of H_2 and CO electrooxidation on well-characterized Pt, Ru and Pt-Ru alloy electrodes for the pure gases and H_2/CO mixtures at room temperature and 62 °C were performed by Gasteiger and coworkers [149, 150] in 1995, using the RDE technique. Hydrogen oxidation was found to be a very fast reaction on both pure platinum and Pt-rich Ru alloy surfaces, whereas it is orders of magnitude slower on a pure ruthenium surface at room temperature. However, in contrast to pure platinum the reaction on pure ruthenium is thermally activated, such that at elevated temperatures the reaction took place at Pt and Ru sites at rates of practical relevance. As has been shown in previous studies [148], the onset potential for CO oxidation is inversely related to the ruthenium content and is lowest for pure Ru. Most remarkably, the 50% alloy showed the maximum current density, probably due to an unique reactivity of species that were formed on Pt/Ru pair sites. In part 2 of this study [150], the electrooxidation of H_2/CO mixtures at 62 °C was compared with direct methanol oxidation as it is carried out in direct methanol fuel cells (DMFC). According to their results, the authors concluded that there is little to no advantage in using reformate as fuel instead of directly electrooxidizing methanol in a DMFC, unless the CO content of the reformate is lowered well below 0.1 %.

In a more recent investigation, Masel et al. [151] studied the effect of ruthenium on the binding of CO, H_2 and H_2O on Pt(110). There still exist contradictory opinions, whether ruthenium improves the CO tolerance of platinum-based fuel cell catalysts by acting as oxygen transfer agent in a bifunctional mechanism or by changing the inherent electronic structure of the platinum, thereby weakening the CO bond. Therefore, temperature programmed desorption (TPD) was applied to measure the magnitude of these two effects in UHV. Depositing 0.25 monolayers of ruthenium on Pt(110), the adsorption properties of the surface changed substantially. The surface adsorbed only about half as much CO and H_2 as before, and the sticking probability of water was also reduced. Data obtained on CO binding energies and the activation barrier for OH recombination on ruthenium modified Pt(110) were used for a rough calculation and resulted in a 170-260 meV reduction in the activation barrier for CO removal from a Ru-decorated platinum surface compared with pure platinum. This is in close agreement with electrochemical measurements by previous workers, who found an approximate 200 meV reduction in the onset potential for CO oxidation at Pt-Ru alloys and Ru-decorated Pt surfaces, respectively. By means of their TPD data, Masel and coworkers tried to quantify the reduction by these two effects and found that only about 40 meV of the total reduction is associated with the ligand effect, whereas the remaining portion is associated with the bifunctional mechanism.

A theoretical approach has been presented by Ge et al. [152], who carried out first-principle studies for energetics and structural properties of CO adsorbed on either Pt-Ru surface alloys or on the surface of Pt-Ru bulk alloys. In their opinion, alloys provide a means by which the strength of metal-adsorbate bonds can be modified, thus opening new possibilities to really control catalytic chemistry rather than acting by "trial and error". In general, alloying of two metals can alter both their electronic as well as their geometric structure in a way, that the metal-adsorbate bond strength on the alloy surface can be very different from that on the pure metal surfaces. According to [152], in the widely-accepted bifunctional mechanism CO adsorption on ruthenium as well as the modification of the CO adsorption properties on platinum because of the alloying interaction with Ru have been ignored. Ge and coworkers conclude from their calculations that bulk Pt-Ru alloys and surface alloys exhibit significant differences in their CO adsorption properties: in the bulk alloys, the Ru-CO bond is strengthened, while the Pt-CO bond is weakened, whereas in the surface alloys both bonds are strengthened. In contrast to assumptions made in the bifunctional mechanism, CO is clearly adsorbed and oxidized on Ru sites. Therefore, bifunctionality of the Pt-Ru electrode is an oversimplified picture of the CO electrooxidation process, neglecting the competition of CO and OH formed by water activation in occupying Ru surface sites.

3.2.2 Anodic methanol oxidation at Pt-Ru catalyst systems

In principle, the mechanisms proposed for the anodic methanol oxidation at Pt-Ru systems are similar to those for the electrooxidation of reformate. However, significant differences occur due to the fact that methanol, in contrast to CO, is not adsorbed on Ru surface sites.

Gasteiger and coworkers [46] were among the first who investigated the methanol electrooxidation on well-characterized Pt-Ru bulk alloys in the context of their use in direct methanol fuel cells. The electrocatalytic activity of single-phase polycrystalline Pt-Ru alloys was determined in sulfuric acid electrolyte at room temperature in dependence of the surface composition. In their studies, it has been found that a sputter-cleaned alloy with a Ru surface of approximately 10 at.% - in contrast to about 50 at.% Ru for reformate electrooxidation – leads to the highest catalytic enhancement compared with pure platinum. Kinetic measurements revealed significant differences between the 10 and the 50 at.% Pt-Ru alloys for the anodic methanol oxidation: while Pt-Ru (1:1) yielded rates, which were close to first order with respect to the methanol concentration in the electrolyte, pure platinum and the 10 at.% Ru alloy showed a relatively weak dependence on the methanol concentration. This was explained by the limiting rate of methanol adsorption on Ru-rich surfaces, whereas the oxidative removal of methanol dehydrogenation fragments is the rate-determining step on pure platinum electrodes. According to their results, Gasteiger et al. concluded that the high electrocatalytic activity of Pt-Ru alloys for the anodic methanol oxidation is well described by the bifunctional mechanism, in which methanol adsorption takes place at platinum ensembles and the further electrooxidation of methanol dehydrogenation fragments is catalyzed by oxygen-containing species, that are adsorbed on adjacent Ru atoms. In agreement with the experimental results, a statistical model based on the bifunctional mechanism of Pt-Ru alloy surfaces has been proposed and found to confirm the optimum surface composition.

Investigations on the temperature-dependent methanol electrooxidation on well-characterized Pt-Ru alloys were also presented by Gasteiger et al. [28]. With increasing temperature, the activity of ruthenium for the dissociative adsorption of methanol is significantly enhanced, producing an increase in the

optimum ruthenium surface composition with temperature from close to 10 at.% Ru at room temperature to a value near 30 at.% at 60 °C. This shift in optimum surface composition with temperature was attributed to a shift in the rate-determining step from methanol adsorption / dehydrogenation at low temperatures to the surface reaction between dehydrogenated intermediates and surface oxygen at elevated temperatures. The apparent activation energies were consistent with this change in the rate-determining step, thus backing their theory.

The current-time behavior of smooth and porous Pt-Ru surfaces for methanol electrooxidation has been studied by Hoster et al. [153]. At a constant potential of 500 mV vs RHE, Pt-Ru alloys showed a characteristic loss of activity and the *i-t* dependence exhibited two well-defined regions: a pronounced decrease during the first 5-10 minutes, followed by a slow decay. The first and steeper part of the activity loss was found to be reversible, as was shown by repetitive potential switches between the initial and the oxidation potential. The slow current decay is irreversible due to a poisoning of the surface via adsorbed species other than CO. In the authors' opinion, the poisoning effect is produced by the slow adsorption of methanol dehydrogenation fragments, formed in a second order surface reaction. However, similar phenomena at high-surface area Pt-Ru catalysts have not been found so far.

Exemplary for the huge number of single-crystal studies, only three selected investigations on Ru-decorated platinum model electrodes will be cited here [42, 154, 155]. Baltruschat et al. [42] studied the formation of intermediates during anodic methanol oxidation by quantitative DEMS in a thin-layer flow cell. The current efficiencies obtained for the formation of CO_2 during methanol oxidation at smooth electrodes were well below 60 % for different single crystal planes. In particular, values as low as 16 % were found in 0.1 M methanol solution at 0.6 V vs RHE, indicating that a large amount of soluble intermediates is formed. A Ru-decorated Pt(332) electrode exhibited both a lower onset potential for the oxidation of adsorbed CO and an increased current efficiency. With respect to the obtained activity enhancement, two different mechanisms were discussed. One possible explanation might be that the fast oxidation of adsorbed CO induces a shift from the reaction path via soluble intermediates to that via adsorbed CO. Another possibility would be that ruthenium promotes the oxidation of soluble intermediates.

In [154], Chrzanowski et al. presented their results for the catalytic activity of several low-index platinum single-crystal faces for methanol electrooxidation. The activity of the respective model systems was enhanced by controlled amounts of electrodeposited ruthenium. It has been found, that the resulting platinum surface structure affects all factors involved in the oxidation process, e.g. methanol oxidation rate, *Tafel* slopes and oxidation current decay. Decorating the Pt(111) surface with 0.2 monolayers of ruthenium yields a turnover number, approximately one order of magnitude higher than that from the industrial Pt/Ru catalyst. Hence, in the authors' opinion, adding the crystallographic control to the creative synthetic design of the electrocatalytic materials seems imperative.

The influence of the surface structure and the Pt-Ru atom distribution for methanol electrooxidation has also been investigated by Iwasita and coworkers [155]. UHV-cleaned Pt-Ru alloys were compared to differently prepared Ru-decorated Pt single-crystal surfaces with and without an additional reduction step under hydrogen atmosphere. STM measurements at Pt(111)/Ru showed the formation of two- and three-dimensional structures, depending on the surface coverage, whereas a molecular insight into the electrochemical reaction is given via in-situ infrared spectroscopy. The electrocatalytic activity of the respective systems is measured in form of current-time curves at constant potentials. In the range of 10-40 % ruthenium, Pt-Ru alloys showed an enhanced activity in comparison with the Ru-decorated model

surfaces. However, the different preparation methods for the decorated surfaces also seem to play an important role, probably due to the formation of smaller islands in the case of spontaneously adsorbed ruthenium.

The exactly opposite opinion is represented by Long et al. [9], who proposed highest electrocatalytic activities, if the formation of a bimetallic alloy can be avoided. Thus, the essential question that has been raised in almost all studies of the past decade and is up to now controversially discussed in literature, is, if alloy formation in the widely-used Pt-Ru system is a necessary prerequisite for its high electrocatalytic activity. Hence, the intention of the next chapter will be to shed some light on this specific problem by quoting several selected papers of the last years.

4 Experimental

In the following section, the syntheses of the different catalyst systems and the preparation of the membrane electrode assemblies will be described. Structural characterization of the supported catalyst powders was performed by a number of methods before and after operation in a fuel cell. Additionally, the pore structure and the metal loading of preselected MEAs were determined by several techniques. Results of the MEA characterization before and after fuel cell operation do not belong to exactly the same samples, as the chosen investigation procedures were destructive. The electrocatalytic activity of the catalysts was measured by cyclic voltammetry under various conditions. These data were compared with measurements in real fuel cells using hydrogen, H_2/CO mixtures and methanol as anode feed.

4.1 Synthesis of the different binary and ternary catalyst systems

Different preparation methods were chosen in order to obtain different nanomorphologies. The reductive precipitation of noble metals on a carbon support had been performed a) in aqueous solution (synthesis I and II) and b) in an organic solvent (synthesis III). The synthesis routes finally employed were selected, based on the information that one of the chosen preparation methods (synthesis I) should result in separate phases [156], another (synthesis III) in an alloy [157], whereas for the last method (synthesis II) no information on the resulting structure had been reported in literature [158].
Carbon black (Vulcan XC-72, Cabot Intern.) with a nominal specific surface area (BET) of 290 m²/g was used as support for all catalysts. Two different reduction methods [156, 158] in aqueous phase were applied for the syntheses of the Pt-Ru/C catalysts, differing in reaction time, pH and temperature. According to a slightly modified colloid method originally developed by Bönnemann et al. [157] another carbon-supported Pt-Ru catalyst and ternary Pt-Ru-W systems with various compositions were synthesized in dry nitrogen atmosphere using dry solvents and non-hydrated salts. Modifications of the colloid synthesis were published by Götz and Wendt [159]. The *Bönnemann* method proved to be suitable for the synthesis of nanodispersed, colloidal binary and ternary noble or non-noble transition metal alloys [47]. Catalysts are prepared by adsorption of these colloidal solutions on the respective carbon black, followed by successive removal of the surfactant. Since the aqueous solutions in synthesis I and II did not contain any surface active substances (surfactants), the resulting catalysts particles were larger in size (see results).

Synthesis I using formaldehyde as reducing agent [156]

An aqueous solution of 0.165 g hexachloroplatinic acid and 0.07 g ruthenium(III)- chloride was added dropwise to a vigorously stirred suspension of 0.4 g carbon black in approx. 200 ml distilled water at room temperature. While the mixture was heated to 80 °C, sodium hydroxide pellets were added, until a pH of 8 was reached. After slow addition of 90 µl of formaldehyde (37 wt.% in water), the suspension was filtered and the filter cake rinsed with hot water several times. The resulting Pt-Ru (1:1) catalyst was

dried at 80 °C in a vacuum drying oven for 4 h. Catalysts prepared according to this method are in the following text denoted as *sample I*.

Synthesis II using hydrazine as reducing agent [158]

An amount of 0.4 g carbon black was suspended in about 200 ml distilled water and heated to 80 °C. An aqueous solution of 0.165 g hexachloroplatinic acid and 0.07 g ruthenium(III)-chloride, neutralized with an appropriate amount of sodium carbonate powder to yield a pH value of 10, was added to the suspension within 10 minutes and refluxed for two hours. After addition of 90 µl hydrazine (1 M solution in THF), the mixture was refluxed for another hour, filtered and washed repeatedly with hot distilled water. The resulting Pt-Ru (1:1) catalyst, further denoted as *sample II*, was air-dried at 110 °C in a drying oven for 4 h.

Synthesis III according to Bönnemann colloid method [157]

According to a slightly modified method, originally developed by Bönnemann et al. [157], both the carbon-supported binary Pt-Ru and ternary Pt-Ru-W catalysts were synthesized in a dry nitrogen atmosphere using dry tetrahydrofurane (THF) and the non-hydrated salts $PtCl_2$, $RuCl_3$, WCl_6 and tetraoctylammoniumbromide.
At first, the reducing agent (tetraoctylammoniumtriethyl hydroborate) was synthesized by mixing stoichiometric amounts of a 0.5 M solution of tetraoctylammonium bromide in THF and a 0.5 M solution of potassium triethylhydroborate in THF. A glass frit (porosity 4) was used to separate precipitated KBr from the solution.
For the binary Pt-Ru catalyst, a mixture of 0.09 g platinum(II)-chloride, 0.07 g ruthenium(III)-chloride and 0.92 g tetraoctylammonium bromide (as surfactant) was dissolved in dry THF and heated to 40 °C in order to yield a binary catalyst of 1:1 stoichiometry. For the ternary Pt-Ru-W systems, the Pt:Ru ratio has been retained unchanged at the established optimum of 1:1 to make an easy comparison of the electrocatalytic activities possible. In order to obtain Pt:Ru:W (1:1:0.5), (1:1:1), (1:1:1.5) and (1:1:2) stoichiometries, amounts of 0.067 g, 0.133 g, 0.199 g and 0.265 g tungsten(VI)- chloride were used, respectively. The appropriate amount of the size-stabilizing tetraoctylammonium bromide was calculated taking into account the sum of the counter ions, that has to be reduced.
After dropwise addition of 10 ml tetraoctylammoniumtriethyl hydroborate solution to the either binary or ternary metal salts solution, the resulting colloidal solution was stirred for 4 h. Then 1 ml of acetone was added to destroy an excess of reducing agent. After another hour, the solution was slowly added to a suspension of 0.4 g carbon black in THF. The slurry was stirred for 12 h, then 150 ml ethanol were added and after another 2 h the solution was filtered over a glass frit (porosity 4). The resulting catalyst was washed with ethanol several times and then dried at 120 °C in nitrogen atmosphere. In the following text, the binary Pt-Ru catalyst was denoted as *sample III*, while the ternary systems were abbreviated by their respective stoichiometry.
All syntheses (I, II and III) were repeated twice with reproducible results for the structural and electrochemical characterization.

4.2 Catalyst characterization

Various methods were applied to obtain a more detailed information on the catalysts stoichiometry, structure and morphology. A combination of different methods was applied in order to obtain a sufficient amount of data to make a correlation between the catalysts nanomorphologies and their electrocatalytic activities possible.

4.2.1 X-ray fluorescence analysis (XFA)

Metal loading and composition of the supported catalysts were measured using a Xlab 2000 (Spectro analytical instruments GmbH) in 90° geometry. As the X-ray source either a Rh or a Pd cathode were applied, using a Ag or Mo target, respectively. Energy-dispersive detection was done by a liquid N_2 cooled Si(Li) detector with a resolution of 145 eV at MnK_α. The catalyst powders were finely grinded in an achate mortar, filled into special sample holders covered by Mylar© foils and mounted into the vacuum chamber of the spectrometer. Specific calibration was realized by measuring a series of the respective Pt, Ru and W oxides on carbon. These were easy to handle and oxygen, in contrast to chloride, gives no contribution to spectral noise. Additionally, the obtained Pt calibration curve was confirmed by measuring commercially-available catalysts of 10 wt.%, 20 wt.% and 30 wt.% Pt on Vulcan XC 72, respectively, while the Ru calibration was compared to the internal standard of the XFA instrument. The experimental error of this procedure lies within 10 % of the effective value. All in-house synthesized catalysts were routinely checked to verify the correct implementation of the syntheses. As several commercial catalysts, purchased from E-TEK inc., were used as reference materials, XFA was applied to verify their specification.

4.2.2 X-ray powder diffraction (XRD)

The catalysts were investigated by X-ray powder diffraction using a STOE STADIP, with germanium monochromized $CuK_{\alpha 1}$ radiation and a position-sensitive detector with 40° aperture in 2θ in transmission mode. For the differently-synthesized Pt-Ru samples, temperature treatments were conducted ex-situ either in a Nabotherm furnace (Schröder, Flörsheim) in air or in a Carbolite© MTF 12/38/400 (Hope, England) under nitrogen flow. The final temperature was achieved by a heating rate of 10 °Cmin^{-1} and held for 5 h. Then the catalysts were cooled down in air or under nitrogen flow, respectively, and checked again by X-ray diffraction.
In the case of the ternary catalyst systems, temperature-dependent in-situ X-ray diffraction measurements were realized by another STOE diffractometer equipped with a special in-situ furnace. The experiments were carried out under nitrogen with $CuK_{\alpha 1}$ radiation in a heating cycle between 100 and 600 °C, followed by a subsequent cooling cycle from 600 °C down to RT in order to check the reversibility of T-induced processes. A heating rate of 10 °Cmin^{-1} and 3 minutes holding time prior to each measurement were applied.
For the diffraction measurements in transmission geometry, sample preparation was done as follows. An appropriate amount of the catalyst powder was grinded in an achate mortar and fixed with 0.5% collodion

in isoamyl acetate between two sheets of acetate foil that proved to give only little contribution to the background of the X-ray pattern. In contrast, the catalyst powder was filled in a capillary for the T-dependent in-situ X-ray experiments under nitrogen.
Due to their small particle sizes, the catalysts are not accessible to X-ray diffraction in any case, as coherently scattering regions below a certain extension can not be distinguished from the (amorphous) background. Therefore, the evaluation of the X-ray patterns was mainly done by checking the apparent crystallographic phases and estimating the particle size according to the *Scherrer* equation (see also chapter 3.1.1).

Scherrer equation:

$$FWHM = \frac{K \cdot \lambda \cdot 57.3}{D \cdot \cos\theta} \qquad [4.1]$$

FWHM = full width half maximum
K = shape factor
D = particle size
θ = respective reflection angle

If possible, the respective lattice spacings (*d* values) of the Pt phase were determined by *Rietveld* analysis using the FULLPROF package [160]. As *Vegard*`s law (linear variation in the lattice parameter as function of composition) holds for the binary Pt-Ru systems in question, the alloy composition of the crystalline phase can be determined by the measured *d* values [46] (fig. 4.1).

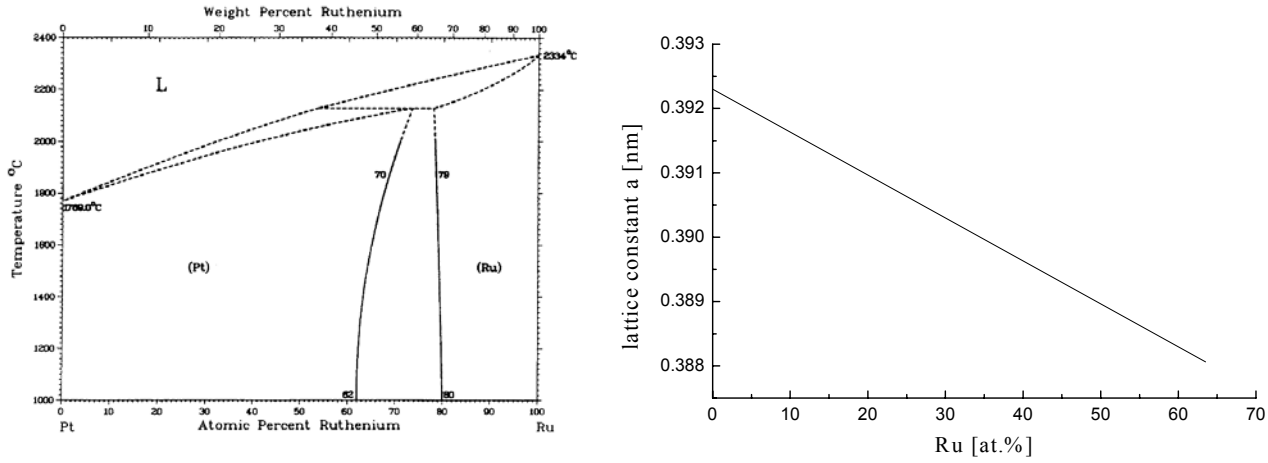

Fig. 4.1 Pt-Ru phase diagram and *Vegard* plot

For sample I and II, *Rietveld* refinement was applied to estimate the approximate amount of crystalline Ru in the heat-treated samples. Additionally, the minimum amount of crystalline Ru, that is visible at a given particle size, could be determined by simulation using FULLPROF. Changes in the intensity of the

Pt(200) reflection due to the contribution of Ru particles smaller than 1.5 nm could be confirmed by the calculated patterns, as proposed by E. Garnier (Poitiers, France, see also section 3.1.1).

4.2.3 Transmission electron microscopy (TEM)

A Philips CM20 instrument with an acceleration voltage of 200 kV and a W cathode was applied for high resolution images of the supported catalysts. Samples were prepared by suspending the catalyst powder in methanol and depositing a drop of the suspension on a standard copper grid covered with carbon. Particle size distributions were determined on those TEM images, that displayed a sufficient number of clearly visible particles. In high-resolution mode, lattice planes of the nanocrystallites were imaged and evaluated using the graphite lattice distances of the carbon support as internal standard. However, values for particles smaller than 3 nm were not reported, due to contraction and dilatation taking place in such small crystallites (compare to chapter 3.1.1).
For analytical TEM experiments, the nano-EDX device, attached to the microscope, was applied to measure the composition of distinct particles. EDX-measurements were performed for all samples with an approximate spatial resolution of 2 nm. Hence, compositions for distinct particles can only be determined in case the particles are either not smaller than 2 nm or the distances between single particles amount to a minimum of 4 nm.

4.2.4 X-ray photoelectron spectroscopy (XPS)

XPS measurements were carried out on a PHI Model 5700 MultiTechnique System (Perkin Elmer) with AlK_α radiation at a power of 300 W. As detector a spherical capacitance analyzer (SCA) was used. A suitable pass energy of 11.75 eV was chosen, while a pressure of $3x10^{-8}$ mbar was maintained within the spectrometer chamber. Samples were prepared by pressing a small amount of the supported catalyst powder into indium foils.
All data measured were calibrated with respect to the C*1s* excitation to account for charging effects by the electron beam. The spectra were fitted and evaluated by a standard calculation software using a mixed Gauss-Lorentzian function for the peak shapes [161].
The binding energy shifts found by the fitting procedure were compared to both, literature values and standard substances. In order to get reliable standards, 5 samples were measured as reference compounds under standardized conditions first, namely RuO_2 and $RuO_2 \cdot xH_2O$ (both from Aldrich), and 20 wt.% Pt on Vulcan XC 72, 20 wt. % Ru on Vulcan XC 72, and 20 wt. % Pt-Ru on Vulcan XC 72 (E-TEK inc.). The results of these measurements are reported in table 4.1. Selected literature data on XPS investigations of fuel cell-relevant systems and their interpretation are summarized in table 4.2.
Due to a strong overlap of the Ru*3d* signal with the C*1s* peak of the carbon support in the carbon-supported systems, the Ru*3p* excitation was used for the measurements in question despite its inadequate statistics. Therefore, a quantitative interpretation of the results was not feasible.

Table 4.1 XPS data for different Pt and Ru reference compounds measured in-house; binding energies for the Pt *4f*7/2, Ru *3d*5/2 and O *1s* signals attributed to the respective oxidation states

Standard	**Pt** BE ***4f*7/2 [eV]**	**State**	**Ru** BE ***3d*5/2 [eV]**	**State**	**O** BE ***1s* [eV]**	**State**
Pt/C E-TEK	71.5	Pt(0)	-	-	530.7 532	Oxide -C=O
Ru/C E-TEK	-	-	462	Ru(0)	530.8 532.5	Oxide -C=O
Pt-Ru/C E-TEK	71.5	Pt(0)	461.9 462.6 463.4 465.2	Ru(0) RuO_2 Hydr. RuO_2		
RuO_2	-	-	462.5	RuO_2	529,4 530,4	Oxide Hydr. oxide
RuO_2*xH_2O	-	-	463.6	Hydr. RuO_2	529,6 530,8	Oxide Hydr. oxide

Table 4.2 Literature XPS data for fuel cell-relevant systems; BEs and corresp. oxidation states

1st author **Reference**	Pt BE ***4f*** **[eV]**	**State**	Ru BE ***3d*** **[eV]**	**Ru** BE ***3p*** **[eV]**	**State**	**O** BE ***1s*** **[eV]**	**State**
Arico [1]	71.5 72.9 74.5	Pt(0) PtO, $Pt(OH)_2$ PtO_2	280.5 281.5	463.4 466.9	Ru(0)alloy RuO_2/RuO_3	530.5 532.5	PtO -C=O
Cattaneo [96]	71.5	Pt(0)		461.8 463.4	Ru(0) RuO_2		
Froment [162]			280.7 282.5		RuO_2 RuO_3		
Hagans [99]			280.1 280.9 282.8 282.0		Ru(0) RuO_2 RuO_3 RuO_2*xH_2O	529.5 530.3 532.5	RuO_4 RuO_2*xH_2O -C=O
Kennedy [103]	71.2	Pt(0)					
Lasch [97]	71.5 74.7	Pt(0) PtO_2		461.1 462.7	Ru(0) RuO_2		
Ramesh [163]	71.3 74.1	Pt(0) PtO_2		460.7 462.6 465	Ru(0) RuO_2 RuO_3/RuO_4		
Rolinson [2]			280.1 280.9 282.0		Ru(0) RuO_2 RuO_2*xH_2O		
Schmidt [95]	70.7	Pt(0)	279.5 280.5		Ru(0) RuO_x		

4.2.5 X-ray absorption spectroscopy (XAS)

All ex-situ and in-situ XAS experiments were performed at the X1 beamline at the synchrotron facility HASYLAB / DESY in Hamburg (Germany). Among other features, this specific beamline offers a very stable photon beam over a large X-ray energy range of 6-80 keV, covering absorption edges of elements between Mn and Au. A comparably high energy resolution of approx. 1 eV at the Pt L_3-edge and approx. 5 eV at the Ru *K*-edge is available. A schematic drawing of the X1 experimental setup in transmission mode, particularly optimized for in-situ investigations, is shown in fig. 4.2. The synchrotron source is operated at an energy of 4.45 GeV and an initial positron beam current of 120 mA.

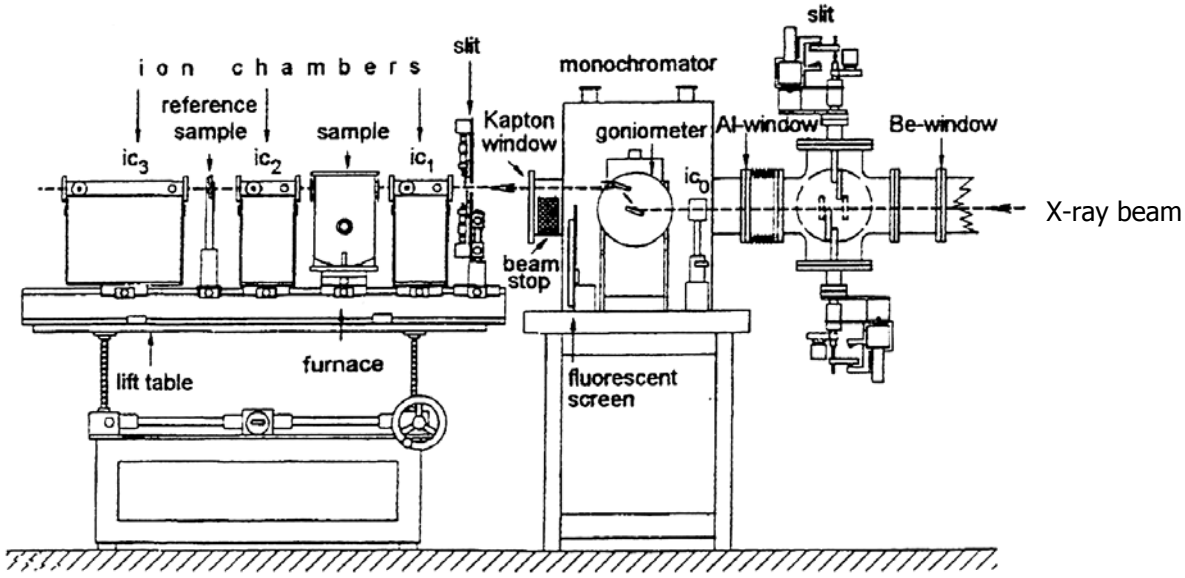

Fig. 4.2 Experimental setup of beamline X1 at HASYLAB, Hamburg (Germany)

The incoming primary radiation is monochromized by a double-crystal monochromator, consisting of two plan-parallel arranged single crystals. The station can be operated with three different crystal pairs, namely Si(111), Si(311), and Si(511), depending on the energy range required and detuned to 50 % intensity to minimize the presence of higher harmonics. Measurements at the Pt L_3-edge were conducted using Si(111), whereas for the Ru *K*-edge the Si(311) monochromator was applied.
The intensities of the focused beam (I_0, before penetrating the sample) and the transmitted beam (I_1, after penetrating the sample) were detected by three gas-filled ion chambers (ic) in series. Different gas mixtures were applied, optimized for either the Pt L_3- or the Ru *K*-edge. Thin samples of Pt or Ru metal were used to calibrate the beam energy during each scan of the Pt L_3-and the Ru *K*-edges, respectively. The calibration measurements were made with the third ion chamber (ic_3). Simultaneously to the absorption experiment, the actual positions of the metal absorption edges (Pt L_3 = 11 564 eV and Ru *K* =

22 117 eV) could then be determined by placing the metal standard between ic_2 and ic_3 and measuring the total absorption in ic_3.

In order to optimize the signal-to-noise ratio of the ex-situ XAS experiments, the samples were prepared according to the following procedure. The optimum mass of the carbon-supported catalysts was calculated using equation 5.2. According to basic XAS literature, absorptions A between 2 and 3 and step heights ΔA (50 eV before and after the absorption edge E_0) of 1-1.5 should lead to spectra, which can be evaluated without any problems. Taking into account the so-called thickness effect [164], a final step height of $\Delta|\mu d| \approx 0.3\text{-}1$ seems adequate. Absorption cross-sections μ/ρ in dependence of the energy can be found in the *McMaster* database [165]. The respective values for Pt, Ru and C 50 eV below the edge, 50 eV above the edge and at the absorption edge E_0 are listed in table 4.3.

Calculated weight-in quantities:

$$A = \frac{m_0}{S_0} \sum_i w_i \cdot \left(\frac{\mu}{\rho}\right)_i \qquad [4.2]$$

μ/ρ absorption cross-section [cm²/g]
m_0 sample mass [g]
S_0 cross-sectional area of the pellet [cm²]
w weight percent

Table 4.3 Mass absorption cross-sections by *McMaster* [165]

Energy E_0[eV]	**Element**	**Absorption cross-section (μ/ρ), at E_0-50 eV**	**Absorption cross-section (μ/ρ) at E_0**	**Absorption cross-section (μ/ρ), at E_0+50 eV**
11 564 (Pt L_3-edge)	Pt	76.781 cm²/g	192.938 cm²/g	190.839 cm²/g
	Ru	67.914 cm²/g	67.107 cm²/g	66.312 cm²/g
	C	1.473 cm²/g	1.455 cm²/g	1.438 cm²/g
22 117 (Ru K-edge)	Pt	58.964 cm²/g	58.616 cm²/g	58.271 cm²/g
	Ru	11.033 cm²/g	68.357 cm²/g	67.977 cm²/g
	C	0.357 cm²/g	0.356 cm²/g	0.355 cm²/g

Samples were prepared by pressing the calculated optimum amount of catalyst powder into pellets using an uniaxial press. As pure catalyst pellets were quite brittle and hence not easy to handle, the powder was diluted in an appropriate amount of polyethylene, which served as a sufficiently stable matrix. Polyethylene is favored as matrix material due to its low X-ray absorption coefficient. Details of the pellet composition for all ex-situ measurements are listed in table 4.4.

Table 4.4 Initial weights for the ex-situ samples (Pt L_3- and Ru *K*-edge)

Sample	**Pt L_3-edge**	**Ru *K*-edge**
Pt-foil	4-5µm thickness	-
Ru-foil	-	24µm thickness
Pt E-TEK	55 mg	-
Ru E-TEK	-	157 mg
Pt-Ru E-TEK	82 mg	250 mg
Pt-Ru sample I	82 mg	250 mg
Pt-Ru sample II	82 mg	250 mg
Pt-Ru sample III	82 mg	250 mg
Pt E-TEK in N_2	55 mg	-
Ru E-TEK in N_2	-	157 mg
PtRu E-TEK in N_2	82 mg	250mg
Pt E-TEK, in air	16 mg	-
Ru E-TEK, in air	-	40 mg
PtRu E-TEK, in air	20 mg	66 mg

The recorded spectra were processed afterwards, using the program packages WinXAS 2.1 [166] and FEFF 8 [167]. In principle, the evaluation of XAS experiments consists always of the following steps:

1) energy calibration
2) separation and subtraction of the pre-edge background
3) normalization
4) determining the edge position
5) conversion from the energy space *E* to the *k* space
6) determination of $\mu_0(k)$
7) weighting of χ(k) by k^n
8) Fourier transformation.

Atomic distances *r* and coordination numbers *N* present parameters that are conventionally extracted out of the XAS data (for details see 3.1.4). More detailed structural information is gained by modelling and simulation, using FEFF. In the context of the fuel cell-relevant Pt-Ru system, Maniguet et al. [137] invented a new evaluation method, using a specific 'interference effect' to draw conclusions on the alloy

formation in their catalysts. This method will be applied for the evaluation of the ex-situ measurements of the different catalysts (results section, chapter 5.1.1.1).

4.2.6 Cyclic voltammetry (CV) and Fourier transform infrared reflectance measurements

Cyclic voltammetry and CO stripping measurements

The electrochemical measurements were conducted in a standard electrochemical cell in 0.1 M perchloric acid (Merck Suprapur) as supporting electrolyte at room temperature. The preparation of the working electrode was done according to a slightly modified method originally developed by Schmidt et al. [95]. An appropriate volume of an ink, consisting of 0.015 g catalyst powder, 85 µl Nafion© (5 wt.% in solution by Aldrich) and ultra pure water (Milli-Q, Millipore System), was pipetted onto a glassy carbon disc, resulting in a metal loading of 7 µg metal/cm². A saturated calomel electrode was used as reference, connected to the working electrode compartment by a *Haber-Luggin* capillary. However, all potentials in the text are referred to the reversible hydrogen electrode (RHE, E_{ref} [mV]= -0.059 pH). Cyclic voltammetry was carried out on all samples in 0.1 M and 1 M methanol, respectively, with sweep rates of 5 mV/s or 20 mV/s and an upper potential limit of 0.7 V to avoid possible Ru dissolution. Additionally, CO-stripping experiments were performed with pure CO (Linde) adsorbed at a potential of 0.05 V for 10 min. Excessive CO in the electrolyte was removed by purging nitrogen for 20 minutes before the measurement was started.
The data obtained were evaluated with regard to two parameters: a) the onset of the oxidation wave and b) the current density at an arbitrarily chosen potential of 550 mV vs RHE (fig. 4.3). The onset potential was defined as the potential at which 5% of the current value at 0.7 V (minus the double-layer capacity) was reached.

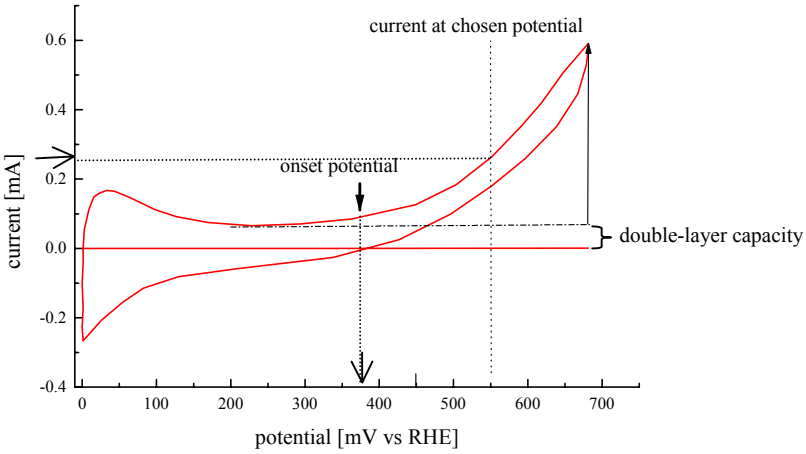

Fig. 4.3 The two parameters evaluated in the recorded cyclic voltammograms;
Onset potential: potential, at which 5% (i @ 700 mV) are reached
Current at a chosen potential of 550 mV

Current vs time measurements at different potentials in 1 M methanol were conducted at room temperature. The electrodes were held for 30 minutes at each potential starting at 0.45 V and continuing up to 0.7 V (potential steps of 50 mV). During the first seconds after the potential step, a sharp current decay is observed. However, the course of the current vs time curves displays marked differences for the different catalysts, thus providing characteristic data with respect to their electrocatalytic features. After holding the electrode at a certain potential for 30 minutes, the currents were recorded and drawn into *Tafel* plots (theoretical treatment, see section 2.3.1).

Fourier transform infrared reflectance measurements

The Fourier transform infrared spectrometer (Bruker IFS 66v) was modified to allow the beam to reflect upon the IR window (CaF_2) of the conventional thin layer spectroelectrochemical cell with an incidence angle of 65^o (fig. 4.4). The whole beam path was held under vacuum, and a liquid N_2 cooled HgCdTe detector (Infrared Associates) was used.

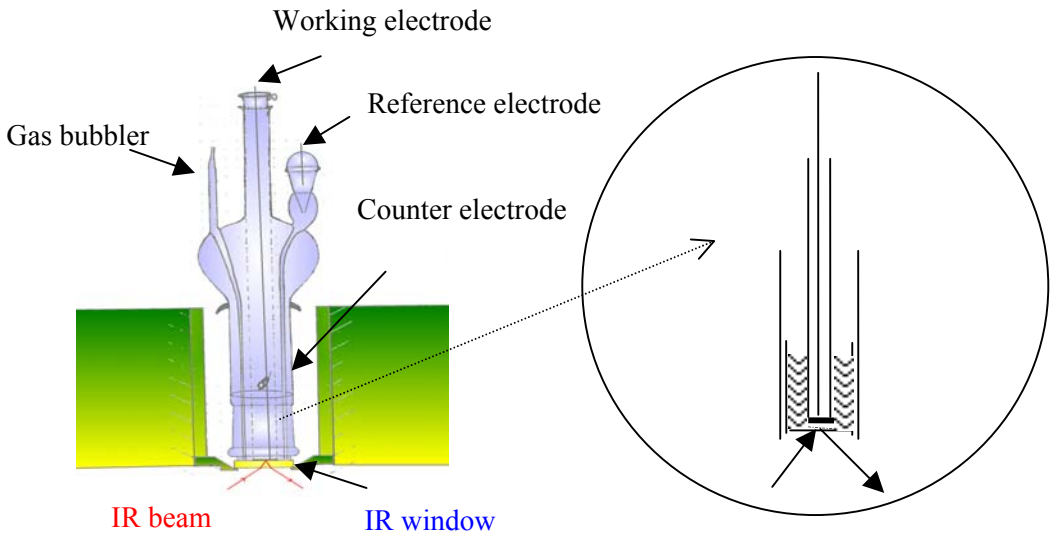

Fig. 4.4 Schematic drawing of the spectroelectrochemical cell

The spectroelectrochemical cell potential was controlled using a LB 81 Wenking potentiostat and a Hi-tek waveform generator, connected to a BD90 X-Y recorder. The counter electrode was a glassy carbon disc and the reference electrode a reversible hydrogen electrode (RHE). Base voltammograms in suprapure 0.5 M perchloric acid (Merck Suprapur©) were recorded first, and then compared with previous recorded CV data to check the quality of the electrode and the reproducibility of the experiments. Then methanol was injected into the cell at a controlled potential to yield a concentration of 1 M. For CO-stripping experiments the cell was bubbled with CO for 10 minutes and afterwards 20 minutes purged with nitrogen at a controlled potential.

Two different methods were applied to characterize the catalysts. The first one was the SPAIRS technique (single potential alteration infrared reflectance spectroscopy) [62, 63, 64], recording the reflectivities each 50 mV during the first slow voltammetric scan (sweep rate 1 mVs^{-1}). Each spectrum resulted from the co-addition of 128 interferograms. The spectra were normalized as $(R_E\text{-}R_{Eref})/R_{Eref}$, whereby the reference reflectivity R_{Eref} was the one recorded at the most negative potential. The second technique, applied to learn more about the catalysts behavior in an electrochemical environment, was denoted as SNIFTIRS (subtractively normalized interfacial Fourier transform infrared reflectance spectroscopy) [62, 64, 65, 115]. Reflectivities were obtained at two electrode potentials (E1 and E2) and added 50 times at each potential. The final spectra were normalized as $(R_{E2}\text{-}R_{E1})/R_{E1}$. Both techniques allow the detection of adsorbed species and of the reaction products near the electrode surface. However, SPAIRS is more convenient for the detection of species in solution, whereas SNIFTIRS is better adapted to the detection of adsorbed species.

An overview of the vibration bands observed in the spectra is given in table 4.5. Not only the CO and CO_2 bands, which play an important role in catalyst research, were detected, but also several other absorption bands, in particular interfacial water and perchlorate anions. The intensity of the respective bands was evaluated either by calculating the height of or by the area below the absorption peak.

Table 4.5 Overview of the most important absorption bands

Absorption band [cm^{-1}]	**Molecular group**	**Description**
1111	ClO_4^-	electrolyte
1640	H_2O	interfacial water
1850	CO_M	multibonded CO
1950	CO_B	bridge-bonded CO
2050	CO_L	linear-bonded CO
2345	CO_2	carbon dioxide

If nanoparticle catalysts instead of single crystal surfaces are investigated, new possibilities but also characteristic difficulties occur. Usually, the detected IR signals are much weaker on rough surfaces because of diffuse scattering in the sample and the electrolyte in between. However, this disadvantage is neutralized by the interesting additional effects, that can be analyzed in nanoparticulate systems, e.g. the shift of the CO stretching frequency in dependence on the particle size (see Rice et al. [115]). Moreover, there exists a response of the vibrational frequency to the applied potential, that is usually denoted as *Stark* effect. For linear-bonded CO on a bulk platinum surface, this effect amounts to approximately 30 $cm^{-1}V^{-1}$, and is clearly seen in the recorded spectra. For nanosystems different values are found, depending among others on the particle size. However, the *Stark* tuning might be superimposed by a coverage dependent shift as well.

4.3 Preparation of the membrane electrode assembly (MEA)

Membrane electrode assemblies (MEA) with an active electrode area of 25 cm² per electrode were manufactured by a spraying technique originally developed by Wilson et al. [168]. Nafion©117 (DuPont) was applied as proton conducting membrane and in all cases provided with a metal loading of 0.4 $mgcm^{-2}$ metal per electrode. A standard 20 wt. % Pt on Vulcan XC-72 catalyst (E-TEK) was used at the cathode, while the anode catalyst was varied in our studies.

The preparation in detail:
A sheet of Nafion© 117 membrane of an appropriate size was ion-exchanged in 2.5 M NaOH at 100 °C for 2 h, as the Na^+-loaded polymer possesses an increased thermostability. Then, the membrane was rinsed with ultrapure water, fixed to a specially designed vacuum table and heated to 100 °C. The catalyst ink was prepared according to Götz et al. [169] by mixing 0.2 g catalyst powder, 2 g Nafion© solution, 1.2 g ultrapure water, 1.7 g glycerol and 0.2 g tetrabutylammonium hydroxide in an ultrasonic bath. The obtained homogeneous suspension was filled into a vaporizer (*EcoSpray* by Roth) and successively sprayed in several thin layers on the membrane surface, allowing each complete layer to dry for 2 min. After one electrode had been manufactured in this way, the membrane was put into distilled water for 30 min to regain its optimum water content (swelling). Then, the other electrode was prepared in the same way. Finally, the obtained MEA was heated to 130 °C for 30 min to remove remains of the solvents, and ion-exchanged in hot 2 M H_2SO_4 for at least 2 h. The preparation process was completed by boiling the ready MEA in ultrapure water for a minimum of 2 h.

4.4 MEA characterization

Fuel cell measurements in a single cell setup are very sensitive to the MEA morphology. Different preparation techniques and slight modifications regarding membrane pretreatment, ink composition, preparation temperature and preparation time cause severe changes in the electrode structure and the membrane-electrode adhesion. Hence, the characteristic properties of the respective MEA should be checked before the fuel cell tests. Essential parameters are the pore size, the pore size distribution and the actual metal loading, that can be measured by atomic absorption spectroscopy and BET analyses. The corresponding morphology of the MEA in top view and cross-section can be imaged by scanning electron microscopy (SEM). However, as these techniques are destructive, results of MEA characterization before and after fuel cell operation do not belong to exactly the same sample.

4.4.1 Atomic absorption spectroscopy (AAS)

AAS measurements were applied to determine the actual platinum loading of a membrane electrode assembly, prepared according to chapter 4.3 by the spraying method. As all catalysts, applied in the experiments, consisted of a fixed ratio Pt:Ru 1:1 (verified by XFA), there was no need to measure the ruthenium loading as well.

First, matrix-adapted standards (in aqua regia) were prepared and a calibration curve in the respective range of concentration was recorded. The main error is that from the preparation of the Pt solution, while the instrumental error is negligible for the measurements presented. Then, a Pt solution adequate for F-AAS (flame mode) analyses was obtained by the following steps: a 2 cm² center piece of the MEA was boiled in hot aqua regia for at least 2 hours to solve the platinum metal. The membrane itself was not attacked by this procedure and could be easily removed from the liquid. The resulting solution was let to cool down and then filled up with H_2O to yield an approximate concentration of 10 mg/l. The measurements were conducted, using the Pt emission at a wavelength of 265.9 nm, 0.2 nm slit width and an air-acetylene flame.

4.4.2 BET analyses

More detailed informations on the MEA morphology were obtained by measuring the average pore size and the pore size distribution. Two different techniques can be applied to determine pore sizes and pore size distributions: the BET (Brunauer, Emmett, Teller) method and Hg porosimetry. In the work presented, the BET method was preferred to Hg porosimetry, due to its less-destructive character. It is a quite important advantage that powders checked in BET measurements can still be used for other characterization techniques, e.g. XRD and TEM. However, the BET technique proved not to be very well-suited for the MEA measurements, as will be commented in the results section.

The measurements were conducted at several membrane electrode assemblies before and after operation in the fuel cell, using an AUTOSORB 3B instrument (by *Quantachrome*). A center part of the MEA (approx. 2 cm²) was cut into small pieces and filled into the glass sample holder. Prior to the measurement, the sample was outgased at 110 °C for at least 10 h, until a pressure of approximately 0.5 mbar was achieved. Standard isotherms were obtained using N_2 at 77 K and carrying out a multipoint BET analysis with the adsorption data in a range $0.08 < p/p_0 < 0.15$. According to the Brunauer, Emmett, Teller equation [170], 5 datapoints of the isotherm were chosen in order to evaluate the specific surface area of the catalyst powder.
Assuming spherical particles with a uniform diameter, the particle size D can then be calculated by equation 4.3 and compared to the values obtained by XRD and TEM:

ρ = theoretical density of the material

$$D = \frac{6000}{\rho\left[g/m^3\right] \cdot S\left[m^2/g\right]}\left[nm\right] \qquad [4.3]$$

In the work presented, the particle size has not been determined. Only pore size distributions have been calculated according to the method of Barret, Joyner and Halenda (BJH method). However, pore size analyses with the BJH method are only feasible for pore sizes between 2 and 50 nm assuming cylindrical pore shapes.

4.4.3 Scanning electron microscopy (SEM)

Images of the MEAs were obtained, using a field emission gun scanning electron microscope (XL30 FEG by Philips). The EDX device, attached to the microscope, was not used for the experiments because of its insufficient lateral resolution. An acceleration voltage of 30 kV was chosen, yielding beam currents of about 150 µA. Secondary electrons (SE) were detected in all cases, as they provide a better morphology contrast than the backscattered electrons (BSE). Due to the poor conductivity of the membrane and the Nafion© ionomer in the electrodes, charging effects occured, that were avoided by gluing the MEA piece to the sample holder with conductive silver solution. This procedure yielded satisfactory results, so that additional Au sputtering was not necessary. Cross-sections were prepared by cutting a small strip (approx. 2 x 0.7 cm) from the MEA and fixing it to the edge of the sample holder. Images of the MEA surface and cross-section were taken at several magnifications. However, the nanoparticles on the carbon support grains could not be imaged, as the resolution of the microscope was limited to about 5 nm.

4.5 Fuel cell measurements

Fuel cell measurements in a single cell setup were carried out in three different operation modes, using hydrogen, H_2/CO mixtures or methanol as anode feed, respectively. A freshly prepared membrane electrode assembly was covered with a diffusion layer (carbon paper, 60% hydrophobized, Toray TGPH-090, E-TEK inc.) of an appropriate size on both sides and mounted into a commercially-available graphite cell block with interdigitated flow fields (FC 25-01 SP, Electrochem. inc.). Prior to the measurements, the fuel cell was heated to the correct working temperature and purged with nitrogen for a couple of minutes to free the hydrogen pipe from air. Then, it was operated at short circuit for at least five days, until a steady-state current was reached and stabilized at an acceptable value. This time period is needed to remove remaining Na^+-ions and organic compounds from the MEA preparation process, that would inhibit the electrode reactions.

4.5.1 Single cell setup

A combined single cell setup, suitable for both gas as well as methanol operation, was constructed (fig. 4.5) and put into operation. This new combined design made switching between gas and methanol operation much easier, as only one pipe connector has to be changed.
Additionally, two setups were taken over from M. Götz (former PhD student of Prof. Wendt, Chemische Technologie, TU Darmstadt) and modified according to the combined design, described schematically in fig. 4.6. Photographs of the newly-built combined single cell setup and the installed graphite cell block, connected to the gas pipes and the electric wires, are shown in fig. 4.5.

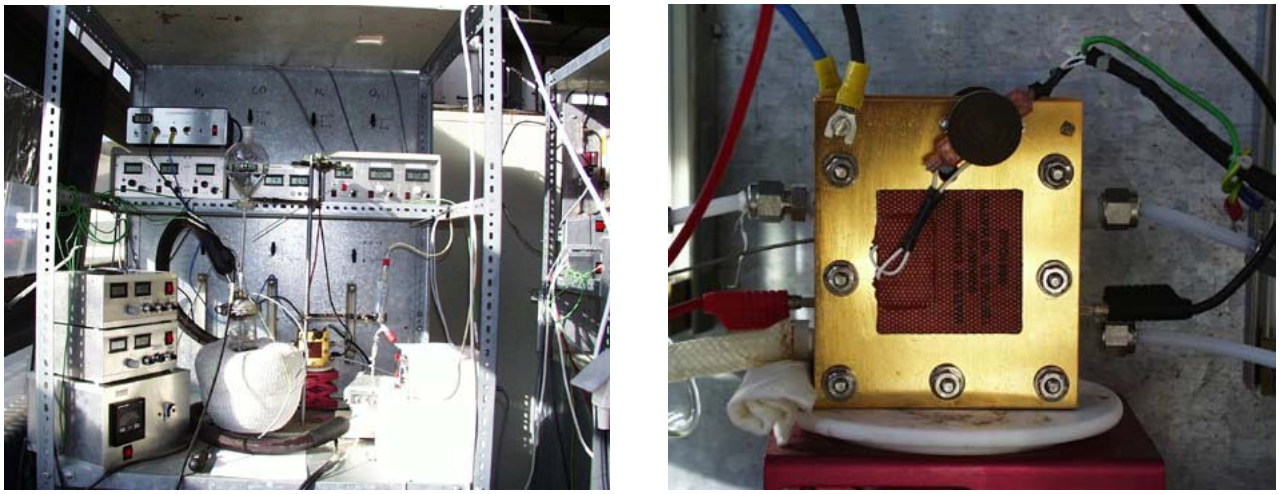

a) b)

Fig. 4.5 Photograph of a) the newly-built combined single cell setup and b) the installed graphite cell block

The feed gases were supplied by commercially-available mass flow controllers. In hydrogen operation, 150 ml/min H_2 (N 5.0, Linde) were loaded with water/steam in a humidifier (T = 70 °C) and fed into the fuel cell anode. The appropriate amount of CO (1,5 vol.% in nitrogen, Linde) was added to achieve either a H_2/75 ppm CO or a H_2/150 ppm CO mixture. The curing tube, connecting the humidifier and the cell, was heated to T = 90 °C in order to avoid steam condensation. As cathode feed, high-purity oxygen was supplied (N 4.6, Linde) at 75 ml/min using both hydrogen and H_2/CO mixtures. High-purity instead of technical purity gases were chosen to guarantee defined conditions and to exclude promoting or inhibiting effects by trace impurities in the feed.

In methanol mode, 1 ml/min of a 1 M aqueous methanol solution was fed into a vaporizer by a peristaltic pump and evaporated at T = 150 °C. The fuel cell supply with the methanol vapor was realized by a supporting nitrogen gas flow (50 ml/min) via a curing tube. The CO concentration in the anode feed thus amounts to approx. 170 ppm. 100 ml/min oxygen (N 4.6, Linde) served as cathode feed in direct methanol operation. In contrast to the gas measurements using H_2 and H_2/CO mixtures, in methanol mode the cell was heated to T = 95 °C and held at this temperature during operation.

The electrocatalytic activities of the catalysts were checked by recording E/i-curves, using an electronic load and a potentiometer both manufactured in-house. The respective curves were measured galvanostatically, beginning at the steady-state current at the short-circuit potential and decreasing it stepwise to zero current. A holding time of 2 minutes at each current value was applied, after which a quasi steady-state potential had been reached. The reproducibility of the results obtained at different single cell setups was checked using three standard MEAs (0.4 mg/cm² Pt E-TEK as anode and cathode catalyst), which showed only minor deviations in their behavior. Likewise, three MEAs per different catalyst system were measured to account for differences in the E/i-curves.

After at least five days of short-circuit operation (‘conditioning’), three E/i-curves in hydrogen operation were recorded, in which usually a slight enhancement of the overall cell performance could be seen. Then, three curves using H_2/75 ppm CO and H_2/150 ppm CO mixtures, respectively, were recorded. The observed activity losses caused by severe CO poisoning were nearly completely reversible, so that only minor degradation was detected in the following E/i-curves in hydrogen mode. Finally, each MEA was

tested in methanol operation. After the electrocatalytic measurements had been completed, the cell was let to cool down, and the MEA was removed and stored in a sealed flask.

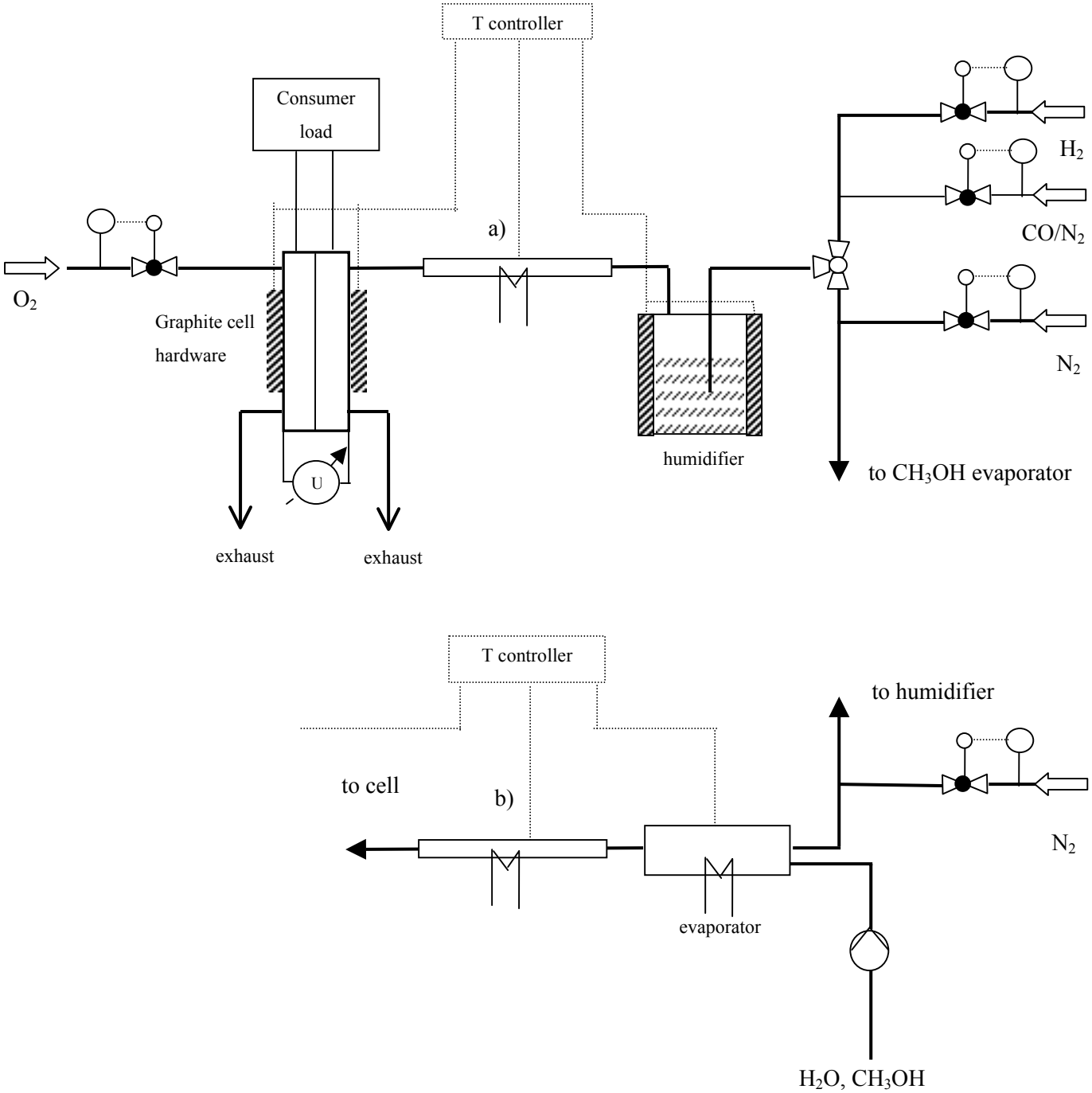

Fig. 4.6 Single cell arrangement for a) hydrogen and H_2/CO mixtures and b) methanol measurements

Since *E*/*i*-curves obtained in fuel cells with a reference electrode are not completely reliable and still show problems in operation [171], the *E*/*i*-curves presented were recorded between anode and cathode only (cell voltage), assuming a reproducible cathode behavior in agreement with most studies in

literature. For comparison of the different catalysts, the current density at 600 mV in H_2/CO operation is given as percentage of the respective performance at 600 mV in hydrogen mode. Thus, the *E*/*i*-curves obtained were evaluated according to the following procedure (fig. 4.7):
the current density at a chosen, fuel cell-relevant potential of 600 mV was read in H_2/CO operation (denoted as *A*) and normalized to the current density at 600 mV in hydrogen mode (denoted as *B*). As the performance in DMFC mode is quite poor compared to measurements using hydrogen or H_2/CO mixtures, the potential value, chosen for the normalization, has been reduced from 600 mV to 400 mV for the experiments in methanol operation. Hence, the data listed in the results section (chapter 5.2.1), correspond to the percentage of the performance in hydrogen operation:

$$\mathbf{i}\ @\ 600\ \text{mV}\ (@\ 400\ \text{mV})\ [\%] = \boldsymbol{A/B} \cdot \mathbf{100}.$$

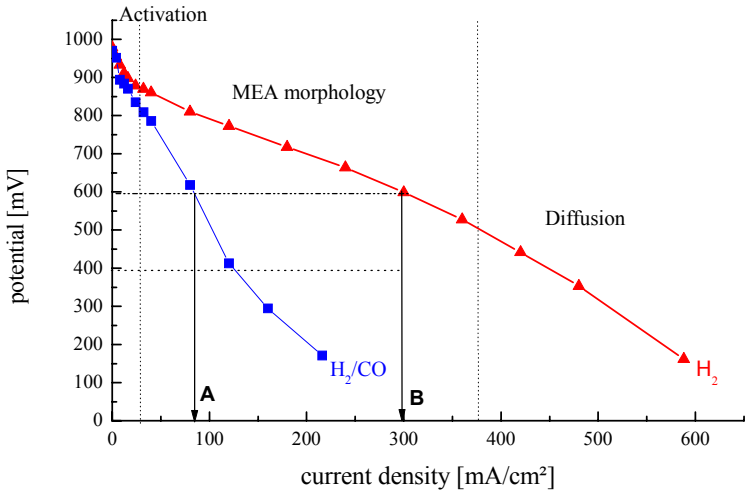

Fig. 4.7 Evaluation of *E*/*i*-curves: normalization, given as percentage of performance in hydrogen mode

Recording a standard *E*/*i*-curve with pure hydrogen at the anode, the curve itself can be split into three different regions, which are either activation-, morphology- or diffusion-controlled. In the middle part of the curve, almost optimum linear behavior is found, while the slope of the line mainly depends on the MEA morphology. At higher current densities, diffusion processes become rate-limiting, as process water in the pores hinders the transport of reaction gases to the three-phase boundary.

4.5.2 Modifications of the fuel cell for in-situ XAS

In-situ XAS experiments at the X1 beamline at Hasylab, Hamburg, have been planned in order to pursue ‘online’ possible changes of the catalyst structure during operation. However, in contrast to previously published results in conventional electrochemical cells (see 3.1.4), the most noteworthy feature of our investigations is that they can be performed in a real fuel cell setup under working conditions. In order to

make these measurements possible, several modifications have been made, concerning the cell hardware as well as the MEA morphology. These will be described in detail below.

First of all, two 1.5 x 0.7 cm windows were cut into the bipolar plates to let the beam pass unhindered in transmission. For this reason, the position of the heating pads had to be slightly changed as well. Then, the commercially-available graphite cell hardware (Electrochem. inc.) has been modified to allow for measurements both perpendicular and parallel to the cell (fig. 4.8). The graphite itself was used as inherent beam window, as it absorbs very little in the respective energy range (11564 eV and 22117 eV). Hence, the graphite material was only thinned in the same areas as the bipolar plates are cut to allow the beam to pass in perpendicular geometry. In order to make measurements parallel to the MEA possible, two additional channels with inherent graphite beam windows were cut into the graphite cell. A window thickness of 0.4 mm proved to be both thin enough for only little contributions to the spectra and thick enough to keep the cell completely gastight and the anode feed separated from the oxygen.

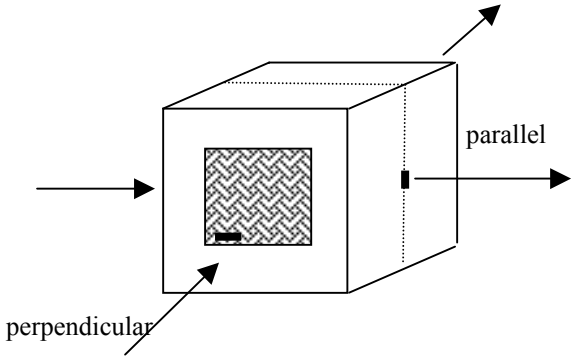

Fig. 4.8 Possible beam geometries for the in-situ XAS experiment

Test experiments without MEA, gas flow and at RT have been conducted to check the suitability of the modified cell in both beam geometries. For this purpose, the cell was placed into the beam, and the beam intensity and the irradiation spot before and after the cell have been determined. The best results were obtained in perpendicular geometry. Consequently, this setup has been chosen for all following measurements.
In subsequent experiments, one of our standard MEAs has been mounted into the cell, and spectra at the Pt L_3-edge have been recorded. However, the raw data obtained with this MEA showed extremely poor signal-to-noise ratios, probably due to both an inadequate Pt loading and an inhomogeneous thickness. In order to improve the quality of the spectra, two strategies were adopted:
First of all, the actual metal loading of the membrane electrode assembly was increased from 0.4 mg/cm² up to at least 1.2 mg/cm² per electrode, providing the best compromise between the calculated optimum signal-to-noise ratio (XAS) and almost unchanged electrode features regarding current distribution and transport processes (single cell setup). The preparation of several additional membrane electrode assemblies for the in-situ measurements has been passed on to J. Scherer (Garche, Jörissen, ZSW Ulm), as particularly the ZSW is renowned for its optimized MEA preparation techniques.

Finally, using the ZSW MEAs with enhanced Pt loading, the feasibility of in-situ EXAFS measurements in real fuel cells could be successfully demonstrated at the beamline X1 at Hasylab, Hamburg (Germany).

However, since the perpendicular geometry has been chosen, anode and cathode side were monitored simultaneously. Thus, changes at the anode side could not be separated from the rest. Two different approaches were proposed to overcome this problem:

a) removal of the cathode side in the respective window region, or
b) measurement at the Ru *K*-edge, since only the anode contains ruthenium.

As part of this work, the first strategy had been adopted and tested for its suitability, although it changes the current distribution within the membrane electrode assembly. Additional experiments at the Ru *K*-edge are planned in future work. However, these will be performed in fluorescence mode, due to the high self-absorption in the electrode layers.

5 Results and Discussion

The following chapter is divided into three subsections, characterization of the catalyst as well as the whole membrane electrode assembly (MEA) *before*, *during* and *after* operation. However, the main emphasis is put on the catalyst side, where the ternary Pt-Ru-W system and differently-synthesized binary Pt-Ru catalysts will be discussed in detail.
Presentation of the obtained results and their discussion will be treated as a whole and will not be separated into two parts of their own, making it easier for the reader to follow the line of argument.

5.1 Structural features *before* operation

Structural characterization of the catalysts by several methods has been carried out prior to the electrochemical testing. Measurements were usually conducted in the following order, XFA, XRD, XRD(T), TEM / nano-EDX, XPS, shortly after the catalyst syntheses to guarantee conditions as similar as possible for the different samples. However, it has been shown exemplary for the commercial carbon-supported Pt and Pt-Ru catalyst by E-TEK inc. as well as for the ternary system that storing the catalysts in sealed snap-cap bottles for several months does not change the XRD and XPS results significantly. Thus, it has been concluded that the catalyst structure is more stable against oxidation processes under atmosphere than expected (compare with [100]).

5.1.1 Characterization of the catalysts

Information on the structure of the respective catalysts has been obtained by the combination of various surface and bulk techniques. Thus, due to the specific properties of each method, a comprehensive idea of the real structure could be achieved.
First of all, the characterization of the ternary Pt-Ru-W system will be presented, in which the potential of the respective techniques has been tested and the measuring conditions and evaluation procedure have been optimized. As systematic questions occurred in the course of this investigation, another approach has been adopted, concentrating on the more simple, but yet not completely understood binary Pt-Ru system first. For comparison, commercially-available Pt, Ru and Pt-Ru catalysts, purchased from E-TEK, have been tested as well. In the following text, these systems were referred to as standard or reference materials. Additionally, plain mixtures of carbon-supported pure Pt and pure Ru catalysts were investigated, which represent the extremest case of non-alloy systems.

5.1.1.1 The ternary Pt-Ru-W system

Ternary systems of different Pt:Ru:W stoichiometries (1:1:0.5, 1:1:1, 1:1:1.5 and 1:1:2, in at.%) were synthesized by the *Bönnemann* colloid method, as described in chapter 4.1. The platinum and ruthenium loading was constantly kept at 20 wt.%, whereas the total metal loading increases, due to the amount of

tungsten added. The constant Pt and Ru metal loading has been chosen in view of the electrochemical testing, as it should allow for a comparison of the electrocatalytic activities between catalysts of various tungsten contents.

X-ray fluorescence analyses

Prior to the real structural characterization, the overall composition of each sample was determined by X-ray fluorescence analysis (XFA) to confirm the correct implementation of the syntheses. In this respect, important parameters were not only the Pt:Ru:W ratio, but also the metal loading on the carbon support. The XFA results of the respective samples and the commercial catalysts, applied as standards, are listed in table 5.1.

Table 5.1 Stoichiometry and metal loading of different carbon-supported catalysts

Sample	**Total metal loading** [wt.%]	**Pt-Ru metal loading** [wt.%]	**Pt** [wt.%]	**Ru** [wt.%]	**W** [wt.%]
Pt-Ru-W (1:1:1.5)	39	21	14	7	18
Pt-Ru-W (1:1:2)	51	22	15	7	29
Pt E-TEK	19	-	19	-	-
Ru E-TEK	12	-	-	12	-
Pt-Ru E-TEK	15	15	10	5	-

As is evident from the results listed above, the stoichiometric quantities employed for the Pt-Ru-W syntheses are in good agreement with the measured stoichiometry in XFA, so that the correct progress of the preparation procedure was confirmed. However, the metal loading of the commercial Ru and Pt-Ru catalysts are less than the specified 20 wt.%, though the correct Pt-Ru 1:1 ratio (at.%) could be verified.

X-ray diffraction

X-ray diffraction was applied to learn more about the crystalline phases in the catalyst. In figure 5.1, the powder pattern of the as-synthesized Pt-Ru-W (1:1:1.5) catalyst is represented. Despite different tungsten contents, the obtained powder patterns look very much alike, so that only the XRD result for the 1:1:1.5 stoichiometry is presented here.

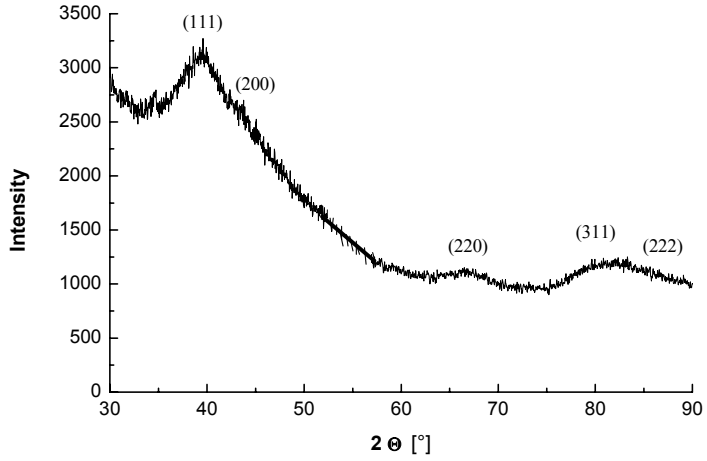

Fig. 5.1 Powder pattern of carbon-supported Pt-Ru-W (1:1:1.5), displaying the Pt fcc structure

The pattern exhibits the wide broadened peaks of the platinum fcc structure with no indication of any reflections of another crystalline phase, e.g. Ru, W, RuO_2 or WO_3. A peak shift to higher 2θ values, due to partial substitution of platinum atoms by ruthenium (or tungsten) was not taken into account, as contraction of the lattice planes, frequently occuring in small Pt particles (see chapter 3.1.1), will make a correct evaluation of the *d* values impossible. Besides, in ternary systems, it is not easy to account for changes in the *d* value: a number of alloys of different compositions might be formed, that can not be distinguished easily. Therefore, *Vegard*'s law was not applied to determine the amount of Ru (or W) in a possible Pt-Ru (or Pt-W or Pt-Ru-W) alloy.
The average size of the crystallites was estimated, using the *Scherrer* equation, and compared with the TEM results, presented later in the text. However, as X-ray diffraction is limited to regions of coherent scattering approximately 2 nm in size, and the average particle size of the sample lies in the same range or even below, only a rough estimation could be given. *Rietveld* analysis, using the FULLPROF package [160], was completely impossible. Thus, an average crystallite size of less than 2 nm has been estimated for the as-synthesized ternary catalysts.

Temperature-dependent X-ray diffraction measurements (XRD(*T*)) were also performed, in order to pursue *T*-induced particle growth, ordering and segregation effects. The 2θ range was restricted to 20°-60° to make reduced measurement times possible.
In figure 5.2, the results obtained for the Pt-Ru-W (1:1:1.5) catalyst under nitrogen atmosphere in a temperature range from 100 °C to 600 °C were shown. In the following cooling cycle from 600 °C to 100 °C (only partially shown) no significant changes, which might be an indication of reversible processes, were observed. Silicon is added to the sample as internal standard, in order to simplify correction of the zero shift in the powder patterns (denoted as Si in the figure). Reflections of the carbon support (S) show up at 2θ approximately 33° and 56°, respectively.

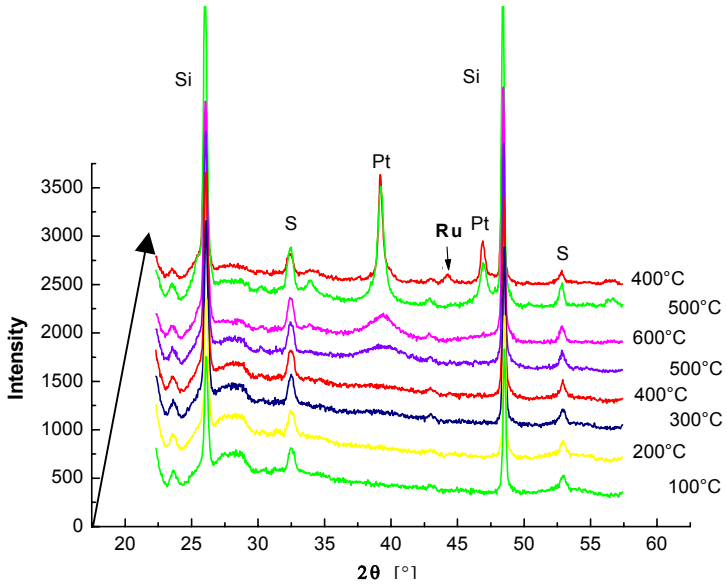

Fig. 5.2 Temperature-dependent XRD measurements of Pt-Ru-W (1:1:1.5) between 100 °C and 600 °C, Si = internal standard, S = carbon support

At 500 °C weak reflections of the hexagonal ruthenium phase show up together with the characteristic reflections of the platinum fcc structure. The reason for the *T*-dependent appearance of the Ru reflections might be either segregation of ruthenium out of a Pt-Ru alloy or ordering and particle growth of an already-existing separate ruthenium phase (compare to [69]). However, the intensity of these reflections indicates an amount of less than 5 wt.% of crystalline ruthenium (compare also to FULLPROF simulations in the binary Pt-Ru system, chapter 5.1.1.2). Thus, the ternary *Bönnemann* catalysts might be described best as partially-alloyed systems. Besides, the temperature treatment under nitrogen atmosphere induced an apparent particle growth, that has been estimated by the *Scherrer* equation, using the Pt(111) reflection and resulting in an increased platinum crystallite size of approximately 7 nm at 500 °C.

However, at this stage of the characterization procedure (after XFA and XRD), it is still unknown, in which form the tungsten is present in the catalysts. Although the respective amount of tungsten was found by XFA, not any evidence of crystalline tungsten or tungsten oxide has appeared in the X-ray patterns. Hence, it is believed that the tungsten is either not reduced properly by the applied synthesis method, forming an amorphous oxide, or that very small tungsten crystallites (< 1.5 nm) are created, which are X-ray amorphous. In order to find out which of these two possibilities is more likely, X-ray photoelectron spectroscopy (XPS) was applied.

X-ray photoelectron spectroscopy

By XPS the oxidation states of the elements present in the catalyst samples were determined. As crystallinity of the specimen is not required, this technique is suitable to solve the question raised above,

if tungsten is present in the form of very small X-ray amorphous particles or as completely amorphous oxide species. Although XPS is a surface-sensitive method, the assumption of obtaining bulk information can be made in the case of very small supported nanoparticles, since most of the cluster atoms are surface atoms (see chapter 3.1.1). Hence, it is acceptable to compare the XPS results with the findings obtained by X-ray diffraction of the bulk material.

In figure 5.3, high resolution spectra of the most-intense platinum and tungsten signal were shown. In the case of ruthenium, the less intense *3p* transition was chosen, due to a severe overlap between the C*1s* of the carbon support and the stronger Ru*3d* signal. Only the high resolution spectra of the Pt:Ru:W (1:1:1.5) catalyst are presented, as the survey spectra of catalysts with different W contents look very much alike, differing merely in the peak intensities (fig. 5.3d).

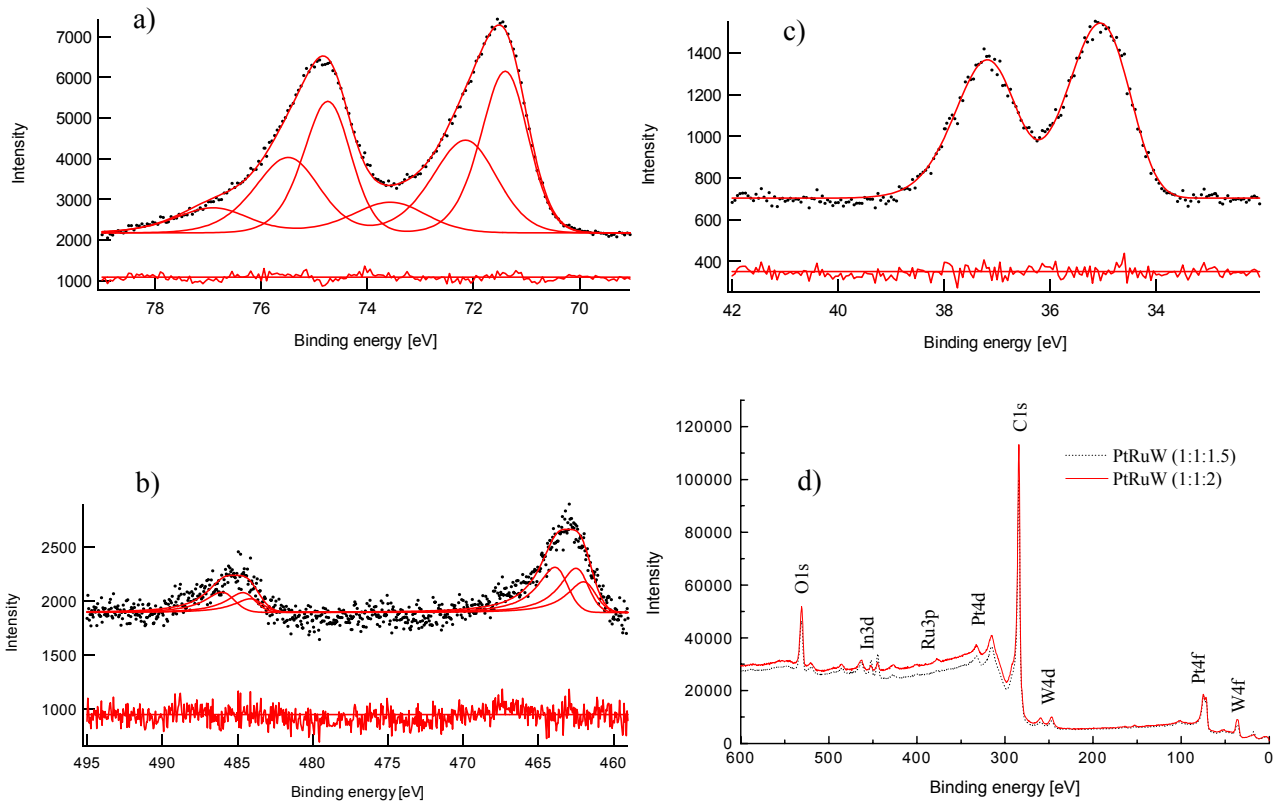

Fig. 5.3 Evaluation of the X-ray photoelectron spectra
a) Deconvolution of the Pt *4f* signal
b) Deconvolution of the Ru *3p* signal
c) Deconvolution of the W *4f* signal
d) Survey spectra of Pt-Ru-W (1:1:1.5) and Pt-Ru-W (1:1:2) catalyst

The obviously asymmetric shaped Pt*4f* and Ru*3p* signals were fitted with a mixed *Gauss-Lorentzian* function. The high resolution spectra were deconvoluted, starting from respective values of reference materials (table 5.1) or from literature (table 5.2), as described in the experimental section.

The Pt*4f* signal could be resolved into three doublets; the most intense peak at 71.4 eV being attributed to metallic Pt, the less prominent doublet at BE 0.8 eV higher than Pt^0 being assigned to Pt(+II) with a BE comparable to that of Pt in $Pt(OH)_2$, while the third doublet at 73.6 eV seems likely to be some kind of surface oxide. The Pt^0 peak is slightly shifted to higher binding energies in accordance with the findings reported by Franke et al. [89].

In the case of ruthenium, the Ru*3p* signal was deconvoluted into three distinguishable peak pairs of different intensities at BE 462.0 eV, 462.4 eV and 463.8 eV. The doublet at BE 462.0 eV was attributed to Ru^0, while the two signals at higher BE were assigned to RuO_2 (BE 462.4 eV) and hydrous RuO_2 (BE 463.8 eV), respectively. The BE of hydrous oxide species is shifted to higher values in comparison to non-hydrous ones, even if the oxidation states are equal [2, 171]. Because of the poor statistics of the Ru*3p* signal, quantitative analyses were not carried out. However, it can be stated that a not negligible share of the ruthenium is present in oxidized form and not in the metallic state.

Tungsten is detected in oxidized form only, exhibiting a binding energy comparable to that of tungsten in WO_3 for all Pt-Ru-W catalysts checked. Hence, the ternary catalyst systems, synthesized according to *Bönnemann*, should be better denoted as Pt-Ru-WO_x, as the tungsten is not reduced properly by the applied synthesis. A reoxidation of metallic tungsten, present in the as-synthesized catalyst shortly after preparation, seems not likely, due to the experiences with storing the catalysts under air (see p. 85).
In line with the XRD results, the ternary catalyst systems consist of Pt, Pt-Ru alloy nanocrystallites and amorphous ruthenium oxides and tungsten oxides. Therefore, transmission electron microscopy has been chosen to localize these phases on the carbon support and to determine the possible contact area between the catalytic active platinum centers and the oxide phases, that might enable enhanced electrocatalytic activities by a so-called spill-over process (see chapter 2.2.2).

Transmission electron microscopy

Images of the ternary catalyst systems, using a low magnification, gave a detailed overview of the catalyst structures (fig. 5.4 a). In principle, they show nanocrystals with particle sizes of 1-2 nm for all Pt-Ru-WO_x catalysts, homogeneously dispersed on the µm-sized carbon support grains. Samples of different compositions do not differ in appearance, therefore only images of the Pt-Ru-WO_x (1:1:1.5) catalyst are presented here. A typical particle size distribution has been derived and is shown in fig. 5.4 b. The mean diameter of the crystalline particles in the respective sample is 1.9 nm, with a standard deviation of 0.4 nm.

a)

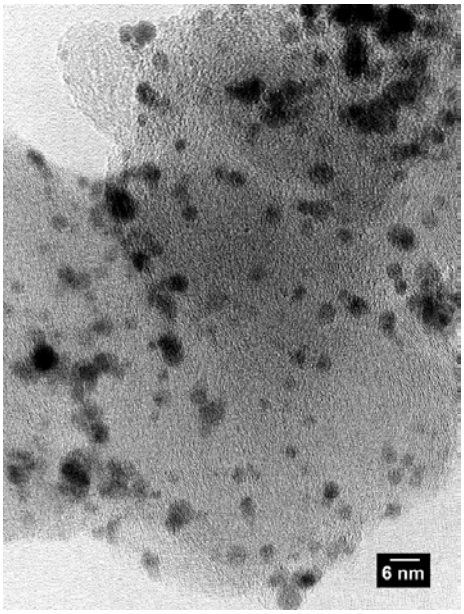

b)

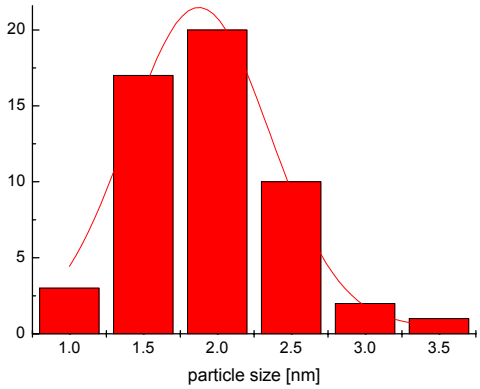

Fig. 5.4 a) TEM image of Pt-Ru-WO_x (1:1:1.5)
b) Typical corresponding particle size distribution

In high-resolution mode (HRTEM), the lattice planes of the nanoparticles are displayed (fig. 5.5), thus giving evidence of the particles crystallinity. Although lattice planes of individual crystallites were clearly resolved and the carbon might serve as an inherent standard, the corresponding *d* values were not determined, as distortion of the lattice planes occurs in small particles [94, 172], compare to 3.1.1.

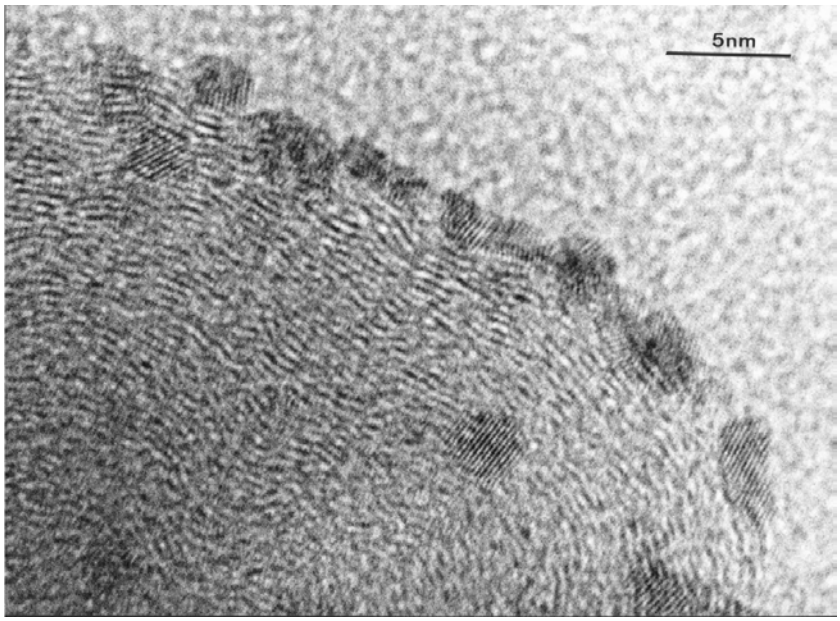

Fig. 5.5 HRTEM image of carbon-supported Pt-Ru-WO_x (1:1:1.5)

The investigation of amorphous phases by TEM imaging presents a quite complex topic, especially, if the amorphous regions have a certain extension in the order of µm and do not provide a specific phase contrast. The diffraction mode generally proves to be more successful, since characteristic halos of the amorphous material are obtained. However, in the case of carbon-supported nanoparticles, additional information on the amorphous phases could be achieved neither by imaging nor by electron diffraction, due to the specific features of these systems. On the one hand, important information might be lost in electron diffraction, as possible halos of the amorphous materials might not be distinguishable from diffraction rings of the small nanocrystallites. On the other hand, the main drawback in TEM imaging is, that not only the ruthenium oxides and tungsten oxides are present as amorphous phases, but also the partly crystalline carbon support and the amorphous carbon film of the TEM grid. Thus, amorphous carbon structures (particle support and TEM grid) might superpose the contributions from the oxide phases, at least, if the oxidic Ru and W species are present in a not well-defined film or in a cloud-like form. However, if the oxidic Ru and W species were small particles of a certain shape, these might be distinguished from the amorphous carbon film. According to the TEM results, the presence of amorphous film-like oxides seems more likely for the systems under investigation, as no amorphous regions, corresponding to either ruthenium oxides or tungsten oxides, were seen in the TEM images. These findings also support the assumption of an improper reduction during preparation instead of a reoxidation by storage under air atmosphere.
In good agreement with the supposition of the amorphous oxides present in a more or less film-like structure, nano-EDX analyses detected platinum, ruthenium and tungsten in varying ratios all over the TEM grid. A correct evaluation of the composition of individual nanocrystallites was not feasible, as the electron beam itself shows a certain extension in the same order of magnitude as the particle size and the interparticle distance. Thus, no detailed information could be obtained, if the metallic ruthenium, observed by XPS, is present in the nanocrystallites in the form of a Pt-Ru alloy.

In summary, a rather detailed idea of the structure of several ternary Pt-Ru-W systems with various tungsten contents was obtained by a combination of XFA, XRD, XPS and TEM. As is evident by the results presented, a variation of the catalyst composition does not affect the structure significantly. It has been confirmed that the *Bönnemann* synthesis is suitable for the preparation of homogeneously-dispersed nanoparticles with an average size of approximately 2 nm and a sharp particle size distribution. However, only a little share of the ruthenium appears in the metallic state, probably forming nanocrystalline Pt-Ru alloy particles, whereas the remaining Ru and the entire tungsten are present as amorphous oxide species. Hence, in order to have a closer look on the effect of the preparation conditions on the alloy formation in the respective systems, different binary Pt-Ru catalysts were investigated. Restriction to a binary system has been chosen in order to simplify systematic studies of the relationship between alloy formation and the corresponding electrocatalytic activity.

5.1.1.2 The different Pt-Ru systems

Three Pt-Ru (1:1) catalysts (20 wt.% on Vulcan XC 72) were synthesized differently to investigate the influence of the chosen preparation route on the resulting catalyst structure. As already mentioned in the experimental section, the synthesis routes employed were selected, based on the information that one of

the chosen preparation methods should result in separate phases (*sample I*, [156]), another in an alloy *(sample III*, [157]), whereas for the third method no information on the resulting structure was reported at all (*sample II*, [158]). For the structural characterization of the respective samples, the same combination of methods was applied, that has proved successful for the investigation of the ternary Pt-Ru-W systems. Additionally, ex-situ EXAFS measurements were performed to draw a final and accurate conclusion on the real catalyst structure. For comparison, a commercially-available Pt-Ru (1:1) catalyst (E-TEK, 20 wt.% on Vulcan XC 72) has been used as reference material.

X-ray fluorescence analyses

First of all, the correct implementation of the three different syntheses has been verified by X-ray fluorescence analysis (XFA), checking the overall metal loading on the support and the correct Pt:Ru ratio. In table 5.2, the XFA results of the respective samples are summarized. The results obtained for the commercial Pt-Ru catalyst are shown for comparison.

Table 5.2 X-ray fluorescence analyses of the differently-synthesized Pt-Ru catalysts

Sample	**Metal loading** [wt.%]	**Pt** [at.%]	**Ru** [at.%]
Pt-Ru E-TEK	15	51.3	48.7
Sample I	21	54.5	45.5
Sample II	22	60.5	39.5
Sample III	17	46.5	53.5

The analytic results show good agreement between the stoichiometric quantities, employed for the catalyst syntheses, and the measured final composition in XFA. The absolute metal loading on the carbon support is even closer to the 20 wt.% value for the in-house synthesized catalysts than for the commercial reference material. Only the Pt:Ru ratio of sample II, synthesized using hydrazine as reducing agent, lies within the borderline of the accepted limit of 10%, as stoichiometries as similar as possible are needed for an accurate comparison of the resulting electrocatalytic activities.

X-ray diffraction

The X-ray patterns of all catalyst samples in the as-synthesized state reveal a fcc pattern with *d* values matching or close to platinum, according to the ICDD database (fig. 5.6). Comparable to the results in the ternary Pt-Ru-W systems, no evidence of metallic Ru or any oxide phases was found. The samples differ only in the average particle sizes, determined by the *Scherrer* equation. However, the fact that no ruthenium reflections appear in the patterns does not rule out the possibility of X-ray amorphous ruthenium particles (< 2nm) present in the catalyst.

The reflections of the commercially-available Pt-Ru catalyst purchased from E-TEK inc. (fig. 5.6 a) shift slightly to higher 2θ values, indicating an alloy formation in the Pt-Ru system, which has already been reported by Arico et al [1]. But in the investigations presented in this work, for neither the commercial catalyst nor sample III (fig. 5.6 b) a precise determination of *d* values was feasible, due to the small particle sizes (≤ 2 nm). Hence, no final conclusion has been drawn on an alloy formation in these systems.

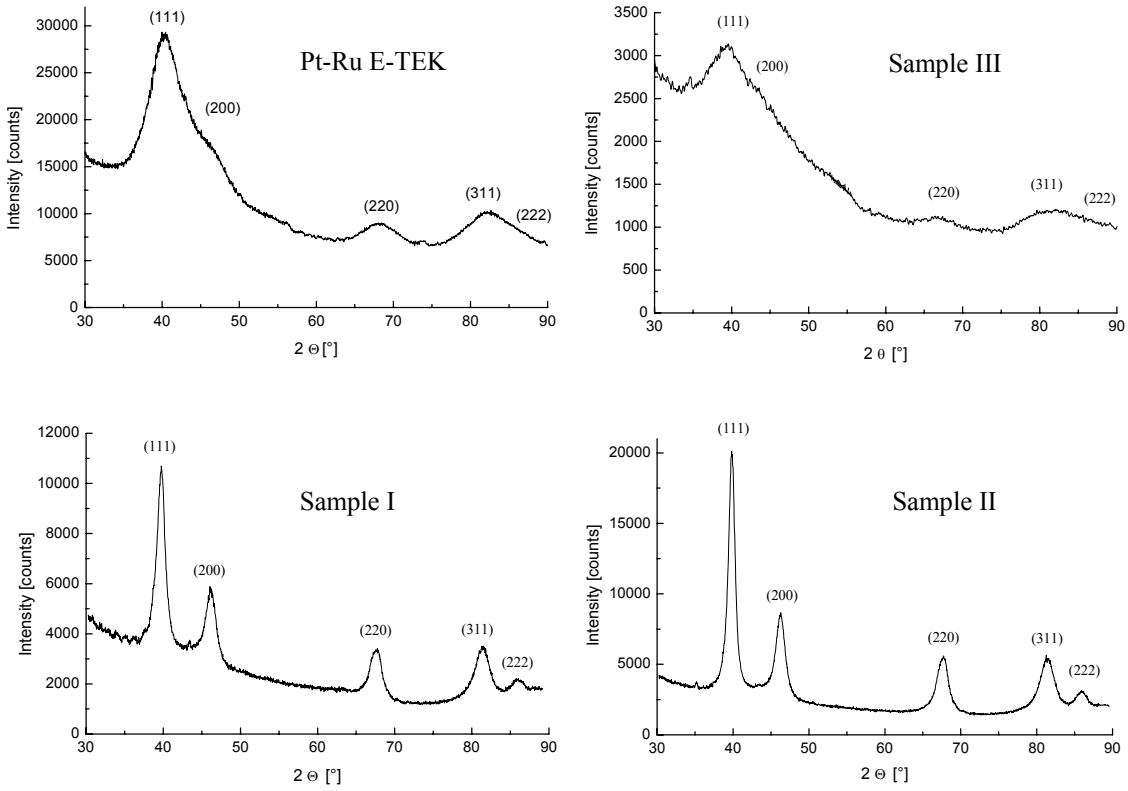

Fig. 5.6 X-ray diffraction patterns of the different carbon-supported Pt-Ru systems

However, lattice parameters for both catalysts (sample I, fig. 5.6 c, sample II, fig. 5.6 d), synthesized by two different reduction methods in aqueous solution, can be determined by *Rietveld* analysis using FULLPROF [160] (table 5.3). The observed values are in good agreement with the lattice parameter of pure platinum, a_{Pt} = 3.9231 Å. Exemplary, the measured and the simulated pattern of sample I are shown in fig. 5.7.

Table 5.3 Particle sizes and *d* values of the respective Pt-Ru catalysts

Parameter	**Pt-Ru E-TEK**	**Sample I**	**Sample II**	**Sample III**
Particle size [nm]	≈ 2	7	9	< 2
d value [Å]	(2.23)	2.26	2.26	-
a [Å]	(3.86 ± 0.02)	3.908(5)	3.916(4)	-

* uncertainties are in agreement with [173]

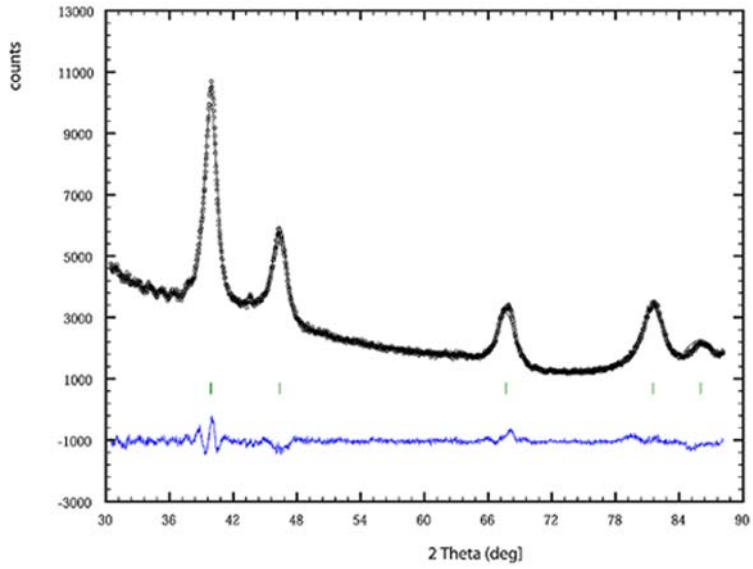

Fig. 5.7 Measured (•) and calculated (–) X-ray pattern and difference plot of sample I directly after preparation, reflection markers Pt

In contrast to the temperature-dependent X-ray diffraction measurements carried out in the ternary system, a different approach has been adopted for the binary catalysts to determine the oxidation state of Ru, that does not appear in the X-ray patterns of the as-synthesized catalysts. Prior to the XRD measurements, all samples were ex-situ heat-treated at 500 °C for 5 h under nitrogen flow. This kind of procedure does not correspond to any working condition in the real fuel cell. But the enhanced temperature might induce particle growth as well as „defect-healing“ processes, thereby increasing the crystallinity of the material. The temperature T = 500 °C has been chosen, as it is a prominent temperature for possible recrystallization processes. Moreover, it has been shown for the ternary Pt-Ru-W system that at 500 °C weak reflections of the hexagonal ruthenium phase appear.

The patterns obtained display significant differences compared to the results of the as-synthesized catalysts (fig. 5.8). For all in-house synthesized samples, the Ru(101) reflection appears in addition to the platinum reflections.
Ru(101) represents the most intense reflection in the hexagonal Ru pattern, hence it can be detected, even if the Ru particles are very small. Nevertheless, the intensity of the Ru reflection is very weak compared to the Pt peaks, an indication of the small amount of coherently scattering Ru particles in the sample. According to the results of the *Scherrer* equation, only minor particle growth occured in the Pt phase during the heat-treatment under nitrogen.

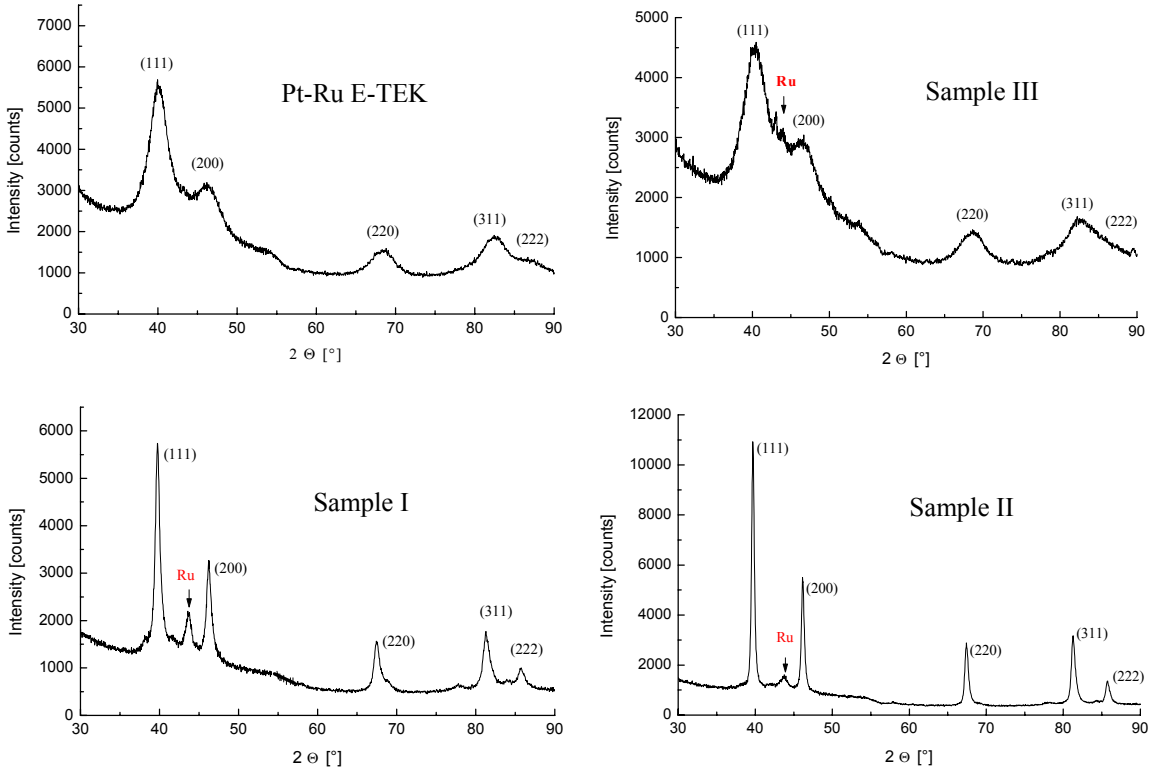

Fig. 5.8 X-ray diffraction patterns of the differently-synthesized Pt-Ru catalysts after heat-treatment at 500 °C under nitrogen flow

Rietveld analysis has been carried out for the two catalysts, synthesized in aqueous phase (samples I and II), and the measured and calculated X-ray pattern of sample I is shown in figure 5.9.

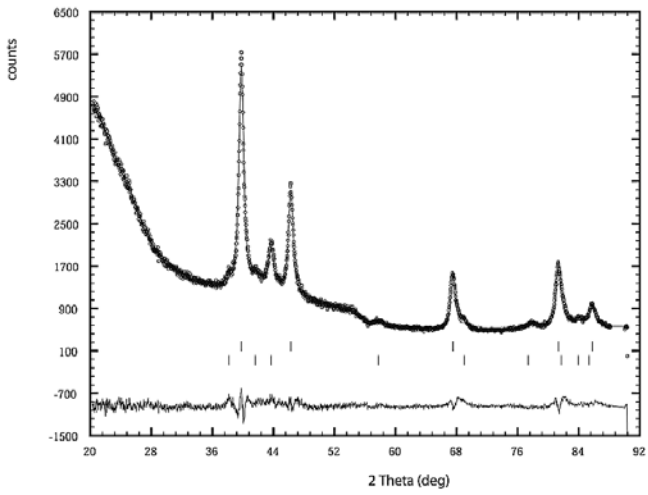

Fig. 5.9 Measured (•) and calculated (–) X-ray pattern and difference plot of sample I after heat-treatment at 500 °C under nitrogen, upper reflection markers Pt, lower Ru

A platinum lattice parameter of a_{Pt} = 3.918(4) Å was obtained for sample I (a_{Pt} = 3.916(4) Å for sample II), while profile matching of the hexagonal ruthenium phase resulted in a_{Ru} = 2.71(8) Å and c_{Ru} = 4.33(7) Å (a_{Ru} = 2.71(5) Å and c_{Ru} = 4.27(9) Å for sample II). However, the results for the ruthenium phase are less precise because of the small Ru particle sizes. The fraction of separate ruthenium hcp crystallites present in the samples is approximately 10 wt.% in sample I and 20 wt.% in sample II.

In addition to the heat-treatment in flowing nitrogen, as-synthesized catalyst samples were also heat-treated at 500 °C for 5 h in air. This procedure was applied in order to uncover possible further differences between the four Pt-Ru systems under investigation. The powder patterns of all catalysts (fig. 5.10) show the formation of a tetragonal RuO_2 phase, but significant differences in the size of the oxide particles.

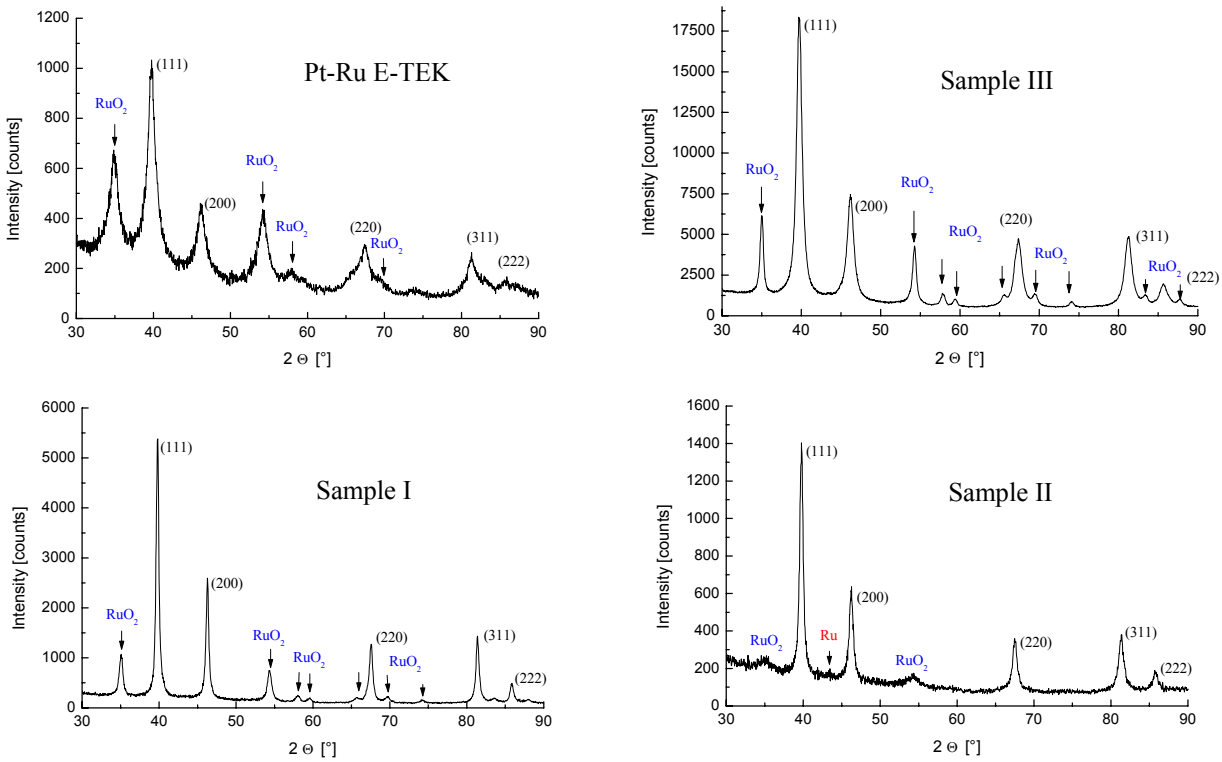

Fig. 5.10 Diffraction patterns of the differently-synthesized Pt-Ru catalysts after heat-treatment at 500 °C in air

For the commercial Pt-Ru E-TEK catalyst, the average size of the ruthenium oxide particles, as determined by the *Scherrer* equation, resembles the respective size of the platinum nanocrystallites (about 7 nm). In sample I and III, larger oxide particles have been found, which are approximately 20 nm in size, compared to the platinum crystallites with an average size of 10 nm. *Rietveld* analysis has been carried out exemplary for sample I, yielding the following values:
a_{Pt} = 3.915(4) Å, a_{RuO2} = 4.487(3) Å and c_{RuO2} = 3.102(3) Å. The measured and calculated X-ray pattern of sample I is shown in figure 5.11.

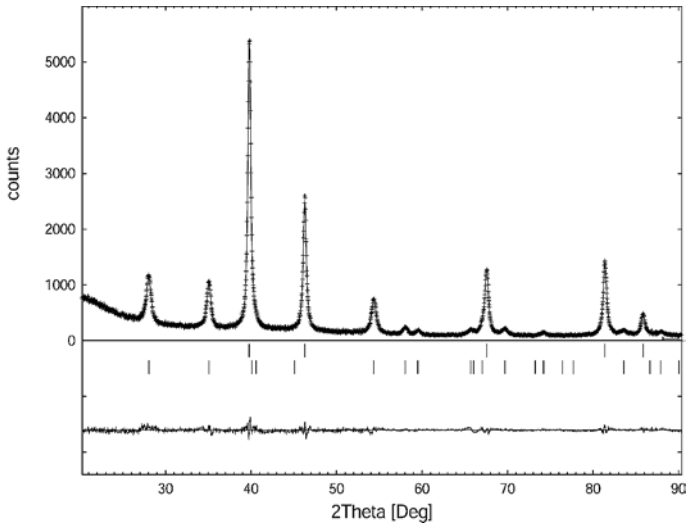

Fig. 5.11 Measured (•) and calculated (–) X-ray pattern and difference plot of sample I after heat-treatment at 500 °C under air, upper reflection markers Pt, lower RuO_2

In contrast to these observations, the powder pattern of the hydrazine-reduced catalyst (sample II) looks completely different, revealing not only RuO_2 reflections, but also the most intense ruthenium reflection, Ru(101). According to the *Scherrer* equation, both nanocrystalline ruthenium phases have comparatively small particle sizes around 2 nanometers.

The differences in the powder patterns observed for sample I and II seem to be due to the different preparation methods, in particular due to the reducing agents and the pH values, as reaction times and temperatures in both syntheses were nearly identical. The main difference between hydrazine and formaldehyde is their reduction potential; hydrazine at pH = 10 being stronger than formaldehyde at pH = 8. Therefore, it seems likely that the less-noble ruthenium is reduced into its metallic form by hydrazine, whereas by formaldehyde only a rather incomplete reduction is achieved. Thus, in the as-synthesized sample I, the ruthenium clusters might be coordinated by weakly-bonded OH species. In contrast, the $RuCl_3$ (educt) might be completely reduced in sample II, and, due to the small particle sizes, easily oxidized by even the low amount of oxygen present in air. However, the differences observed were not completely understood and have to be further investigated.

As a more general remark, enhanced particle growth of the platinum phase takes place in air compared to the particle growth in nitrogen atmosphere (table 5.4), compare with [174].

Table 5.4 Average particle sizes in [nm], estimated via the *Scherrer* equation, after heat-treatment in air and nitrogen atmosphere, respectively

Sample	**As-synthesized**	**in nitrogen**		**in air**	
	Pt	Pt	Ru	Pt	RuO_2
Pt-Ru E-TEK	≈ 2	3	-	7	7
Sample I	7	9	4	11	20
Sample II	9	10	3	18	2
Sample III	< 2	3	n.p.	10	20

According to the predominant opinion, X-ray diffraction is absolutely improper for the characterization of nanosystems. However, by pattern calculation applying the Pt and Ru particle sizes as well as the amount of crystalline ruthenium as parameters, unexpected results were obtained. It looks like that at least rough estimations of the real structure in these catalysts are feasible by X-ray diffraction. Thus, pattern simulations, using the FULLPROF package, can help to get at least an idea of the extent of alloy formation even in complex nanosystems.

The parameters, varied in the FULLPROF sheet, were *Y* taking into account platinum particle sizes between 2 nm and 9 nm and the ruthenium scale factor *sc*, simulating different amounts of crystalline ruthenium, while the scale factor of platinum was kept constant. In order to simplify the procedure, the ruthenium particle size was not varied at all and kept constant at 1.5 nm, which is in good agreement with our previous findings. Indeed, ruthenium particles of such a small size do not appear as discrete reflections in the pattern, but contribute to the changes in the intensity of the platinum (111) and (200) reflection observed in the X-ray patterns of the as-synthesized samples (see also 3.1.1, E. Garnier).

In table 5.5, only platinum particle sizes corresponding to the actual sizes of the different as-synthesized Pt-Ru samples (Pt-Ru E-TEK: 2 nm, sample I: 7 nm, sample II: 9 nm) were considered. The second column displays the ruthenium scale factors applied for the pattern simulation, whereas the corresponding values for the amounts of crystalline ruthenium are shown in the third column. The two last columns list the values for the intensity ratio Pt(111)/(200) and the approximate intensity at the overlap of the Pt(111) and (200) reflection. These two values were obtained from the simulated patterns and applied as a measure for the real patterns of the different catalysts. As the variation of the intensity ratio is comparatively small and therefore quite erroneous, the overlap intensity is chosen as suitable parameter for a rough estimation of the amount of crystalline ruthenium present in the samples.

Table 5.5 Attempt to describe the differences in the patterns of the differently-synthesized Pt-Ru samples by pattern simulation

Particle size	**Scale factor Ru**	**Ru content [%]**	**Intensity (111)/(200)**	**Overlap intensity**
Pt-Ru E-TEK	$0.35 \cdot e^{-2}$	6 %	1.769	781.51
2 nm	$0.70 \cdot e^{-2}$	10 %	1.729	839.14
	$1.0 \cdot e^{-2}$	14 %	1.708	879.47
	$1.4 \cdot e^{-2}$	19 %	1.664	942.86
	$2.2 \cdot e^{-2}$	27 %	1.582	1070.90
Sample I	$0.35 \cdot e^{-2}$	6 %	2.104	335.17
7 nm	$0.70 \cdot e^{-2}$	10 %	2.111	392.80
	$1.0 \cdot e^{-2}$	14 %	2.090	446.46
	$1.4 \cdot e^{-2}$	19 %	2.081	504.08
	$2.2 \cdot e^{-2}$	27 %	2.054	634.57
Sample II	$0.35 \cdot e^{-2}$	6 %	2.105	335.17
9 nm	$0.70 \cdot e^{-2}$	10 %	2.106	388.84
	$1.0 \cdot e^{-2}$	14 %	2.090	446.46
	$1.4 \cdot e^{-2}$	19 %	2.075	504.08
	$2.2 \cdot e^{-2}$	27 %	2.039	619.33

Comparing the measured overlap intensities, observed in the real patterns, with the calculated data, a rough idea of the amount of crystalline ruthenium in the respective samples can be obtained (see table 5.6). An evaluation for sample III was impossible because of its particle size below 2 nm.

Table 5.6 Estimation of the amount of crystalline Ru in the Pt-Ru catalysts (derived by pattern simulation)

Sample	**Overlap intensity**	**Ru content [%]**
Pt-Ru E-TEK	710	0
Sample I	380	< 10
Sample II	610	> 25

However, it should be stressed once more that the values are not quantitative and serve for a qualitative comparison of the synthesized samples only.
It is supposed that the differences in the four catalyst systems, revealed by XRD measurements after heat-treatment in air and nitrogen, respectively, were already inherently present in the as-synthesized samples, but did not show up, due to the limitations of the X-ray technique. By rough pattern simulations it was possible to give at least an estimation of the amount of crystalline ruthenium, that is present as a separate phase in the catalyst. Thus, sample II contains much more separate ruthenium particles than sample I, while no separate ruthenium at all could be detected in the commercial catalyst.

In essence, the results of the X-ray diffraction experiments in the as-synthesized state, in nitrogen and air, respectively, and their rough simulation seem to confirm that different extents of alloy formation can be achieved by the different syntheses. According to our expectations, different degrees of alloy formation were obtained by the different syntheses. Sample II exhibits the highest amount of separate ruthenium, followed by sample I. In contrast, sample III looks like an at least partially alloyed system, whereas the commercial binary catalyst is almost completely alloyed.
However, it is the task of the subsequent investigations of the as-synthesized catalyst samples to achieve a more detailed idea of the different Pt-Ru systems.

X-ray photoelectron spectroscopy

First of all, the oxidation states of platinum and ruthenium were determined for the as-synthesized samples by XPS and compared to those for the commercial Pt-Ru catalyst, acting as reference material. Based on the investigation of the ternary Pt-Ru-W systems, high resolution spectra of the Pt*4f* and the Ru*3p* have been recorded and fitted with a mixed *Gauss-Lorentzian* function. Then, the spectra were deconvoluted, starting from respective values of the reference materials (table 5.1) or from literature values (table 5.2), as described in the experimental section.
The Pt*4f* signal could be resolved into three doublets; the most intense peak attributed to metallic Pt, the less prominent doublet at higher BE being assigned to Pt(+II), while the third doublet seems likely to be some kind of surface oxide. The effect of the platinum particle size on the respective binding energy is clearly visible for the different systems (table 5.7). The commercial catalyst shows the highest binding energy of BE 71.5 eV, due to its small particle size. The data obtained are in good agreement with those, reported by Franke et al. [89].
In the case of ruthenium, pronounced differences between the commercial catalyst and the samples I and II appear. For sample I, the Ru*3p* signal was deconvoluted into three distinguishable peak pairs of different intensity at BE 462.4 eV, 463.1 eV and 465.8 eV. Nearly identical values have been determined for sample II. These were attributed from top to bottom to ruthenium oxide, a hydrous ruthenium oxide species and a highly-oxidized surface oxide, see Ramesh et al. [163]. It should be stressed that no evidence of metallic ruthenium has been found. In contrast to the results for samples I and II, the commercial catalyst shows an additional peak at BE 461.9 eV, corresponding to Ru^0. Quantitative analyses were not carried out because of the poor statistics of the Ru*3p* signal.
The oxygen signals obtained were assigned to ruthenium oxide (about 529.5 eV) and hydrous ruthenium oxide (approximately 530.8 eV). In addition, a BE of roughly 532.6 eV has been detected, that is

attributed to an interaction with the carbon support, as it does not appear in unsupported samples (see chapter 5, table 5.1).

Table 5.7 Evaluation of the high-resolution XPS spectra

Sample	**Pt** BE 4*f* [eV]	**State**	**Ru** BE 3*p* [eV]	**State**	**O** BE 1*s* [eV]	**State**
Pt-Ru E-TEK	71.5	Pt^0	461.9 462.6 463.4 465.2	Ru^0 RuO_2 Hydrous RuO_2	530.7 532.5	Hydroxide -C-O
Sample I	71.3	Pt^0	462.4 463.1 465.8	RuO_2 Hydrous RuO_2	529.8 530.8 532.7	Oxide Hydroxide -C-O
Sample II	71.2	Pt^0	462.5 463.5 465.4	RuO_2 Hydrous RuO_2	530.8 532.9	Hydroxide -C-O

Moreover, an attempt has been made to quantify the amount of oxygen present in the differently-synthesized Pt-Ru systems in order to account for the different XRD results after heat-treatment in air. Integration of the O*1s* peak resulted in a value nearly twice as high for the commercial catalyst than for samples I and II. Though surprising at first sight, this is probably due to the smaller particle sizes in the E-TEK catalyst. In table 5.8, the number of surface atoms has been calculated for various particle sizes, assuming a spherical shape of the clusters. It is evident that the information of the measurements will change significantly from bulk-like to surface-like, when the cluster size is increased from 2 nm (commercial catalyst) to 9 nm (sample II). Thus, a correct evaluation of the data is not possible, as for samples I and II X-ray photoelectron spectroscopy yields mainly surface information, whereas for smaller particles the assumption of achieving bulk information holds best (compare to 3.1.1). Hence, this approach can not be applied to compare all three catalysts with respect to their oxygen content. However, in the case of samples I and II, a comparison obtains valid results, due to their nearly similar particle sizes. Integration of the area under the oxygen peak results in nearly the same value, corresponding to approximately the same amount of oxygen present in both samples.

Table 5.8 Relation between cluster size and calculated number of surface atoms in the respective cluster

Sample	**Particle size** [nm]	**Number of surface atoms**
Pt-Ru E-TEK	2	≈ 65 %
Sample I	7	≈ 10 %
Sample II	9	≈ 10 %

An additional information can be obtained by normalization of the intensity of either the Pt or the Ru signal to the intensity of the C*1s* excitation, taking into account the respective sensitivity factors. The resulting values might be used as a rough measure for the number of particles near the surface of the carbon support. The more clusters in surface regions, from which the generated photoelectrons can reach the surface, the more intense the resulting XPS signal and the higher the obtained value. It has been found that in the case of the E-TEK catalyst in average nearly twice as much catalytic active clusters were near the surface of the support grains than for samples I and II. This will prove to be advantageous for its use in electrocatalysis, as the active centers are more easily accessible for the reactants.

Transmission electron microscopy

TEM images reveal highly-dispersed nanocrystallites with a quite uniform particle size distribution for the E-TEK (fig. 5.12 a) as well as the *Bönnemann* colloid catalyst (sample III, not shown). A typical particle size distribution for the commercial catalyst has been derived and is shown in fig. 5.12 d. The mean diameter of crystalline particles in the respective sample is 2.0 nm, with a standard deviation of 0.3 nm. Both reduction methods in aqueous phase (synthesis II: fig. 5.12 b, synthesis I: fig. 5.12 c), however, lead to the formation of approximately 20 nm-sized agglomerates, consisting of smaller nanocrystallites and with shapes depending on the reduction parameters. In the catalyst, reduced by formaldehyde (sample I), the agglomerates appear to have a rather irregular shape, whereas sample II forms regular spheres. This might be due to the prolonged reduction time in synthesis II compared to the preparation of sample I.

Although the lattice planes of the nanocrystallites were resolved for all samples, only the *d* values of samples I and II were determined, due to the effects, already-explained for the ternary Pt-Ru-W system (see also chapter 3.1.1). The respective *d* values found for samples I and II correspond mostly to the Pt(200) and Pt(111) plane.

Nano-EDX analyses of sample I and II, which were carried out directly on the agglomerates, detected platinum only, whereas only traces of Ru were found (table 5.9). However, if analyses were performed in carbon support regions beneath the agglomerates, where apparently no particles can be distinguished, the ‘missing’ ruthenium has been found. These results are in accordance with the X-ray data, in which a good share of separate ruthenium particles has been found. As the separate ruthenium particles in the as-synthesized samples I and II are neither found as reflections in XRD nor as visible particles in TEM, it is supposed that their size is well below 2 nm.
In contrast, for the commercial Pt-Ru catalyst, purchased from E-TEK, and the colloid catalyst (sample III), platinum as well as ruthenium are detected all over the TEM grid. This result, however, gives no evidence of an alloy formation in these catalysts, as the small particle sizes do not allow an analysis of individual particles.

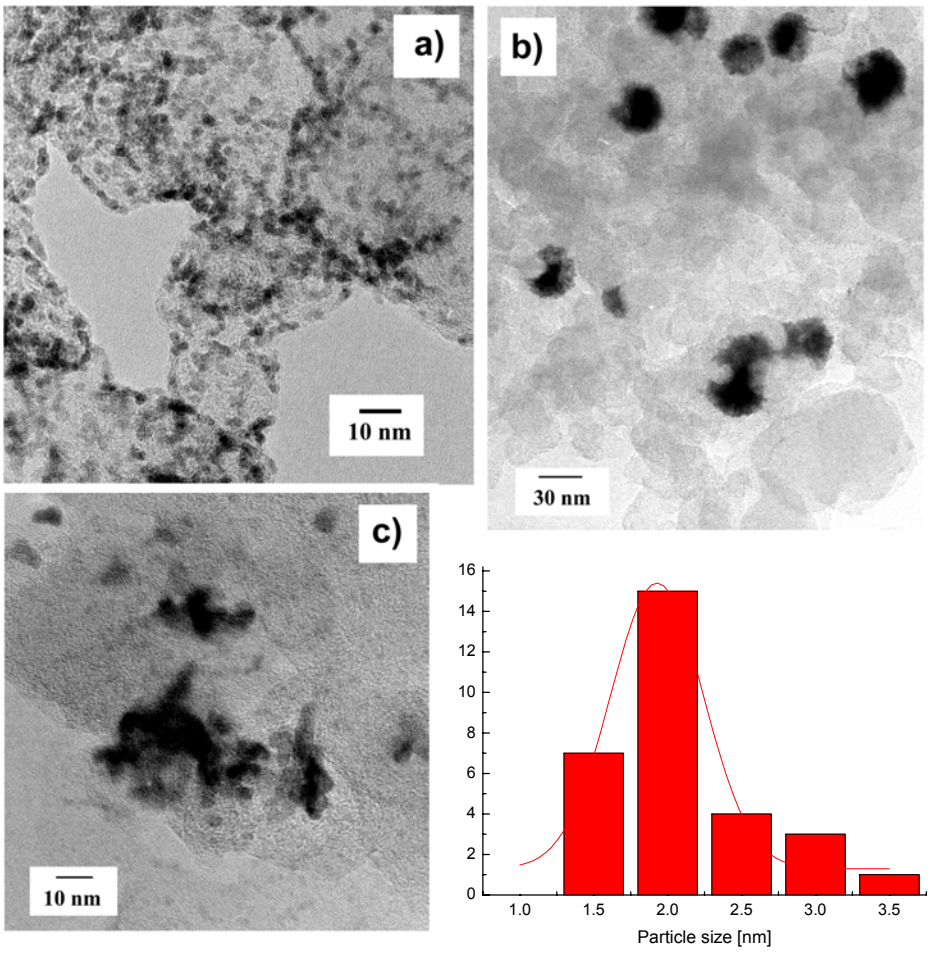

Fig. 5.12 TEM images of the differently-synthesized Pt-Ru catalysts shortly after preparation
a) Pt-Ru E-TEK, b) sample II, c) sample I, d) particle size distribution for Pt-Ru E-TEK

After heat-treatment in flowing nitrogen, TEM images of the catalysts (not shown) revealed no remarkable differences between the heat-treated samples and the catalysts in the as-synthesized state. Only the agglomerates, that consisted of smaller nanocrystallites, have grown into a whole crystallite structure during the heat-treatment. In accordance with the powder data, nano-EDX analyses of the samples (table 5.9), detected individual Ru particles in samples I and II. In the case of the E-TEK and the *Bönnemann* catalyst (sample III), respectively, nano-EDX on distinct particles could not be performed as the distances between neighboring nanocrystallites were still too small.
TEM images of the Pt-Ru catalysts after heat-treatment in air revealed similar results as the powder data (fig. 5.13). In particular, the images of samples I and II display the structural differences between the catalysts: for sample I large ruthenium oxide crystals of a characteristic stick-like shape have been found in close contact to the Pt particles, whereas sample II exhibits large Pt particles, that are surrounded by a huge number of very small nanocrystallites. Both phases are easily discernible, due to their marked phase

contrast. Any contributions of the carbon support have vanished, as it is completely oxidized by the heat-treatment under atmosphere.

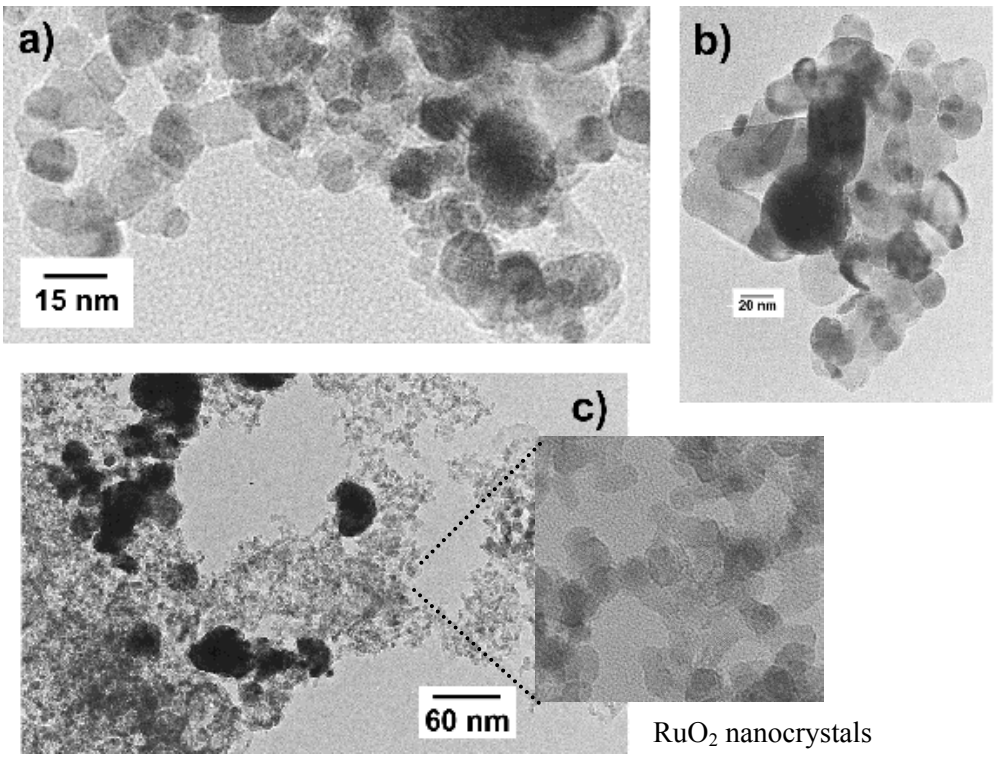

Fig. 5.13 TEM images of the differently-synthesized Pt-Ru catalysts after heat-treatment in air
a) Pt-Ru E-TEK, b) sample I, c) sample II

In high resolution mode, the lattice planes of individual particles could be imaged, the resulting *d* values matching Pt, RuO_2 and in the case of sample II Ru, respectively. The evaluation of the *d* values has been possible, as particle growth is much more pronounced under air than under nitrogen atmosphere and, apart from the ruthenium phases in sample II, measured particle sizes were well-above the critical value of 2 nm. As expected, Pt, RuO_2 and for sample II additionally Ru were detected by EDX (table 5.9), thereby confirming the XRD and TEM results. The Ru:O ratios are given in brackets, as besides ruthenium also silicon has been present in the samples, that is certainly oxidized as well.

Table 5.9 Results of the nano-EDX analyses of samples I and II

Sample	**As-synthesized**			**in nitrogen**			**in air**		
	Pt:Ru	Ru:Pt	Ru:O	Pt:Ru	Ru:Pt	Ru:O	Pt:Ru	Ru:Pt	Ru:O
Sample I	80:20	-	-	90:10	90:10	-	90:10	-	(45:55)
Sample II	85:15	-	-	95:5	97:3	-	90:10	95:5	(30:70)
Interpretation	Pt particles			Pt + Ru particles			Pt + Ru oxide(+Ru)		

Ex-situ X-ray absorption spectroscopy

In contrast to the investigation of the ternary Pt-Ru-W systems, reported previously, ex-situ X-ray absorption spectroscopy has been applied in supplement to the RFA, XRD, XPS and TEM measurements for the differently-synthesized Pt-Ru catalysts. Both the Pt L_3- and the Ru *K*-edge were measured, according to the details given in the experimental section, and the data obtained compared for all catalysts in the as-synthesized state. The main objective of these studies was to confirm the previous findings on the different extent of alloy formation in the catalysts. Hence, a specific evaluation method, published first by Russell et al. [137], was found to meet the requirements best, as it is in particular suitable in giving evidence of alloy formation by mere comparison of the results in *k* space. However, it should be stressed that it acts as a qualitative indication of alloy formation only and is not comparable with criteria like atomic distances *r* and coordination numbers *N*, that are usually applied for the description of the respective short-range order.

According to Russell et al. [137], the spectra were conventionally processed via the steps of energy calibration, normalization and conversion from the *E*- to the *k*-range to obtain the $\mu_0(k)$, using the WINXAS 2.1 software by T. Ressler [166]. In *k* space, the differences between an alloy and separate phases are best visible, as for alloyed systems a "dip" occurs in the curve in the range of 8 to 10 $Å^{-1}$. This corresponds to an additional nearest neighbor distance visible after Fourier transformation, namely the Pt-Ru first-shell contribution. The evaluation procedure is schematically shown in figure 5.14.

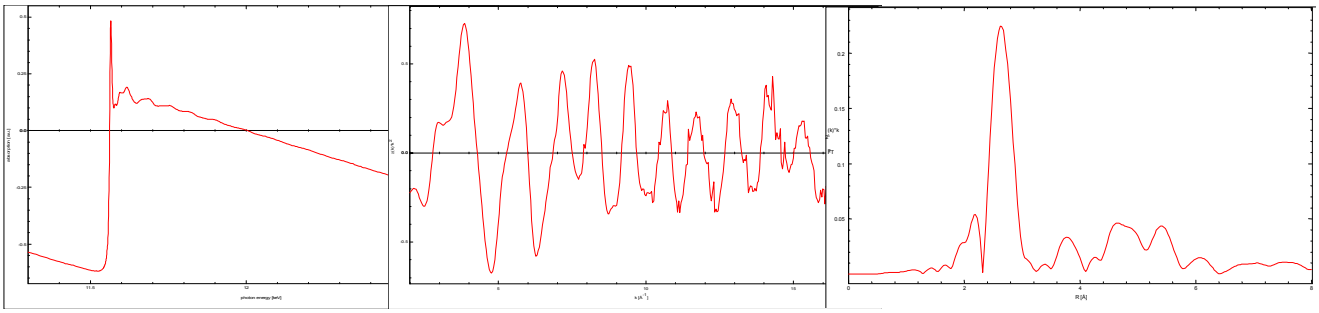

<u>*E* range</u>: *E* vs *I* <u>*k* range</u>: *k* vs χ(k) <u>Fourier transformation</u>: *R* vs FT(χ(k))

Fig. 5.14 Schematic representation of the evaluation procedure

In fig. 5.15, the spectra of the different as-synthesized Pt-Ru catalysts at the Pt L_3-edge and their evaluation is presented. As sample III and the commercial catalyst show the same behavior, only the data of the E-TEK catalyst is represented. The same is valid for samples I and II (only sample II is shown).
It becomes evident at once that the commercial catalyst and sample III exhibit the characteristic "dip" (marked by an arrow), indicating an alloy formation in these systems. In contrast to this result, neither sample I nor sample II show any indication of a local minimum in the envelope. Hence, even if this procedure is not quite accurate, it has been a rather convincing proof of the presence of separate Pt and Ru phases in sample I and II, while the E-TEK and the *Bönnemann* catalyst (sample III) are at least partially-alloyed.

a) b)

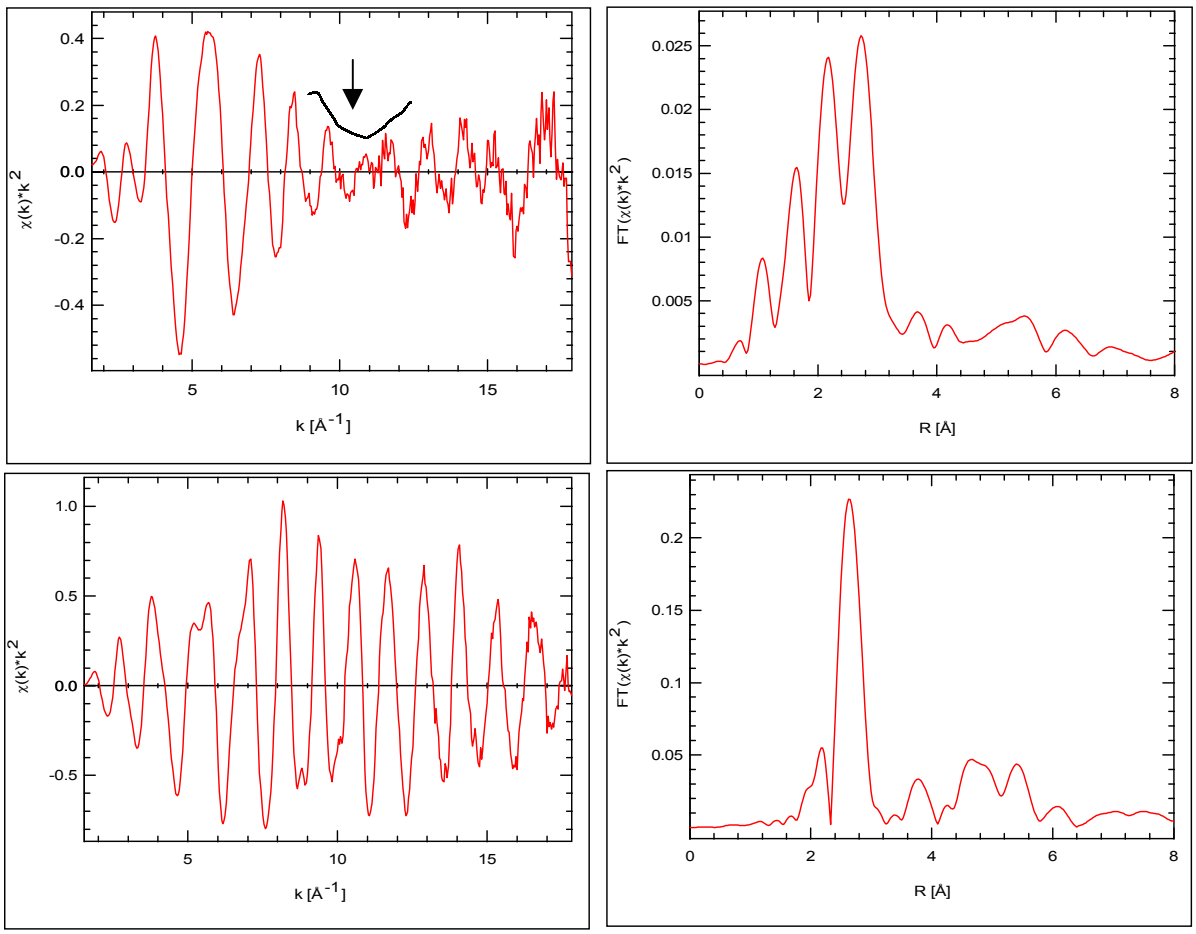

c) d)

Fig. 5.15 Comparison of the commercial Pt-Ru catalyst (in *k* space (a) and its FT (b)) and sample II (in *k* space (c) and its FT (d))

Measurements at the Ru *K*-edge were performed in order to confirm the previous results at the Pt L_3-edge. However, as can be easily seen in fig. 5.16, the oscillatory part of the spectra is not very pronounced and reaches not further than 6 $Å^{-1}$ in *k* space. In contrast to this, a commercial carbon-supported pure ruthenium catalyst, purchased from E-TEK inc., with an average particle size of 8 nm exhibits the typical spectrum of a bulk ruthenium phase. Therefore, it has been concluded that the ruthenium particles in the binary catalysts have particle sizes too small for EXAFS analysis. The average number of nearest neighbors is even not sufficient to contribute to a characteristic short-range order. Consequently, the Ru *K*-edge spectra of the different Pt-Ru catalysts were not evaluated according to the evaluation method of Russell et al. [137].

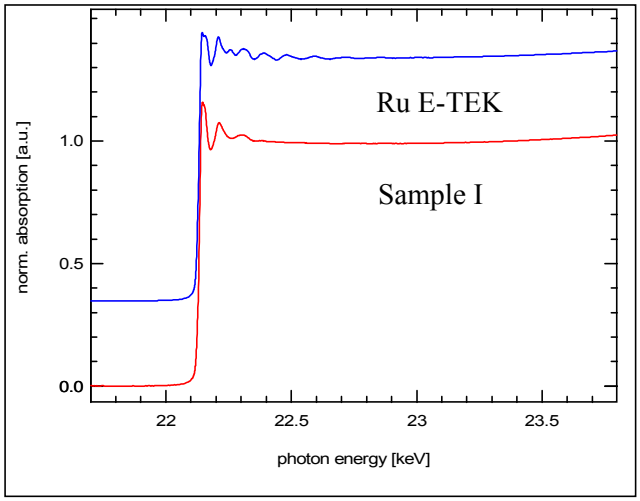

Fig. 5.16 Ru *K*-edge spectra for sample I and a commercial pure ruthenium catalyst (E-TEK inc.)

A simple structure model of the different catalysts

In the following paragraph, the results, obtained by the combination of spectroscopic, microscopic and diffraction techniques, will be summarized. On the basis of these findings, a simple structure model will be deduced.

By comparison of XRD and TEM / nano-EDX data of the catalysts in the as-synthesized state and after heat-treatment under air and nitrogen atmosphere, marked differences have been found. After heat-treatment in nitrogen, the E-TEK catalyst is the only one, that does not show any indication of ruthenium reflections in addition to the platinum fcc pattern. In the TEM images, homogeneously dispersed nanocrystallites were resolved and the EDX results showed both platinum and ruthenium all over the TEM grid. Hence, the commercially-available catalyst is believed to consist of a nanosized Pt-Ru alloy. This finding has also been confirmed by ex-situ EXAFS measurements.

Although the *Bönnemann* catalyst (sample III) appears quite similar in TEM, showing homogeneously-dispersed nanocrystals on the support and a homogeneous distribution of platinum and ruthenium in nano-EDX, significant differences are visible by XRD, as after heat-treatment in flowing nitrogen ruthenium reflections show up. The EXAFS data, however, indicate at least a partial alloy formation by a less pronounced "dip" in the curve in *k* space. Hence, the *Bönnemann* sample is assumed to consist of Pt-Ru nanoparticles, that form a not very "well-mixed" alloy, as this phenomenon is described by Russell et al. [137], but not completely separated Pt and Ru phases.

The two catalysts, synthesized by reduction in aqueous phase (samples I and II), have a completely different appearance in TEM compared with the other catalysts. The platinum nanoparticles show an average particle size of 7 nm and 9 nm, respectively, and tend to form agglomerates of approximately 20 nm in size. The agglomerates differ in shape, due to the reaction conditions (*t*, *T*, pH) in the respective synthesis. X-ray diffraction after heat-treatment in nitrogen flow revealed distinct ruthenium reflections. These results were confirmed by subsequent EXAFS investigations, indicating the presence of separate platinum and ruthenium phases. However, X-ray diffraction and TEM after heat-treatment in air

uncovered even differences between samples I and II. Thus, for sample I approximately 20 nm-sized ruthenium oxides of a characteristic stick-like shape were formed, whereas in sample II large platinum particles are surrounded by very small ruthenium oxide and still ruthenium nanocrystallites. It is assumed that the observed differences arise from features, already present in the as-synthesized samples.

In figure 5.17, a simple structure model, which is deduced from the measurements presented, is shown.

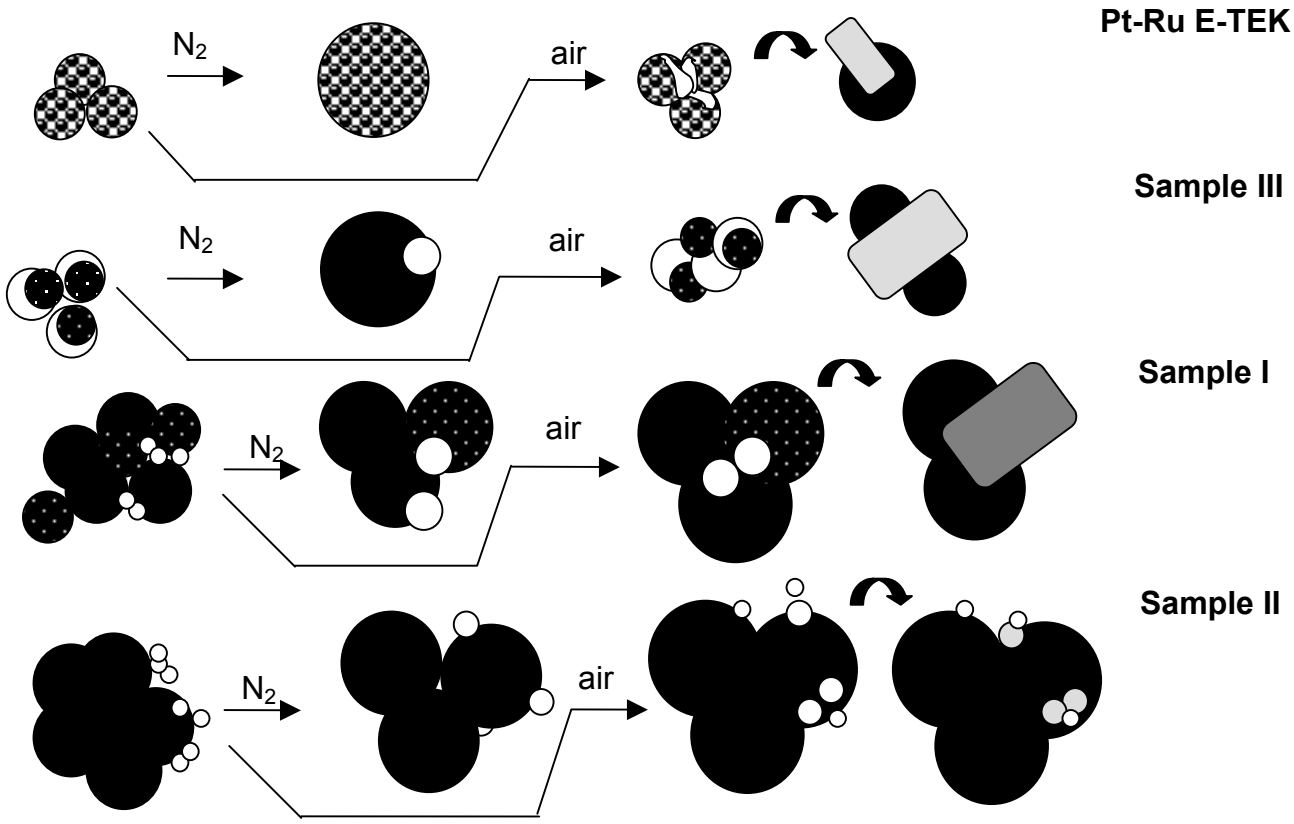

Fig. 5.17 Proposed structure models of the differently-synthesized catalysts
= Pt-Ru alloy, ■ = Pt, □= Ru, ▒ = ruthenium oxide, → = approx. 2 nm

Commercial catalyst:

As-synthesized	"well-mixed" alloy
After flowing nitrogen	only particle growth occurs; because of the stochastic distribution of ruthenium on platinum sites, no driving force for segregation appears
After atmosphere	since ruthenium is more easily oxidized than the more noble platinum, this seems to be the driving force for ruthenium segregation to the particle surface and subsequent oxidation to a ruthenium oxide species

Sample III, Bönnemann catalyst:

As-synthesized	rather inhomogeneous alloy, pure ruthenium zones within the particles
After flowing nitrogen	pure ruthenium zones present the driving force for the formation of quite large ruthenium particles, that separate from the "alloy" crystallites
After atmosphere	large Ru oxide aggregates are formed

Sample I, reduced by formaldehyde:

As-synthesized	separate phases (estimation: crystalline Ru < 10 %); platinum (+Ru) agglomerates with nearby small ruthenium nanoparticles
After flowing nitrogen	pronounced particle growth for the ruthenium phase
After atmosphere	large Ru oxide aggregates with oxygen deficiency are formed

Sample II, reduced by hydrazine:

As-synthesized	separate phases (estimation: crystalline Ru > 25 %); platinum agglomerates surrounded by small ruthenium nanoparticles
After flowing nitrogen	only little particle growth for the ruthenium phase, probably due to the wide-spread distribution of ruthenium within the carbon support
After atmosphere	small Ru oxide particles (Ru:O = 30:70 corresponding to RuO_2) and Ru nanocrystallites are found

5.1.2 Characterization of the MEAs

As fuel cell measurements are very sensitive to changes in the MEA morphology, which arise from differences in the preparation process, the resulting membrane-electrode structure has been characterized for several MEAs with different anode catalysts, using AAS, BET and SEM. Crucial parameters are among others the pore size, the pore size distribution and the actual metal loading, that might change during real cell operation. However, it was not possible to compare the same MEA before and after fuel cell measurement, as the methods, chosen for the MEA characterization, were destructive.

Atomic absorption spectroscopy

AAS measurements were applied to determine the actual platinum loading of the membrane electrode assembly. In order to monitor variations of the platinum loading between edge or center regions, three pieces with an accurately defined area were cut of different regions, but no systematic changes were observed within the limitations of the method. This procedure has been applied to three membrane electrode assemblies, and the results were compared. The actual platinum loading was found to be quite reproducible, amounting to 0.4 ± 0.1 mg/cm^2. The error has to be estimated, as the accuracy of the measurement depends mainly on the MEA cutting and the preparation of the platinum solutions, whereas the instrumental error is negligible. Hence, the resulting inaccuracy of the measurements is rather large, but provides at least a rough criterion for the quality of the chosen preparation procedure. It can be

concluded that the spraying process, chosen for the MEA preparation, is an appropriate method, yielding a reproducible and quite homogeneous platinum loading at the electrode.

BET analyses

Additional information on the MEA morphology can be obtained by measuring the average pore size and the pore size distribution, using the BET method. However, this technique proved to be not very well-suited for the MEA measurements, as it is only applicable for pore sizes in the range from 2 to 50 nm. Figure 5.18 shows a typical adsorption isotherme, that is obtained for a sprayed membrane electrode assembly with Pt-Ru E-TEK as anode catalyst.

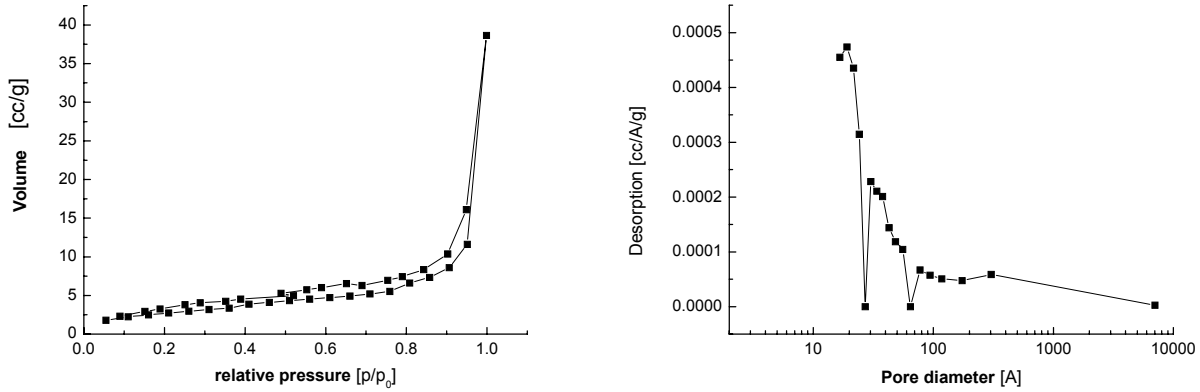

Fig. 5.18 Typical isotherme for a sprayed MEA and the corresponding pore size distribution

Several MEAs were checked and exhibited the same behavior: no peak is observed within the accessible range, corresponding to pore sizes either below 2 nm or above 50 nm or both. It is assumed that small pores are mainly situated in the polymer material, while larger pores appear in the electrode structure. In addition to the pore size and pore size distribution, the specific surface area has been calculated. It varies between 0.5 and 5 m^2/g and is obviously dependent on the ink composition and the final heating process of the finished MEA. Different catalysts applied at the anode do not show any significant effect on the resulting MEA structure. However, although the BET method is unable to provide a detailed insight into the apparent pore structure, it is nevertheless suitable to control the MEAs quality. As long as no significant changes occur in the measured isotherms, reproducible MEA structures are obtained by the respective preparation process.

Scanning electron microscopy

Secondary electron (SE) images of the MEA surfaces and the respective cross-sections were taken at several magnifications in order to achieve an idea of the membrane-electrode composite structure as well as a more detailed impression of the cohesion of individual support grains. In this context, the structure of

the three-phase boundary plays an important role for a good electrocatalytic performance in the fuel cell. However, structures as small as the nanoparticles on the carbon support grains could not be imaged, as the resolution of the microscope is limited to about 5 nm. Even in (400000 x) magnification, no indication of the crystalline nanoparticles has been found, due to the inadequate resolution of the SEM.
In figure 5.19, top view SEM images of a MEA with Pt-Ru E-TEK at the anode are shown, while in fig. 5.20 a typical cross-section is presented.

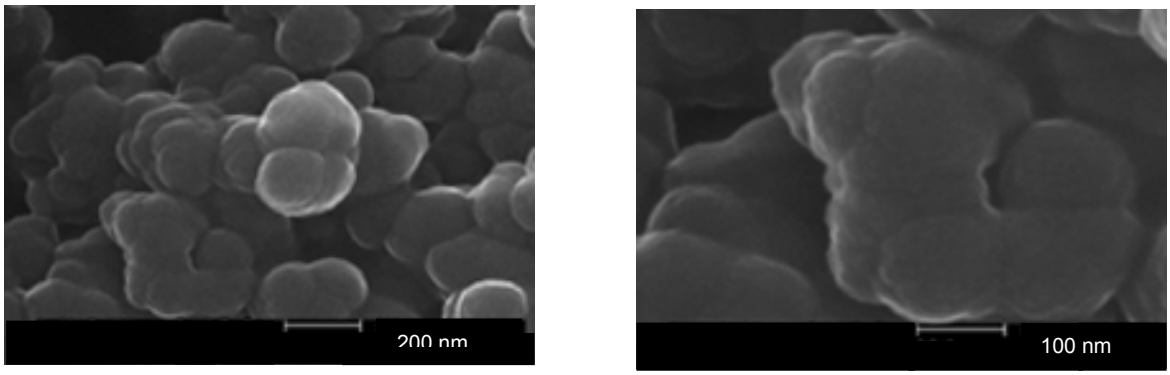

Fig. 5.19 Top view SEM images of a typical sprayed MEA in two magnifications

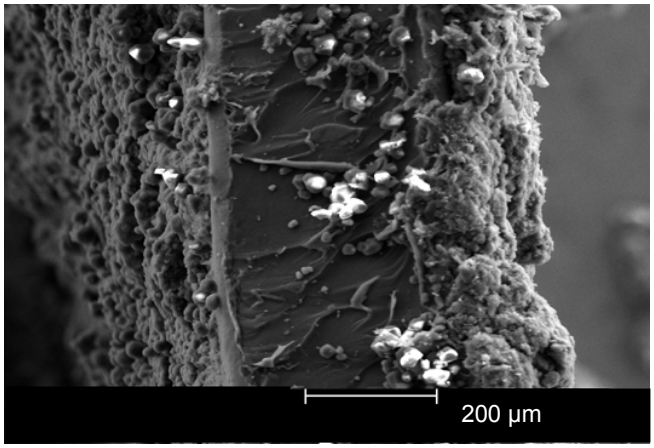

Fig. 5.20 Typical MEA cross-section

The sandwich-like structure of both electrode layers and the Nafion© membrane is clearly visible in the image. Both electrode layers are approximately 30 µm thick, while the thickness of the membrane amounts to about 150 µm. In general, the electrode layers appear rather homogeneous, despite their high porosity. In some spots, the Nafion© ionomer solution, that is mixed with the catalyst powder to obtain a highly fluid ink, forms cobweb-like threads between the carbon support grains.
The results presented above are the first attempt of a comprehensive investigation of MEA structures, obtained by the spraying method originally developed by Gottesfeld et al. [168]. It has been shown by a combination of AAS, BET and SEM measurements that the chosen preparation procedure is quite reproducible and yields a constant MEA quality. The MEA structure obtained is obviously mainly dependent on the preparation technique, the ink composition and the final heating process of the finished MEA, whereas different catalysts applied at the anode do not show an apparent influence.

5.2 Measurement of the electrocatalytic activity

The electrocatalytic activity of the differently-synthesized binary Pt-Ru and the ternary Pt-Ru-W catalysts has been checked by both single cell measurements and cyclic voltammetry. The obtained results were compared to measurements at a commercially-available carbon-supported Pt (20 wt.% on Vulcan XC 72) and a carbon-supported Pt-Ru catalyst both purchased from E-TEK inc. as reference materials. In the following section, the influence of the catalysts specific structure on the electrocatalytic performance will be investigated in detail in order to get a deeper insight into the apparent structure-properties correlation.

5.2.1 Single cell measurements

The different binary and ternary catalyst systems were tested in single cell measurements, closely resembling operation in real fuel cells under realistic conditions. Moreover, the extreme case of a non-alloy system, a plain mixture of the commercial carbon-supported Pt and Ru catalysts (E-TEK) has been investigated. A detailed description of the measurement setup can be found in the experimental section, chapter 4.5.1. After a few days of short-circuit operation, using pure hydrogen as anode feed, three *E*/*i*-curves in hydrogen operation were recorded, in which usually a slight enhancement of the overall cell performance can be seen.
Then, after dosing 75 ppm CO into the hydrogen feed gas, the respective *E*/*i* curves were recorded. After each measurement, the fuel cell was operated under pure hydrogen again for at least 2 hours. The observed activity losses caused by severe CO poisoning were nearly completely reversible, so that only minor degradation was detected in the subsequent *E*/*i*-curve in hydrogen mode. Similarly to the measurements in pure hydrogen, three *E*/*i*-curves were recorded for a H_2/CO mixture, containing 75 ppm CO as well as for a H_2/CO mixture with 150 ppm CO. Exemplary, *E*/*i* curves for the commercial Pt-Ru catalyst and Pt-Ru sample I, in hydrogen and H_2/CO operation are shown in figure 5.21 a) and b).

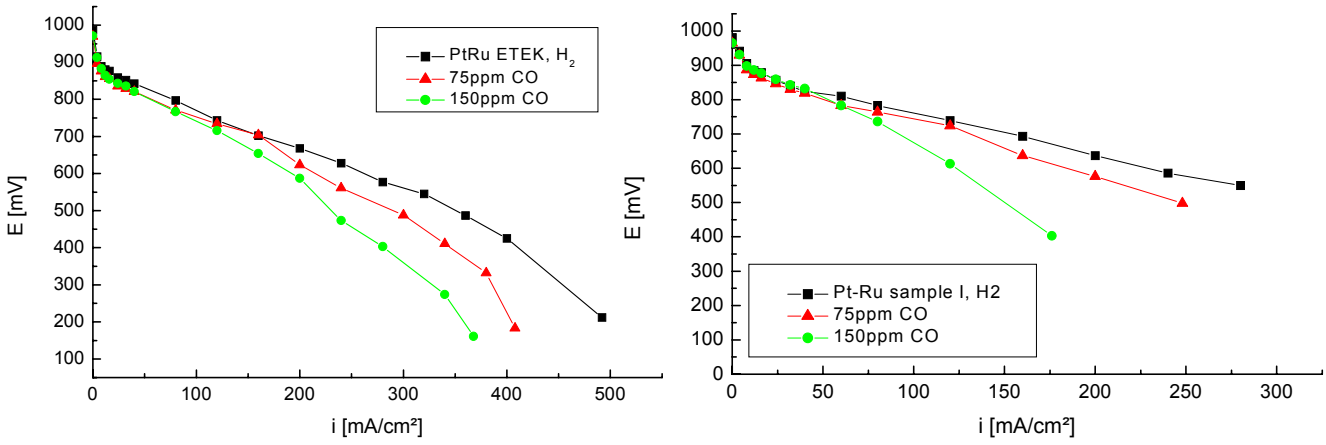

Fig. 5.21 *E*/*i* curves for Pt-Ru E-TEK (a) and Pt-Ru sample I (b), 0.4 mg/cm^2 metal loading, T = 75°C, in hydrogen and H_2/CO operation

The results, summarized in table 5.10 for all catalysts, were the corresponding last runs averaged for three MEAs.

Table 5.10 Results of the single cell measurements: *i* [mA/cm²] at 600 mV (A), normalized to the value in pure hydrogen at 600 mV (B) (see experimental), averaged over three MEAs

Sample	**Particle size** [nm]	**H_2** i_{H2} [mA/cm²] at 600 mV	**75 ppm CO** i [% of i_{H2} at 600 mV in H_2 operation]	**150 ppm CO** i [% of i_{H2} at 600 mV in H_2 operation]
Pt E-TEK	4	231	36	30
Pt-Ru E-TEK	2	256	79	76
Pt-Ru sample I	7	228	81	54
Pt-Ru sample II	9	190	90	52
Pt-Ru-W (1:1:1.5)	< 2	247	94	83
Pt-Ru-W (1:1:2)	< 2	252	67	44
Pt/Ru mixture*	-	252	79	-

* the plain mixture has only been measured twice; thus, the value is not representative

The current densities at 600 mV for the oxidation of pure hydrogen vary slightly, due to either the different particle size in the various catalysts or differences in the MEA structure. As the MEA characterization, reported above, did not indicate significant differences between individual membrane-electrode assemblies, it is rather believed that the variations in hydrogen operation arise from the different particle sizes. According to this assumption, the current densities for the oxidation of pure hydrogen increase with decreasing particle size and increasing surface area (table 5.10). Hence, all results, using H_2/CO mixtures, were normalized to the respective values at 600 mV in hydrogen (for details see experimental) to take into account this structure influence.

A graphical representation of the different electrocatalytic activities in H_2/CO operation is given below (compare with table 5.10). The horizontal line marks the respective value measured at the Pt-Ru E-TEK catalyst, which was applied as reference material. The order of the different catalysts is the same as in the table above. The last bar represents the result of the plain Pt/Ru mixture, that has been tested only for the low CO concentration.

In figure 5.22, the values using 75 ppm CO in the anode feed gas are shown, whereas in figure 5.23 the results obtained for the H_2/150 ppm CO mixture are presented.

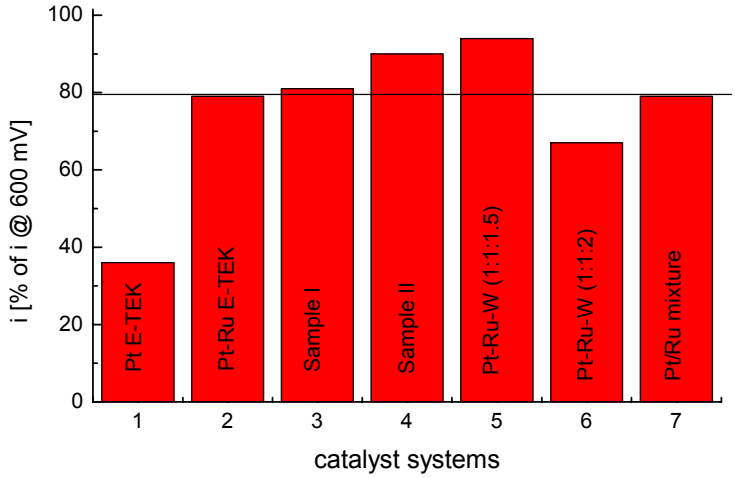

Fig. 5.22 Graphical representation of the electrocatalytic activities of the different catalysts, using a H_2/CO mixture with 75 ppm CO

Without an exception, for all binary and ternary catalysts checked higher activities were found than for pure platinum. For low CO contents, the binary catalysts, sample I and II, and the ternary Pt-Ru-W (1:1:1.5) show higher activities than the Pt-Ru E-TEK catalyst. For the plain Pt/Ru mixture, an electrocatalytic activity comparable to that of the Pt-Ru reference has been found.

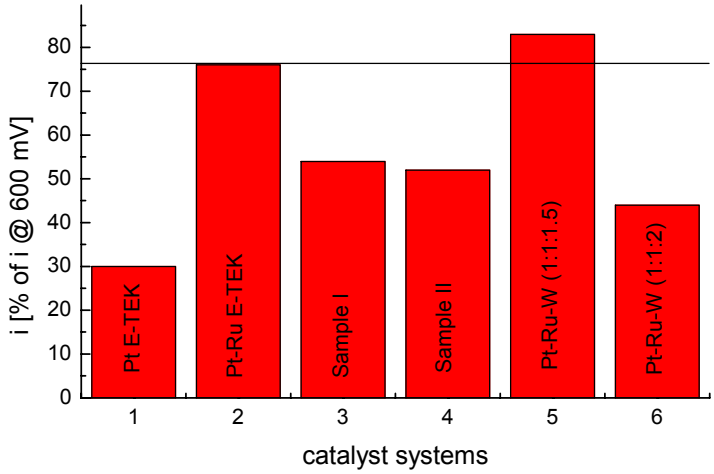

Fig. 5.23 Graphical representation of the electrocatalytic activities of the different catalysts, using a H_2/CO mixture with 150 ppm CO

However, using H_2/CO mixtures with 150 ppm CO, mostly rather poor results have been obtained (see fig. 5.23). Although the pure Pt catalyst has been surpassed by samples I and II, only the ternary (1:1:1.5) system seems to perform significantly better than the binary Pt-Ru reference. Pt-Ru-W (1:1:2) exhibits lower current densities than the binary reference catalyst in both modes.
This is in good agreement with previous measurements by Götz [169] and Krause [176] in the respective system. As the Pt-Ru-W (1:1:1.5) and (1:1:2) composition seem to be the limiting cases, the former displaying the highest and the latter showing the lowest electrocatalytic activity in the investigated ternary Pt-Ru-W systems (see also [169, 176]), in the following part of this work only the results of these two catalysts will be reported.

Finally, all MEAs were tested in methanol operation, using an aqueous 1 M CH_3OH solution in H_2O, that is vaporized and fed into the cell by a nitrogen stream. The corresponding CO concentration in the anode feed amounts to approx. 170 ppm. Prior to the measurement, the fuel cell was held for at least 2 hours at short-circuit in pure hydrogen in order to regain the performance before CO poisoning. As an example for the measurements in methanol operation, the *E*/*i* curves of the commercial Pt-Ru catalyst, sample I and a pure platinum catalyst purchased from E-TEK inc. are shown in comparison in fig. 5.24. It is obvious that anodic methanol oxidation is a reaction not quite as efficient as the hydrogen oxidation reaction for fuel cell applications, yielding short-circuit potentials of only 0.6 V compared to 1.0 V for pure hydrogen (see chapter 2.2).

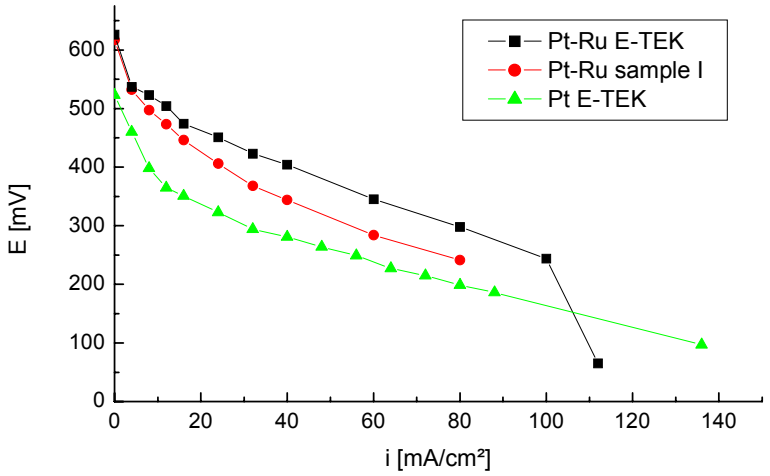

Fig. 5.24 *E*/*i* curves for Pt-Ru E-TEK, sample I and Pt E-TEK, 0.4 mg/cm^2 metal loading, T = 90 °C, methanol operation

Results of all catalysts in methanol operation are summarized in table 5.11. As is clearly visible, only the performance of the ternary Pt-Ru-W (1:1:1.5) catalyst surpasses that of the reference system, while Pt-Ru-W (1:1:2) and sample I show electrocatalytic activities comparable to the commercial catalyst. However, despite its excellent activity for the oxidation of H_2/75 ppm CO mixtures, sample II exhibits a rather poor performance in methanol operation, which is similar to the pure platinum catalyst.
It is assumed that this behavior is due to the large platinum particle sizes of about 9 nm. Thus, large regions within the catalyst resemble the pure platinum catalyst and only a little contact area between Pt

and Ru "zones" is present. The same explanation would hold for sample I, but in this case the predominantly Pt-like parts are smaller (7 nm), so that this effect is less important.
For the plain Pt/Ru mixture a performance slightly better than that for sample II has been observed, probably due to the smaller sizes of the catalytic active particles and the thereby increased contact area between the Pt and the Ru phases.

Table 5.11 Results of the single cell measurements in methanol operation: values at 400 mV, normalized to the value in pure hydrogen at 400 mV, averaged over at least two MEAs

Sample	**H_2** i_{H2} [mA/cm²] at 400 mV	**1 M CH_3OH** i [% of i_{H2} at 400 mV in H_2 operation]
Pt E-TEK	231	3
Pt-Ru E-TEK	256	*16*
Pt-Ru sample I	228	11
Pt-Ru sample II	190	5
Pt-Ru-W (1:1:1.5)	247	**22**
Pt-Ru-W (1:1:2)	252	13
Pt/Ru mixture*	252	7

* the plain mixture has only been measured twice; thus, the value is not representative

In summary, all binary and ternary catalyst formulations checked in single cell measurements have shown higher activities than the pure platinum reference system. Even the plain Pt/Ru mixture exhibits better performance in both H_2/75 ppm CO and methanol operation.
For only minor concentrations of CO in the anode feed, Pt-Ru samples I and II and Pt-Ru-W (1:1:1.5) surpass the commercial Pt-Ru catalyst in activity. However, using either H_2/150 ppm CO or 1 M methanol, only the Pt-Ru-W (1:1:1.5) catalyst exhibits a higher activity than the commercial Pt-Ru catalyst, while sample I and Pt-Ru-W (1:1:2) are in the same range as the reference. In contrast to the satisfactory results using H_2/CO mixtures, sample II shows only poor activity in methanol operation, probably due to the comparatively large zones of pure platinum within the sample.

5.2.2 Cyclic voltammetry (CV)

Another method to investigate the electrocatalytic activities of the catalysts is cyclic voltammetry in a conventional three-electrode electrochemical cell. Compared with the single cell measurements, it has mainly two advantages: fast data acquisition and comparatively simple instrumental setup. However, the interpretation of the obtained voltammograms is often rather complicated. Thus, CV is mainly carried out for screening purposes in multinary systems of various stoichiometries in order to get a quick clue on the electrocatalytic activity of the respective catalysts. In case a specific catalyst formulation shows promising CV results, it might then be tested in more time-consuming single cell measurements. Usually, this presents a reasonable procedure, provided that temperature does not play an important role for the corresponding electrocatalytic activity, as the CV measurements were conducted at RT, whereas the single cell measurements were performed at elevated temperatures. Additional differences between the two methods are the electrode structure (area, thickness, characteristic three-phase boundary) and its specific preparation as well as the supply of the oxidants (methanol as liquid or as gas). Nevertheless, CV measurements allow conclusions on the electrocatalytic activity under fuel cell-relevant conditions, as has been shown among others by Götz [169].

Cyclic voltammetry in 0.1 M and 1 M methanol

In figures 5.25 and 5.26, the voltammograms of Pt-Ru samples I and II and the reference system adding 0.1 M methanol and 1 M methanol, respectively, to the supporting electrolyte are shown exemplary. Because of the correlation between the observed current and the specific surface area of the respective catalyst, the different sizes of the catalytic active metal centers have to be taken into consideration. Therefore, the specific surface areas of the catalysts were calculated, assuming spherical particles and using the average particle size determined by X-ray diffraction. According to this estimation, the specific surface area amounts to approximately 140 m²/g for the commercial catalyst and to about 60 m²/g for samples I and II. In fig. 5.25 b and 5.26 b, the effect of the different specific surface areas is considered.

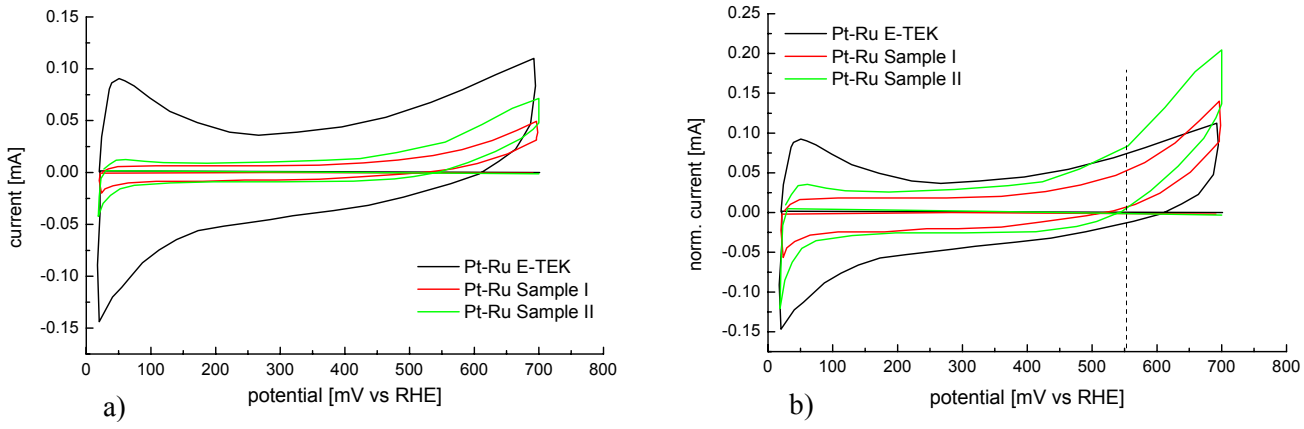

Fig. 5.25 a) Voltammograms of the different Pt-Ru catalysts, adding 0.1 M methanol to the supporting electrolyte ($HClO_4$) at RT, sweep rate 5 mV/s
b) specific surface area is considered

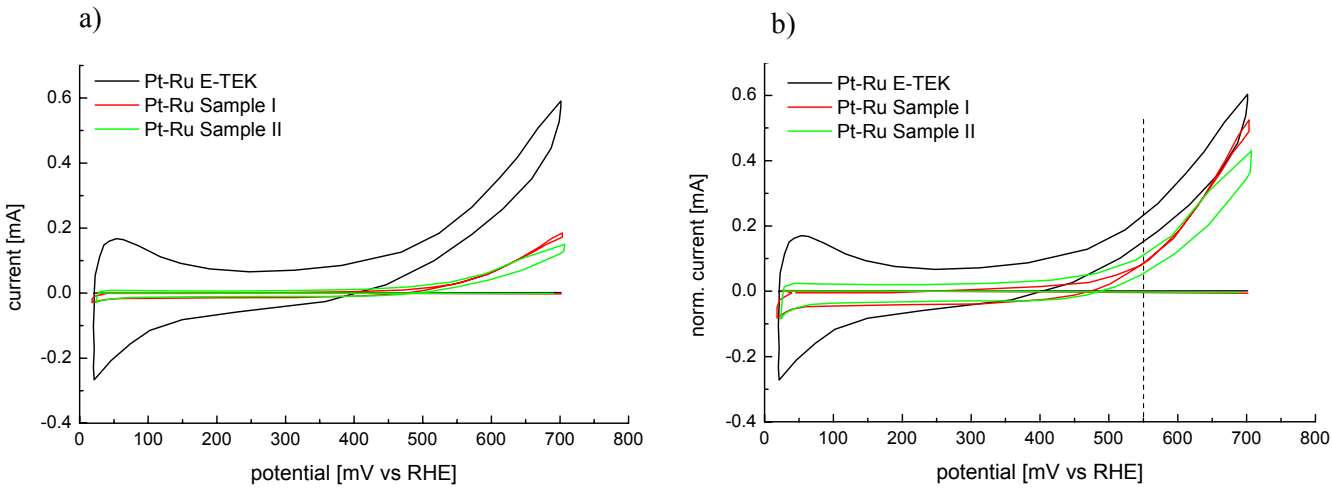

Fig. 5.26 a) Voltammograms of the different Pt-Ru catalysts, adding 1 M methanol to the supporting electrolyte ($HClO_4$) at RT, sweep rate 5 mV/s
b) specific surface area is considered

As already explained in the experimental section (chapter 5.2.6), the data obtained were evaluated with regard to two parameters: a) the onset of the oxidation wave, defined as the potential at which 5% of the current value at 0.7 V vs RHE were reached and b) the current density at an arbitrarily chosen potential of 550 mV vs RHE. In the following text, all potentials are referred to the reversible hydrogen electrode (RHE). In table 5.12, the obtained onset potentials of all catalysts under investigation will be given.

Table 5.12 CV measurements in 0.1 M and 1 M methanol: onset potentials for all catalysts

Sample	**Onset, 0.1 M** [mV]	**Onset, 1 M** [mV]
Pt E-TEK	510	510
Pt-Ru E-TEK	360	410
Pt-Ru sample I	400	470
Pt-Ru sample II	380	440
Pt-Ru-W (1:1:1.5)	410	420
Pt-Ru-W (1:1:2)	420	430
Pt/Ru mixture	420	430

For the pure platinum catalyst, an onset potential of 510 mV has been observed, which does not change for the higher methanol concentration. In the binary systems, ruthenium addition lowers the onset potential of the methanol oxidation by approximately 100 mV. The lowest onset potential has been found for the commercial Pt-Ru catalyst, whereas the ternary Pt-Ru-W systems and the plain mixture show less improvement. However, while for the binary Pt-Ru catalysts the onset potential increases with increasing methanol concentration, the Pt-Ru-W samples and the Pt/Ru mixture are less sensitive to higher CH_3OH contents comparable to the pure platinum catalyst.

In table 5.13, the currents and current densities at the arbitrarily chosen potential of 550 mV are summarized. In the marked columns, the calculated specific surface area has been considered (compare to fig. 5.25 b and 5.26 b). The bold numbers indicate results, that are comparable to the Pt-Ru reference material (marked in italics).

Table 5.13 Currents and current densities at a chosen potential of 550 mV, marked columns: the calculated specific surface area is considered

Sample	**i, 0.1 M** [mA]	**i_{sp}, 0.1 M** [norm., mA]	**i, 1 M** [mA]	**i_{sp}, 1 M** [norm., mA]
Pt E-TEK	0.006	0.009	0.07	0.08
Pt-Ru E-TEK	0.07	*0.07*	0.2	*0.2*
Pt-Ru sample I	0.02	0.05	0.03	0.09
Pt-Ru sample II	0.03	**0.08**	0.04	0.12
Pt-Ru-W (1:1:1.5)	0.07	**0.07**	0.2	**0.2**
Pt-Ru-W (1:1:2)	0.03	0.03	0.08	0.08
Pt/Ru mixture	0.03	0.04	0.05	0.06

For the low methanol concentration, Pt-Ru sample II and Pt-Ru-W (1:1:1.5) show satisfactory results, that were in the same range as the Pt-Ru E-TEK catalyst. Pt-Ru sample I, the Pt-/Ru mixture and the other ternary system were less active, but still much better than the pure platinum catalyst. After addition of 1 M methanol to the supporting electrolyte, only the Pt-Ru-W (1:1:1.5) sample exhibits an electrocatalytic activity comparable to the commercial Pt-Ru system, while all other catalysts show activities similar to that of the pure Pt catalyst. The Pt/Ru mixture is even worse than the pure platinum system from E-TEK. This might be due to reduced methanol adsorption, as methanol is not adsorbed at pure ruthenium surfaces. In the case of Pt-Ru samples I and II, consisting partly of separate Pt and Ru phases, the poor

activity for high methanol concentrations is probably due to the large platinum particle sizes, exhibiting the characteristic pure Pt properties. With increasing number and size of possible contact areas between the separate phases, the electrocatalytic activity increases. Nevertheless, the maximum number of Pt-Ru contacts is inherently preset by the characteristic catalyst structure and thus limited. It seems, as if for low methanol concentrations sufficient contact areas are provided, whereas for higher CH_3OH contents the restricted number of those zones is insufficient. Moreover, methanol dehydrogenation does not take place at pure ruthenium surfaces, and if this would be another rate-limiting step, dehydrogenation fragments might also block electrocatalytic active sites. In this respect, the balance between surface sites blocked by either OH- or CO/CH_3OH fragments and the distance between them seems to be the limiting factor of activity. This model should also hold for the plain catalyst mixture, being the extreme case of a non-alloy system.

CO-stripping experiments

In addition to the CV measurements in methanol, CO-stripping experiments have been carried out to check the CO adsorption and the CO oxidation capacity of the catalysts under investigation. First, pure CO gas was adsorbed at a potential of 0.05 V for a certain time. Then, the excessive CO was removed from the electrolyte by purging nitrogen, before the voltammetric scan was started. Exemplary, the voltammograms for three different binary Pt-Ru catalyst systems in CO-stripping are shown in fig. 5.27. Similar to the previous CV measurements, the specific surface area of the respective catalysts has been taken into consideration (fig. 5.27 b).

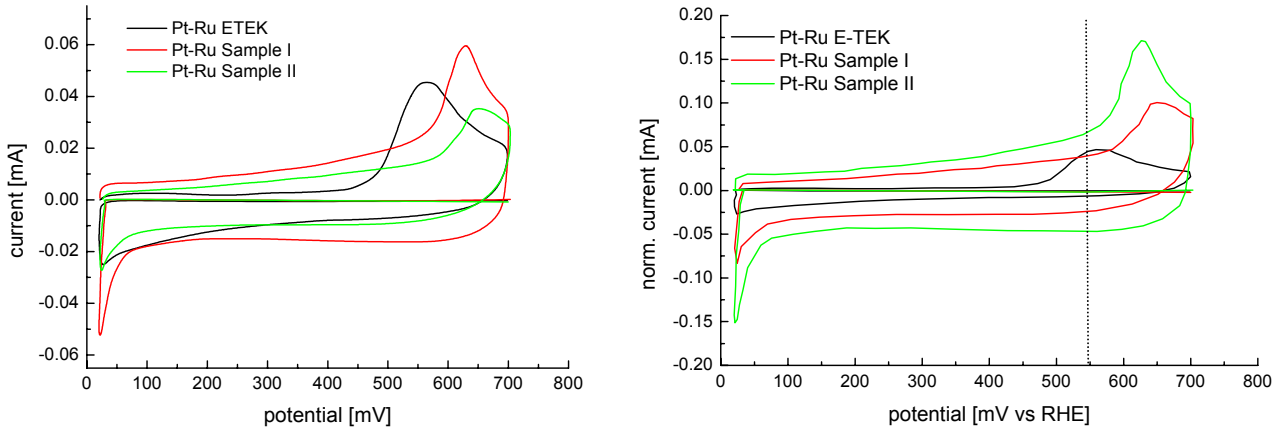

Fig. 5.27 a) Voltammograms of the different Pt-Ru catalysts, CO-stripping at RT, 5 mV/s
b) specific surface area is considered

A marked difference between the in-house synthesized Pt-Ru catalysts and the commercial Pt-Ru system can be seen at lower potentials, beginning at approximately 200 mV. CO-stripping data of samples I and II show an unusual and continuous increase of the current density in the region between approx. 0.2 V and 0.55 V, where apparently the CO oxidation peak begins. In contrast, for the commercial catalyst no indication of any oxidation activity can be seen before the actual onset of the oxidation peak at about 470 mV. This difference is attributed to the presence of pure ruthenium areas within the in-house

synthesized catalysts, as according to current literature the adsorption of oxygen-containing species on pure Ru already starts at potentials as low as 0.2 V. Ru thus facilitates the oxidation of CO to CO_2 at a significantly lower potential compared to Pt. Consequently, the maximum of the CO oxidation peak shifts to lower potentials on pure Ru. Additionally, the peak width increases indicating a minor intrinsic reaction rate constant for the reaction between both poisoning and oxygen species adsorbed on the electrode surface [28]. In table 5.14, the results of the CO-stripping experiments are listed.

Table 5.14 Onset potentials* and oxidation peak maxima of the different Pt-Ru catalysts

Sample	**Onset, CO** [mV]	**Maximum** [mV]	**Continuous increase**
Pt-Ru E-TEK	450	570	no
Pt-Ru sample I*	540	650	yes
Pt-Ru sample II*	500	630	yes
Pt-Ru-W (1:1:1.5)	480	700	no
Pt-Ru-W (1:1:2)	490	700	no

* for systems, in which a continuous increase of the current density between 0.2 and 0.5 V has been observed, the onset potential is defined as the value, where the slope changes significantly into the oxidation peak

Despite the early onset of an apparent oxidation activity for samples I and II, the maximum of the oxidation peak is found at much higher potentials than for the commercial catalyst. One explanation for this specific behavior might be the limited number of metallic Ru sites in contact to Pt particles in the in-house synthesized catalysts, so that the specific Pt characteristics dominate the voltammograms at higher potentials.
In contrast to the binary Pt-Ru systems, the ternary Pt-Ru-W catalysts display a remarkably higher capability for CO adsorption corresponding to extremely high oxidation peak currents. The amount of adsorbed CO is even so high that more than one scan (usually up to three) is needed to free the whole catalyst surface from the poisoning species.

Comparison of CV results and single cell measurements

In principle, the CV results for high methanol concentration are in good agreement with the single cell measurements in methanol operation. It has been confirmed by both techniques that the ternary Pt-Ru-W

(1:1:1.5) catalyst exhibits the highest activity followed by the commercial Pt-Ru catalyst. The other catalysts and the Pt/Ru mixture show rather poor performances, using high methanol concentrations. In accordance with the CO-stripping data, samples I and II display an improved activity in real fuel cell operation with H_2/CO mixtures, containing only 75 ppm of CO impurities. However, single cell measurements showed that this holds only for low CO concentrations, while for higher CO contents less satisfactory results were obtained.

In general, catalysts with partly separate Pt and Ru phases show the highest activities for low CO and methanol concentrations. This might be due to the characteristic properties of the pure metals, that are maintained in these non-alloy catalysts. However, increasing the amount of poisoning species in the feed up to 150 ppm CO and 1 M methanol, respectively, causes a drastic loss in activity. It is assumed that in this case increased poisoning occurs, as only a rather limited number of Ru sites, facilitating the adsorption of oxygen-containing species, is available. Moreover, in methanol operation the dehydrogenation activity of the catalysts plays an important role for the resulting performance. Since methanol is not adsorbed or at least not fragmented on pure ruthenium sites, lower activities might be obtained.

Current vs time curves recorded in 1 M methanol

Additionally to the voltammetric scans, current vs time measurements in 1 M methanol were conducted at room temperature by a potential stepping technique. The experimental procedure is described in detail in chapter 4.2.6. During the first seconds after the potential step, a sharp current decay can be seen (not shown). Then, the current increases or decreases slightly with time, depending on the applied potential. This characteristic behavior is exemplary shown for the ternary Pt-Ru-W (1:1:1.5) catalyst in fig. 5.28.

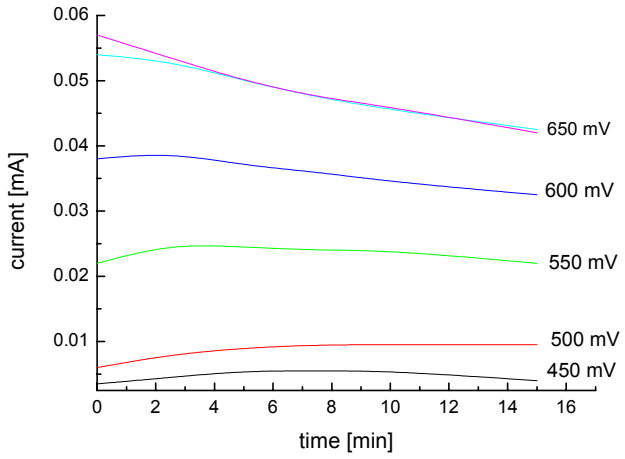

Fig. 5.28 Current vs time curves for Pt-Ru-W (1:1:1.5), adding 1 M methanol to the supporting electrolyte

In general, the course of the current vs time curves reveals marked differences between the different catalysts. For instance, at 600 mV the commercial Pt-Ru catalyst still displays a current increase during

the first few minutes. In contrast, for sample I a decrease in current is observed even at 450 mV. After approx. 5 min, the obtained currents remain nearly constant for all catalysts. The differences observed might be due to restructuring of the catalysts by processes like particle growth or oxidation and reduction reactions. However, experimental evidence of such processes can only be obtained by 'online' monitoring of the catalyst structure during electrochemical measurements. In this respect, it seems absolutely demanding to perform in-situ investigations in order to achieve a more detailed knowledge about possible structural changes in the catalyst during operation.

Besides the rather qualitative approach discussed above, the currents obtained just before the next potential step have also been recorded and drawn into *Tafel* plots (theoretical treatment, see section 2.3.1) in order to learn more about the respective electrode mechanisms (fig. 5.29).

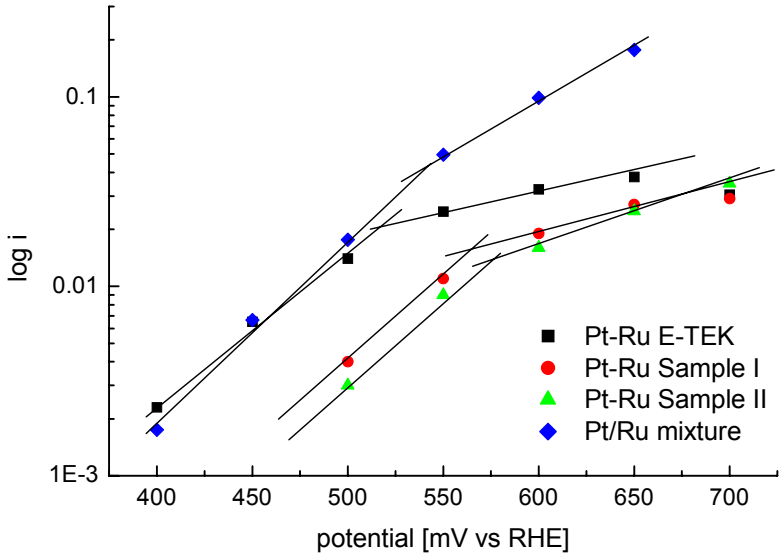

Fig. 5.29 *Tafel* plots for the different Pt-Ru systems

The obtained *Tafel* plots can be fitted by two lines with different slopes, that intersect at a potential of approximately 550 mV in all cases. The two slopes point to a change in the mechanism or at least a change in predominance of different processes. In the lower potential region (below 550 mV), the samples show rather similar slopes of about 110 mV per decade (*E-TEK*: 125 mV per decade, *samples I, II*: 110 mV per decade, *mixture*: 100 mV per decade), indicating similar behavior. At higher potentials, different slopes were found for each catalyst (*E-TEK*: 450 mV per decade, *samples I, II*: 325 mV per decade, *mixture*: 200 mV per decade). It is supposed that the predominant process below 550 mV corresponds to the methanol dehydrogenation activity, while the predominant process above 550 mV is assigned to the CO oxidation. Thus, the results obtained might be interpreted by rather similar methanol dehydrogenation activities for all catalysts, whereas the CO oxidation seems to be significantly affected by the number of neighbored Ru sites available.
However, a more detailed kinetic interpretation of the results is difficult, as the electrocatalytic oxidation of methanol is a very complex reaction involving the transfer of six electrons.

5.3 Investigations *during* operation

In the previous passages, results of the structural and electrochemical characterization of the different catalysts were reported. One aim of these investigations was to get a more detailed insight into the apparent correlation between the catalyst structure and its electrocatalytic activity. It has been evidenced that mainly the degree of alloying, the size of the electrocatalytic active clusters and their distance affect the resulting performance. However, as the catalyst structure was determined before operation and the electrocatalytic activity is measured during operation, the respective relationship has to take into account possible structural changes. Hence, in-situ investigations are of crucial importance for a correct evaluation of the data.
In the work presented, two different approaches have been adopted to monitor the catalysts during operation: in-situ XAS-single cell measurements and quasi in-situ CV/FTIRS studies. The in-situ XAS technique is almost comparable to fuel cell measurements in single cell arrangements, since the applied experimental setup remains essentially the same. Changes in the catalyst structure in dependence on the potential can be pursued by recording EXAFS spectra at different points of the measured *E*/*i*-curve. In contrast, quasi in-situ CV/FTIRS belongs to the spectroelectrochemical methods, as discussed in detail in chapter 2.3. FTIR spectra were either measured during a slow voltammetric scan (SPAIRS) or in potential-switch mode (SNIFTIRS) to monitor species nearby or adsorbed at the electrode surface.

5.3.1 In-situ XAS single cell measurements

The in-situ XAS-single cell measurements were conducted in a specially designed fuel cell in both hydrogen and methanol operation at the beamline X1, Hasylab, Hamburg (Germany). It has been decided to leave as many parameters untouched as possible to retain the original conditions in a real fuel cell. Hence, working temperatures and gas flows similar to those applied in previous single cell measurements were chosen. As described in detail in the experimental section, only the metal loading had to be increased up to at least 1.2 mg/cm^2 per electrode to obtain an optimum signal-to-noise ratio at the Pt L_3-edge in transmission. The investigations presented were carried out at two different membrane electrode assemblies (MEA I and MEA II) in order to verify the reproducibility of the experiments. Both of them were prepared by J. Scherer (ZSW, Ulm, Germany), using the spraying method. Pt E-TEK (20 wt.% on Vulcan XC 72) served as cathode catalyst in all cases, whereas Pt-Ru E-TEK (20 wt.% on Vulcan XC 72) was applied at the anode side.
During the in-situ studies, a conventional *E*/*i* curve was measured and spectra were recorded at the Pt L_3-edge at several points of the curve in the activation-, morphology- and diffusion-controlled regime (see fig. 5.7). The best results were obtained in perpendicular beam geometry, as already discussed in the experimental section. Therefore, only measurements in this specific geometry are shown in the following text.

Spectra of MEA I recorded at the Pt L_3-edge before operation, in hydrogen and methanol operation, were processed using WinXAS 2.1 [166], according to the procedure described in chapter 5.5.2. In figure 5.30, the resulting Fourier transforms of MEA I during operation at a current *I* of 2 A are represented and

compared to the same MEA before operation. The term “before operation” in this context means that the MEA is already mounted into the fuel cell, but at RT and without gas flow.

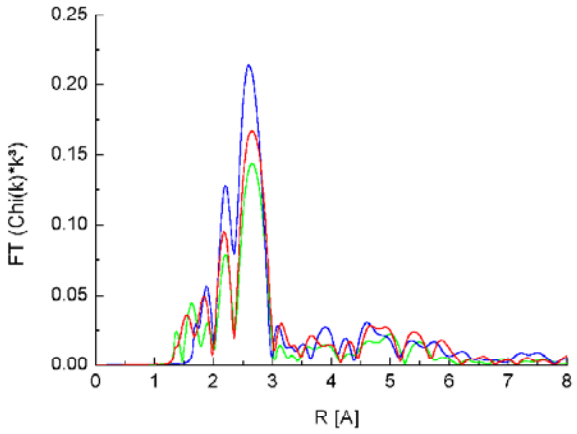

Fig. 5.30 Fourier transforms of MEA I at I = 2 A in hydrogen (■), in methanol (■) and before operation (■)

It is obvious that no evidence of any structural changes during operation was found by comparison of the Fourier transforms.

However, a great disadvantage of the perpendicular geometry is that anode and cathode side are monitored simultaneously. Thus, the results obtained can not be separated, unless either the Ru *K*-edge is investigated or the cathode side is removed in the beam window region. In the work presented, the second strategy has been adopted, since the ruthenium loading is not sufficient for an accurate measurement in transmission.

Hence, for the experiments at MEA II, the cathode side has been removed in the respective region prior to the measurements. In fig. 5.31, the results at different potentials in methanol operation (cathode partially removed) are shown.

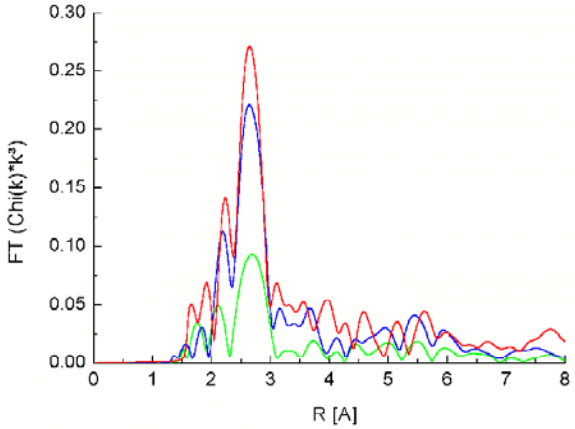

Fig. 5.31 Fourier transforms of MEA II (cathode partially removed) at I = 2 A (■) and I = 1 A in methanol operation (■) and before operation (■)

In agreement with the measurements at MEA I in hydrogen and methanol operation, also no structural changes occur at MEA II in dependence on the applied potential. The Fourier transforms obtained in the diffusion-controlled region look nearly identical to those of the activation-dominated regime.

Several possible reasons, why no significant changes appear in the spectra, neither during different operation modes nor at different potentials, might be discussed: First of all, either the catalyst structure is indeed insensitive to potential changes or merely those active sites change, which are situated within three-phase boundary regions. Since only a small share of all nanoparticles is present in those regions and XAS is a bulk method, it might be insensitive to these comparatively small changes. Moreover, it can not be excluded that the removal of the cathode side in the region of the beam window might modify the original current distribution in this part of the electrode to a far greater extent than assumed. Thus, the current in the respective electrode area might be rather different from the overall current.

It is obvious that in this special case simulation of the spectra and calculation of the *r* and *N* values will not lead to any essential insights. In consequence, a more phenomenological approach has been adopted by comparison of the normalized absorption spectra in *E* space (fig. 5.32).

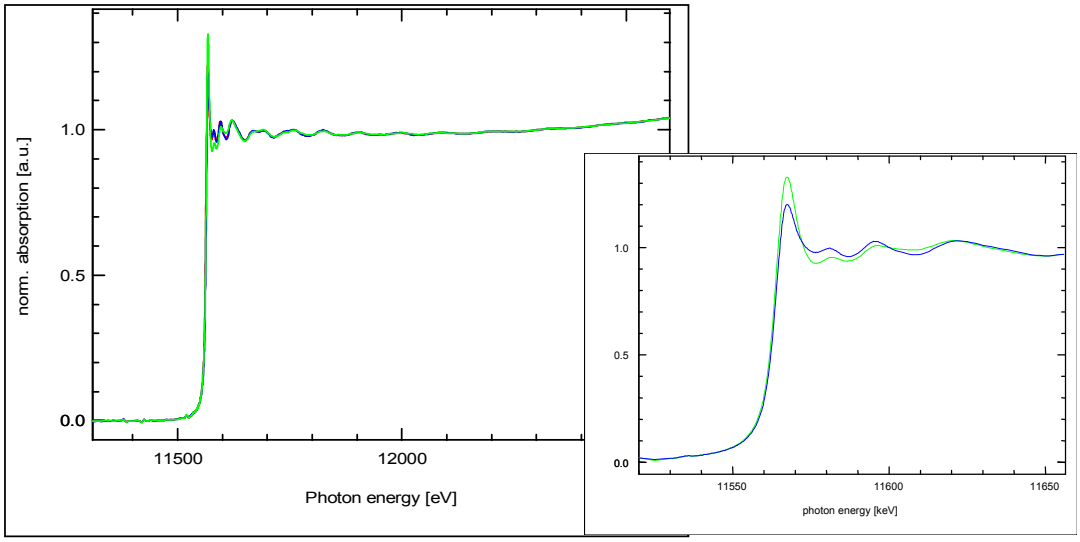

a) b)

Fig. 5.32 a) Comparison of the normalized absorption spectra for MEA II, before operation (■), in hydrogen (■) and methanol (■) operation
b) Closer look at the absorption edge

Although apparently no structural changes could be seen in the Fourier transforms of the MEAs under different conditions, analysis of the normalized absorption spectra in *E* space revealed significant differences in the respective white-line intensities. These are an indication for a different degree of oxidation before and during operation in hydrogen and methanol. In both operation modes, the white-line intensity decreases corresponding to a decrease in the oxidation state.
This is in good agreement with XANES measurements by O'Grady et al. [138], who compared spectra of commercial Pt-Ru fuel cell catalysts before and after operation with reference substances, e.g. Pt, Ru and

their respective oxides. They also found decreased white-line intensities for their catalysts, operated either at 100 mV in a conventional electrochemical cell or in a real fuel cell, that point to a reduction of oxide species during operation (see also chapter 3.1.4).

In summary, the feasibility of our in-situ approach, which applies XAS in transmission to a real fuel cell during operation, has been demonstrated. It is evidenced by comparison of the XAS spectra in *E* space that a commercial Pt-Ru anode catalyst becomes reduced in contact with hydrogen as well as methanol during real cell operation. In contrast, no significant structural changes showed up in the corresponding Fourier transforms, which reflect the respective short-range order of the catalysts.
However, one essential drawback of the chosen experimental setup with perpendicular geometry is the superposition of anode and cathode effects, since both electrodes are monitored at once. In this context, it is even more surprising that an overall reduction of the catalysts has been observed, although the cathode catalyst is in contact with pure oxygen. Another problem is the removal of the cathode side in the beam window region, which might modify the respective current distribution. Thus, the effect of different potentials will not be properly accessible by the chosen in-situ cell setup. According to the data presented above, it seems absolutely necessary to repeat the measurements at the Ru *K*-edge in fluorescence mode, as by this procedure only the anode catalyst contributes to the results and more definite findings are expected.

5.3.2 Quasi in-situ CV/FTIRS-investigations of the catalysts

In contrast to the in-situ XAS-measurements, which resemble a real fuel cell setup, the quasi in-situ CV/FTIRS investigations were carried out at RT in a thin layer spectroelectrochemical cell with three-electrode arrangement. The cell was placed into a conventional infrared spectrometer, and FTIR spectra were recorded at different potentials in 1 M methanol operation and in CO-stripping mode, respectively. Quasi in-situ CV/FTIRS is in particular suited to pursue the progress of certain reactions at the electrode/electrolyte interface, e.g. the occurence of educts, products and reaction intermediates. Hence, it has been applied to study the CO adsorption and CO oxidation properties of the different Pt-Ru and Pt-Ru-W catalysts.
Since the CO adsorption takes place at the electrode surface, SNIFTIRS (subtractively normalized interfacial Fourier transform infrared reflectance spectroscopy) has been chosen to find out, at which potentials and to what extent linear-bonded CO (CO_L) is present at the catalyst surface. In contrast, the oxidation product CO_2 usually desorbs rather fast from the surface, and thus can be detected in the vicinity of the electrode by the SPAIRS (single potential altered infrared spectroscopy) technique.

SPAIRS measurements, 1 M methanol

In SPAIRS mode, spectra for all catalysts were collected between 100 and 700 mV every 100 mV during the first slow voltammetric scan applying scan rates of 5 mV/s. The strong absorption band at a wave number ν* of about 2345 cm^{-1} is attributed to CO_2. Beside this band, several other vibrational bands can be observed, especially interfacial water at around 1640 cm^{-1}, perchlorate anions at approximately

1110 cm^{-1} and various bands from methanol, e.g. CH from $–CH_3$ at 2950 cm^{-1}. Exemplary, the SPAIRS spectra of Pt-Ru-W (1:1:1.5), recorded between 0 and 550 mV adding 1 M methanol to the electrolyte are presented in fig. 5.33.

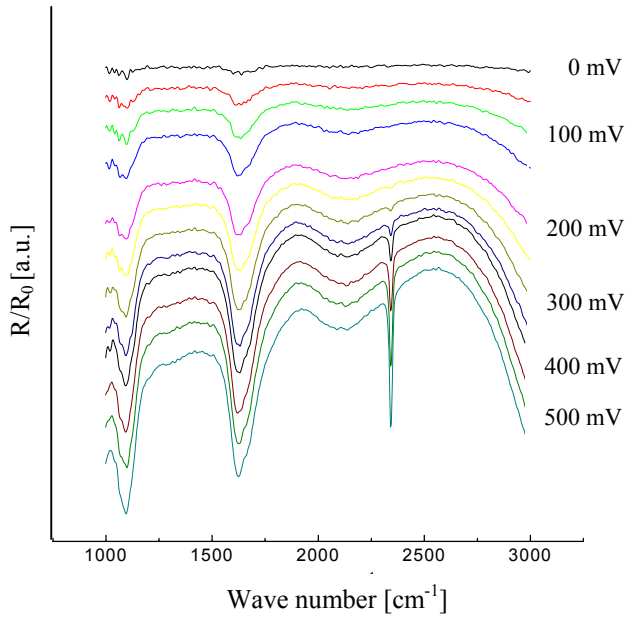

Fig. 5.33 SPAIR spectra of Pt-Ru-W (1:1:1.5) in 1 M methanol

In principle, the SPAIRS measurements were used to confirm previous CV results on the onset of CO_2 evolution and its extent. The CO_2 evolution in dependence on the potential is exemplary shown in fig. 5.34 for samples I and II and the ternary Pt-Ru-W (1:1:1.5) system in comparison to the commercial Pt-Ru catalyst.

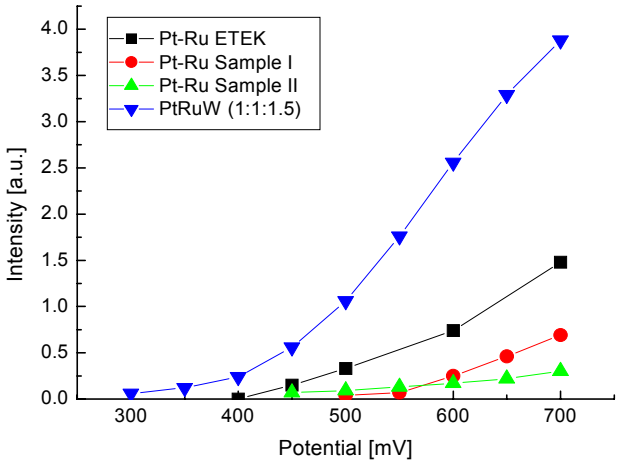

Fig. 5.34 Variation of the extent of CO_2 evolution with applied potential

In table 5.15, the CV results, namely the onset potentials and current densities at an arbitrarily-chosen potential of 550 mV, were compared with the respective values measured by SPAIRS. The intensities of

the CO_2 adsorption band ($\nu^* = 2345\ cm^{-1}$) at 550 mV are given in arbitrary units, but normalized to the specific surface area of the respective catalysts.

Table 5.15 Comparison of SPAIRS and CV results in methanol

Sample	**Onset potential** [mV, CV results]	**Onset potential** [mV, IR results]	**Intensity** at 550 mV [a.u., CV results]	**Intensity** at 550 mV [a.u., IR results]
Pt-Ru E-TEK	410	approx. 400	0.2	0.5
Pt-Ru sample I	470	approx. 500	0.09	0.09
Pt-Ru sample II	440	approx. 450	0.12	0.14
Pt-Ru-W (1:1:1.5)	420	approx. 400	0.2	1.5

The IR results are in very good agreement with the CV data for the onset potential as well as the extent of CO_2 evolution. The E-TEK reference system displays both, a comparatively low onset potential and a high oxidation activity, followed by the ternary Pt-Ru-W catalyst. In contrast, the in-house synthesized Pt-Ru catalysts show higher onset potentials and only little CO_2 intensities in dependence on the potential, resembling the single cell measurements in 1 M methanol. It is supposed that this might be caused by either an inadequate CO oxidation capability at low potentials or an insufficient methanol adsorption and dehydrogenation at the separated Pt and Ru surface sites. The latter seems more likely, taking into account the CV and current vs time results, which display an improvement of the CO oxidation with increasing potential for samples I and II and the plain Pt/Ru mixture.

SNIFTIRS measurements in 1 M methanol

By SNIFTIRS, the relative amount of CO at the electrode is measured, when the actual potential is switched by 300 mV between two values (e.g. 0/300, 100/400, 200/500 mV) and the respective reflectivities are recorded and co-added 50 times for each potential. The results obtained give information about the balance between the methanol adsorption and subsequent dehydrogenation at one hand and the adsorbed CO and the CO oxidation capability of the different catalyst systems at the other hand in dependence on the potential. Additionally, the variation of the CO frequency with potential (*Stark* effect) can be evaluated. In fig. 5.35, the spectra of the ternary Pt-Ru-W sample are exemplary shown for several potential switches. Compared with the SPAIR spectra, in SNIFTIRS the CO vibration band(s) is/are much more pronounced for all catalysts under investigation, due to the specific features of this method.

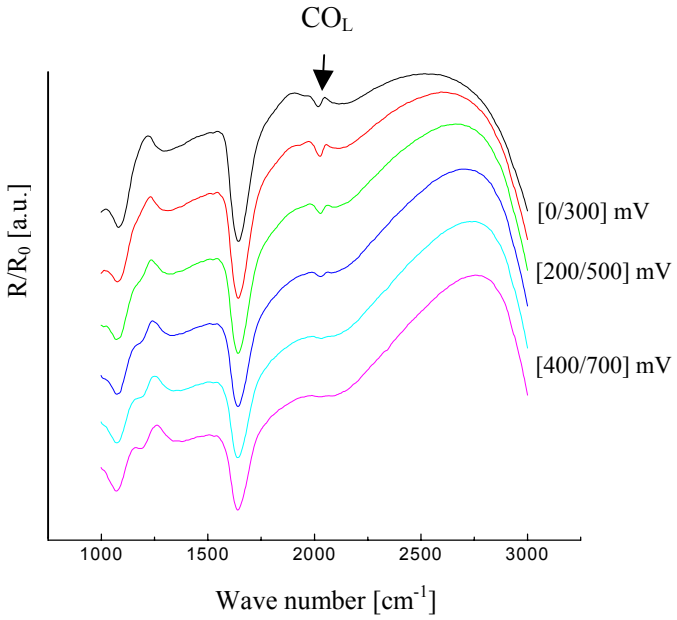

Fig. 5.35 SNIFTIR spectra of Pt-Ru-W (1:1:1.5) in 1 M methanol

For the in-house synthesized Pt-Ru catalysts and the ternary Pt-Ru-W system, only one CO absorption band is detected, and its position at approx. 2050 cm^{-1} corresponds to linear-bonded CO (CO_L). However, for the commercial catalyst purchased from E-TEK indications for multibonded (CO_M) and bridge-bonded CO (CO_B) were found in addition to the vibration band of CO_L. In fig. 5.36, the intensity of the CO vibration (in arbitrary units) at several potential switches is presented.

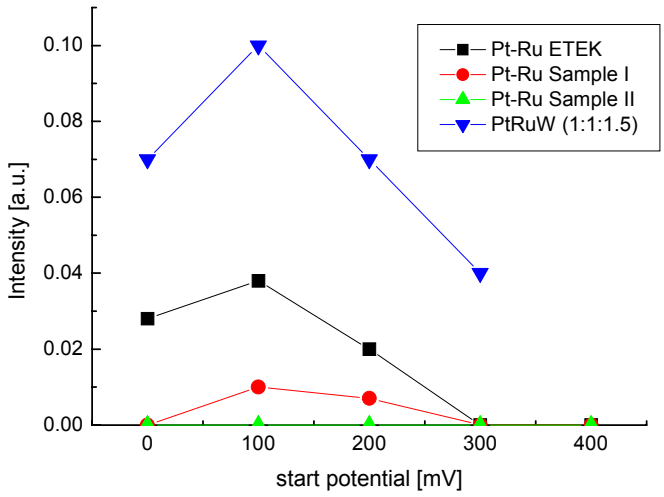

Fig. 5.36 Variation of the CO_L vibration band intensity with applied potential; for simplification only the lower potential value is given on the x-axis (e.g. 100 corresponds to 100/400 mV)

The investigations in methanol show markedly higher CO accumulation on the electrode surface of the commercial catalyst and the ternary Pt-Ru-W system than for samples I and II. For sample II, the CO coverages are even below the detection limit in the whole potential range, probably due to the balance between comparably weak methanol adsorption and dehydrogenation followed by immediate oxidative CO removal. The highest CO absorption band intensity is detected for a potential modulated between 100 and 400 mV for all catalysts, pointing towards increased methanol adsorption and dissociation activity at 100 mV compared with only minor oxidation activity at 400 mV.

SPAIRS in CO-stripping mode

Similar to the measurements in methanol, SPAIRS in CO-stripping mode was used to confirm previous CV results on the onset of CO_2 evolution and its extent. The CO-stripping was carried out as previously described for the CV measurements, but without removing excessive CO from the electrolyte, and the respective reflectivities were recorded during a slow voltammetric scan applying scan rates of 5 mV/s.

The CO_2 evolution as a function of the potential is shown in fig. 5.37 for the different binary and ternary catalysts. In contrast to the measurements in methanol, the CO_2 evolution curves in the CO-stripping mode display a maximum. This is caused by the limited amount of CO, which is adsorbed on the catalysts surface. Thus, the subsequent decrease is due to depletion of the electrode surface in CO.

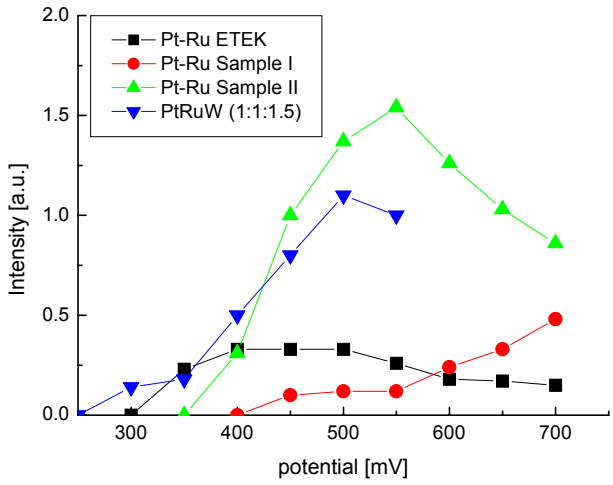

Fig. 5.37 Variation of the extent of CO_2 evolution with applied potential

In table 5.16, a comparison of the CV and IR data is presented. For the intensities of the CO_2 absorption band at 550 mV and the respective current densities in CV, the different particle sizes and specific surface areas of the catalysts have been considered.

Table 5.16 Comparison of SPAIRS and CV results in CO-stripping mode

Sample	**Onset potential** [mV, CV results]	**Onset potential** [mV, IR results]	**Intensity** at 550 mV [a.u., CV results]	**Intensity** at 550 mV [a.u., IR results]
Pt-Ru E-TEK	450	approx. 300	0.04	0.3
Pt-Ru sample I	540	approx. 400	0.03	0.45
Pt-Ru sample II	500	approx. 350	0.06	**4.5**

In contrast to the SPAIRS results in methanol, which were in good agreement with the CV data, the results in CO-stripping show significant differences. First of all, the onset of CO_2 evolution occurs at lower potentials compared to the CV results. However, the order of the different catalysts is at least constant (Pt-Ru E-TEK < sample I < sample II). The observed shift of the onset potentials to lower values might be caused by the different conditions in the CV and IR investigations, as in the case of the IR measurements CO is not only present as a monolayer on the catalyst surface but also in the electrolyte. Besides the differences for the onset potentials, surprising results for the oxidation activity have been found. Sample II shows the highest activity for CO oxidation in the IR measurements, even surpassing the commercial Pt-Ru catalyst, whereas sample I displays activities in the same range as the commercially-available system. These findings are in good agreement with the single cell measurements performed at low CO concentrations in the anode feed, presenting an improved performance of the in-house synthesized Pt-Ru catalysts.

SNIFTIRS in CO-stripping mode

In CO-stripping measurements, SNIFTIRS investigations give information about the balance between the CO adsorption and the CO oxidation capability of the different catalysts in dependence on the applied potential. Similar to the measurements in methanol, only one CO absorption band is detected for samples I and II, and its position at approx. 2050 cm^{-1} corresponds to linear-bonded CO. In contrast, evidence for the presence of multibonded and bridge-bonded CO has been found for the commercial catalyst and the ternary Pt-Ru-W sample. In fig. 5.38, the intensity of the CO vibration band (in arbitrary units) at several potential switches is presented.

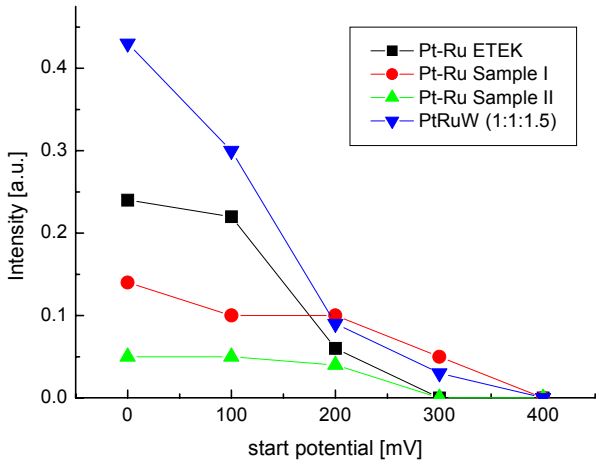

Fig. 5.38 Variation of the CO_L vibration band intensity with applied potential; for simplification only the lower potential value is given on the x-axis (e.g. 100 corresponds to 100/400 mV)

At [0/300 mV], the intensity of the CO_L band is highest for both the ternary system and the commercial Pt-Ru catalyst indicating an increased uptake of CO and only little oxidation activity. When the potential is rapidly changed from 200 mV to 500 mV, the intensity is strongly decreasing, probably due to increased oxidation at higher potentials. In contrast, samples I and II show only weak CO adsorption at the electrode surface, that seems to remain almost constant up to high potentials ([300/600] mV). One possible explanation for this behavior might be a pronounced ability of these catalysts to oxidize low CO concentrations at potentials as low as 200 mV. This is comparable to the properties of pure Ru electrodes, and was also found by the CV measurements.

A comparison of the SPAIRS and SNIFTIRS results in methanol or by CO-stripping with the respective fuel cell measurements in single cell arrangements will be given in chapter 5.5.

Particle size effects

In addition to the results discussed above, the *Stark* tuning rate (see experimental) and the shift of the CO_L frequency with particle size have been determined. The data obtained in CO-stripping mode were interpreted, according to the work of Rice et al. [115] dealing with CO on Pt nanoparticles. In fig. 5.39, the variation of the *Stark* tuning and the CO_L stretching frequency with particle size is presented. The corresponding values are summarized in table 5.17.

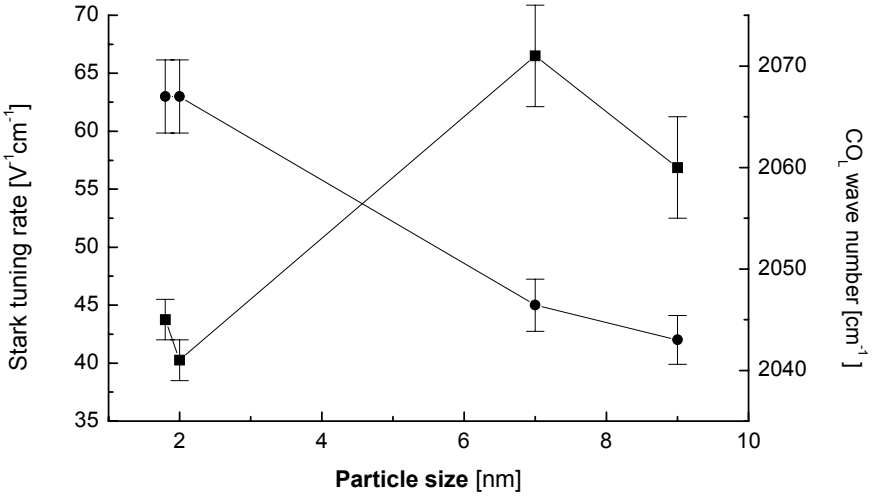

Fig. 5.39 Plot of the CO peak position (■) and the *Stark* tuning rate (●) vs particle size

Table 5.17 Dependence of the CO_L vibration band and the *Stark* tuning rate on the particle size

Sample	**Particle size** [nm]	**CO_L vibration** [cm^{-1}]	**Stark tuning rate** [cm^{-1}V^{-1}]
Pt-Ru E-TEK	2	2045 ± 2	63 ± 3
Pt-Ru-W (1:1:1.5)	< 2	2041 ± 2	63 ± 3
Pt-Ru sample I	7	2071 ± 5	42 ± 2
Pt-Ru sample II	9	2060 ± 5	45 ± 2

The findings are in good agreement with those reported by Rice et al. [115]. Thus, for the commercial Pt-Ru catalyst a *Stark* tuning rate of approximately 63 ± 3 cm^{-1}V^{-1} has been observed, in agreement with 62 ± 2 cm^{-1}V^{-1} (Pt, particle size 2 nm) reported in [115]. With increasing particle size the *Stark* tuning decreases significantly, as can be clearly seen from fig. 5.39.

Moreover, the CO stretching band shifts to higher frequencies, when the particle size increases. But since the CO stretching frequency increases with increasing coverage as well, this effect might be also caused by a coverage-dependent frequency shift. The CO coverage for all binary and ternary systems was therefore analyzed independently from CO-stripping peak currents determined via cyclic voltammetry. However, the different catalysts behave very similar, showing nearly identical coverages. Thus, a coverage-dependent shift has not been taken into account.

It can be concluded from the results presented above that characteristic features in the FTIR spectra were significantly affected by the size of the electrocatalytic active centers. The same has already been reported by Rice et al. [115] for CO on Pt nanoparticles and has been attributed to a variation in the $2\pi^*$ back-donation from metal to CO caused by strong metal-support interactions. Since the values measured for the binary Pt-Ru catalysts were in very good accordance with the investigations of Rice and coworkers [115] on pure platinum, it is supposed that neither the specific properties of the elements nor the alloy formation have a crucial influence on the CO frequency shift and the *Stark* tuning rate.

5.4 Structural features *after* operation

After operation in real fuel cells, both the catalysts and the MEAs were investigated once more with respect to changes in structure and morphology, that had occured under fuel cell-relevant conditions. XRD and TEM were applied to reveal changes in the catalyst structure, e.g. particle growth or formation of crystalline oxide phases, while the morphology of the whole MEA was checked by BET and SEM. The results obtained were compared to the findings before operation and discussed in the light of the in-situ measurements.

5.4.1 Characterization of the catalysts

For the characterization of the anode catalyst, part of the porous anode was removed from the membrane and grind into fine powder. Although this powder might contain also Nafion© ionomer and traces of substances from the MEA preparation, it is denoted as *catalyst* in the following paragraph. Besides, it seems unlikely that the ionomer or impurities contribute much to or falsify the results.
In fig. 5.40, a comparison of X-ray patterns before and after operation in a fuel cell is presented for different catalysts.
Similar to the powder patterns before fuel cell operation, only the Pt fcc phase has been observed and no indications of any other crystalline phase have been found. The corresponding average particle sizes, estimated by the *Scherrer* equation, are listed in table 5.18.

Table 5.18 Estimation of the average particle size of the different Pt-Ru catalysts before and after fuel cell operation

Sample	**Particle size** [nm] **before operation**	**Particle size** [nm] **after operation**
Pt-Ru E-TEK	2	4
Pt-Ru sample I	7	8
Pt-Ru sample II	9	5

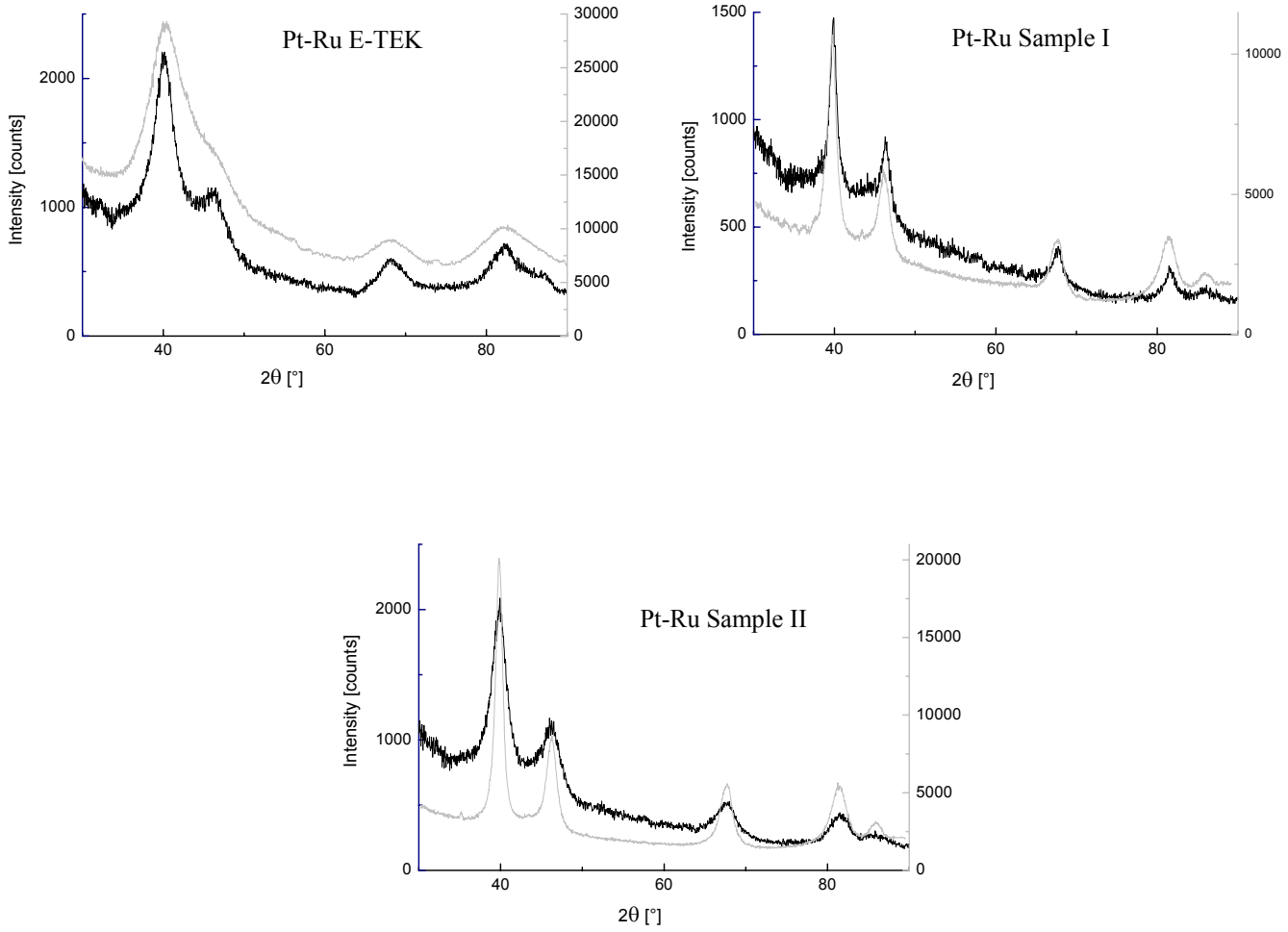

Fig. 5.40 Comparison of X-ray patterns before (■) and after (■) fuel cell operation

As can be easily seen, a significant particle growth was observed for the commercial Pt-Ru catalyst during operation. Sample I, however, seems almost unchanged by the working conditions of 75 °C in hydrogen and 95 °C in methanol vapor. In contrast, for sample II smaller particle sizes were found after operation than before, which seems absolutely unlikely at first. However, by XRD alone no further conclusions can be drawn. Hence, further catalyst characterization by another method is required.
Therefore, TEM images were recorded in order to monitor changes in the dispersion of the nanoparticles on the carbon support. Exemplary, TEM images before and after fuel cell operation are shown for samples I and II in fig. 5.41.

a)

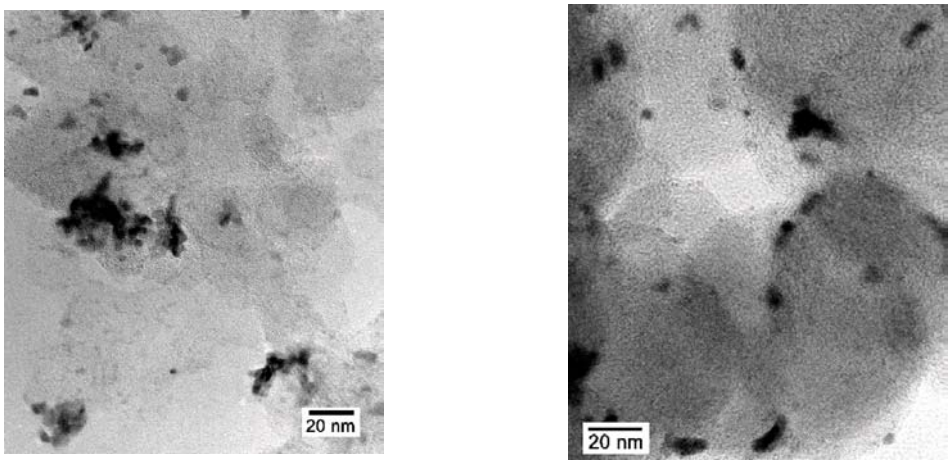

before after

b)

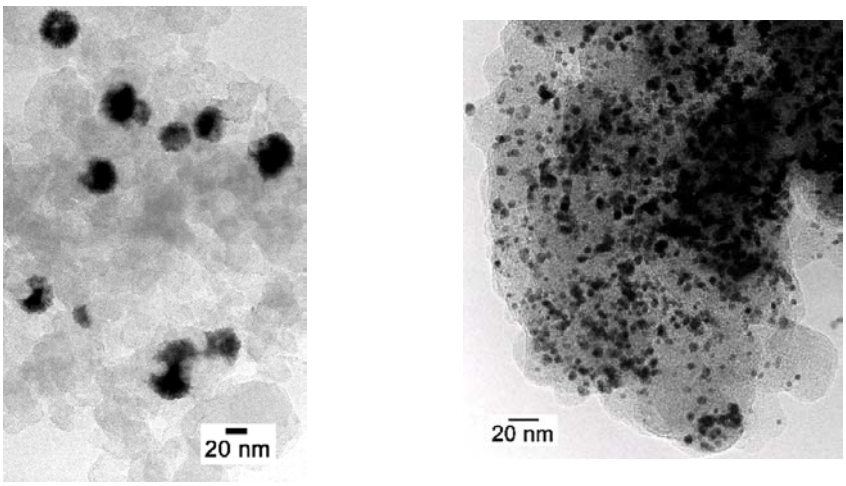

before after

Fig. 5.41 TEM images before and after fuel cell operation: a) Pt-Ru sample I
b) Pt-Ru sample II

In principle, TEM images taken before and after operation of the Pt-Ru E-TEK catalyst (not shown) and sample I look very much the same. For the commercial Pt-Ru system, slightly larger particles were found in homogeneous distribution on the carbon support, whereas sample I still consists of irregular particle agglomerates. However, TEM images of sample II display marked differences. Instead of sphere-like agglomerates as before operation, distinct particles can be seen in quite homogeneous distribution on the carbon support grains after operation.

The TEM results obtained are in good agreement with the X-ray patterns of the catalysts. Even the surprising findings for sample II are reasonable in the light of the TEM images, as the average particle size determined by XRD before operation might be strongly affected by the formation of agglomerates. The calculated value might be slightly higher compared with the real size, since two or more neighboring particles in the agglomerate might have the same orientation. As by the *Scherrer* equation the size of coherently-scattering regions is determined, the value obtained is in this case larger than the actual particle size. After operation, individual crystallites were found instead of agglomerates, and a decreased

average particle size was determined. Hence, also the average particle size obtained for sample I might be larger than its actual crystallite size, whereas the value for the commercial catalyst should be quite reliable due to the homogeneous particle distribution.

Additionally, a detailed profile analysis of the X-ray pattern has been carried out in order to elucidate the above findings for sample II (fig. 5.42). Before operation, an average particle size of 7.5 nm and a microstrain of $4.2 \cdot 10^{-3}$ were calculated, whereas after operation values of 3 nm and $1 \cdot 10^{-3}$ have been determined.

a)

b)

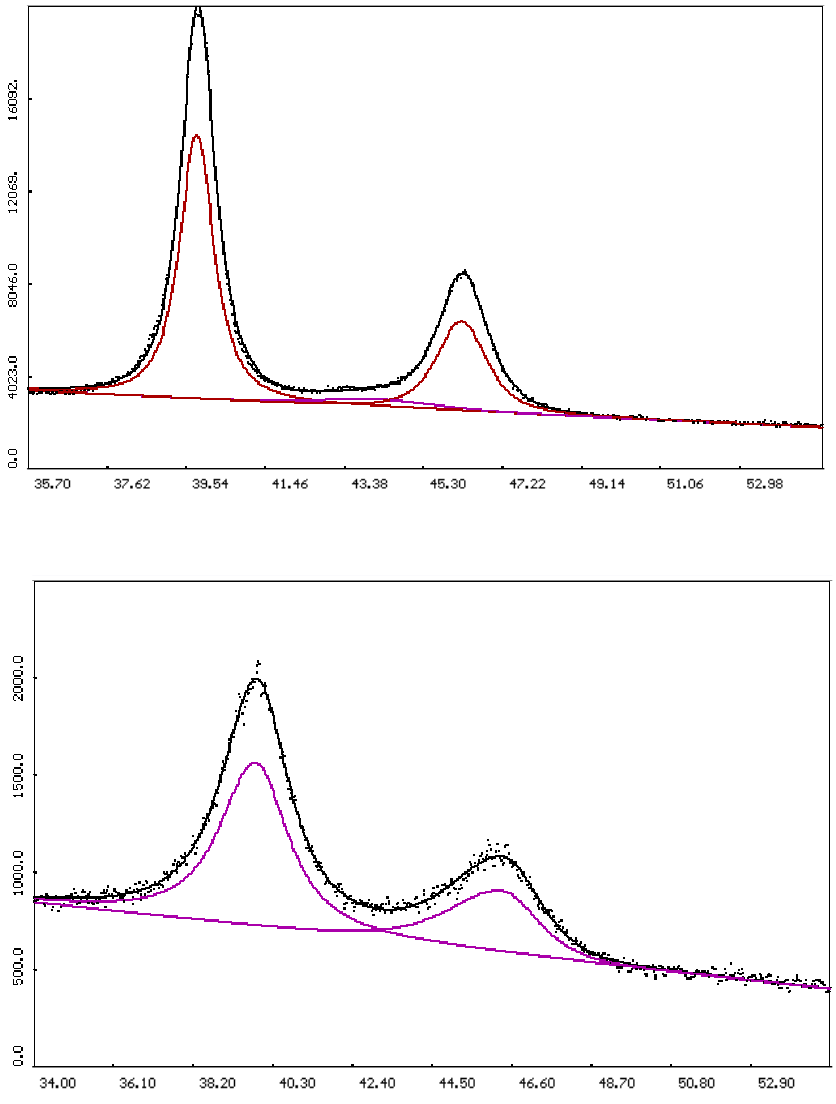

Fig. 5.42 Profile analysis of the X-ray pattern of sample II before (a) and after (b) fuel cell operation

According to the results obtained on the particle size and the microstrain, the observed phenomena for sample II might be explained as follows:
Prior to the fuel cell operation, the crystallites create agglomerates, in which the individual crystallites are partially coherent (on an atomic level), although their macroscopic orientation is different. This phenomenon leads to an apparently larger crystallite size, as some of the neighboring crystallites contribute to the coherent diffraction. On the other hand, such agglomerates behave like highly- defect crystallites, apparently having a high density of structure faults. The impact of the structure faults on the diffraction pattern is predominantly in the line broadening, which increases with increasing size of the diffraction vector. Consequently, higher microstrain was found in sample II before operation.
After fuel cell operation, the agglomerates split into separate crystallites, which are smaller than before but behave like having less structural faults. Accordingly, this process is interpreted by X-ray diffraction as a reduction of both the crystallite size and the microstrain.
Moreover, the effect discussed above was accompanied by a reduction of the line asymmetry after fuel cell operation compared to the one observed before operation. As all diffraction lines were asymmetric to the left side, we can draw the conclusion that the line asymmetry in sample II before operation is caused by a residual concentration profile in individual crystallites.

By additional nano-EDX investigations after fuel cell operation, no significant changes in the composition of individual particles were revealed. For the commercial catalyst, both platinum and ruthenium were detected within the particles, whereas for the in-house synthesized Pt-Ru catalysts only Pt was found in those crystallites, that could be resolved in TEM. These findings are in good agreement with the results obtained before fuel cell operation.
However, before operation in samples I and II the “missing” ruthenium has been detected in carbon regions, where no distinct particles were resolved. In contrast, only a small share of Ru has been detected and not any single ruthenium nanoparticle has been found in the in-house synthesized Pt-Ru catalysts after operation. Thus, it is believed that either the operation conditions are not sufficient to induce particle growth and ordering phenomena in the Ru phase, comparable to those observed after heat-treatment of the catalysts (chapter 5.1.1.2), or Ru is leached out of the catalyst during operation. The second assumption seems more likely, since pure ruthenium is not very stable in an acidic medium under fuel cell working conditions. However, ruthenium dissolution and subsequent recrystallization on top of Pt particles during operation, as suggested by A. Kucernak [177], could not be confirmed by the applied characterization methods.

5.4.2 Characterization of the MEAs

Similar to the procedure before operation, the MEAs were tested by BET after fuel cell operation. As the method is destructive, different MEAs were investigated before and after use. However, it has been confirmed that the chosen MEA preparation yields quite reproducible results (5.1.2), and therefore a comparison seems acceptable.
In fig. 5.43, a typical adsorption isotherm and the corresponding pore size distribution after operation are shown for sample I as anode catalyst. As already indicated by the measurements before operation, different catalysts did not show any effect on the resulting MEA morphology.

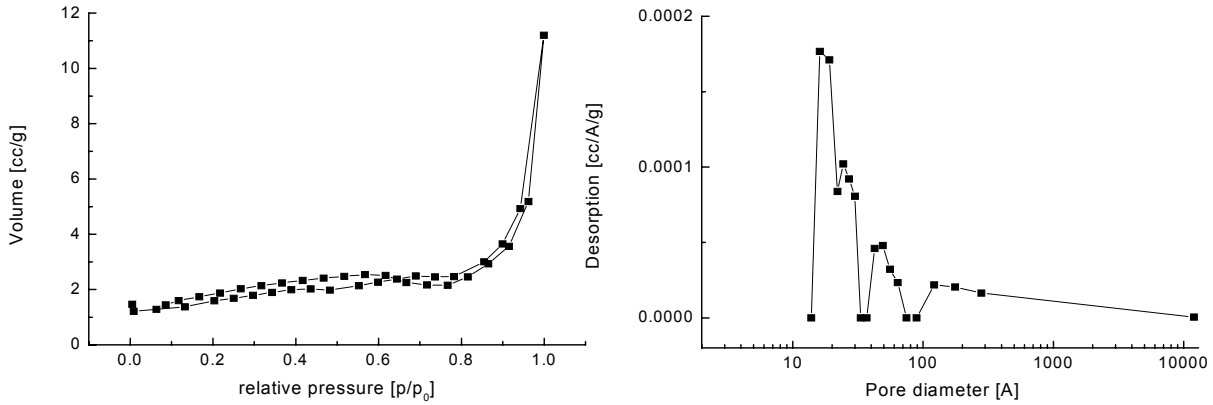

Fig. 5.43 Typical adsorption isotherm and corresponding pore size distribution for sample I

Apparently, no significant differences can be seen, when the results are compared to those obtained before operation (see fig. 5.18). Thus, the fuel cell-relevant working conditions seem not to cause any changes of the MEA morphology.

In order to verify the BET results, SEM images were taken in top view and in cross-section after operation. The TEM images of a MEA with Pt-Ru E-TEK as anode catalyst are exemplary shown in fig. 5.44. Neither the electrode thickness nor its porosity seem to change significantly, in agreement with the BET investigations. The porous electrodes still appear rather homogeneous and no striking changes in the MEA morphology have been found. Thus, it has been concluded that the MEAs are rather insensitive to the working conditions in fuel cells and the specific properties, varied by different preparation methods, will be maintained during operation.

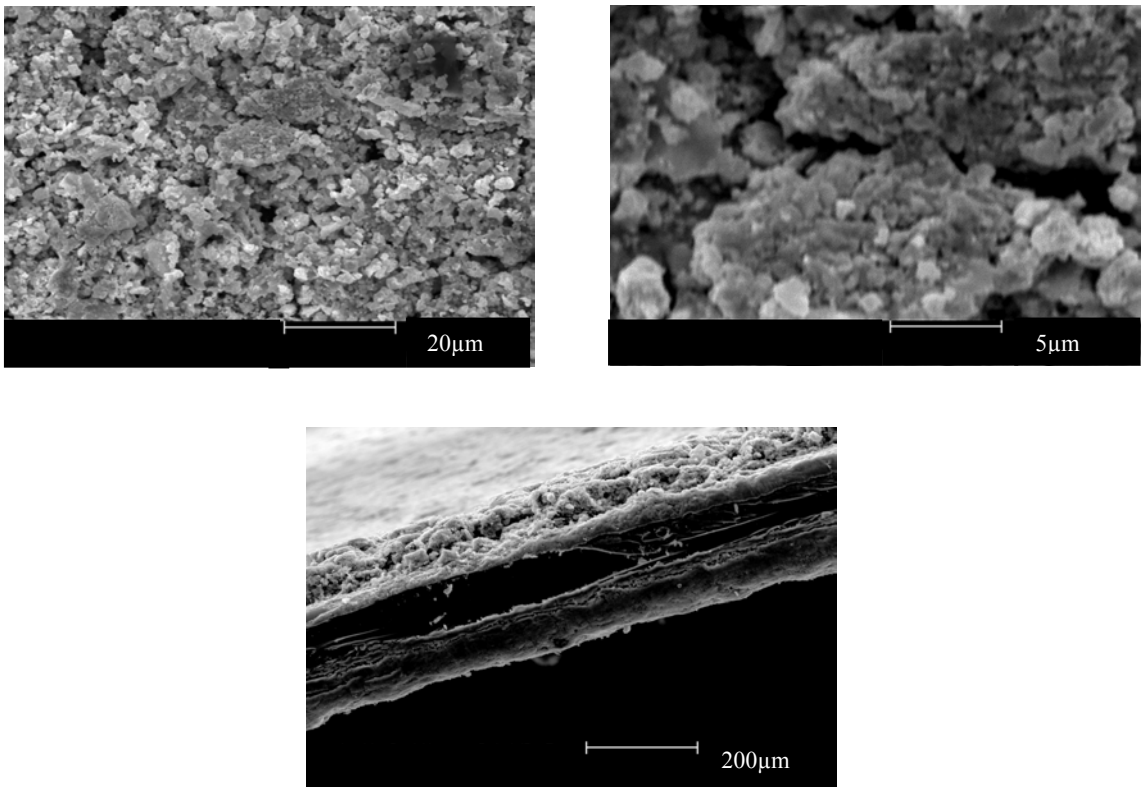

Fig. 5.44 SEM images in top view (a, b) and cross-section (c) after operation

5.5 Summary of the structural and electrochemical characterization

Structural characterization

First of all, carbon-supported ternary Pt-Ru-W catalysts with varying tungsten content were synthesized by the *Bönnemann* colloid method and their structure and composition were investigated by a combination of spectroscopic, microscopic and diffraction techniques. XRD and TEM revealed nanoparticles of approximately 2 nm size, homogeneously dispersed on the carbon support. However, all reflections observed in the X-ray patterns could only be attributed to the Pt fcc phase, whereas no evidence of any other crystalline phases has been found. By XPS, the corresponding oxidation states of the elements have been determined. Platinum is mainly detected in its metallic state, whereas tungsten appears exclusively as WO_3 species. In contrast, the ruthenium XPS signal can be deconvoluted into at least two contributions: metallic Ru and a ruthenium oxide species. A varying W content does not seem to have any significant impact on the resulting catalyst structure. According to the XRD, TEM and XPS data, the ternary systems consist most likely of highly dispersed nanocrystalline Pt-Ru alloy particles next to amorphous ruthenium and tungsten oxide species. As it has not been possible to locate these amorphous oxide species on the carbon support grains, it has been decided to concentrate the further investigations on the binary Pt-Ru system. This has been done in order to reduce free parameters and so to simplify systematic studies of the relationship between alloy formation and the corresponding electrocatalytic activity.

Three different carbon-supported Pt-Ru systems, which were expected to differ in the degree of alloy formation, were synthesized via two different syntheses in aqueous phase using different reducing agents (sample I and II) and the *Bönnemann* colloid method (sample III), respectively, and compared with a commercially-available Pt-Ru catalyst purchased from E-TEK inc. In the following paragraph, only the essential findings are summarized.

Structural characterization by a combination of XRD, XPS, TEM and EXAFS confirmed indeed that different degrees of alloy formation were obtained. Sample III resembles the ternary Pt-Ru-W systems, also prepared by the colloid method, showing homogeneously dispersed nanocrystallites of about 2 nm in size. In contrast, sample I exhibits irregularly shaped particle agglomerates, that consist of nanocrystallites with an average size of 7 nm. For sample II, nanocrystals with an average size of 9 nm were found, forming larger sphere-like agglomerates. X-ray patterns for all binary catalysts showed merely reflections of the Pt fcc phase, while no indication for any other crystalline phase appeared. However, after heat-treatment at 500 °C under nitrogen, marked differences between the catalysts were observed. Samples I, II and III display additional reflections, that correspond to hexagonal ruthenium, whereas the commercial system looks almost unchanged, besides some particle growth. After heat-treatment at 500 °C under air, further differences between the different samples were revealed. Thus, the Pt-Ru E-TEK catalyst forms RuO_2 particles with sizes comparable to the platinum particles. Sample I and III behave quite similar, forming Ru oxide particles, that were almost double in size compared to the platinum particles. For sample II, rather different results were obtained, since not only very small RuO_2 nanoparticles were found, but also hexagonal ruthenium. By simulation of the respective X-ray patterns, using the FULLPROF package, the amount of separate ruthenium has been estimated. According to these results, the commercial catalyst originally contained no separate ruthenium phase, whereas sample I

consisted of < 10 % separate ruthenium and sample II of > 25 % separate Ru. A simple structure model, based on the XRD, XRD (T), XPS, TEM and nano-EDX data obtained, is presented on p. 109.

Electrochemical characterization

The electrochemical characterization of the different catalysts was performed by cyclic voltammetry and in real fuel cell tests (FC). For the ternary Pt-Ru-W systems, the CV and FC results were in very good agreement, showing activities comparable to those of the commercial Pt-Ru catalyst. In H_2/CO operation, Pt-Ru-W (1:1:1.5) even surpasses the performance of the binary E-TEK catalyst. In contrast, the in-house synthesized Pt-Ru catalysts, consisting of separate Pt and Ru phases (samples I and II), display high activities for low methanol and CO concentrations in the anode feed only. Thus, using H_2/75 ppm CO mixtures, both samples I and II exceed the commercial catalyst in performance. However, with 1 M methanol, the separate-phase catalysts show rather poor activities in CV as well as in real fuel cell tests in DMFC mode.
Therefore, a spectroelectrochemical approach applying a combination of CV and FTIRS (SPAIRS and SNIFTIRS) has been adopted in order to achieve a more detailed understanding of the differences between the catalysts under investigation. Regarding the onset potential and the extent of CO_2 evolution, a very good correlation has been found for the CV data in methanol and the FTIRS results. Compared with the in-house synthesized Pt-Ru and Pt-Ru-W catalysts, the commercial system exhibits both a lower onset potential for an apparent oxidation activity and higher oxidation activities. These results resemble those of the FC measurements in DMFC mode.
In CO-stripping, less consistency for CV and FTIRS data has been observed, probably due to the different conditions in the electrochemical and spectroelectrochemical setup, as in the case of the FTIR measurements CO is not only present as a monolayer on the catalyst surface but also in the electrolyte. The onsets of an apparent oxidation activity, determined by the FTIRS investigations, were shifted to lower potentials with respect to the CV results. Besides the differences for the onset potentials, surprising results for the oxidation activity have been found. Thus, sample II shows the highest activity for CO oxidation, even surpassing the commercial Pt-Ru catalyst. This finding was in good agreement with the single cell measurements with low CO concentrations in the anode feed, presenting an improved performance of the in-house synthesized Pt-Ru catalysts.
However, the most striking difference, found for the catalyst systems, is the varying CO accumulation on the electrode surface. For Pt-Ru samples I and II, the amount of CO adsorbed at the electrode surface is orders of magnitudes lower than for the commercial catalyst and the ternary Pt-Ru-W (1:1:1.5) system. In the following paragraph, this phenomenon will be discussed in more detail.

For achieving high activities in fuel cell operation, three main parameters have to be considered and fulfilled by the tailor-made anode catalyst:
- in DMFC mode: excellent methanol adsorption and dehydrogenation activity,
- using H_2/CO mixtures: little CO adsorption,
- in both: excellent hydrogen and CO oxidation activity.

According to the CV results, the Pt-Ru catalysts, consisting of separate Pt and Ru phases (samples I and II), display excellent CO oxidation activities already at very low potentials. Thus, comparatively little CO

accumulation has been found on the electrode surface by FTIRS, since the oxidation proceeds rather fast. However, for H_2/CO mixtures, containing relatively high CO concentrations, less satisfactory results have been obtained. Consequently, this must be due to the restricted number of contact areas between platinum and ruthenium sites. Thus, only an insufficient number of platinum sites can be freed from the poisoning CO species.
In the case of methanol operation, a rather different situation occurs. As CO oxidation proceeds quite fast, methanol adsorption and dehydrogenation must be the rate-determining step in the methanol oxidation reaction. In the phase-separate catalysts (samples I and II), less methanol adsorption takes place, since methanol is not adsorbed on pure ruthenium. For little methanol concentrations, this is of only little importance, as enough platinum sites are available, and thus better results have been observed.

In-situ XAS measurements

The suitability of XAS for the in-situ investigation of catalysts in a real PEM fuel cell in hydrogen and methanol operation has been demonstrated. As many parameters as possible have been left untouched in order to retain the original operation conditions. Only the metal loading had to be increased from 0.4 mg/cm² up to 1.2 g/cm² to obtain an optimum signal-to-noise ratio. Three MEAs have been tested to guarantee the reproducibility of the experiment. Structural changes of the catalysts have been pursued at the Pt L_3-edge in transmission geometry. The respective spectra were recorded at several points of the E/i curve in the activation-, MEA- and diffusion-controlled region (fig. 5.7).
By analysis of the Fourier transforms, no significant changes in the radial distribution function have been observed. The short-range order around the platinum absorber atoms seems to stay unchanged during operation. However, comparison of the normalized absorption spectra in E space reveals pronounced differences between the XAS results at the MEA before operation and the data in methanol and hydrogen operation. The white-line intensities decrease during operation, indicating a reduction of oxides, previously present in the as-synthesized catalysts. Since anode and cathode were monitored at once (see experimental), it is even more surprising that an overall reduction of the catalysts has been observed, although the cathode catalyst is in contact with pure oxygen.
In subsequent experiments, the cathode side was removed in the respective beam regions to allow for measurements at the anode only. However, it is supposed that the effect of the electrode potentials had not been properly-accessible by this cell modification, as the removal of the cathode side in the beam window region might modify the respective current distribution. Therefore, it seems absolutely necessary to repeat the measurements at the Ru K-edge, as by this procedure only the anode catalyst contributes to the results and removal of the pure Pt cathode will not be necessary. Thus, more definite findings are expected.

6 Discussion and conclusion: Alloy formation essential for the electrocatalytic performance?

In chapter 1, the question has been raised, if alloy formation is really necessary for outstanding electrocatalytic activity. In recent literature, some doubts were uttered in this respect [2, 8], but systematic investigations to solve this question have not been reported so far.

In the work presented, a possible approach to this problem by varying the degree of alloy formation is shown. In this context, three different syntheses were chosen and the structure of the resulting catalysts was determined by a combination of spectroscopic, microscopic and diffraction techniques. According to the obtained results, the commercially-available Pt-Ru system is mainly alloyed, while the in-house prepared catalysts show either only partial alloy formation or even separate phases. Additionally, a plain mixture of carbon-supported platinum and carbon-supported ruthenium, presenting the extremest case of separate, non-alloy phases was investigated.

After their structural characterization, the catalysts electrocatalytic activities were determined by cyclic voltammetry and in real fuel cell experiments, yielding surprising results, as the separate phases and the plain mixture showed enhanced activities for low CO and CH_3OH concentrations compared to the commercial Pt-Ru catalyst. These results seem to be in strong contrast to common electrochemical principles and fundamental knowledge. Hence, as there is no doubt that the in-house synthesized catalysts consist of separate Pt and Ru phases, the obtained results should be discussed in the light of these new findings in order to find reasonable explanations for their improved performance.

It is well known that CO molecules adsorbed on the electrocatalytic active Pt sites show comparatively high mobility [5]. Hence, they can easily move from Pt to Ru surface sites. However, common electrochemical knowledge is demanding that Pt and Ru atoms have to occupy neighboring positions to make the widely accepted bifunctional mechanism possible. Pt-Ru alloys of different stoichiometries should meet these requirements best, due to their more or less stochastic distribution of Pt and Ru atoms in the supported nanoparticles. But then, why do non-alloy catalysts show improved electrocatalytic activities for low CO and methanol concentrations?

Answering this question should take into account two different approaches, (i) the not yet completely understood diffusion phenomena of both CO and also OH, which could be the diffusing component as well [6], in nanosystems and (ii) the unknown extent of close contact between Pt agglomerates and Ru and Ru oxide particles, respectively. In contrast to CO diffusion, not much information has been published on the diffusion of oxygen-containing species on Pt and Ru surfaces. Additionally, as the diffusion phenomena were measured in bulk systems, it is not clear, if nanoparticle surfaces influence the diffusion behavior of CO and OH, due to their specific properties, e.g. the high concentration of edge- and kink sites. Besides, close contact between Pt and Ru atoms is a prerequisite for high electrocatalytic activities and plays a crucial role for the catalysts performance. That is why Long et al. [9] claim that the structure of a custom-designed Pt-Ru catalyst should provide a maximized number of contact sites between metallic Pt on one side and Ru and hydrous Ru oxide, respectively, on the other side in order to maintain high activity for methanol oxidation.

However, separate Pt and Ru phases, as obtained by the structural characterization presented (see chapter 5.1.1.2), should be understood in crystallographic terms. Hence, the term “separate Pt and Ru phases” does not exclude contact between Pt and Ru atoms, and pure ruthenium regions will be found close to

areas of pure platinum. For example, the structure of a Ru-decorated single crystal model electrode has been described by an oriented Pt substrate with ruthenium "nano-electrodes" deposited on it [5]. In the case of a real carbon-supported fuel cell catalyst, consisting of separate Pt agglomerates and Ru particles, a rather similar picture might be a not too bad description of the catalysts structure, as the extension of the platinum regions is approximately one order of magnitude larger than that of the Ru nanoparticles. Moreover, TEM and nano-EDX analyses gave evidence of contact between Pt and Ru atoms, as shown in the results section, so that at least some Ru particles must have crystallized on top or close to the platinum agglomerates. Nevertheless, compared with an alloy, it is less probable to find Pt and Ru atoms occupying neighboring sites, except the edges of ruthenium particles, decorating the bigger Pt agglomerates, see also [8]. Thus, mainly two factors limit the reaction kinetics: (i) the balance between accessible CO- and OH-adsorption sites and (ii) the surface mobility of either CO or oxygen-containing species. This explanation would fit rather well with the improvement of the electrocatalytic activities observed for low CO concentrations in the H_2/CO mixtures and for low methanol contents at phase-separated catalysts. For instance, if the rate of methanol electrooxidation is limited by the methanol adsorption and decomposition at Pt ensembles only [46], the restricted number of such Pt ensembles in the non-alloy catalysts does not play an important role for methanol concentrations below a certain limit. In contrast to the methanol oxidation reaction, however, CO from the H_2/CO mixture can be adsorbed at both Pt and Ru sites. In such cases, catalysts consisting of separate phases seem to be more effective than alloyed systems, as the specific properties of the pure elements, like their capability of hydrogen adsorption and oxidation, are maintained, while the contact between Pt and Ru atoms makes the synergetic reaction possible.

In this work, the superior electrocatalytic activities of non-alloy catalysts for the anodic oxidation of H_2/CO mixtures, which contain only low CO concentrations, have been demonstrated. Consequently, the success should be an incentive for increased research activities. By selective variation of the composition, the share of separate phases and the contact area between them, catalyst systems might be developed, which surpass the currently applied commercial catalysts by far. In particular, the preparation of plain catalyst mixtures is rather simple and cost-efficient. Moreover, not only binary but also multinary catalyst systems could be checked and their compositions varied with virtually no limits.
However, changes in the catalysts morphology and composition during operation under varying working conditions, due to the oxidation or dissolution of the less noble elements in the respective systems, e.g. Ru in Pt-Ru catalysts, should be considered as well. For instance in Pt-Ru catalysts consisting of separate Pt and Ru phases, the ruthenium atoms might become leached out, and work either as promoting agent in the electrolyte itself or recrystallize on top of the Pt agglomerates [177]. With respect to the enhanced performances obtained even for plain Pt and Ru mixtures, these possibilities should be further investigated by suitable techniques, as helpful information on how to tailor and optimize prospective fuel cell catalysts in future might be obtained. In this respect, standardized in-situ measurements could be of great importance for the future catalyst development, since the catalysts structure can be pursued during operation. The optimum structure could thus be adjusted to the actual operation conditions, and leaching phenomena could be detected and perhaps prevented. As part of this work, the suitability of X-ray absorption spectroscopy for in-situ fuel cell measurements has already been demonstrated. Consequently, the combination of simple synthesis routes for the preparation of phase-separate catalysts and in-situ XAS measurements for the online-monitoring of the catalyst structure during operation might open new ways in catalyst research.

7 References

[1] A. S. Arico, P. Creti, H. Kim, R. Mantegna, N. Giordano and V. Antonucci, 'Analysis of the Electrochemical Characteristics of a Direct Methanol Fuel Cell based on a Pt-Ru/C Anode Catalyst', *J. Electrochem. Soc.*, 1996, **143 (12)**, 3950-3959.

[2] D. R. Rolinson, P. L. Hagans, K. E. Swider, J. W. Long, 'Role of Hydrous Ruthenium Oxide in Pt-Ru Direct Methanol Fuel Cell Anode Electrocatalysts: The Importance of Mixed Electron/Proton Conductivity', *Langmuir*, 1999, **15**, 774-779.

[3] W. E. O'Grady, 'In Situ XAFS Studies of Pt/Ru Alloys Operating Under Electrochemical Methanol Oxidation Conditions', American Crystallographic Association, 1997.

[4] T. J. Schmidt, H. A. Gasteiger, R. J. Behm, 'Methanol Electrooxidation on a Colloidal PtRu Alloy Fuel Cell Catalyst', *Electrochem. Comm*., 1999, **1**, 1-4.

[5] K. A. Friedrich, K.-P. Geyzers, U. Linke, U. Stimming, J. Stumper, 'CO Adsorption and Oxidation on a Pt(111) electrode modified by Ruthenium Deposition: An IR-Spectroscopic Study', *J. Electroanal. Chem.*, 1996, **402**, 123.

[6] J. C. Davies, B. E. Hayden, D. J. Pegg, M. E. Rendall, 'The electro-oxidation of carbon monoxide on ruthenium modified Pt(111)', *Surf. Sci.*, 2002, 496 (1-2), 110-120.

[7] M. Watanabe, S. Motoo, 'Electrocatalysis by Ad-atoms Part III. Enhancement of the Oxidation of Carbon Monoxide on Platinum by Ruthenium Ad-atoms', *J. Electroanal. Chem.*, 1975, **60**, 275.

[8] P. Waszczuk, J. Solla-Gullón, H.-S. Kim, Y. Y. Tong, V. Montiel, A. Aldaz, A. Wieckowski, 'Methanol Electrooxidation on Platinum/Ruthenium Nanoparticle Catalysts', *J. Catalysis*, 2001, **203** (1),1-6.

[9] J. W. Long, R. M. Stroud, K. E. Swider-Lyons, D. R. Rolinson, 'How To Make Electrocatalysts More Active for Direct Methanol Oxidation-Avoid PtRu Bimetallic Alloys!', *J. Phys. Chem. B*, 2000, **104** (42), 9772-9776.

[10] W. Strobl, E. Heck, 'Wasserstoffantrieb und mögliche Zwischenschritte', *VDI-Berichte*, 1995, **1201**, 173-185.

[11] K. Kordesch, G. Simader, 'Fuel Cells and Their Applications', VCH-Verlag, Weinheim, 1996.

[12] DaimlerChrysler Kommunikation, 'Premiere auf der IAA: A-Klasse mit Brennstoffzellen-Antrieb', Presseinformation, Stuttgart, 3/1999.

[13] M. Specht, F. Staiss, A. Bandi, T. Weimer, 'Comparison of Renewable Transportation Fuels, Liquid Hydrogen and Methanol, with Gasoline - Energetic and Economic Aspects', *Int. J. Hydrogen Energy*, 1998, **23** (5), 387-396.

[14] C. Lamy, 'Direct Anodic Oxidation of Methanol, Ethanol and Higher Alcohols and of Hydrocarbons in PEM Fuel Cells', ECS workshop on fuel cells in Portoroz, 1999.

[15] J. Wang, S. Wasmus, R. F. Savinell, 'Real-Time Mass Spectrometric Investigation of the Methanol Oxidation in a Direct Methanol Fuel Cell', *J. Electrochem. Soc.*, 1995, **142** (11), 4218-4026.

[16] M. Weber, J.-T. Wang, S. Wasmus, R.F. Savinell, 'Formic Acid Oxidation in a Polymer Electrolyte Fuel Cell - A Real-Time Mass Spectrometry Study', *J. Electrochem. Soc*., 1996, **143** (7), L158-L161.

[17] A. Heinzel, R. Holze, C. H. Hamann, J. K. Blum, 'On the Electrooxidation of Methanol and Formaldehyde at a Platinum Electrode: a SEESR-Study of Radical Intermediates', *Electrochim. Acta*, 1989, **34**, 657.

[18] P. Ekdunge, M. Raberg, 'The Fuel Cell Vehicle: Analysis of Energy Use, Emissions and Cost', *Int. J. Hydrogen Energy*, 1998, **23** (5), 381-385.

[19] G. Scharfenberger, MPI, Mainz, DFG-Kolloquium Pommersfelden, poster contribution.

[20] J. Kerres, ICVT, Stuttgart, DFG-Kolloquium Pommersfelden, poster contribution.

[21] H.-J. Bargel, G. Schulze, 'Werkstoffkunde', Springer Verlag, Berlin Heidelberg, 2000, 32-35.

[22] P. K. Shen, A. C. C. Tseung, 'Anodic Oxidation of Methanol on Pt/WO_3 in Acidic Media', *J. Electrochem. Soc.*, 1994, **141**, 3082-3090.

[23] M. M. P. Janssen, J. Moolhuysen, 'Binary Systems of Platinum and a second Metal as Oxidation Catalysts for Methanol Fuel Cells', *Electrochim. Acta*, 1976, **21**, 861-878.

[24] B. N. Grgur, N. M. Markovic, P. N. Ross, 'The Electro-oxidation of H_2 and H_2/CO Mixtures on Carbon-Supported Pt_xMo_y Alloy Catalysts', *J. Electrochem. Soc.*, 1999, **146**, 1613-1619.

[25] R. Adzic, 'Recent Advances in the Kinetics of Oxygen Reduction', in *Electrocatalysis*, P. N. Ross (Ed), Wiley-VCH, Weinheim, 1998, 197-242.

[26] B. N. Grgur, N. M. Markovic, P. N. Ross, 'Temperature-dependent oxygen electrochemistry on platinum low-index single crystal surfaces in acid solutions', *Can. J. Chem.*, 1997, **75**, 1465.

[27] T. Frelink, W. Visscher, J. A. R. van Veen, 'On the role of Ru and Sn as promoters of methanol electro-oxidation over Pt', *Surf. Sci.*, 1995, **335**, 353.

[28] H. A. Gasteiger, N. M. Markovic, P. N. Ross, E. J. Cairns, 'Temperature-Dependent Methanol Electro-oxidation on Well-Characterized Pt-Ru Alloys', *J. Electrochem. Soc.*, 1994, **141** (7), 1795-1803.

[29] G. Faubert, R. Coté, J. P. Dodelet, M. Levèbvre, P. Bertrand, 'Oxygen reduction catalysts for polymer electrolyte fuel cells from the pyrolysis of FeII acetate adsorbed on 3,4,9,10-perylenetetracarboxylic dianhydride'**,** *Electrochim. Acta*, 1999, **44**, 2589-2603.

[30] J. A. R. van Veen, J. F. van Baar, K. J. Kroese, 'Effect of Heat-Treatment on the Performance of Carbon-Supported Transition-metal Chelates in the Electrochemical Reduction of Oxygen', *J. Chem. Soc. Faraday Trans.*, 1981, **77**, 2827--2843.

[31] H. Jahnke, M. Schönborn, G. Zimmermann (Eds), 'Dyestuffs*',* in *Topics in current chemistry*, Springer Verlag Berlin, 1976, 165.

[32] M. Kirschenmann, D. Wöhrle, W. Vielstich, 'Synthesis of 5,10,15,20-Tetrakisphenylporphins on a Carbon Support for the Cathodic Reduction of Oxygen in Fuel Cells', *Ber. Bunsenges. Phys. Chem.*, 1988, **92**, 1403-1406.

[33] J. A. R. van Veen, H. A. Colijn, 'Oxygen Reduction on Transition-Metal Porphyrins in Acid Electrolyte: I. Activity', *Ber. Bunsenges. Phys. Chem.*, 1981, **85**, 693-700.

[34] H. P. Dhar, R. Darby, V. Y. Young, R. E. White, 'The Effect of Heat Transfer Atmospheres on the Electrocatalytic Activity of Cobalt Tetraazaanulene: Preliminary Results', *Electrochim. Acta*, 1985, **30**, 423.

[35] J. F. van Baar, J. A. R. van Veen, N. de Wit, 'Selective Electro-Oxidation of Carbon monoxide with carbon-supported Rh- and Ir- Porphyrins at low Potentials in acid Electrolyte', *Electrochim. Acta*, 1982, **27**, 57-59.

[36] H. Wendt, S. Rausch, T. Borucinski, 'Advances in applied electrocatalysis', in *Advances in catalysis*, 1994, **40**, 92.

[37] J. O'M. Bockris, A. K. N. Reddy (Eds), *Modern Electrochemistry*, Vol. *2*, Plenum Press, New York, 1970.

[38] H. Igarashi, T. Fujino, M. Watanabe, 'Hydrogen Electro-oxidation on Platinum Catalysts in the Presence of Trace Carbon Monoxide', *J. Electroanal. Chem.*, 1995, **391**, 119.

[39] H. Kita, S. Ye, K. Sugimura, 'Effects of adsorbed CO on the electrode reactions at platinum'; *J. Electroanal. Chem.*, 1991, **297**, 283.

[40] S. Gottesfeld, J. Pafford, 'A New Approach to the Problem of Carbon Monoxide Poisoning in Fuel Cells Operating at low Temperatures', *J. Electrochem. Soc.*, 1988, **135** (10), 2651-2653.

[41] C. Lamy, J.-M. Léger and S. Srinivasan, in *Modern Aspects of Electrochemistry*, J. O'M. Bockris, B. E. Conway and R. E. White (Eds), Vol. 34, Plenum Press, New York, 2001, 53.

[42] H. Wang, T. Löffler, H. Baltruschat, 'Formation of intermediates during methanol oxidation: A quantitative DEMS study', *J. Appl. Electrochem.*, 2001, **31**, 759-765.

[43] J.-M. Léger, 'Mechanistic aspects of methanol oxidation on platinum-based electrocatalysts', *J. Appl. Electrochem.*, 2001, **31**, 767-771.

[44] V. S. Bagotzky, Y. B. Vassilyev, *Electrochim. Acta*, 1967, **12**, 1323.

[45] Z. Jusys, R. J. Behm, 'Methanol Oxidation on a Carbon-Supported Pt Fuel Cell Catalyst - A Kinetic and Mechanistic Study by Differential Electrochemical Mass Spectrometry', *J. Phys. Chem. B*, 2001, **105** (44), 10874-10884.

[46] H. A. Gasteiger, N. M. Markovic, P. N. Ross, E. J. Cairns, 'Methanol Electrooxidation on Well-Characterized Pt-Ru Alloys', *J. Phys. Chem.*, 1993, **97**, 12020-12029.

[47] M. Götz, H. Wendt, 'Screening binary and ternary catalyst formulations for direct-methanol-PEM fuel cells', *Electrochem. Soc. Proc.*, 1998, **27**, 291-299.

[48] Y. Zhu, H. Uchida, T. Yajima, M. Watanabe, 'Attenuated Total Reflection-Fourier Transform Infrared Study of Methanol Oxidation on Sputtered Pt Film Electrodes', *Langmuir*, 2001, **17**, 146-154.

[49] G.-Q. Lu, W. Chrzanowski, A. Wieckowski, 'Catalytic Methanol Decomposition Pathways on a Platinum Electrode', *J. Phys. Chem. B*, 2000, **104**, 5566-5572.

[50] K. J. Vetter, *Elektrochemische Kinetik*, Springer Verlag, Berlin, 1961.

[51] C. H. Hamann, A. Hamnett, W. Vielstich, *Electrochemistry*, Wiley-VCH, Weinheim, 1998.

[52] C. M. A. Brett, A. M. Oliveira Brett, *Electroanalysis*, Oxford University Press, 1998.

[53] I. Barin (Ed), *Thermodynamical Data of pure Substances*, Wiley-VCH, Weinheim, 1995.

[54] H. Wendt, G. Kreysa, 'Electrochemical Engineering - Science and Technology in Chemical and other Industries', Springer Verlag, Berlin Heidelberg, 1999, 39-49.

[55] Y. Sone, P. Ekdunge, D. Simonsson, 'Proton conductivity of Nafion 117 as measured by a four-electrode AC impedance method', *J. Electrochem. Soc.*, 1996, **143**, 1254-1259.

[56] J. Clavilier, K. El Achi, M. Petit, A. Rodes, M.A. Zamakhchari, *J. Electroanal. Chem*., 1990, **295**, 333.

[57] J. Clavilier, A. Rhodes, M. A. Zamakhachari, *J. Chim. Phys.*, 1991, **88**, 1291.

[58] H. Ogasawara, M. Ito, 'Hydrogen adsorption on Pt(100), Pt(110), and Pt(111) electrode surfaces studied by in situ infrared reflection absorption spectroscopy', *Chem. Phys. Lett*., 1994, **221**, 213.

[59] R. J. Gale (Ed), *Spectroelectrochemistry: Theory and Practice*, Plenum Press, New York, 1988.

[60] http://www.staff.ncl.ac.uk/p.a.christensen/ftir3.htm

[61] W. Göpel, C. Ziegler, *Struktur der Materie: Grundlagen, Mikroskopie und Spektroskopie*, B. G. Teubner Verlagsgesellschaft Stuttgart, Leipzig, 1994.

[62] D.S. Corrigan, L-W.H. Leung, M.J. Weaver, 'Coverage Dependent Orientation of Adsorbates as Probed by Potential-Difference Infrared Spectroscopy: Azide, Cyanate, and Thiocyanate at Silver Electrodes', *J. Phys. Chem*., 1986, **90**, 5300.

[63] B. Beden, *Spectra 2000*, 1984, **13**, 19.

[64] B. Beden, C. Lamy, in R.J. Gale (Ed), *Spectroelectrochemistry, Theory and Practice*, Plenum Press, New York, 1988.

[65] S. Pons, *J. Electroanal. Chem.*, 1983, **150**, 495.

[66] D. P. J. Barz, V. M. Schmidt, 'Addition of dilute H_2O_2 solutions to H_2-CO fuel gases and their influence on performance of a PEFC', *Phys. Chem. Chem. Phys.*, 2001, **3**, 330-333.

[67] D. R. Hodgson, B. May, P. L. Adcock, D. P. Davies, 'New lightweight bipolar plate system for polymer electrolyte membrane fuel cells', *J. Power Sources*, 2001, **96**, 233-235.

[68] B.Beden, J.-M. Léger, C. Lamy, 'Electrocatalytic Oxidation of Oxygenated Aliphatic Organic Compounds at Noble Metal Electrodes', in *Modern Aspects of Electrochemistry*, J. O'M. Bockris, B. E. Conway and R. E. White (Eds), Vol. 22, Plenum Press, New York, 1991, 97-264.

[69] B. Gurau, R. Viswanathan, R. Liu, T. J. Lafrenz, K. L. Ley, E. S. Smotkin, E. Reddington, A. Sapienza, B. C. Chan, T. E. Mallouk, S. Sarangapani, 'Structural and Electrochemical Characterization of Binary, Ternary, and Quarternary Platinum Alloy Catalysts for Methanol Electro-oxidation', *J. Phys. Chem. B*, 1998, **102**, 9997-10003.

[70] B. E. Warren, B. L. Averbach, *J. Appl. Phys.*, 1950, **21**, 595.

[71] R. J. Matyi, L. H. Schwartz, B. Butt, *Catal. Rev. Sci. Eng.*, 1987, **29**, 41-99.

[72] G. K. Williamson, W. H. Hall, 'X-ray Line Broadening from Filed Al and W*', Acta Metall.*, 1953, **1**, 22.

[73] J. I. Langford, D. Louër, P. Scardi, 'Effect of a crystallite size distribution on X-ray diffraction line profiles and whole-powder-pattern fitting', *J. Appl. Cryst.*, 2000, **33**, 964-974.

[74] T. Ungár, J. Gubicza, G. Ribárik, A. Borbély, 'Crystallite size distribution and dislocation structure determined by diffraction profile analysis: principles and practical application to cubic and hexagonal crystals', *J. Appl. Cryst.*, 2001, **34**, 298-310.

[75] L. H. Germer, A. H. White, *Phys. Rev.*, 1941, **60**, 447.

[76] B. D. Hall, R. Flüeli, R. Monot, J.-P. Borel, *Z. Phys. D: At., Mol. Clusters*, 1989, **12**, 97.

[77] V. Gnutzmann, W. Vogel, 'Structural Sensitivity of the Standard Pt/SiO_2 Catalyst EuroPt-1 to H_2 and O_2 Exposure by In Situ X-ray Diffraction', *J. Phys. Chem.*, 1990, **94**, 4991-4997.

[78] W. Vogel, B. Rosner, B. Tesche, 'Structural Investigations of Au_{55} Organometallic Complexes by X-ray Powder Diffraction and Transmission Electron Microscopy', *J. Phys. Chem.*, 1993, **97**, 11611-11616.

[79] W. Vogel, P. Britz, H. Bönnemann, J. Rothe, J. Hormes, 'Structure and Chemical Composition of Surfactant-Stabilized PtRu Alloy Colloids', *J. Phys. Chem. B*, 1997, **101**, 11029-11036.

[80] E. Garnier, personal communication, Poitiers, March 2001.

[81] H. A. Gasteiger, P. N. Ross, E. J. Cairns, 'LEIS and AES on sputtered and annealed polycrystalline Pt-Ru bulk alloys', *Surf. Sci.*, 1993, **293**, 67-80.

[82] H. Miura, T. Suzuki, Y. Ushikubo, K. Sugiya, M. Matsuda, R. D. Gonzales, 'The Surface Composition and Structure of Supported Pt-Ru Bimetallic Clusters', *J. Catal.*, 1984, **85**, 331.

[83] R. Liu, H. Iddir, Q. Fan, G. Hou, A. Bo, K. L. Ley, E. S. Smotkin, Y.-E. Sung, H. Kim, S. Thomas, A. Wieckowski, 'Potential-Dependent Infrared Absorption Spectroscopy of Adsorbed CO and X-ray Photoelectron Spectroscopy of Arc-Melted Single-Phase Pt, PtRu, PtOs, PtRuPs, and Ru Electrodes', *J. Phys. Chem. B*, 2000, **104**, 3518-3531.

[84] H. Igarashi, T. Fujino, Y. Zhu, H. Uchida, M. Watanabe, 'CO Tolerance of Pt alloy electrocatalysts for polymer electrolyte fuel cells and the detoxification mechanism', *Phys. Chem. Chem. Phys.*, 2001, **3**, 306-315.

[85] A. Hamnett, B. J. Kennedy, 'Bimetallic Carbon Supported Anodes for the Direct Methanol-Air Fuel Cell', *Electrochim. Acta*, 1988, **33** (11), 1613-1618.

[86] J. Pollmann, R. Franke, J. Hormes, H. Bönnemann, W. Brijoux, A. Schulze Tilling, 'An X-ray photoelectron spectroscopy investigation of a novel Pd-Pt colloid catalyst', *J. Electron Spectrosc. Relat. Phenom.*, 1998, **94**, 219-227.

[87] C. C. Kao, S. C. Tsai, M. K. Bahl, Y. W. Chung, W. J. Lo, *Surf. Sci.*, 1980, **95**, 1.

[88] W. Eberhardt, P. Fayet, D. Cox, Z. Fu, A. Kaldor, R. Sherwood, D. Sondericker, 'Photoemission from Mass-Selected Monodispersed Pt Clusters', *Phys. Rev. Lett.*, 1990, **64**, 780.

[89] R. Franke, Habilitationsschrift, Bonn, 1999.

[90] X. Cheng, B. Yi, M. Han, J. Zhang, Y. Qiao, J. Yu, 'Investigation of platinum utilization and morphology in catalyst layers of polymer electrolyte fuel cells', *J. Power Sources*, 1999, **79**, 75-81.

[91] V. Radmilovic, H. A. Gasteiger, P. N. Ross, 'Structure and Chemical Composition of a Supported Pt-Ru Electrocatalyst for Methanol Oxidation', *J. Catal.*, 1995, **154**, 98-106.

[92] C. Goyhenex, C. R. Henry, 'In-situ measurements of the lattice parameter of supported palladium clusters', *Phil. Mag.*, 1994, **69** (6), 1073-1084.

[93] C. Solliard, M. Flüeli, 'Surface stress and size effect on the lattice parameter in small particles of gold and platinum', *Surf. Sci.*, 1985, **156**, 487.

[94] K. Narui, H. Yata, K. Furuta, A. Nishida, Y. Kohtoku, T. Matsuzaki, 'Effects of addition of Pt to PdO/Al_2O_3 catalyst on catalytic activity for methane combustion and TEM observations of supported particles', *Appl. Catal. A*, 1999, **179**, 165-173.

[95] T. J. Schmidt, M. Noeske, H. A. Gasteiger, R. J. Behm, P. Britz, H. Bönnemann, 'PtRu Alloy Colloids as Precursors for Fuel Cell Catalysts', *J. Electrochem. Soc.*, 1998, **145** (3), 925-931.

[96] C. Cattaneo, M. I. Sanchez de Pinto, H. Mishima, B. A. López de Mishima, D. Lescano, L. Cornaglia, 'Characterization of platinum-ruthenium electrodeposits using XRD, AES and XPS analysis', *J. Electroanal. Chem.*, 1999, **461**, 32-39.

[97] K. Lasch, L. Jörissen, J. Garche, 'The effect of metal oxides as co-catalysts for the electro-oxidation of methanol on platinum-ruthenium', *J. Power Sources*, 1999, **84**, 225-230.

[98] C. Roth, M. Goetz, H. Fuess, 'Synthesis and characterization of carbon-supported Pt-Ru-WO_x catalysts by spectroscopic and diffraction methods', *J. Appl. Electrochem.*, 2001, **31 (7)**, 793-798.

[99] P. L. Hagans, K. E. Swider, D. R. Rolinson, 'The Chemical State of Ru in Pt-Ru Direct Methanol Fuel Cell Anode Electrocatalysts', *Electrochem. Soc. Proc.*, 1997, **13**, 86-105.

[100] J. T. Mueller, P. M. Urban, 'Characterization of direct methanol fuel cells by ac impedance spectroscopy', *J. Power Sources*, 1998, **75**, 139-143.

[101] J. T. Mueller, P. M. Urban, W. F. Hoelderich, 'Impedance studies on direct methanol fuel cell anodes', *J. Power Sources*, 1999, **84**, 157-160.

[102] C. A. Schiller, F. Richter, E. Gülzow, N. Wagner, 'Relaxation impedance as a model for the deactivation mechanism of fuel cells due to carbon monoxide poisoning', *Phys. Chem. Chem. Phys.*, 2001, **3**, 2113-2117.

[103] A. Hamnett, B. J. Kennedy, F. E. Wagner, 'Pt-Ru Anodes for Methanol Electrooxidation: A Ruthenium-99 Mössbauer Study', *J. Catal.*, 1990, **124**, 30-40.

[104] D. A. Scherson, C. Fierro, E. B. Yeager, M. E. Kordesch, J. Eldridge, R. W. Hoffman, A. Barnes, 'In Situ Mössbauer Spectroscopy on an Operating Fuel Cell', *J. Electronanal. Chem.*, 1984, **169**, 287-302.

[105] H. Miura, R. D. Gonzalez, 'Temperature-Programmed Desorption and Temperature-Programmed Reaction Studies of CO over Well-Characterized Silica-Supported Pt-Ru Bimetallic Clusters', *J. Phys. Chem.*, 1982, **86**, 1577-1582.

[106] J. Bergeld, B. Kasemo, D. V. Chakarov, 'CO oxidation on Pt(111) promoted by coadsorbed H_2O', *Surf. Sci.*, 2001, **495** (3), L815-821.

[107] H.-G. Haubold, P. Hiller, H. Jungbluth, T. Vad, 'Characterization of Electrocatalysts by In Situ SAXS and XAS Investigations', *Jpn. J. Appl. Phys.*, 1999, **38**, 36-39.

[108] F. Atamny, A. Baiker, 'Investigation of carbon-based catalysts by scanning tunneling microscopy: Opportunities and limitations', *Appl. Catal.*, 1998, **173**, 201-230.

[109] A. Crown, A. Wieckowski, 'Scanning tunneling microscopy investigations of ruthenium- and osmium-modified Pt(100) and Pt(110) single crystal substrates', *Phys. Chem. Chem. Phys.*, 2001, **3**, 3290-3297.

[110] J. P. Bucher, J. Buttet, J. J. van der Klink, M. Graetzel, E. Newson, T. B. Troung, '^{195}Pt NMR Studies of Supported Catalysts', *Colloids and Interfaces*, 1989, **36**, 155.

[111] C. Rice, Y. Tong, E. Oldfield, A. Wieckowski, 'Cyclic voltammetry and ^{195}Pt nuclear magnetic resonance characterization of graphite-supported commercial fuel cell grade platinum electrocatalysts', *Electrochim. Acta*, 1998, **43**, 2825-2830.

[112] Y. Tong, C. Rice, N. Godbout, A. Wieckowski, E. Oldfield, 'Correlation between the Knight Shift of Chemisorbed CO and the Fermi Level Local Density of States at Clean Platinum Catalyst Surfaces', *J. Am. Chem. Soc.*, 1999, **121**, 2996-3003.

[113] Y. Tong, C. Rice, A. Wieckowski, E. Oldfield, 'A Detailed NMR-Based Model for CO on Pt Catalysts in an Electrochemical Environment: Shifts, Relaxation, Back-Bonding, and the Fermi-Level Local Density of States', *J. Am. Chem. Soc.*, 2000, **122**, 1123-1129.

[114] Y. Tong, C. Rice, A. Wieckowski, E. Oldfield, '^{195}Pt NMR of Platinum Electrocatalysts: Friedel-Heine Invariance and Correlations between Platinum Knight Shifts, Healing Length, and Adsorbate Electronegativity', *J. Am. Chem. Soc.*, 2000, **122**, 11921-11924.

[115] C. Rice, Y. Tong, E. Oldfield, A. Wieckowski, F. Hahn, F. Gloaguen, J.-M. Léger, C. Lamy, 'In Situ Infrared Study of Carbon Monoxide Adsorbed onto Commercial Fuel-Cell-Grade Carbon-supported Platinum Nanoparticles: Correlation with ^{13}C NMR results', *J. Phys. Chem. B*, 2000, **104**, 5803-5807.

[116] K. Kunimatsu, K. Shimazu, H. Kita, 'Electrochemical oxidation of CO on Pt in acidic and base solutions. Part II. Structural change of the Pt surface and mechanism of electrooxidation of CO studied by in-situ infrared reflection spectroscopy', *J. Electroanal. Chem.*, 1988, **256**, 371-385.

[117] A. V. Petukhov, W. Akemann, K. A. Friedrich, U. Stimming, 'Kinetics of electrooxidation of a CO monolayer at the platinum/electrolyte interface', *Surf. Sci.*, 1998, **402-404**, 182-189.

[118] R. Ianiello, V. M. Schmidt, U. Stimming, J. Stumper, A. Wallau, 'CO Adsorption and Oxidation on Pt and Pt-Ru Alloys: Dependence on Substrate Composition', *Electrochim. Acta,* 1994, **39**, 1863-1869.

[119] M.-S. Zheng, S.-G. Sun, S.-P. Chen, 'Abnormal infrared effects and electrocatalytic properties of nanometer scale thin films of PtRu alloys for CO adsorption and oxidation', *J. Appl. Electrochem.*, 2001, **31**, 749-757.

[120] Y. Morimoto, E. B. Yeager, 'Comparison of methanol oxidations on Pt, Pt/Ru and Pt/Sn electrodes', *J. Electroanal. Chem.*, 1998, **444**, 95-100.

[121] P. A. Christensen, A. Hamnett, J. Munk, G. L. Troughton, 'An in situ FTIR study of the electrochemical oxidation of methanol at small platinum particles', *J. Electroanal. Chem.*, 1994, **370**, 251-258.

[122] G. Vlaic, D. Andreatta, P. E. Colavita, 'Characterisation of heterogeneous catalysts by EXAFS', *Catal. Today*, 1998, **41**, 261-275.

[123] S. D. Lin, T.-C. Hsiao, J.-R. Chang, A. S. Lin, 'Morphology of Carbon Supported Pt-Ru Electrocatalyst and the CO Tolerance of Anodes for PEM Fuel Cells', *J. Phys. Chem. B*, 1999, **103**, 97-103.

[124] T. Page, R. Johnson, J. Hormes, S. Noding, B. Rambabu, ' A study of methanol electro-oxidation reactions in carbon membrane electrodes and structural properties of Pt alloy electro-catalysts by EXAFS', *J. Electroanal. Chem.*, 2000, **485**, 34-41.

[125] A. I. Frenkel, C. W. Hills, R. G. Nuzzo, 'A View from the Inside: Complexity in the Atomic Scale Ordering of Supported Metal Nanoparticles', *J. Phys. Chem*., 2001, **105** (51), 1268912703.

[126] S. Mukerjee, J. McBreen, 'Effect of particle size on the electrocatalysis by carbon-supported Pt electrocatalysts: an in situ XAS investigation', *J. Electroanal. Chem.*, 1998, **448**, 163-171.

[127] M.-K. Min, J. Cho, K. Cho, H. Kim, 'Particle size and alloying effects of Pt-based alloy catalysts for fuel cell applications', *Electrochim. Acta*, 2000, **45**, 4211-4217.

[128] J. McBreen, 'In Situ Synchrotron Techniques in Electrochemistry', in *Physical Electrochemistry: Principles, Methods and Applications*, I. Rubinstein (Ed), Marcel Dekker, Inc., New York, Basel, Hongkong, 1995, 339-391.

[129] J. McBreen, S. Mukerjee, 'In Situ X-ray Absorption Studies of Carbon-supported Pt and Pt Alloy Nanoparticles', in *Interfacial Electrochemistry*, A. Wieckowski (Ed), Marcel Dekker, New York, 1998, 895-914.

[130] M. S. Nashner, A. I. Frenkel, D. L. Adler, J. R. Shapley, R. G. Nuzzo, 'Structural Characterization of Carbon-Supported Platinum-Ruthenium Nanoparticles from the Molecular Cluster Precursor $PtRu_5C(CO)_{16}$', *J. Am. Chem. Soc.*, 1997, **119**, 7760-7771.

[131] M. S. Nashner, A. I. Frenkel, D. Somerville, C. W. Hills, J. R. Shapley, R. G. Nuzzo, 'Core Shell Inversion during Nucleation and Growth of Bimetallic Pt/Ru Nanoparticles', *J. Am. Chem. Soc.*, 1998, **120**, 8093-8101.

[132] C. W. Hills, M. S. Nashner, A. I. Frenkel, J. R. Shapley, R. G. Nuzzo, 'Carbon Support Effects on Bimetallic Pt-Ru Nanoparticles Formed from Molecular Precursors', *Langmuir*, 1999, **15**, 690-700.

[133] R. A. Lampitt, L. P. L. Carrette, M. P. Hogarth, A. E. Russell, 'In situ and model EXAFS studies of electrocatalysts for methanol oxidation', *J. Electroanal. Chem.*, 1999, **460**, 80-87.

[134] J. McBreen, S. Mukerjee, 'In Situ X-Ray Absorption Studies of a Pt-Ru Electrocatalyst', *J. Electrochem. Soc.*, 1995, **142** (10), 3399-3404.

[135] S. Mukerjee, J. McBreen, 'Hydrogen Electrocatalysis by Carbon Supported Pt and Pt Alloys', *J. Electrochem. Soc.*, 1996, **143** (7), 2285-2294.

[136] D. Aberdam, R. Durand, R. Faure, F. Gloaguen, J. L. Hazemann, E. Herrero, A. Kabbabi, O. Ulrich, 'X-ray absorption near edge structure study of the electro-oxidation reaction of CO on $Pt_{50}Ru_{50}$ nanoparticles', *J. Electroanal. Chem.*, 1995, **398**, 43-47.

[137] S. Maniguet, R. J. Mathew, A. E. Russell, 'EXAFS of Carbon Monoxide Oxidation on Supported Pt Fuel Cell Electrocatalysts', *J. Phys. Chem. B*, 2000, **104**, 1998-2004.

[138] W. E. O'Grady, P. L. Hagans, K. I. Pandya, D. L. Maricle, 'Structure of Pt/Ru Catalysts Using X-ray Absorption Near Edge Structure Studies', *Langmuir*, 2001, **17**, 3047-3050.

[139] B. W. Holland, J. B. Pendry, R. F. Pettifer, J. Bordas, *J. Phys. C: Solid State Phys.*, 1978, **11**, 633.

[140] D. E. Ramaker, B. L. Mojet, D. C. Koningsberger, W. E. O'Grady, 'Understanding atomic x-ray absorption fine structure in x-ray absorption spectra', *J. Phys.: Condens. Matter*, 1998, **10**, 8753-8770.

[141] J. J. Rehr, S. I. Zabinsky, A. Ankudinov, R. C. Albers, 'Atomic-XAFS and XANES', *Physica B*, 1995, **208/209**, 23-26.

[142] W. E. O'Grady, X. Qian, D. E. Ramaker, 'Systematic Chemical Effects Observed in "Atomic" X-ray Absorption Fine Structure', *J. Phys. Chem. B*, 1997, **29**, 5624-5626.

[143] W. E. O'Grady, D. E. Ramaker, 'Atomic X-ray absorption fine structure: a new tool for examining electrochemical interfaces', *Electrochim. Acta*, 1998, **44**, 1283-1287.

[144] A. Russell, personal communication, Loughborough, 2001.

[145] G. Köhl, personal communication, Pommersfelden, 2001.

[146] G. Tremiliosi-Filho, H. Kim, W. Chrzanowski, A. Wieckowski, B. Grzybowska, P. Kulesza, 'Reactivity and Activation Parameters in Methanol Oxidation on Platinum Single Crystal Electrodes Decorated by Ruthenium Adlayers', *J. Electroanal. Chem.*, 1999, **467**, 143-156.

[147] Y. Ishikawa, M. S. Liao, C. R. Cabrera, 'Oxidation of methanol on platinum, ruthenium and mixed Pt-M metals (M=Ru, Sn): a theoretical study', *Surf. Sci*., 2000, **463**, 66-80.

[148] H. A. Gasteiger, N. M. Markovic, P. N. Ross, E. J. Cairns, 'CO Electrooxidation on Well-Characterized Pt-Ru Alloys', *J. Phys. Chem.*, 1994, **98**, 617-625.

[149] H. A. Gasteiger, N. M. Markovic, P. N. Ross, E. J. Cairns, 'H_2 and CO Electrooxidation on Well-Characterized Pt, Ru, and Pt-Ru. 1. Rotating Disk Electrode Studies of the Pure Gases Including Temperature Effects', *J. Phys. Chem.*, 1995, **99**, 8290-8301.

[150] H. A. Gasteiger, N. M. Markovic, P. N. Ross, E. J. Cairns, 'H_2 and CO Electrooxidation on Well-Characterized Pt, Ru, and Pt-Ru. 2. Rotating Disk Electrode Studies of CO/H_2 Mixtures at 62°C', *J. Phys. Chem.*, 1995, **99**, 16757-16767.

[151] C. Lu, R. I. Masel, 'The Effect of Ruthenium on the Binding of CO, H_2, and H_2O on Pt(110)', *J. Phys. Chem. B*, 2001, **105**, 9793-9798.

[152] Q. Ge, S. Desai, M. Neurock, K. Kourtakis, 'CO Adsorption on Pt-Ru Surface Alloys and on the Surface of Pt-Ru Bulk Alloys', *J. Phys. Chem. B*, 2001, **105**, 9533-9538.

[153] H. Hoster, T. Iwasita, H. Baumgärtner, W. Vielstich, 'Current-Time Behavior of Smooth and Porous PtRu Surfaces for Methanol Oxidation', *J. Electrochem. Soc.*, 2001, **148** (5), A496-501.

[154] W. Chrzanowski, A. Wieckowski, 'Surface Structure Effects in Platinum/Ruthenium Methanol Oxidation Electrocatalysis', *Langmuir*, 1998, **14**, 1967-1970.

[155] T. Iwasita, H. Hoster, A. John-Anacker, W. F. Lin, W. Vielstich, 'Methanol Oxidation on PtRu Electrodes. Influence of Surface Structure and Pt-Ru Atom Distribution', *Langmuir*, 2000, **16**, 522-529.

[156] E. Auer, A. Freund, T. Lehmann, K.-A. Starz, R. Schwarz, U. Stenke, EP 0 880 188 A2.

[157] H. Bönnemann, W. Brijoux, R. Brinkmann, E. Dinjus, T. Joußen, B. Korall, 'Erzeugung von kolloidalen Übergangsmetallen in organischer Phase und ihre Anwendung in der Katalyse', *Angew. Chem., Int. Ed. Engl.*, 1991, **30**, 1312-1314.

[158] J. B. Goodenough, A. Hamnett, B. J. Kennedy, R. Manoharan, S. A. Weeks, 'Porous Carbon anodes for the direct methanol fuel cell - I. The role of the reduction method for carbon supported platinum electrodes', *Electrochim. Acta*, 1990, **35**, 199-207.

[159] M. Götz, H. Wendt, 'Binary and ternary anode catalyst formulations including the elements W, Sn and Mo for PEMFCs operated on methanol and reformate gas', *Electrochim. Acta*, 1998, **43 (24)**, 3637-3644.

[160] J. Rodriguez-Carvajal, 'FULLPROF: A Program for Rietveld Refinement and Pattern Matching Analysis', *Abstracts of the Satellite Meeting on Powder Diffraction of the XV Congress of the IUCr*, Toulouse, France, 1990, 127.

[161] I. Kojima and M. Kurahashi, *J. Electr. Spectr. Rel. Phen.*, 1987, **42**, 177.

[162] P. Froment, M.J. Genet and M. Devillers, 'Surface reduction of ruthenium compounds with long exposure to an X-ray beam in photoelectron spectroscopy', *J. Electron Spectr. Rel. Phen.*, 1999, **104**, 119-126.

[163] K. V. Ramesh, P. R. Sarode, S. Vasudevan, A. K. Shukla, 'Preparation and Characterization of Carbon-based Fuel Cell Electrodes with Platinum-Group Bimetallic Catalysts', *J. Electroanal. Chem.*, 1987, **223**, 91-106.

[164] E.A. Stern and K. Kim, 'Thickness Effect on the Extended-X-ray-Absorption Fine-Structure Amplitude', *Phys. Rev. B*, 1981, **23**(8), 3781.

[165] http://ixs.csrri.iit.edu/database/programs/mcmaster.html

[166] T. Ressler, 'WinXAS: A program for x-ray absorption spectroscopy data analysis under MS-Windows', *J. Synchr. Rad*., 1998, **5**, 118-122.

[167] A. L. Ankudinov, B. Ravel, J. J. Rehr, S. D. Conradson, 'Real-space multiple-scattering calculation and interpretation of x-ray absorption near-edge structure', *Phys. Rev. B*, 1998, **58**, 7565-7576.

[168] M. S. Wilson and S. Gottesfeld, 'Thin-film catalyst layers for polymer electrolyte fuel cell electrodes', *J. Appl. Electrochem.*, 1992, **22**, 1-7.

[169] a) M. Götz, H. Wendt, 'Composite Electrocatalysts for anodic methanol and methanol-reformate oxidation', *J. Appl. Electrochem.*, 2001, **31**, 811-817.
b) M. Götz, 'Katalysatorentwicklung für die anodische Oxidation von Methanol und CO-haltigem Wasserstoff in Membranbrennstoffzellen', PhD thesis, Darmstadt, 1999.

[170] S. Brunnauer, P. H. Emmett und E. Teller, *J. Amer. Chem. Soc*. , 1938, **60**, 309.

[171] J. Scherer, personal communication, Pommersfelden, 2001.

[172] J. F. Moulder, W. F. Stickle, P. E. Sobol and K. D. Bomben in *Handbook of X-ray photoelectron spectroscopy*, J. Chastain, R. C. King jr. (Eds), 1992.

[173] M. Ya. Gamarnik, 'On the Physical Nature of the Decrease in Lattice Parameters of the Small Metal Particles', *Phys. Stat. Sol. B*, 1990, **160**, K1-4.

[174] J. F. Berar, P. Lelann, 'E.s.d.'s and estimated probable error obtained in Rietveld refinements with local correlations', *J. Appl. Cryst.*, 1991, **24**, 1-5.

[175] J.H. Vleeming, B.F.M. Kuster, G.B. Marin, F. Oudet, P. Courtine, 'Graphite-supported platinum catalysts: Effects of gas and aqueous phase treatments', *J. Catal*., 1997, **166**, 148-159.

[176] B. Krause, 'Chemische Zusammensetzung, Nanomorphologie und elektrokatalytische Aktivität von Mischkatalysatoren für die Direktoxidation von Methanol in Membranbrennstoffzellen', Diploma thesis, Darmstadt, 1998.

[177] A. Kucernak, personal communication, Loughborough, 2001.

Figure index

Chapter 2

Chapter 4

Chapter 5

Table index

Abbreviations

AAS	atomic absorption spectroscopy
AES	Auger electron spectroscopy
AFC	alkaline fuel cell
AFM	atomic force microscopy
AXAFS	atomic X-ray absorption fine structure
BE	binding energy
BET	Brunauer-Emmett-Teller (isotherme)
BSE	backscattered electrons
CV	cyclic voltammetry
DEMS	differential electrochemical mass spectrometry
DFA	differential Fourier analysis
DMFC	direct methanol fuel cell
DTA	differential thermo analysis
EIS	electrochemical impedance spectroscopy
ESR	electron spin resonance (spectroscopy)
EXAFS	extended X-ray absorption fine structure
FTIRS	Fourier transform infrared spectroscopy
FT-IRAS	Fourier transform infrared absorption spectroscopy
FWHM	full width half maximum
HOR	hydrogen oxidation reaction
HREM	high resolution electron microscopy
HRTEM	high resolution transmission electron microscopy
IMFC	indirect methanol fuel cell
IR	infrared (spectroscopy)
LEED	low energy electron diffraction
LEIS	low energy ion scattering
MCFC	molten carbonate fuel cell

MEA	membrane electrode assembly
MOR	methanol oxidation reaction
Nano-EDX	nano-sized energy dispersive X-ray analysis
NMR	nuclear magnetic resonance (spectroscopy)
ORR	oxygen reduction reaction
PAFC	phosphoric acid fuel cell
PEMFC	polymer electrolyte / proton exchange membrane fuel cell
PROX	preferential oxidation reaction
RDE	rotating disc electrode
RHE	reversible hydrogen electrode
RT	room temperature
SAXS	small angle X-ray spectroscopy
SE	secondary electrons
SEELFS	surface electron energy loss fine structure
SEM	scanning electron microscopy
SFG	sum frequency generation
SNIFTIRS	subtractively normalized intensity Fourier transform infrared spectroscopy
SOFC	solid oxide fuel cell
SPAIRS	single potential altered infrared spectroscopy
SPM	surface probe microscopies
STM	scanning tunneling microscopy
TEM	transmission electron microscopy
TGA	thermo gravimetric analysis
THF	tetrahydrofurane
TPD	temperature programmed desorption
TPR	temperature programmed reaction
UHV	ultra-high vacuum
VIS	visible light
XAFS	X-ray absorption fine structure
XANES	X-ray absorption near edge structure
XAS	X-ray absorption spectroscopy
XFA	X-ray fluorescence analysis
XPS	X-ray photoelectron spectroscopy
XRD	X-ray diffraction

Symbol index

ΔA	step height
A	absorption [1/cm]
A	area [cm²]
a	activity
a	lattice parameter [Å]
c	concentration [mol/l]

c_0	bulk concentration [mol/l
c_s	surface concentration [mol/l
D	Diffusion coefficient [cm²/s]
D	particle size [nm]
d	lattice distance [Å]
d	thickness [cm]
E	potential [V]
E_0	zero-current cell voltage, electro-motive force [V]
EMF	electro-motive force [V]
E_r	rest potential [V]
F	Faraday constant
G_r	*Gibbs* free energy [kJ/mol]
H	Enthalpie [kJ/mol]
h	*Planck*'s constant
I	current [A]
I	intensity [counts]
i	current density [A/cm²]
i_0	exchange current density [A/cm²]
i_a	anodic current density [A/cm²]
i_c	cathodic current density [A/cm²]
J	total flux [mol/s]
j	total flux density [mol/(cm²s)]
K	shape factor
m_0	sample mass [g]
N	coordination number
p	pressure [Pa]
Q	charge [C]
R	gas constant
R	resistance [Ω]
R_E	reflectivity
r	atomic distance [1/Å]
S	entropy
S	specific surface area [m²/g]
S_0	cross-sectional area of the XAS pellet [cm²]
T	temperature [K]
t	time [s]
ΔV	potential difference
V	volume [m³]
W_{el}	electrical work [J]
w	weight percent
x	distance [cm]
α	asymmetry parameter
β	asymmetry parameter

δ_N	Nernst diffusion layer thickness [cm]
η	efficiency [%]
η	overpotential [V]
η_a	anodic overpotential [V]
η_c	cathodic overpotential [V]
λ	wavelength [cm]
μ	absorption coefficient
μ/ρ	absorption cross-section [cm²/g]
ν	frequency [1/cm]
ν	sweep rate [cm/s]
ν_e	number of exchanged electrons
θ	angle [°]
θ	degree of coverage [atoms/cm²]
ρ	density [g/l]
σ	cross-section [1/cm²]

Danksagung

An dieser Stelle möchte ich mich ganz herzlich bedanken

- bei **Herrn Prof. H. Fueß** für die ansprechende und zukunftsorientierte Themenstellung und das große Maß an eigenverantwortlichem Handeln, das er mir während meiner Arbeit zugestand, sowie für seine herzliche Betreuung
- bei **Herrn Prof. Wendt**, der immer ein offenes Ohr für die Probleme eines Materialwissenschaftlers mit der Elektrochemie hatte und sich viel Zeit für kurzweilige Diskussionen nahm.

in Poitiers:
- bei **Herrn Prof. C. Lamy** für die freundliche Aufnahme in seinen Arbeitskreis und sein Bemühen um die "deutsch-französische Verständigung"
- bei **Herrn Dr. J.-M. Léger**, der mich in die Geheimnisse der zyklischen Voltametrie einweihte,
- bei **Herrn Prof. N. Alonso-Vante** für seine Herzlichkeit und die zahlreichen "multilingualen" Treffen mit seinen Doktoranden
- bei **Frau Dr. F. Hahn**, mit der ich viele Stunden am FTIR-Spektrometer - aber auch in gemütlichen morgendlichen Kaffeerunden - verbrachte
- bei **Séverine**, **Magalie** und **Ibtissam** für ihre Freundschaft und den Urlaub in Royan
- sowie bei den Doktoranden und DEA der Arbeitsgruppe in Poitiers, die mich vorbehaltlos und herzlich in ihren Kreis aufnahmen.

in Darmstadt:
- bei **N. Martz** und **G. Miehe** für die zahlreichen TEM-Untersuchungen
- bei meinen Meßhelfern **N. Martz, T. Buhrmester, R. Theissmann** und **A. Adams** für nervenstrapazierende und nachtschichtintensive EXAFS-Messungen am Hasylab
- bei **T. Hartmann** und **D. Rafaja** für ihre Ausdauer darin, mir die Grundlagen der Röntgenbeugung und Rietveldanalyse näherzubringen
- bei **E.G. Franco** (IPEN, Saõ Paulo, Brasilien) für die überaus angenehme Zusammenarbeit bei seinem Aufenthalt in unserer Arbeitsgruppe und seine ausgeprägte Diskussionsbereitschaft
- bei **M. Beerbom**, **J. Fritsche** und **T. Mayer** (Arbeitskreis Jägermann) für ihre Hilfe bei den XPS-Messungen und deren Auswertung sowie bei **T. Kessler**, **M. Heck** und **C. Brockmann** (Arbeitsgruppe Ortner) für die Unterstützung bei RFA und AAS
- bei meinen Vorgängern **M. Götz** und **B. Krause** für die Einführung in die Brennstoffzellentechnik
- bei den **Werkstätten** der Materialwissenschaft und auch der Chemie für die stets reibungslose Zusammenarbeit
- bei **Nathalie** und **Adnan**, die mir in den drei Jahren, in denen wir ein Zimmer teilten, unvermeidlich ans Herz gewachsen sind
- bei meinen Freunden **Ingrid**, **Thomy** und **Martin** für ausdauerndes Korrektur lesen und moralische Unterstützung
- bei meinen **Eltern** und meinem **Bruder**, die mir in dieser Zeit den Rücken freihielten
- sowie bei den Mitgliedern des Arbeitskreises Fueß für drei verrückte und unvergeßliche Jahre.

Nicht zuletzt sei der DFG für die Finanzierung des Forschungsvorhabens Fu 125/34-1,2,3 gedankt.

Curriculum Vitae

Personal

Name: Christina Roth
Date of birth: 05.02.1974, Jugenheim (Germany)
Nationality: German

Scientific Education:

Oct 1993-
Sept 1998 Studies in ***Materials Science***

Main emphasis:
Electrochemistry, Kinetics, Thin Films, Metals and Corrosion

1995 German *Vordiplom*
1998 German *Hauptdiplom*

Diploma Thesis:
Corrosion of Titanium Alloys for Medical Applications

Oct 1998-
present Beginning of doctorate
Structural and Electrochemical Characterization of Carbon-supported Pt-Ru and Pt-Ru-W Catalysts for PEM Fuel Cell Applications

Feb 2001-
June 2001 Stay at the 'Laboratoire de Catalyse en Chimie Organique' (LACCO) in Poitiers (France)

Internships:

Mar 1994 MERCK Darmstadt, Materials Research,
Section *Metals and Corrosion*
Mar 1995-
Oct 1996 GSI Darmstadt, Materials Research Group,
Tribological Investigation of Titanium Alloys for Medical Applications

List of publications:

Research papers

1) C. Roth, N. Martz, H. Fuess, 'Characterization of different Pt-Ru catalysts by X-ray diffraction and transmission electron microscopy', *Phys. Chem. Chem. Phys.* **3** (2001) 315-319.
2) C. Roth, M. Goetz, H. Fuess, 'Synthesis and characterization of carbon-supported Pt-Ru-WO_x catalysts by spectroscopy and diffraction methods', *J. Appl. Electrochem.* **31** (2001) 793-798.
3) E. G. Franco, E. Arico, M. Linardi, C. Roth, N. Martz, H. Fuess, 'Synthesis and characterization of electrocatalyst powders for application in PEM fuel cells', submitted
4) C. Roth, N. Martz, F. Hahn, J.-M. Leger, C. Lamy, H. Fuess, 'Characterization of differently-synthesized Pt-Ru fuel cell catalysts by cyclic voltammetry, FTIR spectroscopy and in single cells', accepted in *J. Electrochem. Soc.*
5) C. Roth, N. Martz, Th. Buhrmester, J. Scherer, H. Fuess, 'In-situ XAFS measurements of a carbon-supported Pt-Ru anode electrocatalyst in hydrogen and direct methanol operation', accepted in *Phys. Chem. Chem. Phys*.

Articles

1) C. Roth, H. Fuess, Z. Lemes, T. Hartkopf, J. Seydel, H. Hahn, 'Die Brennstoffzelle - eine Option für die Zukunft?', *Thema Forschung* 2/2001.

Conferences

1) 99. Bunsentagung in Würzburg (Germany), 1-3rd june 2000, oral presentation
2) European Crystallographic Meeting in Nancy (France), 25-31st august 2000 , oral presentation
3) SCI in Loughborough (UK), 16-19th september 2001, oral presentation

4) XXXII. Katalytikertagung in Friedrichroda (Germany), 17-19th march 1998, poster presentation
5) Ulmer Electrochemical Talks in Ulm (Germany), 26-27th june 2000, poster presentation
6) Usermeeting HASYLAB in Hamburg (Germany), january 26th 2001, poster presentation
7) XXXIV. Katalytikertagung in Weimar (Germany), 21-23rd march 2001, poster presentation
8) Usermeeting HASYLAB in Hamburg (Germany), january 25th 2002, poster presentation
7) X. Katalytikertagung in Weimar (Germany), 20-22nd march 2002, poster presentation

Christina Roth
Rügnerstr. 67 a
64319 Pfungstadt

Darmstadt, den

Eidesstattliche Erklärung

Hiermit erkläre ich an Eides statt, daß ich meine Dissertation selbständig und nur mit den angegebenen Hilfsmitteln angefertigt habe.

_____

Christina Roth

Christina Roth
Rügnerstr. 67 a
64319 Pfungstadt

Darmstadt, den

Erklärung

Hiermit erkläre ich, noch keinen Promotionsversuch unternommen zu haben.

_____

Christina Roth